

**Multiscale Modeling of
Materials—2000**

DISTRIBUTION STATEMENT A
Approved for Public Release
Distribution Unlimited

MATERIALS RESEARCH SOCIETY
SYMPOSIUM PROCEEDINGS VOLUME 653

Multiscale Modeling of Materials—2000

Symposium held November 27–December 1, 2000, Boston, Massachusetts, U.S.A.

EDITORS:

Ladislav P. Kubin

LEM, CNRS-ONERA
Châtillon, France

Robin L. Selinger

Catholic University of America
Washington, D.C., U.S.A.

John L. Bassani

University of Pennsylvania
Philadelphia, Pennsylvania, U.S.A.

Kyeongjae Cho

Stanford University
Stanford, California, U.S.A.



Materials Research Society
Warrendale, Pennsylvania

20010716 102

This work was supported in part by the Office of Naval Research under Grant Number N00014-01-1-0101. The United States Government has a royalty-free license throughout the world in all copyrightable material contained herein.

This work was supported in part by the Army Research Office under Grant Number DAAD19-01-1-0005. The views, opinions, and/or findings contained in this report are those of the author(s) and should not be construed as an official Department of the Army position, policy, or decision, unless so designated by other documentation.

Funding was provided by the National Institute of Standards and Technology: NA1341-01-N-0286.

Single article reprints from this publication are available through
University Microfilms Inc., 300 North Zeeb Road, Ann Arbor, Michigan 48106

CODEN: MRSPDH

Copyright 2001 by Materials Research Society.
All rights reserved.

This book has been registered with Copyright Clearance Center, Inc. For further information, please contact the Copyright Clearance Center, Salem, Massachusetts.

Published by:

Materials Research Society
506 Keystone Drive
Warrendale, PA 15086
Telephone (724) 779-3003
Fax (724) 779-8313
Web site: <http://www.mrs.org/>

Library of Congress Cataloging-in-Publication Data

Multiscale modeling of materials—2000 : symposium held November 27–December 1, 2000,
Boston, Massachusetts, U.S.A. / editors, Ladislav P. Kubin, Robin L. Selinger, John L. Bassani,
Kyeongjae Cho
p.cm.—(Materials Research Society symposium proceedings,
ISSN 0272-9172 ; vol. 653)
Includes bibliographical references and indexes.
ISBN 1-55899-563-3
1. Manufacturing processes—Mathematical models—Congresses. I. Kubin, Ladislav P.
II. Selinger, Robin L. III. Bassani, John L. IV. Cho, Kyeongjae V. Materials Research Society
symposium proceedings ; v. 653
TS183 .M85 2001
670.4—dc21

2001032988

Manufactured in the United States of America

CONTENTS

Preface	ix
Materials Research Society Symposium Proceedings	x

ATOMIC AND MESOSCOPIC STUDIES

Multiscale Modeling of Dislocation Processes in bcc Tantalum: Bridging Atomistic and Mesoscale Simulations	Z1.2
L.H. Yang, Meijie Tang, and John A. Moriarty	
Periodic Boundary Conditions for Dislocation Dynamics Simulations in Three Dimensions	Z1.3
Vasily V. Bulatov, Moon Rhee, and Wei Cai	
Dislocation Exhaustion During Plastic Deformation	Z1.7
Olivier Couteau, Corinne Charbonnier, Tomas Kruml, and Jean-Luc Martin	
New Line Model for Optimized Dislocation Dynamics Simulations	Z1.8
Ronan Madec, Benoit Devincere, and Ladislav P. Kubin	
Interactions Between Edge Dislocations and Interstitial Clusters in Iron and Copper	Z3.4
Yu.N. Osetsky, D.J. Bacon, A. Serra, and B.N. Singh	
Atomic Scale Simulation of the Effect of Hydrogen on Dislocations in Zr	Z3.8
C. Domain and A. Legris	
Bond-Order Potentials With Analytic Environment-Dependent Tight-Binding Integrals: Application to bcc Molybdenum	Z6.3
Matous Mrovec, Duc Nguyen-Manh, David G. Pettifor, and Vaclav Vitek	
Lattice Trapping of Cracks in Fe Using an Interatomic Potential Derived From Experimental Data and Ab Initio Calculations	Z6.4
D. Farkas, M.J. Mehl, and D.A. Papaconstantopoulos	

Hybrid Electronic-Density-Functional/Molecular-Dynamics Simulation on Parallel Computers: Oxidation of Si Surface	Z6.5
Shuji Ogata, Fuyuki Shimojo, Aiichiro Nakano, Priya Vashishta, and Rajiv K. Kalia	
Parallel Tight-Binding Simulations of Nanophase Ceramics: Atomic and Electronic Transport at Grain Boundaries	Z6.7
Kenji Tsuruta, Hiroo Totsuji, and Chieko Totsuji	
Coupling of Length Scales: Hybrid Molecular Dynamics and Finite Element Approach for Multiscale Nanodevice Simulations	Z9.3
Elefterios Lidorikis, Martina E. Bachlechner, Rajiv K. Kalia, George Z. Voyiadjis, Aiichiro Nakano, and Priya Vashishta	
Atomically-Based Field Formulations for Coupled Problems of Composition and Mechanics	Z9.6
Krishna Garikipati and Lori C. Bassman	
Features of Vacancy Interaction With Interstitial Clusters in bcc Metals	Z9.8
Marta Pelfort, Yuri N. Osetsky, and Anna Serra	
Al Grain Boundary Embrittlement Promoted by Na Impurity: An Ab Initio Study	Z7.17
Guang-Hong Lu, Masanori Kohyama, and Ryoichi Yamamoto	
Efficient Treatment of Fixed and Induced Dipolar Interactions	Z7.22
Celeste Sagui and Thomas Darden	

**MESOSCOPIC STUDIES: THIN FILMS
AND LAYERS**

Unstable Motion of an Edge Dislocation in a Solute Atom Atmosphere Studied by Kinetic Monte Carlo Simulations	Z4.7
X.M. Gu and Y.Q. Sun	
Coarse Slip Bands in a Single-Crystalline Aluminum Alloy	Z4.9
Seung-Yong Yang, Xianghong Li, and Wei Tong	
Dynamics and Patterning of Screw Dislocations in Two Dimensions	Z5.4
Robin L.B. Selinger, Brian B. Smith, and Wei-Dong Luo	
Dislocation Multiplication in Germanium Single Crystals	Z5.7
Corinne Charbonnier, Tomas Kruml, and Jean-Luc Martin	

FACET: A Two Dimensional Simulator of Polycrystalline Thin Film Growth	Z10.1
Jie Zhang and James B. Adams	
Calculation of Intrinsic Stresses and Elastic Moduli in Nonhomogeneous Thin Films	Z10.3
Pedro C. Andia, Francesco Costanzo, Gary L. Gray, and Thomas J. Yurick	
Stresses in Thin Coatings from Curvature Measurements on Non-Planar Substrates	Z10.4
A. Wikström and P. Gudmundson	
Modeling Stress and Failure in Shrinking Coatings	Z10.5
Herong Lei, Lorraine F. Francis, William W. Gerberich, and L.E. Scriven	
A Method to Simulate the Interface-Diffusion in Solid-State Bonding-Processes Considering the Elastic Deformation	Z10.8
Takehiko Ito, Shigeki Saito, Kunio Takahashi, and Tadao Onzawa	
Effective Determination of Coexistence Curves Using Reversible-Scaling Molecular Dynamics Simulations	Z10.9
Maurice de Koning, Alex Antonelli, and Sidney Yip	
Monte-Carlo Simulation of Three-Dimensional Ion Dynamics in Polymers	Z10.10
A. Wagner and H. Kliem	
Self-Affinity Analysis of the Fracture Surfaces of Polypropylene and Opal Glass	Z7.7
M. Hinojosa, E. Reyes, C. Guerrero, and U. Ortiz	

***MECHANICS OF PLASTICITY
AND FRACTURE***

A Discrete Dislocation Approach to Crack Propagation	Z2.4
E.D. Metselaar, J.Th.M. De Hosson, and E. Van der Giessen	
Mechanics of Crack Bridging Under Dynamic Loads	Z2.5
N. Sridhar, B.N. Cox, C.L. Dunn, and I.J. Beyerlein	

Multiscale Simulations of Brittle Fracture and the Quantum-Mechanical Nature of Bonding in Silicon	Z2.7
N. Bernstein and D. Hess	
Crack Behavior at Bi-Crystal Interfaces: A Mixed Atomistic and Continuum Approach	Z2.9
Arun R. Pillai and Ronald E. Miller	
*Cosserat Modeling of Size Effects in Crystalline Solids	Z8.2
Samuel Forest	
*Intrinsic and Extrinsic Size Effects in Plasticity by Dislocation Glide	Z8.5
J. Gil Sevillano	
Experimental Assessment of Strain Gradient Plasticity	Z8.6
Monica M. Barney, Geoffrey H. Campbell, James S. Stölken, Adam J. Schwartz, Jürgen M. Plitzko, Wayne E. King, and John W. Morris, Jr.	
Micromechanical Modeling of Two-Phase Steels	Z8.8
Mikael Nygåards, Dilip Chandrasekaran, and Peter Gudmundson	
Transition Regime Fracture Toughness-Temperature Properties of Two Advanced Ferritic-Martensitic Steels	Z7.8
Philippe Spätig, Eric Donahue, George R. Odette, Glenn E. Lucas, and Max Victoria	
A Theory for Multi Damage Evaluation of TiN Thin Film	Z7.10
Kazunori Misawa, Tomonaga Okabe, Masaaki Yanaka, Masao Shimizu, and Nobuo Takeda	
Modeling of the Heterogeneous Deformation of an Aggregate of Grains	Z7.11
Philippe P. Ericau, Thierry P. Hoc, and Colette C. Rey	

Author Index

Subject Index

*Invited Paper

PREFACE

Multiscale simulation and modeling of materials phenomena have received much attention in many engineering and scientific disciplines including mechanics, physics and materials sciences, with far reaching applications to electronic materials, polymers and biochemical systems. With rapid advances in computing power and multiscale simulation techniques, the hope of modeling material behavior beginning with atomistic simulation and reaching macroscopic phenomena is becoming a realistic goal.

This volume contains papers presented at Symposium Z, "Multiscale Materials Modeling," at the 2000 MRS Fall Meeting in Boston, Massachusetts. This symposium brought scientists from various disciplines together to discuss the state-of-the-art methodologies for linking different length and time scales, and for understanding and predicting the behavior of complex materials systems. The symposium was organized around several major themes representing current challenges in multiscale simulation and modeling: length-scale and time-scale problems, applications to microstructure evolution, plastic deformation and fracture, multiscale modeling schemes, length scales and size effects. We hope that this volume will serve as a useful tool for the reader interested in these recent achievements.

The support of the Army Research Office, the Office of Naval Research and the National Institute of Standards and Technology-Center for Theoretical/Computational Materials Science is gratefully acknowledged. Thanks are due to Huajian Gao who assisted in the preliminary planning of the symposium.

Ladislav P. Kubin
Robin L. Selinger
John L. Bassani
Kyeongjae Cho

February 2001

MATERIALS RESEARCH SOCIETY SYMPOSIUM PROCEEDINGS

- Volume 609 Amorphous and Heterogeneous Silicon Thin Films 2000, R.W. Collins, H.M. Branz, M. Stutzmann, S. Guha, H. Okamoto, 2001, ISBN: 1-55899-517-X
- Volume 610 Si Front-End Processing Physics and Technology of Dopant-Defect Interactions II, A. Agarwal, L. Pelaz, H-H. Vuong, P. Packan, M. Kase, 2001, ISBN: 1-55899-518-8
- Volume 611 Gate Stack and Silicide Issues in Silicon Processing, L.A. Clevenger, S.A. Campbell, P.R. Besser, S.B. Herner, J. Kittl, 2001, ISBN: 1-55899-519-6
- Volume 612 Materials, Technology and Reliability for Advanced Interconnects and Low-k Dielectrics, G.S. Oehrlein, K. Maex, Y-C. Joo, S. Ogawa, J.T. Wetzell, 2001, ISBN: 1-55899-520-X
- Volume 613 Chemical-Mechanical Polishing 2000 Fundamentals and Materials Issues, R.K. Singh, R. Bajaj, M. Moynpour, M. Meuris, 2001, ISBN: 1-55899-521-8
- Volume 614 Magnetic Materials, Structures and Processing for Information Storage, B.J. Daniels, T.P. Nolan, M.A. Seigler, S.X. Wang, C.B. Murray, 2001, ISBN: 1-55899-522-6
- Volume 615 Polycrystalline Metal and Magnetic Thin Films 2001, B.M. Clemens, L. Gignac, J.M. MacLaren, O. Thomas, 2001, ISBN: 1-55899-523-4
- Volume 616 New Methods, Mechanisms and Models of Vapor Deposition, H.N.G. Wadley, G.H. Gilmer, W.G. Barker, 2000, ISBN: 1-55899-524-2
- Volume 617 Laser-Solid Interactions for Materials Processing, D. Kumar, D.P. Norton, C.B. Lee, K. Ebihara, X.X. Xi, 2001, ISBN: 1-55899-525-0
- Volume 618 Morphological and Compositional Evolution of Heteroepitaxial Semiconductor Thin Films, J.M. Millunchick, A-L. Barabasi, N.A. Modine, E.D. Jones, 2000, ISBN: 1-55899-526-9
- Volume 619 Recent Developments in Oxide and Metal Epitaxy Theory and Experiment, M. Yeadon, S. Chiang, R.F.C. Farrow, J.W. Evans, O. Auciello, 2000, ISBN: 1-55899-527-7
- Volume 620 Morphology and Dynamics of Crystal Surfaces in Complex Molecular Systems, J. DeYoreo, W. Casey, A. Malkin, E. Vlieg, M. Ward, 2001, ISBN: 1-55899-528-5
- Volume 621 Electron-Emissive Materials, Vacuum Microelectronics and Flat-Panel Displays, K.L. Jensen, R.J. Nemanich, P. Holloway, T. Trottier, W. Mackie, D. Temple, J. Itoh, 2001, ISBN: 1-55899-529-3
- Volume 622 Wide-Bandgap Electronic Devices, R.J. Shul, F. Ren, W. Pletschen, M. Murakami, 2001, ISBN: 1-55899-530-7
- Volume 623 Materials Science of Novel Oxide-Based Electronics, D.S. Ginley, J.D. Perkins, H. Kawazoe, D.M. Newns, A.B. Kozyrev, 2000, ISBN: 1-55899-531-5
- Volume 624 Materials Development for Direct Write Technologies, D.B. Chrisey, D.R. Gamota, H. Helvajian, D.P. Taylor, 2001, ISBN: 1-55899-532-3
- Volume 625 Solid Freeform and Additive Fabrication 2000, S.C. Danforth, D. Dimos, F.B. Prinz, 2000, ISBN: 1-55899-533-1
- Volume 626 Thermoelectric Materials 2000 The Next Generation Materials for Small-Scale Refrigeration and Power Generation Applications, T.M. Tritt, G.S. Nolas, G.D. Mahan, D. Mandrus, M.G. Kanatzidis, 2001, ISBN: 1-55899-534-X
- Volume 627 The Granular State, S. Sen, M.L. Hunt, 2001, ISBN: 1-55899-535-8
- Volume 628 Organic/Inorganic Hybrid Materials 2000, R. Laine, C. Sanchez, C.J. Brinker, E. Giannelis, 2001, ISBN: 1-55899-536-6
- Volume 629 Interfaces, Adhesion and Processing in Polymer Systems, S.H. Anastasiadis, A. Karim, G.S. Ferguson, 2001, ISBN: 1-55899-537-4
- Volume 633 Nanotubes and Related Materials, A.M. Rao, 2001, ISBN: 1-55899-543-9
- Volume 634 Structure and Mechanical Properties of Nanophase Materials Theory and Computer Simulations vs. Experiment, D. Farkas, H. Kung, M. Mayo, H. Van Swygenhoven, J. Weertman, 2001, ISBN: 1-55899-544-7
- Volume 635 Anisotropic Nanoparticles Synthesis, Characterization and Applications, S.J. Stranick, P. Searson, L.A. Lyon, C.D. Keating, 2001, ISBN: 1-55899-545-5
- Volume 636 Nonlithographic and Lithographic Methods of Nanofabrication From Ultralarge-Scale Integration to Photonics to Molecular Electronics, L. Merhari, J.A. Rogers, A. Karim, D.J. Norris, Y. Xia, 2001, ISBN: 1-55899-546-3

MATERIALS RESEARCH SOCIETY SYMPOSIUM PROCEEDINGS

- Volume 637 Microphotonics Materials, Physics and Applications, K. Wada, P. Wiltzius, T.F. Krauss, K. Asakawa, E.L. Thomas, 2001, ISBN: 1-55899-547-1
- Volume 638 Microcrystalline and Nanocrystalline Semiconductors 2000, P.M. Fauchet, J.M. Buriak, L.T. Canham, N. Koshida, B.E. White, Jr., 2001, ISBN: 1-55899-548-X
- Volume 639 GaN and Related Alloys 2000, U. Mishra, M.S. Shur, C.M. Wetzel, B. Gil, K. Kishino, 2001, ISBN: 1-55899-549-8
- Volume 640 Silicon Carbide Materials, Processing and Devices, A.K. Agarwal, J.A. Cooper, Jr., E. Janzen, M. Skowronski, 2001, ISBN: 1-55899-550-1
- Volume 642 Semiconductor Quantum Dots II, R. Leon, S. Fafard, D. Huffaker, R. N tzel, 2001, ISBN: 1-55899-552-8
- Volume 643 Quasicrystals Preparation, Properties and Applications, E. Belin-Ferr , P.A. Thiel, A-P. Tsai, K. Urban, 2001, ISBN: 1-55899-553-6
- Volume 644 Supercooled Liquid, Bulk Glassy and Nanocrystalline States of Alloys, A. Inoue, A.R. Yavari, W.L. Johnson, R.H. Dauskardt, 2001, ISBN: 1-55899-554-4
- Volume 646 High-Temperature Ordered Intermetallic Alloys IX, J.H. Schneibel, S. Hanada, K.J. Hemker, R.D. Noebe, G. Sauthoff, 2001, ISBN: 1-55899-556-0
- Volume 647 Ion Beam Synthesis and Processing of Advanced Materials, D.B. Poker, S.C. Moss, K-H. Heinig, 2001, ISBN: 1-55899-557-9
- Volume 648 Growth, Evolution and Properties of Surfaces, Thin Films and Self-Organized Structures, S.C. Moss, 2001, ISBN: 1-55899-558-7
- Volume 649 Fundamentals of Nanoindentation and Nanotribology II, S.P. Baker, R.F. Cook, S.G. Corcoran, N.R. Moody, 2001, ISBN: 1-55899-559-5
- Volume 650 Microstructural Processes in Irradiated Materials 2000, G.E. Lucas, L. Snead, M.A. Kirk, Jr., R.G. Elliman, 2001, ISBN: 1-55899-560-9
- Volume 651 Dynamics in Small Confining Systems V, J.M. Drake, J. Klafter, P. Levitz, R.M. Overney, M. Urbakh, 2001, ISBN: 1-55899-561-7
- Volume 652 Influences of Interface and Dislocation Behavior on Microstructure Evolution, M. Aindow, M. Asta, M.V. Glazov, D.L. Medlin, A.D. Rollet, M. Zaiser, 2001, ISBN: 1-55899-562-5
- Volume 653 Multiscale Modeling of Materials 2000, L.P. Kubin, J.L. Bassani, K. Cho, H. Gao, R.L.B. Selinger, 2001, ISBN: 1-55899-563-3
- Volume 654 Structure-Property Relationships of Oxide Surfaces and Interfaces, C.B. Carter, X. Pan, K. Sickafus, H.L. Tuller, T. Wood, 2001, ISBN: 1-55899-564-1
- Volume 655 Ferroelectric Thin Films IX, P.C. McIntyre, S.R. Gilbert, M. Miyasaka, R.W. Schwartz, D. Wouters, 2001, ISBN: 1-55899-565-X
- Volume 657 Materials Science of Microelectromechanical Systems (MEMS) Devices III, M. deBoer, M. Judy, H. Kahn, S.M. Spearing, 2001, ISBN: 1-55899-567-6
- Volume 658 Solid-State Chemistry of Inorganic Materials III, M.J. Geselbracht, J.E. Greedan, D.C. Johnson, M.A. Subramanian, 2001, ISBN: 1-55899-568-4
- Volume 659 High-Temperature Superconductors Crystal Chemistry, Processing and Properties, U. Balachandran, H.C. Freyhardt, T. Izumi, D.C. Larbalestier, 2001, ISBN: 1-55899-569-2
- Volume 660 Organic Electronic and Photonic Materials and Devices, S.C. Moss, 2001, ISBN: 1-55899-570-6
- Volume 661 Filled and Nanocomposite Polymer Materials, A.I. Nakatani, R.P. Hjelm, M. Gerspacher, R. Krishnamoorti, 2001, ISBN: 1-55899-571-4
- Volume 662 Biomaterials for Drug Delivery and Tissue Engineering, S. Mallapragada, R. Korsmeyer, E. Mathiowitz, B. Narasimhan, M. Tracy, 2001, ISBN: 1-55899-572-2

Prior Materials Research Society Symposium Proceedings available by contacting Materials Research Society

Atomic and Mesoscopic Studies

Multiscale Modeling of Dislocation Processes in Bcc Tantalum: Bridging Atomistic and Mesoscale Simulations

L. H. Yang, Meijie Tang, and John A. Moriarty

Physics and Advanced Technologies Directorate, Lawrence Livermore National Laboratory,
Livermore, CA 94551, USA

ABSTRACT

Plastic deformation in bcc metals at low temperatures and high-strain rates is controlled by the motion of $a/2\langle 111 \rangle$ screw dislocations, and understanding the fundamental atomistic processes of this motion is essential to develop predictive multiscale models of crystal plasticity. The multiscale modeling approach presented here for bcc Ta is based on information passing, where results of simulations at the atomic scale are used in simulations of plastic deformation at mesoscopic length scales via dislocation dynamics (DD). The relevant core properties of $a/2\langle 111 \rangle$ screw dislocations in Ta have been obtained using quantum-based interatomic potentials derived from model generalized pseudopotential theory and an *ab-initio* data base together with an accurate Green's-function simulation method that implements flexible boundary conditions. In particular, the stress-dependent activation enthalpy for the lowest-energy kink-pair mechanism has been calculated and fitted to a revealing analytic form. This is the critical quantity determining dislocation mobility in the DD simulations, and the present activation enthalpy is found to be in good agreement with the previous empirical form used to explain the temperature dependence of the yield stress.

INTRODUCTION

The low-temperature and high-strain-rate plastic deformation properties of bcc metals are controlled by $a/2\langle 111 \rangle$ screw-dislocation behavior in the crystalline lattice. In particular, the motion of the screw dislocation is believed to be associated with the formation and expansion of kink pairs on the screw dislocation line. Thus, the accurate prediction of kink-pair activation energetics is essential to the understanding and determination of the mobility of screw dislocations in these materials. In turn, an atomistic-based dislocation mobility model is a key ingredient needed to develop predictive multiscale simulations of crystal plasticity for bcc metals.

At higher length scales, the dislocation dynamics (DD) simulation approach has shown some predictive power of the macroscopic plastic response of bcc single crystals based on the fundamental mechanisms of dislocation behavior [1]. However, the accuracy of DD simulations is limited in part by our understanding of the unit dislocation mechanisms and in part by the local rules that dominate the DD simulation process. Therefore, validating a realistic atomistic mobility model is an important first step in developing predictive DD simulations that intend to use atomistic data generated by the proposed kink-pair mechanism. The objectives of this study are twofold. First, it provides a critical link to allow data generated at the atomic length scale to be used directly in mesoscale DD simulations. Second, the DD simulation results can in turn

provide a direct comparison with experiment, which is essential to the validation of the atomistic modeling.

In this paper, we report a systematic study of atomistic kink-pair modeling in Ta under an applied shear stress up to $0.4\tau_p$, where τ_p is the calculated Peierls stress to move the straight screw dislocation at 0K. Two distinct atomistic approaches were applied to calculate the kink-pair activation enthalpy as a function of applied stress. The results were then fitted to an analytic form that can be directly used as input into the DD simulations. The fitted activation enthalpy obtained from the present atomistic calculations shows good agreement with that previously obtained empirically and used to simulate the observed temperature dependence of the yield stress in Ta [1].

COMPUTATIONAL METHODS

MGPT interatomic potentials

The present calculations in Ta have been carried out using quantum-based, multi-ion interatomic potentials derived from model generalized pseudopotential theory (MGPT) [2]. This approach is based on the corresponding first-principles generalized pseudopotential theory (GPT) [3], which provides a rigorous real-space expansion of the total energy for a bulk transition metal in the form

$$E_{tot}(R_1 \dots R_N) = NE_{vol}(\Omega) + \frac{1}{2} \sum'_{i,j} v_2(ij;\Omega) + \frac{1}{6} \sum'_{i,j,k} v_3(ijk;\Omega) + \frac{1}{24} \sum'_{i,j,k,l} v_4(ijkl;\Omega), \quad (1)$$

where $R_1 \dots R_N$ denote the positions on the N ions in the metal, Ω is the atomic volume, and the prime on each sum over ion positions excludes all self-interaction terms where two indices are equal. The leading volume term in this expansion, E_{vol} , as well as the two-, three-, and four-ion interatomic potentials, v_2 , v_3 , and v_4 , are volume-dependent, but structure-independent quantities and thus transferable to all bulk ion configurations. The angular-force, multi-ion potentials v_3 and v_4 reflect contributions from partially-filled d bands and are generally important for central transition metals. Within the MGPT framework [3], these potentials are systematically approximated by introducing canonical d bands and other simplifications to achieve short-ranged, analytic forms, which can then be applied to both static and dynamic simulations with the Green's function techniques described below. To compensate for the approximations introduced into the MGPT, a limited amount of parameterization is allowed in which the coefficients of the modeled potential contributions are constrained by experimental or volume-dependent *ab-initio* theoretical data. The details of this parameterization for Ta, together with extensive validation tests of the potentials, are discussed in Ref. 4.

Green's function simulation method

In the present work, a method for dynamically updating the boundary conditions of atomistic simulations [5] has been applied to the kink and kink-pair calculations. This approach extends the 2D lattice Green's function (GF) boundary relaxation method originated by Sinclair et al. [6] to 3D simulations, including kink and kink-pair formation. The boundary conditions for 2D and

3D defect cells are evaluated using line [7] and point [8] force distributions, respectively. In this flexible boundary condition method, the simulation box is divided into three regions: atomistic, GF, and continuum. In the continuum region, the atomistic positions are initially determined according to the anisotropic elastic displacement field [7] for a dislocation line defect at the center of the atomistic region. Complete atomistic relaxation is performed in the atomistic region according to the interatomic forces generated from Eq. (1). Forces develop in the GF region as relaxation is achieved in the atomistic region are then used to relax atoms in all three regions by the 2D or 3D lattice and elastic GF solutions for line [5,7] or point [5,8] forces. The atomistic and GF relaxation are iterated until all force components on each atom are sufficiently small ($< 10^{-4}$ eV/Å).

3D dislocation dynamics simulations

The 3D dislocation dynamics simulations are based on a screw-edge description [1], where the dislocation lines are represented by piece-wise connected edge and screw segments. The slip planes are {110} and the Schmid law is assumed to be valid. The unit screw and edge segments are defined as the smallest vectors in $\langle 111 \rangle$ and $\langle 112 \rangle$ directions, respectively, in a {110} plane and in a simple cubic lattice with a lattice parameter of 2.43 nm. Isotropic elasticity is used to calculate the elastic interactions between the segments. Dislocation mobility for the edge and the screw is the key input in the DD simulation and their behavior is constrained by so-called 'local rules' [1,9]. In particular, the screw dislocations move via a thermally activated kink-pair mechanism, and the velocity takes the form [1]:

$$v = b \frac{L}{l_c} (v_D \frac{b}{l_c}) \exp\left(-\frac{\Delta H(\tau)}{k_B T}\right), \quad (2)$$

where b is the magnitude of the Burgers vector, v_D the Debye frequency, L the screw dislocation length, l_c the critical activation length of a kink pair, and $\Delta H(\tau)$ is the activation enthalpy under the local resolved shear stress τ . The edge dislocation mobility is significantly higher than those of screws [10] and the edges are assumed to move infinitely fast and only stop at their equilibrium lattice positions or when meeting another dislocation line.

The activation enthalpy $\Delta H(\tau)$ was previously extracted from experimental data [1]. It was fitted in the form

$$\Delta H = \Delta H(0) [1 - (\tau/\tau_p)^p]^q \quad (3)$$

proposed by Kocks, Argon and Ashby [10] with parameters $\Delta H(0) = 1.08 \text{ eV}$, $p = 0.75$, $q = 1.17$, and $\tau_p = 248 \text{ MPa}$. The critical activation kink-pair length l_c for the nucleation of a kink pair is taken as $15b$. This set of input to the DD simulations has allowed us to perform simulations at different temperatures and obtain yield stresses as a function of temperature that agree reasonably well with experimental data [1].

RESULTS AND DISCUSSIONS

The unstressed screw dislocation core is predicted to be doubly degenerate and weakly polarized, leading to multiple possible kink pairs involving positive- (p) and negative- (n) polarized segments [4]. In the low stress limit, when the kink separation is very large ($> 20b$), the lowest-energy configuration is found to be $plnnp$ [4,11], where l and r denote left and right,

respectively. This kink pair has calculated formation energy of $0.96eV$, which is in close agreement with the empirical zero-stress activation enthalpy obtained in Eq. (3).

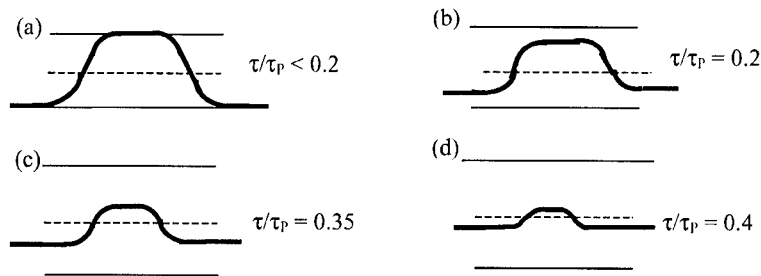


Figure 1. Schematic drawings of atomistic kink-pair models at different levels of applied shear stress (τ). At low stress levels ($\tau/\tau_p < 0.2$), three straight dislocation arms that form the kink-pair are located at the bottom of valley, while at higher stress levels ($\tau/\tau_p > 0.2$) the three arms form a metastable configuration that is balanced by the applied shear stress.

At finite separation, the left and right kinks will elastically attract each other yielding an interaction energy in addition to the zero-stress formation energy. If the kink-kink separation λ is larger than the kink width ($\sim 7b$ for bcc Ta) [4] and the kink height ($h = 2\sqrt{3}b/3$), the total formation energy E_{tot} of a kink pair can then be calculated by summing over the atom-to-atom energy difference between the final equilibrium configuration and a reference configuration, which is a linear combination of unit dislocation disks with p or n symmetry [4]. In addition, during the kink pair activation process, the energy required to generate the kink pair is supplied partly by thermal activation and partly by the work done by the applied shear stress τ ($\{110\}/\langle 111 \rangle$ in this case) needed to maintain the pair at separation distance λ . The activation enthalpy for such a balanced kink pair is given by

$$\Delta H = E_{tot} - \lambda b h \tau. \quad (4)$$

To investigate the relationships between E_{tot} , and λ and the applied stress τ , we have performed atomistic simulations of a kink-pair under an applied shear stress in a cylinder with the radius of $15b$ (for the atomistic region) and the length of $120b$. For very large separations, the formation energy approaches the zero-stress value of $0.96eV$ asymptotically. At small separations, the energy decreases rapidly and the stress required to stabilize the kink pair increases sharply. When the separation λ is smaller than the kink width, which corresponds to an applied shear stress $\tau > 0.2\tau_p$, the assumption of weakly interacting kinks in our atomistic simulations is breaking down in this regime [4]. This may be attributed to the fact that the assumed dislocation configuration is in an unstable equilibrium state. At higher stress levels, a self-consistent 3D atomistic model of kink-pair formation and migration is therefore necessary (Fig. 1) [12]. Here we report simulation results up to an applied shear stress level of $0.4\tau_p$. To calculate the kink-pair formation enthalpy under such an applied shear stress, three new steps are taken in our 3D atomistic simulations: (1) A straight $a/2\langle 111 \rangle$ screw dislocation is constructed

and is then fully relaxed under a pre-defined applied stress. This procedure provides the necessary building block for the 3D kink-pair model that will be constructed in step (2). As a result, the straight screw dislocation line is lifted above the valley of the Peierls potential, and the degree of lifting depends on the magnitude of the applied shear stress. (2) A 3D atomistic kink-

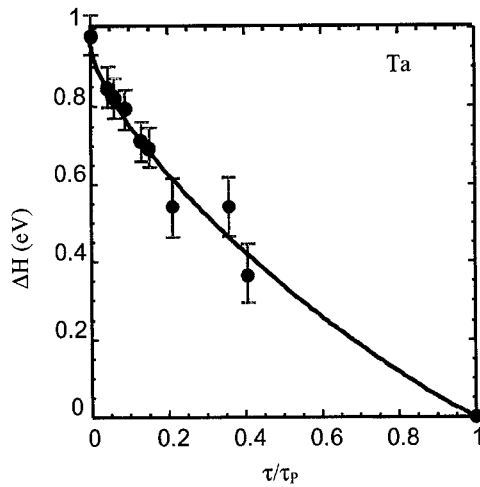


Figure 2. Activation enthalpy (ΔH) as a function of applied stress (τ/τ_p) for bcc Ta. Here two different atomistic kink-pair models are used for these calculations, depending on whether $\tau/\tau_p < 0.2$ or > 0.2 (Fig. 1). The solid line is a fit to the calculated results in the form of Eq. (3) and the error bars indicate the numerical uncertainty in our atomistic simulations.

pair model is constructed according the reference configuration generated from step (1). Under this construction, the separation λ is treated as a fixed parameter during the atomistic energy minimization. The total energy (E_{tot}) is then calculated by summing over the atom-to-atom energy difference between the fully relaxed 3D configuration and the fundamental straight screw dislocation under the pre-defined applied shear stress. (3) Finally, the work done by the applied stress is then estimated using a trapezoid model [13] and the response stress due to the kink-pair formation at the separation λ . The calculated activation enthalpy is displayed in Fig. 2. This result shows great improvement over using the low-stress kink-pair model at stresses $\tau/\tau_p > 0.2$, as in Ref. [4], where the kink pair was constructed from a relaxed straight dislocation at zero stress [Fig. 1(a)].

The new data was then fitted to Eq. (2) for the kink-pair activation enthalpy. In this fit we used $\Delta H(0) = 0.96 \text{ eV}$, the kink-pair formation energy at zero stress, and $\tau_p = 606 \text{ MPa}$, the calculated Peierls stress in $\{110\}$ plane. Our calculated τ_p is actually about 2 times larger than the best available experimental estimate (248 MPa) for bcc Ta [14], and the possible reasons for this discrepancy are discussed in Ref. 4. This is an issue for further study. However, when fitting to the scaled stress value τ/τ_p , the fitted parameters $p = 0.71$ and $q = 1.10$ are in accord with the parameters obtained by empirical form, 0.75 and 1.17, respectively [1]. Despite the fact

that the atomistic and mesoscale DD simulations bear some degree of uncertainties of their own, the present attempt to link between atomistic simulation and 3D DD simulation suggests that 3D DD simulations can provide a good validation tool between atomistic simulations and experiments

SUMMARY

In summary, we have reported a systematic study of atomistic kink-pair modeling in Ta under an applied shear stress up to $0.4\tau_p$. Low- and high-stress atomistic models were used to calculate the kink-pair activation enthalpy as a function of applied shear stress. The results were then fitted to an analytic form that provides critical input into 3D DD simulations. Within the accuracy of our atomistic simulations, the fitted parameters agree well with the ones used in previous DD simulations to accurately calculate the single-crystal yield stress as a function of temperature [1]. In the near future, we plan to apply the present approach over a wide range of pressure- and stress-orientation conditions. This will provide the necessary input into the 3D DD simulations to predict the yield stress in bcc Ta at these conditions.

ACKNOWLEDGMENTS

Many discussions with the late Dr. M. Duesbery and Prof. V. Vitek are greatly appreciated. This work was performed under the auspices of the U.S. Department of Energy by the University of California Lawrence Livermore National Laboratory under contract number W-7405-ENG-48.

REFERENCES

1. M. Tang, L. P. Kubin, and G. R. Canova, *Acta Mater.* **46**, 3221 (1998).
2. J. A. Moriarty, *Phys. Rev.* **B 42**, 1609 (1990); *Phys. Rev.* **B 49**, 12431 (1994).
3. J. A. Moriarty, *Phys. Rev.* **B 38**, 3199 (1988).
4. L. H. Yang, P. Söderlind, and J. A. Moriarty, *Philos. Mag. A* (in press).
5. S. Rao, C. Hernandez, J. P. Simmons, T. A. Parthasarathy, and C. Woodward, *Philos. Mag.* **A 77**, 231 (1998).
6. J. E. Sinclair, P. C. Gehlen, R. G. Hoagland, and J. P. Hirth, *J. Appl. Phys.*, **49**, 3890 (1978).
7. A. N. Stroh, *Philos. Mag.* **3**, 625 (1958); *J. Math. Phys.* **41**, 77 (1962).
8. P. H. Dederichs and G. Leibfried, *Phys. Rev.* **188**, 1175 (1969); G. Leibfried and N. Breuer, *Point Defects in Metals I*, *Springer Tracts in Modern Physics*, Vol. 81 (Springer, Berlin, 1978).
9. L. P. Kubin, B. Devincere, and M. Tang, *J. Comp.-Aided Mater. Design* **5**, 31-54 (1998).
10. U. F. Kocks, A. S. Argon, and M. F. Ashby, in *Prog. Mater. Sci.; Vol. 19*, edited by B. Chalmers, J. W. Christian, and T. B. Massalski (Pergamon Press, 1975).
11. M. S. Duesbery, private communication and unpublished.
12. V. Vitek, private communication.
13. H. Koizumi, H. O. K. Kirchner, and T. Suzuki, *Philos. Mag. A* **69**, 805 (1994).
14. R. Lachenmann and H. Schultz, *Scripta Met.* **4**, 709 (1970).

Periodic Boundary Conditions for Dislocation Dynamics Simulations in Three Dimensions

Vasily V. Bulatov¹, Moon Rhee¹, and Wei Cai²

¹Lawrence Livermore National Laboratory, University of California

²Massachusetts Institute of Technology.

ABSTRACT

This article presents an implementation of periodic boundary conditions (PBC) for Dislocation Dynamics (DD) simulations in three dimensions (3D). We discuss fundamental aspects of PBC development, including preservation of translational invariance and line connectivity, the choice of initial configurations compatible with PBC and a consistent treatment of image stress. On the practical side, our approach reduces to manageable proportions the computational burden of updating the long-range elastic interactions among dislocation segments. The timing data confirms feasibility and practicality of PBC for large-scale DD simulations in 3D.

INTRODUCTION

Treatment of boundary conditions is an important element of Dislocation Dynamics (DD) methodology. There are two distinct classes of DD simulations that necessitate different approaches to boundary conditions. When the simulation volume is close to an internal or external interface (surface, crack, grain or phase boundary, etc.), it is necessary to account for stress variations associated with the interface. In other cases, dislocation behavior in the bulk single crystal, far removed from any interfaces, is of interest. The first case is generally difficult requiring the use of sophisticated numerical methods [1,2] to calculate the elastic (image) stress associated with the interfaces. In the second case, the material volume can be regarded as a small part of an infinitely large single crystal justifying the use of the relatively simple analytical solutions of the continuous theory of dislocations obtained for the infinite elastically homogeneous solid [3].

Understandably, in the early stages of development, DD simulations focused on the simpler case of bulk single crystals. Many years ago von Karman suggested a trick by which a small representative volume of material is replicated by periodic continuation to make up the infinite crystal and to preserve its translational invariance. Since then, this trick has been routinely employed in computer simulations of solids. In 2D, where dislocations appear as point objects carrying tensorial (Burgers) charges, periodic boundary conditions (PBC) have been successfully implemented [4,5]. However in 3D, the models used for DD simulations in the bulk remain inconsistent with the absence of material interfaces and translational invariance of the infinite crystal. In fact, most simulations performed so far employ free boundaries. To simplify the treatment, the boundaries are allowed to exist only in the sense that they absorb dislocations that happen to approach the boundary, whereas the image stresses induced by the free surfaces are simply ignored [6]. In order to mitigate such undesirable effects, a smaller spherical volume in the center of the simulation box is sometimes used to control the loading conditions and to monitor dislocation behavior [2]. Unfortunately, the spurious dislocation loss can not be fully prevented even using such an embedded sphere approach. Furthermore, the remainder of the

simulation volume ($\sim 80\%$) is wasted because its only function is to buffer the central sphere from the free surfaces. Mirror reflection approach developed in [7] addresses the problem of image stress but the spurious loss of dislocation to the boundaries remains an issue. Recently, free surface boundary conditions have been augmented with a procedure that monitors the rate of dislocation loss to the boundaries and re-introduces dislocations at random, to counter the loss [2,8]. Although these modifications offer significant improvement over the use of plain free surface boundary conditions, the fact remains: all of them contain some sort of boundaries thus violating the translation invariance and, except for [7], ignore or distort the image stress fields associated with the boundaries.

At a first glance, an extension of PBC to 3D appears very appealing since, by their very nature, PBC preserve translational invariance and balance dislocation fluxes in and out of the box. Countering such warm feelings for the von Karmann's trick are the warnings against the use of PBC in 3D given in the earlier papers on the DD methods [6,9]. Subsequent publications reinforce the early doubts suggesting that line connectivity can not be preserved in 3D PBC [2,7, 10]. This contribution is intended to dispel the doubts and to clear the PBC for use in DD simulations in 3D. In the following we show that consistent application of PBC in three dimensions is not exactly trivial, yet its potential advantages should convince those in doubt that PBC is a good alternative to the other types of boundary conditions currently in use.

NUMERICAL IMPLEMENTATION

In this section we consider three aspects of periodic boundary conditions relevant for practical numerical implementation: (1) line connectivity, (2) initial dislocation arrangements compatible with PBC and (3) treatment of image stress.

Line connectivity

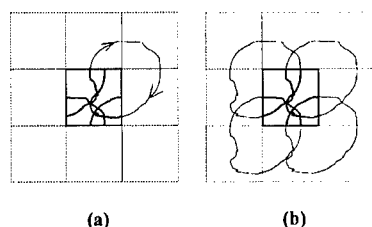


Fig. 1 Closed loops in PBC: in (a) the primary loop (thin line) is folded in the primary box (thick line) whereas in (b) the same result is obtained by periodic loop replication.

That there is really no problem maintaining line connectivity in PBC is illustrated in Fig. 1 that shows a closed loop of arbitrary shape partly contained in the primary box. The box is periodically replicated in 2D (only a few relevant replicas are shown for clarity). Periodic replication of the loop demands that, every time the line crosses the imagined boundary of the primary box or any of its replicas, another line enters the primary box at the periodically equivalent position on an appropriate face. By tracing the primary loop along its contour direction, one can “fold” the entire line in the primary box. To complete the periodic continuation, such folded lines are replicated in all

other boxes as well. Alternatively, the same periodic arrangement of loops and boxes can be obtained without ever tracing and folding the primary loop, by simply replicating the whole loop with the same periodicity vectors as used for replicating the primary box (Fig. 1(b)). Although the illustration is 2D, exactly the same folding and replication procedures apply in 3D.

The fact that folding and replication are equivalent can be used constructively in a numerical implementation. In particular, instead of tracing the events of boundary crossing within the primary box, the algorithm can focus on the unfolded primary loop spanning many periodic boxes but perform the arithmetic manipulations with the vectors *modulo periodicity vectors*. From this point of view, there are no boundaries to deal with in the periodic boundary conditions, since the origin of periodic replication can be arbitrarily shifted with respect to the primary loop. Translational periodicity of PBC is not only physically realistic but also numerically convenient.

That line continuity is maintained in DD simulations is proven by simple induction: starting from an initial configuration such as shown in Fig. 1, line continuity is preserved in all subsequent topological transformations, e.g. recombination, multiplication, junction reactions, etc.

Initial conditions

One likely reason for the persistent prejudice against using PBC in 3D is not appreciating the fact that, when it comes to translational periodicity, not all dislocation arrangements are created equal. In fact, general dislocation configurations in the primary box can not be periodically continued in all directions without breaking the lines, however similar they may look to the one shown in Fig. 1. The latter is compatible with PBC but, having been constructed by folding a closed loop into the primary box, is by no means arbitrary. In addition to closed loops, infinite dipoles can be used to generate PBC-compatible initial configurations¹. In this case, it is necessary to make sure that each line of the dipole eventually re-enters itself so that its total span (the vector connecting its two ends) is a multiple of the periodicity vectors. We have developed a simple algorithm of self-correcting random walk by which a line spanning a given multiple of the periodicity vectors can be generated using a sequence of random numbers. Although the class of PBC-compatible initial configurations may appear rather narrow, this is not a serious constraint for large-scale DD simulations.

It is interesting to note that all PBC-compatible dislocation configurations correspond to a net zero integral over the primary box of the so-called dislocation density or Nye's tensor [11]

$$\alpha \equiv \frac{1}{V} \int_L \mathbf{b} \otimes \mathbf{t} ds = 0, \quad (1)$$

where \mathbf{b} is the Burgers vector, \mathbf{t} is the line tangent vector, ds is an element of arc length along the dislocation line, and L is the total length of dislocation lines within box volume V . For our purposes the integral is conveniently reduced to a simpler form [12]

$$\alpha_{ij} \equiv \frac{1}{V} \sum b_i (x_j^+ - x_j^-) = 0, \quad (2)$$

where x^- and x^+ are the positions of entry and exit points of the line segments and the sum includes all dislocations inside the box.

Although the condition of zero Nye's tensor integral is realized for all initial configurations that are truly compatible with PBC, the compatibility requirement can be somewhat relaxed in practical DD simulations. For example it is possible, starting with a PBC-compatible configuration, to add one or several infinite dislocations that will introduce a small amount of unbalanced dislocation density in the box. Although physically this would introduce a non-zero net lattice curvature that is impossible to accommodate in the infinite translationally-invariant

¹ In a sense, an infinite dipole can be viewed as a loop closed through infinity.

crystal, this curvature can be neglected for as long as $Lb\rho \ll 1$, where ρ is the density of geometrically-necessary dislocations (GND) added to the box and L is the box size. For a typical box size of $10\ \mu$ and the GND density $\rho = 10^{12}\ \text{m}^{-2}$, the dimensionless ratio above is of the order of 10^{-3} . Whichever initial arrangement of lines is considered, the use of PBC will ensure that Nye's tensor integrated over the box volume is conserved in the course of DD simulations.

Treatment of image stress

Fully consistent application of PBC requires that additional stress associated with the periodic images of dislocation be accounted for. This is the most involved part of the whole implementation. In DD, the lion's share of computations goes to calculations of elastic interactions between dislocation segments. The unit element of such calculations is the

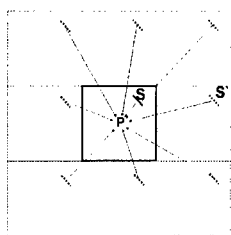


Fig. 2 Periodic lattice of image

evaluation of stress produced at a given material point P by a dislocation segment centered at position S . Using the analytical formulae developed in the continuum theory [3, 13], such a calculation takes a few hundred arithmetic operations to obtain all six components of stress from a general dislocation segment of finite length. In PBC, the computational burden increases many-fold because stress from the periodic images of the primary segment has to be evaluated. Considering that the overall effort already scales as $O(N^2)$, where N is the number of dislocation segments, the brute force treatment of image stress in PBC becomes prohibitive. Earlier, one of us found a practical solution in a similar situation, for

computationally expedient evaluation of periodic corrections to the elastic Green's function in 2D [14]. The idea was to pre-tabulate the correction stress on a regular grid within the computational volume and then use these grid values for fast interpolation. The interpolation itself is based on the minimum image convention which dictates that the total stress due to a given segment and all of its periodic images, is associated with the replica of the segment that is nearest to the field point (Fig. 2). Practically, the calculation requires that the box is centered on the field point, and the look-up procedure goes over all segments, primary or replicas, that fall inside this box.

Extension of this idea to DD simulations in 3D encounters considerable but manageable difficulties. The most obvious of them is the high dimensionality of the required look-up tables. To improve the situation we created the tables only for differential, or point-like dislocation segments, i.e. such segments whose length is considerably smaller than their distance to the field point. Compared to the case of straight segments of finite length, the use of point-like segments reduces the dimensionality of the tables from four to three. Still, it appears one needs to pre-calculate 54 image correction tables, one for each of the six components of stress generated by nine components of the tensorial charge $d\mathbf{b} \otimes \mathbf{t}$ (here $d\mathbf{l}$ is the length of the differential segment). However, using cubic periodic boxes and taking advantage of the cubic symmetry, the number of independent tables can be reduced from 54 to eight. The same symmetry allows reduction of the amount of computations by 48 times, by considering only the grid points in the irreducible zone of the cube. This also reduces the amount of memory required to store the tables, if this is a limiting factor. For a given accuracy of interpolation, the number of grid points

can be reduced by making the tabulated functions as smooth as possible inside the cube. Since the stress field of the nearest image of the segment diverges as $1/r^2$ at the origin, we exclude the nearest image from the correction tables and evaluate its contribution analytically instead. This eliminates the singularity since all the replicas other than minimum images lie outside the box by definition.

The most serious problem we had to face was *conditional convergence* of the lattice (Madelung) sums that need to be evaluated for every entry of the stress correction tables. In a forthcoming publication we present a thorough discussion of this important mathematical aspect of the continuum theory of dislocations. Here we only briefly recount that the naïve lattice summation of the stress terms associated with the primary and replica segments is convergent, but the end result depends on the order of summation. In general, such conditional sum gives rise to an arbitrary average stress in the simulation cell which will cause problems for DD simulations. The physically meaningful part of the Madelung sum is therefore the stress field variation over the simulation cell, which converges absolutely and thus does not depend on the order of summation. We have implemented an effective numerical procedure *MadSum* for subtracting the spurious parts of the lattice sums and used the remaining stress field variations as the entries for the stress correction tables.

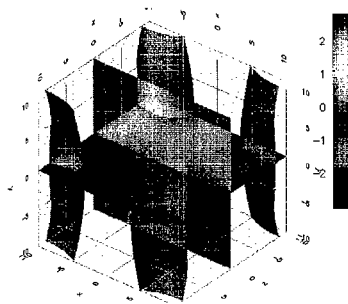


Fig. 3. Zero-value iso-surfaces of the tabulated stress correction term for σ_{13} , interpolated in the unit cube as a function of segment position. Note zero-value region near the origin.

Fig. 3 is an example of one such correction function tabulated on a cubic grid $32 \times 32 \times 32$ in the unit cube. Several features of this function are noteworthy. First, the displayed function retains periodicity and some symmetries of the cube. Second, except for several symmetry lines, the function is non-zero on the cube faces. This observation calls in question the use of a cut-off distance for reducing the cost of computing the interactions between dislocation segments in DD simulations in 3D. Third, the correction function is zero in the center of the cube, indicating that within some radius (~ 0.2 of the cube size) no correction is needed. In the context of large-scale DD simulations, elastic interactions between the segments beyond certain range are usually evaluated using the multipole expansion

techniques. That the correction functions are zero around the cube center, suggests a procedure in which only the multipole terms are corrected, whereas interactions between the segments at a shorter range require no correction at all. Comparison of the computational cost among the different ways of treating the interaction stress reveals that numerical interpolation of the image-corrected stress takes some four times longer than the analytical evaluation of stress from the same number of dislocation segments. However, because the number of multipole momenta that have to be corrected is generally smaller than the number of segments demanding “personal attention”, the total amount of time spent on analytical (uncorrected) and numerical (image-corrected) stress evaluation, are comparable.

SUMMARY

In this short contribution we intended to show that there is nothing particularly nasty about PBC as the boundary conditions for DD simulations in 3D. On the other hand, with the obvious advantage of retaining translational invariance and effectively eliminating the boundaries, PBC are well positioned for 3D simulations of single crystal plasticity in the bulk. As always, one has to be vigilant and watch for the artifacts associated with the small system size. In particular, any length scale emerging in the simulations that appears comparable to the periodic box size, should be treated with suspicion. Interaction of dislocations with their own images may be a cause of spurious effects, e.g. artificially enhanced dislocation recombination or formation of strong dipoles immobilizing the dislocations. In particular, the use of cubic boxes for the high symmetry FCC and BCC systems will cause each slip plane to self-connect after two periodic translations. Although various fixes to alleviate such undesirable behaviors can be devised, in our view there is only one real solution. It is to make the system large enough so that the finite size effects become insignificant. For example, to avoid spurious reconnection before one percent of plastic strain is accumulated (assuming dislocation density $\rho = 10^{12} \text{ m}^{-2}$) the cube should be at least 20μ on the side. Obviously, periodic boundary conditions do not make the system infinite. Nonetheless, they hold considerable computational advantages over the other types of boundary conditions currently employed for 3D simulations of bulk crystal plasticity.

ACKNOWLEDGEMENTS

We thank T. Diaz de la Rubia, N. Ghoniem, H. Huang, D. Lassila, K. Schwarz and L. Wickham for their continued interest and support. This work was performed under the auspices of the U.S. DOE by LLNL under contract No. W-7405-ENG-48. WC acknowledges support from LLNL under an ASCI-level 2 award. VVB and MR acknowledge support from the Office of Basic Energy Sciences, the U.S. Department of Energy.

REFERENCES

1. E. Van der Giessen and A. Needleman, *MSMSE*, **3**, 689 (1995).
2. M. Fivel and G.R. Canova, *MSMSE* **7**, 752 (1999).
3. J.P. Hirth and J. Lothe, *Theory of Dislocations* (Wiley, New York, 1982).
4. N.M. Ghoniem and R.J. Amodio, *Solid State Phenomena*, **3-4**, 377 (1988).
5. H. Y. Wang and R. LeSar, *Philos. Mag.*, **A 71**, 149 (1995).
6. L. P. Kubin et al., *Solid State Phenomena*, **23-24**, 455 (1992).
7. H. M. Zbib, M. Rhee and J. P. Hirth, *Int. J. Mech. Sci.*, **40**, 113 (1998).
8. M. Tang and A. El-Azab, submitted (2000).
9. G. R. Canova, Y. Brechet and L. P. Kubin, *Modeling of Plastic Deformation and Its Engineering Applications*, edited by S. I. Andersen et al. (13th RISO Int. Symp. Mater. Sci. 1992), p. 27.
10. B. Devincere, *Computer Simulations in Materials Science*, edited by H. O. Kirchner et al. (Kluwer 1996), p. 309.
11. J. F. Nye, *Acta Metall.*, **1**, 1 (1953).
12. A. Arsenlis and D. M. Parks, *Acta Mater.*, **47**, 1597 (1999).
13. V. L. Indenbom and J. Lothe, *Elastic Strain Field and Dislocation Mobility* (North Holland, Amsterdam, 1992).
14. V. V. Bulatov and A. S. Argon, *MSMSE*, **2**, 167 (1994).

Dislocation Exhaustion During Plastic Deformation

Olivier Couteau, Corinne Charbonnier, Tomas Kruml and Jean-Luc Martin

Ecole Polytechnique Fédérale (EPFL), Département de Physique, CH 1015 Lausanne, Switzerland

ABSTRACT

Repeated stress-relaxation experiments are used to characterize the deformation parameters in 3 types of single crystals (Cu, Ni₃Al and Ge) in which different dislocation mechanisms are known to operate. Mobile dislocation exhaustion rates and the amplitude of the yield point at reloading after stress-relaxation are measured. These two parameters are discussed in terms of the work-hardening coefficient in monotonic tests.

INTRODUCTION

Repeated stress-relaxation tests have already proved their relevance in the determination of thermal activation parameters and mobile dislocation characteristics [1, 2]. The aim of this paper is to characterize by this technique dislocation exhaustion in Cu, Ni₃Al and Ge single crystals in which the plastic deformation mechanisms are known to be different. The conditions used in the present study are the following: copper crystals are in symmetrical orientation at low temperatures so that athermal dislocation interactions dominate; Ni₃Al is strained in the temperature range which corresponds to the strength anomaly where dislocation exhaustion is pronounced; Ge, which deforms by single slip at temperatures where multiplication processes dominate the onset of deformation, is strained by a few percent above the lower yield point [3].

THEORY

The repeated stress-relaxation technique has been well developed over the years [4]. The associated procedure and assumptions for interpretation are briefly recalled here. For further details, one can report to former reviews [2]. The Orowan's law is used, which expresses the plastic strain-rate $\dot{\gamma}_p$ in terms of the mobile dislocation velocity v and the mobile dislocation density ρ_m . The velocity is assumed to be thermally activated. In the case of logarithmic stress-relaxations, the time dependence of stress is described by :

$$\tau - \tau_0 = \Delta\tau = -\frac{kT}{V_a} \ln\left(1 + \frac{t}{c_r}\right) \quad \text{where } V_a \text{ and } c_r \text{ are constant.} \quad (1)$$

The apparent activation volume V_a is :

$$V_a = kT \frac{\partial \ln \dot{\gamma}_p}{\partial \tau} \quad (2)$$

V_a is accessible in single stress-relaxation tests, strain-rate change experiments in monotonic deformation or stress change tests in creep. It is also proportional to the reciprocal of the strain-rate sensitivity.

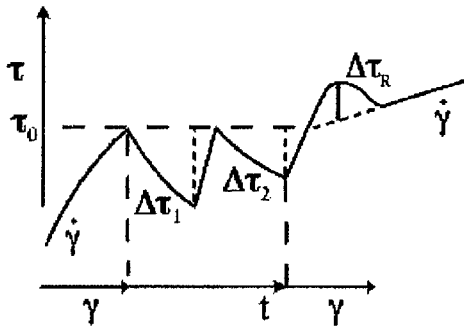


Figure 1 : Schematic representation of a repeated stress-relaxation test. τ_0 corresponds to the onset of relaxation.

Figure 1 is a schematics of a series of two stress-relaxations (corresponding to a positive work-hardening coefficient) and introduces the notations used. τ and γ are respectively the resolved shear stress and strain. $\Delta\tau_1$ and $\Delta\tau_2$ represent the stress decrease during relaxations 1 and 2 respectively. Consecutive relaxations are observed to slow down in relation with mobile dislocation exhaustion. Consequently, a small yield point $\Delta\tau_R$ occurs during constant strain-rate reloading after the transient. It corresponds to dislocation multiplication or unlocking which compensates for exhaustion during the stress relaxation test. A combination of the above assumptions yields a power dependence of ρ_m as a function of v :

$$\rho_m/\rho_{m0} = (v/v_0)^\beta \quad (3)$$

where ρ_{m0} and v_0 respectively correspond to the onset of relaxation. Repeated stress-relaxations provide V_a , V and β [2]. V is the activation volume of the dislocation velocity. It provides information about the stress dependence of v and β expresses the variation of ρ_m during the transient test.

In the case of non logarithmic relaxations, V_a depends on $\Delta\tau$ and on the derivatives of V with respect to stress. Then, the determination of V , when V_a is known, is not as straightforward.

EXPERIMENTAL DETAILS

Specimen dimensions are 8 mm in length and cross-section in the range 10-16 mm². Great attention is paid to the parallelism of the compression faces. Compression tests are performed on a SCHENCK RMC 100 machine. The control and data acquisition software have been developed especially for this experiment. An accurate measurement of stress during the stress-relaxation and the subsequent reloading at constant strain-rate is performed (see additional details in [5]).

RESULTS AND DISCUSSION

Copper

$\langle 011 \rangle$ oriented Cu single crystals are compressed at various temperatures with a $3.8 \times 10^{-5} \text{ s}^{-1}$ strain-rate. Figure 2 represents stress-strain curves for three different temperatures which start in stage II for this multiple slip orientation. Within the experimental error, the yield stress is athermal between 77 K and 142 K. Work-hardening is athermal too. It increases as a function of γ at the beginning of plastic deformation at 77 K and 90 K. Stress-relaxations are analysed by plotting the logarithm of $-\dot{\tau}$ (which is proportional to $\dot{\gamma}_p$ [1]) as a function of the stress decrease, $\Delta\tau$. Figure 3 proves the logarithmic nature of the stress-relaxation at 156 K. Moreover, along 90 K and 142 K stress-strain curves (figure 2), repeated stress-relaxation tests are made, which permit us to measure the mobile dislocation exhaustion rate $\Delta\rho_m/\rho_{m0}$ ($\Delta\rho_m = \rho_m - \rho_{m0}$) during relaxation. This parameter is plotted as a function of stress in figure 4.

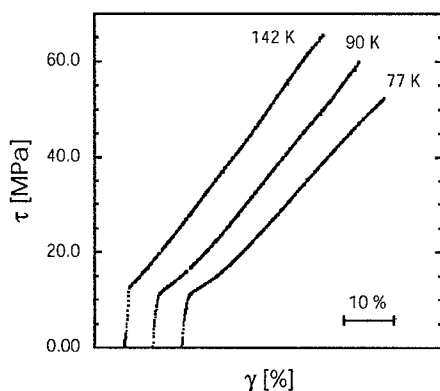


Figure 2. Stress-strain curves of $\langle 011 \rangle$ Cu single crystals at various temperatures. $\dot{\gamma} = 3.8 \times 10^{-5} \text{ s}^{-1}$ (stress-relaxation experiments are performed where the stress-strain curves are interrupted).

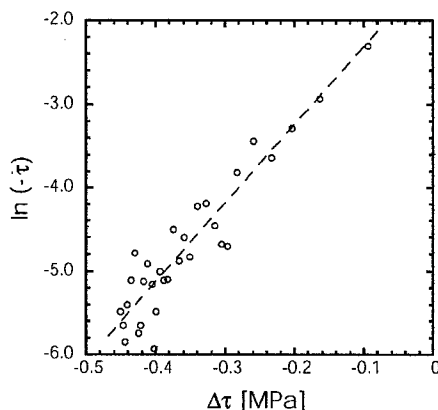


Figure 3. Plot of $\ln(-\dot{\tau})$ versus $\Delta\tau$ (see text) corresponding to a stress-relaxation experiment of 30 s duration. $\langle 011 \rangle$ Cu single crystal. $T = 156 \text{ K}$. $\tau = 48 \text{ MPa}$. $\gamma_p = 2 \%$. (the linear relation is the signature of a logarithmic stress-relaxation [2])

As the work-hardening coefficient θ is constant as a function of stress along the stress-strain curve ($T = 142 \text{ K}$ in figure 2), $\Delta\rho_m/\rho_{m0}$ is constant too (figure 4). As θ increases ($T = 90 \text{ K}$ in figure 2), $\Delta\rho_m/\rho_{m0}$ increases too (figure 4). In these two situations, similar trends are noticed between the work-hardening coefficient and the mobile dislocation exhaustion rate. In addition, these results show that at 90 K, the crystal hardens progressively up to values that are characteristic of stage II. At 142 K, however, both the work-hardening coefficient and the dislocation exhaustion rate are constant from the onset of plastic deformation. After some

amount of deformation, the values of both parameters do not depend on temperature (figures 2 and 4), a feature typical of the work-hardening in stage II of face centered cubic metals.

Ni₃Al

The $\langle 123 \rangle$ Ni₃Al single crystals contain 3.3 at% Hafnium. Details about their peculiar deformation properties are reported in several publications [6, 7]. They are deformed at the strain rate $\dot{\gamma} = 4.8 \times 10^{-5} \text{ s}^{-1}$. As in the case of Cu single crystals, the stress-relaxation appears to be logarithmic. Furthermore, after a series of stress-relaxation tests, the mobile dislocation exhaustion rate and the yield point amplitude $\Delta\tau_R$ at reloading normalized to stress exhibit parallel trends, as shown in figure 5.

In the present case, $\Delta\tau_R$ can be interpreted as the stress increment necessary to multiply dislocations at the end of the transient test after the exhaustion of the mobile dislocation density by an amount $\Delta\rho_m$. The mechanism of exhaustion by Kear-Wilsdorf lock formation is well established in this material [8]. It is responsible for the high values measured for the work-hardening coefficient and $\Delta\rho_m/\rho_{m0}$, as compared to Cu. Figure 5 exhibits two distinct exhaustion rates as a function of stress below and above 360 MPa respectively.

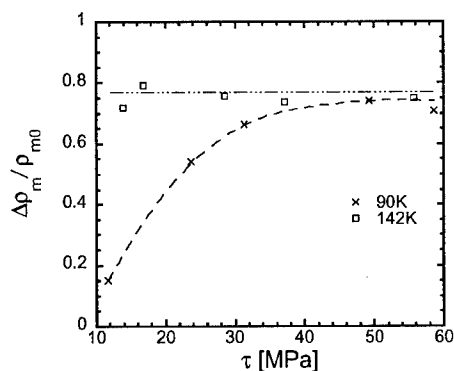


Figure 4. Mobile dislocation exhaustion rate $\Delta\rho_m/\rho_{m0}$ as a function of stress along two different stress-strain curves at respectively 90 K and 142 K. $\langle 011 \rangle$ Cu single crystal. $\dot{\gamma} = 3.8 \times 10^{-5} \text{ s}^{-1}$.

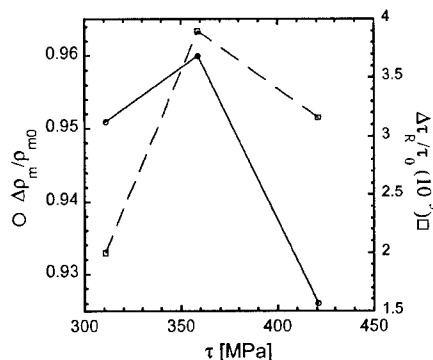


Figure 5. $\Delta\tau_R$ yield point amplitude at reloading after a stress-relaxation series normalized to stress and mobile dislocation exhaustion rate $\Delta\rho_m/\rho_{m0}$ after the same series of stress-relaxations as a function of stress along a stress-strain curve. $\langle 123 \rangle$ Ni₃(Al,Hf) single crystal. $T = 373 \text{ K}$. $\dot{\gamma} = 4.8 \times 10^{-5} \text{ s}^{-1}$.

Germanium

$\langle 123 \rangle$ intrinsic Ge single crystals are tested in compression at a strain-rate $\dot{\gamma} = 4.8 \times 10^{-5} \text{ s}^{-1}$ and stress-relaxation series are carried out along the stress-strain curve shortly after the lower

yield point [3]. Figure 6 represents $\ln(-\dot{\tau})$ versus $\Delta\tau$ for a stress-relaxation, which reveals a non logarithmic behaviour at 700 K. The stress variation during a relaxation of 30 s duration normalized to stress is much higher than for Copper or $\text{Ni}_3(\text{Al,Hf})$ single crystals.

The yield point amplitude at reloading after a stress-relaxation series $\Delta\tau_R$, normalized to stress, and the work-hardening θ along the stress-strain curve are represented in figure 7.

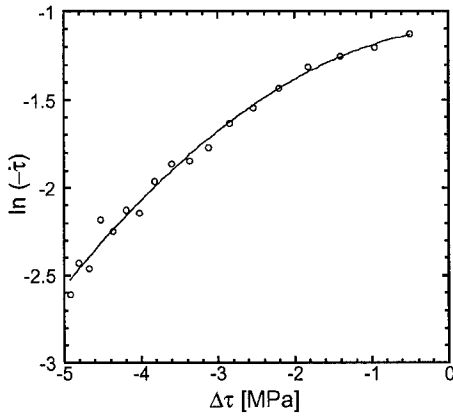


Figure 6. Plot of $\ln(-\dot{\tau})$ versus $\Delta\tau$ corresponding to a stress-relaxation experiment of 30 s duration. $\langle 123 \rangle$ Ge single crystal. $T = 700$ K. $\tau = 47$ MPa. $\gamma_p = 30$ %.

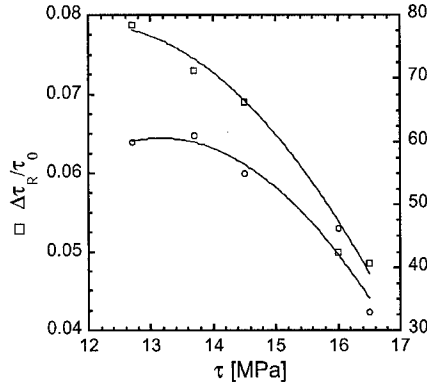


Figure 7. Work-hardening θ and yield point amplitude at reloading after a stress-relaxation series $\Delta\tau_R$ normalized to stress versus stress along the stress-strain curve. $\langle 123 \rangle$ Ge single crystal. $T = 800$ K. $\dot{\gamma} = 4.1 \times 10^{-5} \text{ s}^{-1}$.

The large amount of relaxed stress (up to 40 % of the onset stress over 300 s) can be understood in terms of a large strain-rate sensitivity (or a small V_a). In addition, a good correlation is found again between $\Delta\tau_R/\tau_0$ and the work-hardening θ along the stress-strain curve. A more detailed description of the deformation behaviour of Ge is proposed elsewhere [3].

CONCLUSION

From the above results, the crystals considered in the present study behave differently as far as stress-relaxation experiments are concerned. For the conditions imposed on the specimens, Cu and Ni_3Al exhibit logarithmic relaxations while Ge does not.

The above results are summarized in table I. Mobile dislocation exhaustion is characterized by the parameters $\Delta\rho_m/\rho_{m0}$ and $\Delta\tau_R/\tau_0$. Comparing Cu and $\text{Ni}_3(\text{Al,Hf})$, the exhaustion parameters increase as the work-hardening normalized to the shear modulus G increases as well. Work is in progress for a full characterization of multiplication and exhaustion processes in Ge.

Table I. Exhaustion parameters and work-hardening

material	Cu	Ni ₃ (Al,Hf)	Ge
orientation	<110>	<123>	<123>
testing conditions	142 K stage II	373 K $\gamma_p \approx 3\%$	800 K after the lower yield point
relaxations	logarithmic	logarithmic	non logarithmic
θ/G	3×10^{-3}	3.3×10^{-2}	1.2×10^{-3}
$\Delta\rho_n/\rho_{m0}$	76 %	96 %	
$\Delta\tau_R/\tau_0$	≈ 0	0.004	0.06

These examples emphasize the fair agreement between mechanical parameters measured using transient and monotonic tests. They show that the two parameters $\Delta\rho_n/\rho_{m0}$ and $\Delta\tau_R/\tau_0$ measured respectively during and after the transient tests are accurate indicators of the net dislocation storage rate during plastic deformation. The latter is directly connected with the work-hardening. These experiments also provide some information about the mobile dislocation density ρ_m of the Orowan relation, a poorly documented parameter.

ACKNOWLEDGEMENTS

The authors wish to acknowledge fruitful discussions with Dr P. Spätig and Dr. D. Caillard. They are grateful to the Swiss National Foundation for the financial help.

REFERENCES

1. V.I. Dotsenko, *Phys. Stat. Sol.*, **93b**, 11 (1979)
2. J.L. Martin, B. Lo Piccolo, T. Kruml and J. Bonneville, accepted in *Mater. Sc. Eng. A*.
3. C. Charbonnier, T. Kruml and J.L. Martin, , in Proceedings of the MRS Fall meeting 2000, Symposium on "Multiscale Materials modeling".
4. P. Spätig, J. Bonneville and J.L. Martin, *Mater. Sci. Eng. A*, **167**, 73 (1993).
5. O. Couteau, Diploma thesis in Materials Science, INP Grenoble, France, sept. 2000.
6. P. Spätig, PhD thesis N° 1407, EPFL Lausanne, Suisse, 1995.
7. T. Kruml, J.L. Martin and J. Bonneville, *Phil. Mag. A*, **80**, 1545 (2000).
8. H.B. Kear and H.G. Wilsdorf, *Trans. TMS-AIME*, **224**, 382 (1962)

New Line Model for Optimized Dislocation Dynamics Simulations

Ronan Madec, Benoit Devincere and Ladislav P. Kubin

Laboratoire d'Etude des Microstructures, CNRS-ONERA,
29 Av. de la Division Leclerc, B.P. 72, 92322 Châtillon Cedex, France.

ABSTRACT

A new model for the discretisation of dislocation lines is presented, which is optimised for mesoscale simulations of dislocation dynamics. By comparison with the existing "edge-screw" model, the present one provides a better description of the stress field close to the dislocation lines. It simplifies the modelling of dislocation reactions and accelerates computations by allowing to make use of larger time steps. An application to attractive junctions and forest hardening is briefly sketched.

INTRODUCTION

Ten years ago the first three-dimensional mesoscopic simulation of dislocation dynamics (DD) was proposed [1]. In the latter, a simplified description of dislocation core properties was combined with an elastic frame in order to model the dynamics of dense dislocation microstructures. The most noticeable aspect of this model was the geometrical solution proposed to discretise the dislocation lines [2]. Indeed, for the sake of computing efficiency, it was proposed to replace the continuous lines by a succession of discrete segments with edge and screw characters. This "edge-screw" simulation has been successfully used to study plastic deformation in different types of crystals, hence demonstrating its versatility (see ref. [3] for a short review). More recently, it has been coupled with a finite element code in order to deal with complex boundary value problems and/or complex loadings [4-5].

Other three-dimensional DD simulations have been developed in the past years [6-8]. They differ from the "edge-screw" model mainly in their geometrical formulation. The decomposition of a segment length and character is not performed on a finite set but in the continuum, in order to reproduce the line curvature as closely as possible. In spite of some technical complexities, this approach has the ability of better reproducing the elastic field close to the dislocation lines.

Whatever the geometrical model considered, the computations have been restricted up to now to relatively small simulated volumes $\sim (15\mu\text{m})^3$ and plastic strains ($<1\%$), mostly because of two critical issues. First, the CPU requirement for DD simulations increases extremely fast with the number of interacting segments yielded by the discretisation. The use of algorithmic solutions that reduce such dependence has alleviated but not removed this difficulty. Secondly, many degrees of freedom must be updated along the moving lines and the elementary time steps can be fairly small in materials with high dislocation mobility. As a result, quasi-continuous models favour a reduction of the number of segments per unit line length, whereas fully discretised models favour larger time steps. Thus, a compromise between the two types of discretisations should yield an optimum efficiency.

A modified version of the "edge-screw" model, the "edge-mixed-screw" model, is presented here, which includes two additional characters per slip system. The improvement thus obtained is briefly discussed and illustrated by validation tests. An application is presented to the treatment of dislocation junctions.

DISLOCATION DISCRETIZATION

To preserve the advantages of the "edge-screw" model, the latter has been modified by adding new directions into the finite base of vectors used to discretise the dislocation lines and their displacement steps [1]. These mixed directions, ξ_m , are defined as linear combinations of the edge and screw vectors, i.e., $\xi_m = n\xi_s + m\xi_e$.

As illustrated by Figure 1, the simplest modification consists of adding two 60° directions ($n, m = -1$) per slip system. This solution was found to give satisfactory results in several respects. i) - It does not involve drastic changes in the "edge-screw" model. ii) - It provides an improved description of the dislocation self-stress field (cf. Figure 3 of [9] for a detailed discussion). iii) - It significantly reduces the number of segments required to model a given dislocation microstructure. This last improvement is particularly important for such frequently met configurations as dipoles of arbitrary line orientation and junctions. For instance, as shown in Figure 2 for the case of f.c.c. crystals, the possible directions of the Lomer locks are parallel to either the screw or mixed direction (their character being either edge or mixed) and can be modelled with very few segments.

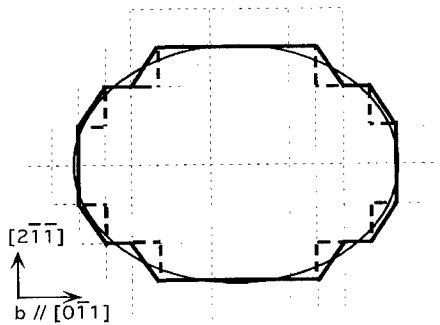


Figure 1. Modelling a small dislocation loop by the "edge-screw" line model (dotted lines) and the "edge-mixed-screw" line model (bold lines). The latter involves both a reduced number of segments and a better description of the continuous shape. The figure is drawn for a (111) slip plane in an f.c.c. crystal, with a Burgers vector b parallel to the $[0\bar{1}1]$ direction.

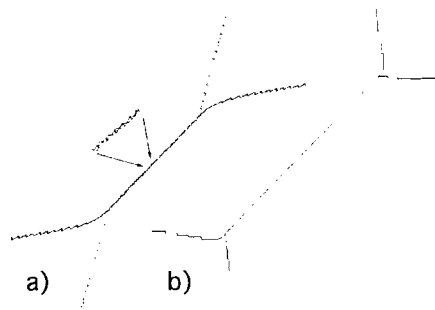


Figure 2. A relaxed junction between two dislocation lines treated with (a) - the "edge-screw" model and (b) - the "edge-mixed-screw" model. In (a), more than 50 segments are needed to obtain an accurate description of the junction line, whereas 2 segments only are sufficient in (b). Notice that the line tension equilibrium at the triple nodes is better achieved at short distances in (b) due to the better description of the line directions.

In addition, the use of edge, screw and -60° characters is of interest for the treatment of the lattice friction or Peierls stress when they are significant. In such cases, dislocations slip occurs by a kink-pair mechanism and results at the mesoscale in the motion of straight and rigid lines parallel to dense atomic rows. This applies typically to the screw line directions in b.c.c. crystals, the screw and -60° directions in diamond cubic crystals and the screw directions in the $\{111\}$ slip planes of $L1_2$ alloys.

DISLOCATION DYNAMICS

The modifications brought into the simulation do not affect the parts of the code devoted to the calculation of the internal stresses and the integration of the equations of motion. They induce an increase of the time spent in the computation of the interaction stresses by about 50%. This extra computing time stems from the relative increase, in the new line model, of the number of non-screw segments, whose stress field is more complex than that of screws. However, due to the decrease in the total number of segments, the net result is an overall decrease in computing time.

The constitutive rules that maintain the connectivity of the segments during their displacement, as well as the procedures for the discretisation of dislocation line curvatures are not significantly altered. The main changes are due to the fact that the length of a segment is now modified during its displacement. This is not the case with the "edge-screw" model, since the segments always move along a direction parallel to that of their neighbours. As a result, the algorithm dealing with the search of obstacles (e.g., forest dislocations, precipitates, interfaces, ...) in the swept area becomes more complex. Nevertheless, most of the related procedures can still be tabulated.

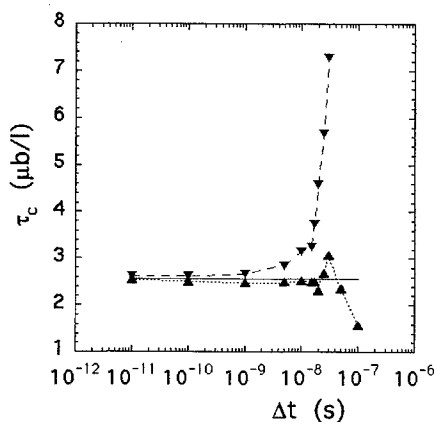


Figure 3. Simulation of the critical stress of a Frank-Read source in copper (in units of $\mu b/L$, where L is the length of the source segment, of screw character, and μ the shear modulus) as a function of the time step. The domain where a good agreement between theory (continuous line, after Foreman [10]) and simulation is obtained extends to larger time step values with the "edge-mixed-screw" model (upwards triangles) than with the "edge-screw" model (downwards triangles). In the present case, the new line model allows increasing the time step value and speeding up the simulation by one order of magnitude.

Altogether, this part of the simulation is significantly accelerated not only because of the reduction in the number of segments but also due to the increase in the time step value. This last important result is illustrated by Figure 3 and has two origins. First, the discretisation leads to smoother shapes and smaller fluctuations in the local line tension. Hence, this allows making use of larger elementary displacements. Secondly, with a smaller number of segments, the number of degrees of freedom per unit line length is decreased. As a consequence, the occurrence of parasite transversal wave modes along the lines is strongly reduced.

CONTACT REACTIONS

The "edge-mixed-screw" model also provides a better description of the dislocation stress field close to the lines. This improves the quantitative aspects of the simulations, particularly regarding the modelling of contact reactions. For instance, in the "edge-screw" formulation, some local rules are commonly used to help implementing the formation and destruction of junctions [11]. These phenomenological rules are useful to by-pass a detailed description of the junction geometry, as the latter requires, a substantial amount of small segments (cf. Figure 2) and a small time step (cf. Figure 3). Such simplifications are no longer necessary with the "edge-mixed-screw" model and the junction properties can be treated without approximation. The problem of dealing with the equilibrium configuration of junctions is then reduced to a simple question of force balance at the triple nodes. The corresponding validation tests are given in the next section. For the same reasons, the new line model allows performing a better treatment of the short-range interactions with any type of elastic defect. Finally, if the use of the -60° mixed directions is well suited for treating junctions, different line directions could be preferred for dealing with other specific problems. For instance, when treating plastic deformation in the vicinity of an interface, it could be advantageous to introduce segments parallel to the latter.

JUNCTION PROPERTIES

From the numerous previous investigations carried out in the early days of dislocation theory (see e.g. [12, 13]), it was concluded that the formation and destruction of junctions constitutes the major contribution to strain hardening. Further, it was shown that junctions are basically low energy configurations whose main properties can be predicted with the help of simple elastic arguments involving a simplified formulation of the line energy.

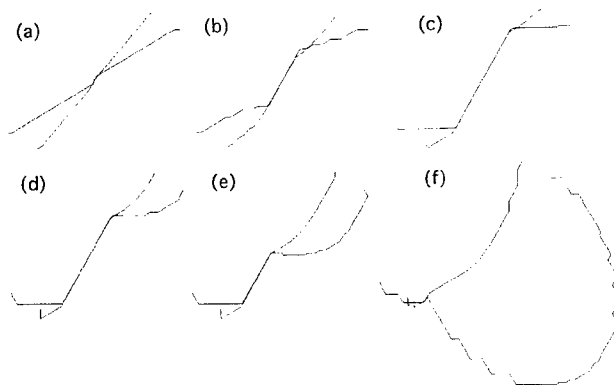


Figure 4. (a) - (c): Zipping of a junction in the absence of applied stress and under the effect of the elastic interactions between the two attractive segments. (d) - (f) : Unzipping of the same configuration under stress. The two interacting slip systems are $1/2[\bar{1}01](\bar{1}\bar{1}1)$ and $1/2[1\bar{1}0](1\bar{1}\bar{1})$.

This last result was confirmed by more recent calculations, both at atomic and mesoscopic scales [14-16]. Detailed checks have been performed on the "edge-mixed-screw" model and are illustrated by Figures 4 and 5. Figures 4-a to -c show the zipping of a junction under zero stress from two attractive segments which cross each other at their mid-point. The sequence of Figures 4-d to -f shows the unzipping of the same configuration under stress. From such tests, one can derive a mapping of the various possible configurations, of the junction lengths and the critical stresses for junction unzipping as a function of the initial orientation of the segments [16]. For instance, Figure 5 shows the simulated junction length when the orientation of one segment is fixed to an angle $\phi_0 = -0.47$ rad. with respect to the $[0\bar{1}\bar{1}]$ junction direction, whereas the other angle ϕ is let to vary. Junctions of different lengths ℓ_j are formed within a range of values of the angle ϕ . The slight asymmetry of this domain is due to the dependence of the self-energy on dislocation character. For large values of ϕ , either repulsive configurations or attractive configurations that do not form junctions (crossed-states) are obtained. The excellent agreement obtained with respect to a simple elastic model (see ref. 15 for detail) confirms that the "edge-mixed-screw" model can realistically treat junction properties.

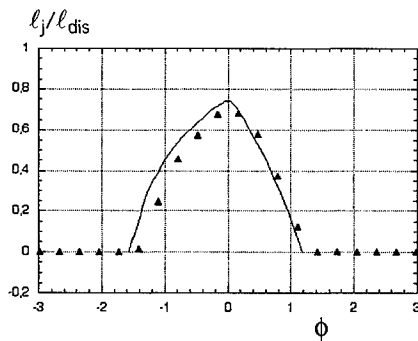


Figure 5. Junction length ℓ_j , reduced by the initial length of the segments ℓ_{dis} , as a function of the orientation ϕ of one of the segments, the other one being fixed. The data points show the simulation results. The full line is a prediction obtained from a balance of energy involving a simplified line energy model.

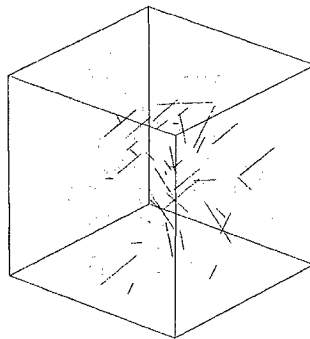


Figure 6. A multiple slip configuration obtained with a $[100]$ stress axis in a simulated box of dimension $(15 \mu m)^3$. The junction lines are shown in black and the dislocation lines in grey.

The modelling of "forest" hardening involves performing a global average over the strengthening effect of all the junctions present in a model crystal (cf. Figure 6). In a mass simulation, the various junctions formed differ not only by several geometrical parameters (Burgers vector, slip plane, length and orientation of the lines, position of the intersection point) but also by their frequency of occurrence. For instance, one can see from Figure 5 that the configuration involving a segment parallel to the incipient junction line ($\phi = 0$) produces a junction of maximum length. This configuration relaxes a maximum of elastic energy and exhibits maximum stability under stress. However, it only occurs for one particular geometry.

A global check of the new line model can be performed by investigating from mass simulations the well-known scaling law that relates the flow stress τ to the square root of the forest dislocation density, ρ_f : $\tau = \alpha \mu b \sqrt{\rho_f}$, where α is a coefficient whose value is about 0.3-0.4 in f.c.c. crystals [17]. Preliminary simulation results yield a value $\alpha = 0.38$ that falls within the expected range. These numerical experiments deserve a careful discussion, which is postponed to a further publication.

CONCLUSION

The "edge-mixed-screw" line model provides an interesting compromise between an increased computing efficiency and a better description of the dislocation fields. Through a self-consistent elastic treatment of dislocation reactions it will allow quantitative simulations of forest and strain hardening to be performed.

REFERENCES

1. L.P. Kubin, G. Canova, M. Condat, B. Devincere, V. Pontikis and Y. Br chet, *Solid State Phenomena*, **23-24**, 455 (1992).
2. B. Devincere and M. Condat, *Acta metall. mater*, **40**, 2629 (1992).
3. B. Devincere and L. Kubin, *Mat. Sci. Eng.*, **A234-236**, 8 (1997).
4. M. Fivel, M. Verdier and G. Canova, *Mat. Sci. Eng.*, **A234-236**, 923 (1997).
5. C. Lemarchand, B. Devincere, L. Kubin and J.L. Chaboche, *MRS Symp. Proc.*, **538**, 63 (1999).
6. H. M. Zbib, M. Rhee, and J.P. Hirth, *Int. J. Mech. Sci.* **40**, 113 (1998).
7. K. W. Schwarz, *J. Appl. Phys.* **85**, 108 (1999).
8. N. M. Gohniem and L. Z. Sun, *Phys. Rev. B* **60**, 128 (1999).
9. B. Devincere, L. P. Kubin, C. Lemarchand and R. Madec, *Mat. Sci. Eng. A*, in press.
10. A. Foreman, *Phil. Mag.* **15**, 1011 (1967).
11. B. Devincere and L.P. Kubin, *Modelling Simul. Mater. Sci. Eng.* **2**, 559 (1994).
12. G. Saada, *Acta metall.* **8**, 841 (1960).
13. G. Schoeck and R. Frydman, *Phys. Stat. Sol. (b)*, **53**, 661 (1972).
14. V. B. Shenoy, R. V. Kukta and R. Phillips, *Phys. Rev. Lett.* **84**, 1491 (2000).
15. L.K. Wickham, K. Schwarz and J. S. St lken , *Phys. Rev. Lett.* **83**, 4574 (1999).
16. R. Madec B. Devincere and L. P. Kubin, *Comp. Mat. Sci.*, in press.
17. J. Gil Sevillano, in H. Mughrabi (Ed.), *Plastic Deformation and Fracture of Materials* (Materials Science and Technology, Vol. 6), VCH, D-Weinheim, p. 40 (1993).

Interactions between Edge Dislocations and Interstitial Clusters in Iron and Copper

Yu.N. Osetsky^{1*}, D.J. Bacon¹, A.Serra² and B.N.Singh³

¹) Materials Science and Engineering, Department of Engineering, The University of Liverpool, Liverpool L69 3GH, UK

²) Dept. Matemàtica Aplicada III, Universitat Politècnica de Catalunya, Jordi Girona 1-3, E-08034 Barcelona, Spain.

³) Materials Research Department, Risø National Laboratory, P.O.Box 49, DK-4000 Roskilde, Denmark

ABSTRACT

Dislocations decorated by both clusters of self-interstitial atoms (SIAs) and small dislocation loops, are one of the microstructure features which can play an important role in post-irradiated deformation processes. The interactions between dislocations and clusters are important and are usually treated within the framework of isotropic elasticity theory. However, it is still not clear whether or not these interactions, especially for small clusters at short distances, can be treated accurately by elasticity theory. Comparative studies by atomistic simulation and elasticity theory can clarify this. Here we present a simple example of such a study where interactions between a glissile SIA cluster and an edge dislocation are studied in bcc-Fe and fcc-Cu using both techniques. In Fe we have studied the interaction of a dislocation with Burgers vector $\mathbf{b} = \frac{1}{2}\langle 111 \rangle$ lying along $\langle 112 \rangle$ direction with a SIA cluster with the same \mathbf{b} situated at different distances below the extra half-plane. In Cu, the dislocation and cluster had $\mathbf{b} = \frac{1}{2}\langle 110 \rangle$ and the dislocation line was along the $\langle 112 \rangle$ direction. Interactions with clusters of diameter about 1 nm were simulated. Elastic calculations were made within the isotropic theory with parameters estimated from atomistic simulation. The results obtained by both techniques are discussed and some preliminary conclusions for different cases are drawn.

INTRODUCTION

In recent years, results of atomic-scale computer modelling of displacement cascades in metals (see [1] for reviews) and the theoretical treatment known as the production bias model [2] have emphasised the significance of intracascade clustering of self interstitial atoms (SIAs) and one-dimensional (1-D) mass transport by SIA clusters. One of the consequences of the formation of glissile SIA clusters is the creation of a vacancy supersaturation, which leads to void swelling. Another important consequence of the 1-D glide of SIA clusters is the creation of a specific microstructural feature in neutron-irradiated metals, such as decoration of dislocations by SIA loops [3-8]. According to the cascade-induced source hardening model [7-9], the increase in the upper yield stress during neutron irradiation occurs because most grown-in dislocations are locked due to decoration by small SIA clusters and dislocation loops. Dislocation-loop interactions [7-8] and their effect on dislocation dynamics [9] are usually treated in terms of elasticity theory.

However, it is still not clear whether or not dislocation-loop and loop-loop interactions, especially at close distances, can be calculated with enough accuracy within the framework of elasticity theory. Clearly, atomic scale simulations are necessary to eliminate this uncertainty. Although in recent years a large number of atomic simulations have been carried out to determine the properties of SIA clusters [10], only a few studies have considered interactions between clusters and other microstructural features. The interaction of small glissile SIA

clusters with a dissociated $\frac{1}{2}\langle 110 \rangle$ dislocation in Ni was studied in [11]. For the case of non-parallel directions of the axis of the SIAs and \mathbf{b} of the dislocation, it was found that the cluster is absorbed by the Shockley partials in both static and gliding dislocations. The absorbed cluster creates a pinning effect and can be reoriented to the same orientation as that of \mathbf{b} as a result of further interaction with the gliding dislocation. The interaction energy between a perfect SIA cluster and $\frac{1}{2}\langle 111 \rangle$ dislocation in Fe was studied in [12] by molecular statics and simple infinitesimal approximation of isotropic elasticity. It was concluded that short-range effects cannot be treated within such an approach. Therefore a lack of data on details of dislocation–cluster interaction still exists. This information is important for further development of continual models for dislocation dynamics for which such details are necessary input parameters. The present study contributes to this effort by making it possible to compare directly the results of atomistic simulations with that of the calculations using the isotropic elasticity theory. We studied interactions between dislocations and SIA clusters/loops having the same Burgers vector, as formed by a decoration–like microstructure in bcc and fcc structures.

CALCULATIONAL METHOD

Molecular statics was used to study the cluster-dislocation interaction energy at a temperature of zero Kelvin in bcc and fcc lattices. The crystallites of about a million atoms were oriented along $[1\bar{1}0]$, $[11\bar{2}]$ and $[111]$ directions in both cases. In both cases the size along the Burgers vector, \mathbf{b} , was about $110|\mathbf{b}|$ and approximately $15nm$ along the dislocation line. The usual boundary conditions for static dislocation studies were applied, i.e. periodic along the dislocation line direction and rigid along the other two directions. The atoms in rigid boundaries were displaced according to the elastic solution for the dislocation. An isolated dislocation was first introduced and relaxed. A cluster with the same Burgers vector as that of the dislocation was then created at a certain distance, $r_{\langle 110 \rangle}$ (e.g. along $[1\bar{1}0]$ direction for the bcc crystallite) or $r_{\langle 111 \rangle}$ (e.g. along $[111]$ direction for the fcc crystallite) below the dislocation slip plane, e.g. below the extra half-plane, and the crystallite was relaxed again. Clusters of 37 and 49 SIAs (of effective loop radii 1.3 and 1.5 nm) were studied in the bcc and fcc crystallites respectively. The dislocation-cluster interaction energy was calculated using the energies of a previously-relaxed isolated dislocation and a cluster. The interatomic interactions were described by many-body potentials derived in [13] for α -Fe and Cu.

The interaction energy, E_{INT}^C , obtained in the computer simulation, was compared with two theoretical approaches based on isotropic elasticity. The first is the simple infinitesimal loop approximation evaluated in [14] and, for the case considered, the interaction energy, E_{INT}^I can be written as

$$E_{INT}^I = -\frac{\mu b^2 S}{2\pi(1-\nu)} \frac{1}{r} \quad (1)$$

where S is the loop area and r is the distance between the cluster centre and dislocation line and μ and ν have usual meaning. In addition to the assumption of isotropic elastic behaviour, eq.(1) is based on the approximation that $r^2 \gg S$, so that the loop size and geometry are ignored.

The second approach evaluates the interaction energy, E_{INT}^E , through the full integration of the dislocation stress over the planar surface enclosed by the loop, e.g. hexagon for bcc Fe and rhombus for Cu. The details of the infinite dislocation stress field interaction with a dislocation segment can be found in [15].

RESULTS AND DISCUSSION

Energy of a straight dislocation.

In the isotropic elasticity theory the interaction energy is determined by the self-energy factor for a straight edge dislocation line given by $2A = \mu b^2 / 2\pi(1-\nu)$ [16] (see also eq.1). In an anisotropic crystal this factor does not have a unique value and depends on the line direction and \mathbf{b} , and must be obtained either by anisotropic elasticity theory [17] or by atomistic simulation [18]. We have applied the later since it gives the energy factor for the particular interatomic potential employed and takes into account the atomic structure of the dislocation core. The method is based on the evaluation of the strain energy E_S within a cylinder containing the dislocation along its axis. This energy can be expressed (per unit length of the dislocation line) as $E_S = A \ln(R_C / r_o) + E_C$, where R_C is the radius of the cylinder, r_o is the core radius and E_C is the core energy. The slope of the plot of E_S versus $\ln(R_C)$ (in the region where it is linear) defines the factor A . It is straightforward to obtain this parameter for the $\frac{1}{2}\langle 111 \rangle$ dislocation in Fe but the validity of this approach is less obvious in Cu due to the dissociation of the $\frac{1}{2}\langle 110 \rangle$ dislocation into two Shockley partials. Nevertheless atomistic simulation has shown that the cylinder energy approach can be applied to a dissociated dislocation and the effective values of A and r_o can be estimated. The dependence of the cylinder energy versus its radius is presented in Fig.1 for the two dislocations considered. Parameters estimated are : $A=3.99\text{eV/nm}$, $r_o = 0.69\text{nm}$ and $E_C = 7.43\text{eV/nm}$ for the edge dislocation in Fe and $A = 2.82\text{eV/nm}$, $r_o = 2.81\text{nm}$ and $E_C = 6.54\text{eV/nm}$ for the dissociated dislocation in Cu. In the case of Cu note the extended area where E_S is very low due to the low stacking fault energy and the high value of the effective core radius due to dissociation. The fact that beyond r_o the cylinder strain energy is linear confirms that the approximation of an effective edge dislocation can be used for distances sufficiently away from the partials ($R_C > 3\text{nm}$).

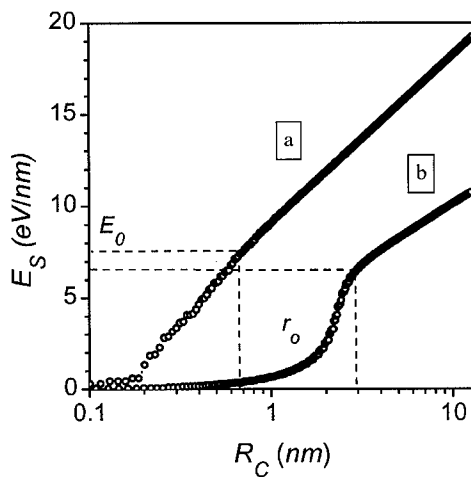


Figure 1 Strain energy within the cylinder containing the dislocation versus the cylinder radius in (a) Fe and (b) Cu.

Loop-dislocation interaction.

The interaction energy of a 37-SIA cluster with an edge dislocation in Fe as a function of the separation $r_{\langle 110 \rangle}$ is presented in fig.2. The estimation of the same energy by the two theoretical approaches is also shown. In fig.2(a) all dependencies seem to be in satisfactory agreement, however in fig.2(b), where E_{INT} is shown versus the reciprocal separation distance, a significant difference, especially at short distances, can be clearly seen. Note that the fitting of simulation data by the power function, $E_{INT} = E_o r^S$, yields an exponent S equal to -1.14 whereas the long-range interactions described within the isotropic elasticity follow the reciprocal

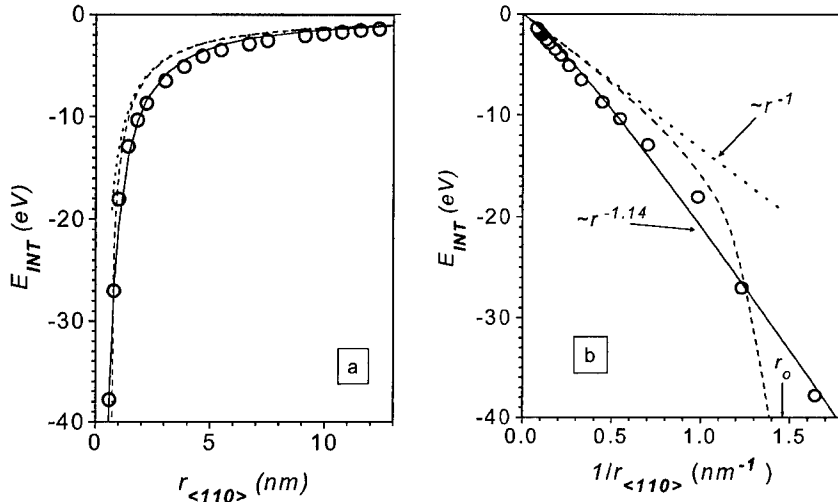


Figure 2 Interaction energy between $\frac{1}{2}\langle 111 \rangle$ edge dislocation and 37 SIA perfect cluster in bcc Fe (a) versus separation along $\langle 110 \rangle$ direction and (b) versus the reciprocal distance. Full line – power function fitted to the simulation data (indicated in (a)), dashed line – full isotropic elasticity calculation, dotted line – infinitesimal loop approximation (reciprocal distance low). The vertical arrow in (b) indicates the effective size of dislocation core obtained from Fig.1.

dependence. The difference is accentuated if the interaction force (for climb) between the line and loop is considered.

The results for Cu are presented in Fig.3. In this case even figure (a) shows a significant difference between the results of analytical calculations and that of atomistic simulation over the whole range $r_{\langle 111 \rangle}$ studied. A power function fitting of simulation data yields an exponent equal to -0.82 (Fig.3b). There is also a qualitative difference in interaction forces between a SIA cluster and a dislocation in Fe and a dissociated dislocation in Cu. Further investigation of this difference has shown that the change in the structure of the 49 SIA cluster in Cu due to the dislocation stress field is the main cause. In earlier simulations [19], isolated small SIA clusters (<100 SIAs), similar to that considered here, were found to have the structure of perfect $\frac{1}{2}\langle 110 \rangle$ dislocation loops. Larger clusters, which are definitely dislocation loops, dissociate into two loops of partials with stacking faults between. Such dissociation decreases the loop formation energy. In the present study even small cluster, i.e. 49 SIAs, shows features of dislocation loop and can dissociate in the vicinity of a dislocation. The degree of dissociation increases and, therefore the cluster/loop formation energy decreases, at shorter distance. This phenomenon is responsible for the change in the cluster-dislocation interaction versus distance behaviour. It can be anticipated therefore that the qualitative form of such interaction in Cu would be dependent on the cluster size. Thus, very small clusters may not dissociate and $E_{INT}^C(r_{\langle 111 \rangle})$ may be similar to that obtained for Fe. Large clusters/loops, which can dissociate even when isolated, should also follow similar behaviour possibly with a higher value of interaction energy. The case studied here, when the dissociation occurs due to the dislocation stress field and depends on the distance to dislocation, is the most complicated and cannot be treated simply in terms of elasticity theory.

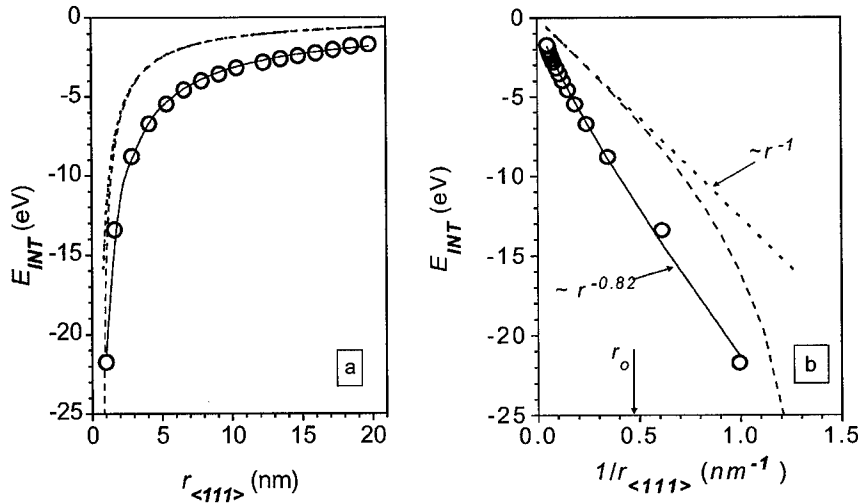


Figure 3 Interaction energy between $\frac{1}{2}\langle 110 \rangle$ dissociated dislocation and 49 SIA perfect cluster in Cu (a) versus separation along $\langle 111 \rangle$ direction and (b) versus the reciprocal distance. Full line – power function fitted to the simulation data (indicated in (a)), dashed line – full isotropic elasticity calculation, dotted line – infinitesimal approximation (reciprocal distance law).

CONCLUSIONS

1. Atomistic simulation and two approaches of isotropic elasticity calculations were applied to study the interaction energy between an edge dislocation and a compact cluster of crowdions aligned parallel to the dislocation Burgers vector in Fe and Cu.
2. In the case of Fe full isotropic elasticity calculations give satisfactory results on dislocation-loop interaction energy at distances larger than several dislocation core radii but overestimate the interaction force at short distances. The approximation of an infinitesimal loop gives satisfactory agreement on the interaction energy at large distances.
3. The interaction between the dissociated edge dislocation and a 49-SIA cluster in Cu is complicated since the dislocation enhances the dissociation of the cluster. This increases the dislocation-cluster interaction energy. This interaction cannot be treated simply by elasticity theory. The possible effect of the cluster size on the character of dislocation-cluster interaction is discussed.

ACKNOWLEDGEMENTS

This research was supported by the Engineering and Physical Sciences Research Council (UK). It has been partly carried out using the facilities of CESA and CEPBA (Barcelona, Spain) under the coordination of C4. BNS acknowledges the support from European Fusion Technology Programme.

REFERENCES

- [1] D.J.Bacon and T.Diaz de la Rubia, *J. Nucl. Mater.*, **216** (1994) 275; D.J.Bacon, A.F.Calder and F.Gao, *J.Nucl.Mater.*, **251** (1997) 1; D.J. Bacon, F. Gao and Yu.N. Osetsky, *Nucl. Instr. And Methods. In Phys. Research*, **B 153** (1999) 87; D.J. Bacon, F. Gao and Yu.N. Osetsky, *J.Nucl. Mater.*, 276 (2000) 1.
- [2] C.H.Woo and B.N.Singh, *Philos. Mag.A*, **65** (1992) 889; B.N.Singh and A.J.E.Foreman, *Ibid*, **66** (1992) 975; B.N.Singh, S.I.Golubov, H.Trinkaus, A.Serra, Yu.N.Osetsky and A.V.Barashev, *J.Nucl.Mater.* **251** (1997) 107; S.I.Golubov, B.N.Singh and H.Trinkaus, *J.Nucl.Mater.* **276** (2000) 78.
- [3] J.O.Stiegler and E.E.Bloom. *Rad. Effects*, **8** (1971) 33.
- [4] R.Bullough, In: *Dislocations and Properties of Real Materials*, The Institute of Metals, London (1985) 283.
- [5] B.N.Singh, A.Horsewell, P.Toft and D.J.Edwards, *J.Nucl.Mater.* **224** (1995) 131.
- [6] M.Kiritani, *J.Nucl.Mater.*, **216** (1994) 220.
- [7] B.N.Singh, A.J.E.Foreman and H.Trinkaus, *J.Nucl.Mater.*, **249** (1997) 103.
- [8] H.Trinkaus, B.N.Singh and A.J.E.Foreman, *J.Nucl.Mater.*, **249** (1997) 91; H.Trinkaus, B.N.Singh and A.J.E.Foreman, *J.Nucl.Mater.*, **251** (1997) 172.
- [9] N.M.Ghoniem, B.N.Singh, L.Z.Sun and T.Diaz de la Rubia, *J.Nucl.Mater.*, **276** (2000) 166; N.M.Ghoniem and B.N.Singh, Proc. Of 20th Risø Int. Symp. on Materials Science : *Deformation-Induced Microstructures : Analysis and Relation to Properties*, Eds: J.B.Bilde-Sørensen *et al.*, Risø National Laboratory, Roskilde, Denmark, (1999) 41.
- [10] B.D.Wirth, G.R.Odette, D.Maroudas and G.E. Lucas, *J.Nucl.Mater.*, **244** (1997) 185; Yu.N.Osetsky, M.Victoria, A.Serra, S.I.Golubov and V.Priego, *J.Nucl.Mater.*, **251** (1997) 34; Yu.N.Osetsky, A.Serra and V.Priego, *Mat. Res. Soc. Symp. Proc.*, **527**, 59 (1998); Yu.N.Osetsky, D.J.Bacon and A.Serra, *Philos.Mag.Lett.* **79** (1999) 273; Yu.N. Osetsky, D.J.Bacon and A.Serra, *Mat. Res. Soc. Symp. Proc.*, vol. 538 (1999) 649; Yu.N. Osetsky, F.Gao and D.J.Bacon, *Ibid.*, vol. 540 (1999) 691; Yu.N.Osetsky, D.J.Bacon, A.Serra, B.N.Singh and S.I.Golubov, *J.Nucl.Mater.*, **276** (2000) 65; A.V.Barashev, Yu.N.Osetsky and D.J.Bacon, *Philos.Mag.*, **A 80** (2000) 2709.
- [11] D.Rodney and G.Martin, *Phys.Rev.Lett.*, **82** (1999) 3272; *Phys.Rev.*, **B 61** (2000) 8714.
- [12] Yu.N.Osetsky, D.J.Bacon, F.Gao, A.Serra and B.N.Singh, *J.Nucl.Mater.*, **283-287** (2000) 784.
- [13] G.J.Ackland, G.Tichy, V.Vitek, M.W.Finnis, *Philos. Mag.*, **A, 56** (1987) 735; G.J.Ackland, D.J.Bacon, A.F.Calder and T.Harry, *Philos. Mag.*, **A, 75**, (1997) 713
- [14] A.J.E.Forcman, *AERE Report - R 4654* (1964).
- [15] J.P.Hirsch and J.Lothe, *Theory of dislocations*, Wiley (1982).
- [16] D.Hull and D.J.Bacon, *Introduction to Dislocations*, Butterworth-Heinemann, Oxford (1984)
- [17] D.J.Bacon, D.M.Barnett and R.O.Scattergood, *Progress in Mat. Science*, **23** (1979) 51.
- [18] J.O.Schiffgens and K.E.Garrison, *J.Appl.Phys.*, **43** (1972) 3240.
- [19] Yu.N.Osetsky, A.Serra, B.N.Singh, S.I.Golubov, *Philos. Mag.*, **A 80** (2000) 2131

ATOMIC SCALE SIMULATION OF THE EFFECT OF HYDROGEN ON DISLOCATIONS IN Zr

C. Domain¹ and A. Legris²

¹ EDF – R&D Département EMA, Les Renardières, F-77818 Moret sur Loing Cédex, France

² Laboratoire de Métallurgie Physique et Génie des Matériaux, UMR 8517, Université de Lille I, F-59655 Villeneuve d'Ascq Cédex, France

ABSTRACT

In nuclear power plants, Zr-based cladding is corroded by the primary coolant. Concomitantly, it undergoes hydrogen pick-up which induces modifications of its mechanical properties, especially creep and recrystallization rates. Below 600K, the deformation in hcp Zr is partially controlled by screw dislocations, which due to their intricate core structure have reduced intrinsic mobility. Here, we address the possible hydrogen induced modifications of the core structure of screw dislocations. We used first-principle calculations based on the density functional theory to evaluate the interaction between hydrogen and screw dislocation cores and also to evaluate the hydrogen induced modifications of the prismatic and basal gamma surfaces. We show that the presence of hydrogen results in significant reductions of the stacking fault energies.

INTRODUCTION

The deleterious effect of hydrogen on mechanical properties of metallic alloys was documented since the end of the 19th century, with an increasing interest for an understanding of the mechanisms involved at the atomic scale. A first distinction of the hydrogen effects can be made between systems that undergo hydrogen-induced phase transitions and those that do not. In Zr alloys, hydrogen is known to modify the mechanical behaviour both in solid solution and as hydride precipitates [1].

Experimental and theoretical studies of hcp Zr alloys show that, at temperatures of interest (i.e. below 600 K), the plastic behaviour is controlled by the mobility of screw dislocations. Since they have a core spread in the basal and prismatic planes, their mobility is low. Whatever the type of mechanism mentioned (locking-unlocking, Peierls-like [2]) to explain the low-temperature plastic deformation, the lattice friction that results from the intricate core structure seems to be the key-phenomenon governing plasticity. To understand the influence of hydrogen on the mechanical behaviour of Zr alloys, it is therefore necessary to know the energies of intricate ionic and electronic configurations involving Zr and H atoms. This requires accurate atomic-scale numerical simulations. Despite their high computational efficiency for metals, empirical energetic models cannot be used as they deal only implicitly with the electronic density and consequently suffer from poor transferability, specially in alloys. Electronic structure calculations can be performed at various levels, going from simple quantum mechanics formulations (diffusion of free electrons by a central potential) to self-consistent fully ab initio quantum mechanics models, through intermediate tight-binding models with firm quantum mechanics foundations but involving fitted parameters [3].

In this work, we present ab initio calculations concerning the interactions between H and screw dislocation cores in α Zr. Among self-consistent ab initio models, the Density-Functional Theory (DFT) [4] is nowadays largely used in materials science, and can be applied to the present issue owing to the enormous enhancement of the available computer power. The DFT model was carefully checked in a variety of H-Zr configurations [5]. Despite the continuous improvements in computational speed, memory capacity and efficiency of the numerical

methods, the number of transition metal atoms in a tractable system is limited to about 100. Therefore we performed only a few calculations involving a screw dislocation core, and in order to get further information about the core structure, we studied the so-called Gamma surface introduced by Vitek et al. (see [6] for instance and references therein). We focussed on the influence of hydrogen in solid solution on the basal and prismatic Gamma surfaces. Particular attention was paid to H-induced modifications to the basal and prismatic stable stacking fault energy.

COMPUTATIONAL PROCEDURE

Our calculations were performed using the Vienna ab initio simulation package (VASP) [7]. This code implements the main concepts of the DFT combined with very efficient numerical algorithms for the self consistent resolution of the one-electron effective hamiltonian. The calculations were performed in a plane wave basis, using fully non local Vanderbilt-type ultrasoft pseudopotentials to describe the electron-ion interaction [8]. Exchange and correlation were described by the Perdew and Zunger functional adding nonlocal corrections in the form of the Generalized Gradient Approximation (GGA) of Perdew et al. [9]. The pseudopotentials used were taken from the VASP library. For Zr, the six 4p electrons were considered as valence ones together with the two 5s and the two 4d ones. A unique cut-off energy of 225 eV was used for all the systems. The supercell approach was used to simulate perfect crystals as well as crystals containing defects. Brillouin zone (BZ) sampling was performed using the Monkhorst and Pack and related schemes. A convergence within 2 meV per atom with respect to the discrete BZ sampling was achieved using a k -points density close to $3000 \cdot V_a$, where V_a is the volume of the simulation cell. As previously mentioned, this model was carefully checked in a variety of Zr-H configurations [5]. Using similar parameters, other authors working on Zr surface relaxations and ZrO_2 polymorphism, obtained results that provide further validation to our DFT approach [10].

RESULTS

Concerning the Zr-H system, we start by recalling results of interest in the present context (also reported elsewhere [5]). As regards the hydrogen site occupancy, the model in the GGA approximation predicts the tetrahedral site to be more stable by about 60 meV at 0 K than the octahedral one. This is in agreement with experimental observations [11] and gives an insight into the model accuracy. Moreover, in δ ZrH hydride with fcc structure, hydrogen atoms distributed in the tetrahedral sites prefer drastically (by 0.16eV per H atom) to adopt a planar distribution in $\{110\}$ planes rather than a diamond-like structure (see Figure 1).

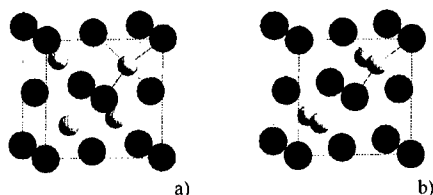


Figure 1: ZrH hydride a) diamond like structure, b) most stable configuration

Stacking fault energy calculations can be performed using several geometries. When considering stable faults, it is possible to use supercells with periodic boundary conditions (PBC) along the three directions implying the presence of two faults in the cell. Alternatively, triclinic

supercells having an xy plane parallel to the fault and a z direction forming a small angle with the fault plane normal in order to compensate the fault vector can be used. In this case there is only one fault per simulation cell. The most practical geometry is probably a supercell containing a sufficient number of Zr planes surrounded by vacuum along the fault plane normal. The results presented here were obtained using the last type of geometry containing 10 Zr planes embedded in the equivalent of 5 vacuum planes. The Zr atoms on each side of the fault were allowed to relax only perpendicularly to the fault plane in order to cancel out possible compressive stresses. The ionic relaxations were stopped when the forces on the atoms reached values below 0.05 eV/atom. In pure Zr, the values of the basal and prismatic static fault energies calculated in this way are within 5% of those calculated using full PBC. The results are reported in table 1 together with those obtained by Legrand [12] using a tight-binding model.

Table 1: Basal and prismatic fault energies and Legrand's parameter $R = C_{66} \gamma_{\text{basal}} / C_{44} \gamma_{\text{pris}}$, for two different models: DFT (this work) and tight-binding one [12].

Calculation type	Energy (mJ/m ²)	Fault plane	Fault vector	Legrand's Param. R [12]
Tight binding	340	basal	$a/3 \langle 1 \bar{1} 0 0 \rangle$	
Tight binding	150	prismatic	$a/6 \langle 2 \bar{1} \bar{1} 0 \rangle$	2.3
Present work	200	basal	$a/3 \langle 1 \bar{1} 0 0 \rangle$	
Present work	144	prismatic	$a/6 \langle 2 \bar{1} \bar{1} 0 \rangle$	1.9

In Table 1 is also reported the parameter $R = C_{66} \gamma_{\text{basal}} / C_{44} \gamma_{\text{pris}}$ introduced by Legrand to characterize the slip type. Values of R greater than one indicate that prismatic slip should be favored, while values of R less than one are an indication of basal slip. From Table 1 it appears that our results and those of Legrand almost coincide for the prismatic fault. However for the basal fault we obtain a value almost half that predicted by the tight-binding model. Despite this discrepancy, the calculated R values for both models are rather close because the C_{44} value calculated with our model is lower than the experimental one and partly compensate for the lower γ_{basal} value.

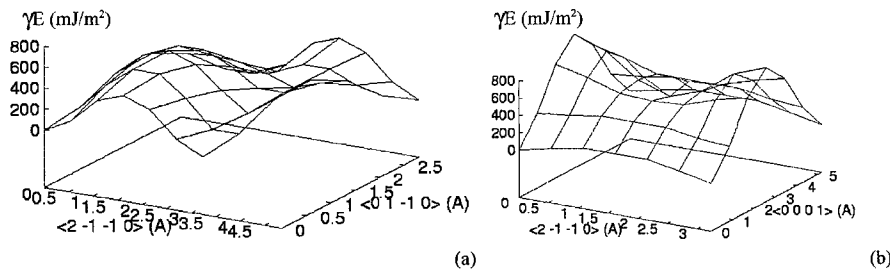


Figure 2: calculated basal (a) and prismatic (b) Gamma surface for pure hcp zirconium.

Figure 2 a and b represents the basal and prismatic Gamma surface respectively for pure Zr calculated with our model. To study the influence of H on the Gamma surfaces, we introduced H atoms in their most stable configuration between the Zr planes defining the fault for each geometric configuration corresponding to a given fault vector. The general consequence of the presence of hydrogen is an overall decrease in the Gamma surface energies, whatever the

fault plane and the fault vector considered. Figure 3 plots a cut of both the basal and prismatic Gamma surfaces along the Burgers vector $b=a/3\langle 2 \ -1 \ -1 \ 0 \rangle$. It was obtained for a surface coverage fraction Θ (defined as the number of H atoms between the fault planes divided by the number of Zr atoms in one fault plane) equal to 1 in both cases. Note that the atomic fraction, although largely used, may be misleading. Indeed, due to the atomic surface density difference, $\Theta = 1$ represents one H atom per 9 \AA^2 for the basal fault and only one H atom per 17 \AA^2 for the prismatic one. It clearly appears that the presence of hydrogen also induces a stable stacking fault energy lowering, the magnitude of which depends on Θ . In Tables 2 and 3, we report the stable basal and prismatic fault energies values for several Θ values. For the basal fault, the minimum is reached at $\Theta = 1$, while for the prismatic fault the corresponding value is 2, which approximately gives the same hydrogen surface density.

Table 2: Basal stacking fault energy as a function of the H coverage in the fault.

Surface Coverage Fraction Θ	γ_{basal} (mJ/m ²)
0	200
$\frac{1}{4}$	120
$\frac{1}{2}$	80
1	-60
2	-14

Table 3: Prismatic fault energy as a function of the H coverage in the fault.

Surface Coverage Fraction Θ	γ_{prism} (mJ/m ²)
0	144
1	67
2	-90

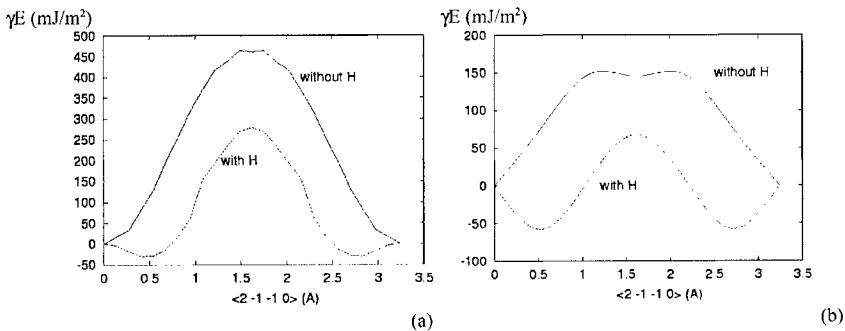


Figure 3: Gamma surface energy cut along the Burgers vector in the basal (a) and prismatic plane (b), obtained for $\Theta=1$ in both cases.

These results indicate that H is attracted to planar defects. However, they can not be considered as a direct evidence of the H affinity for screw dislocations cores. To assess this

particular point, we performed a few simulations of screw dislocation cores, using an orthogonal cell containing 64 Zr atoms placed in adjacent $\langle 2 \ -1 \ -1 \ 0 \rangle$ planes. Along this direction PBC were applied, while along the perpendicular directions free-surface conditions were adopted by embedding the simulation cell in a 3 Å thick vacuum ribbon. As a starting geometry, we adopted that predicted by continuum elasticity (see Figure 4 a) and then relaxed all Zr atoms but those close to the cell boundaries. An H atom was introduced between the cell boundaries and the dislocation core, and the energy of this atomic configuration was compared to that corresponding to an H atom placed inside the core (see figure 4 b). The energy of the last configuration is lower by about 0.2 eV per H atom, a value that can be considered as an estimation of the H – dislocation core attractive interaction energy.

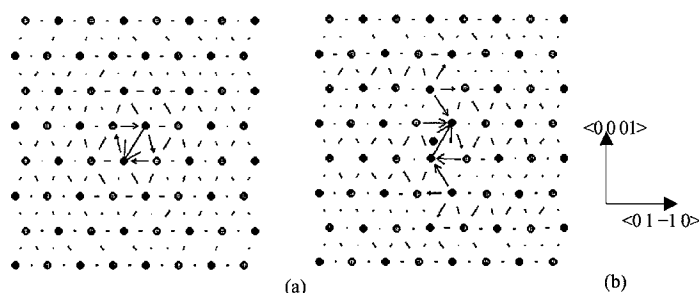


Figure 4: (a) Geometrical screw dislocation core predicted by continuum elastic theory and (b) relaxed core containing one hydrogen atom. The normal to the figure plane is $\langle 2 \ -1 \ -1 \ 0 \rangle$.

DISCUSSION

Although the correlation between stacking fault energies and mechanical properties is not straightforward, our results give however an insight into the H-induced dislocations mobility modifications. If as a starting point one assumes that H atoms are arranged in a prismatic plane, the corresponding prismatic fault energy is lowered. This should favour a spread of the dislocation core mainly in this plane, and lead to two somehow contradictory consequences. On one hand, as suggested by the results in Figure 3, the lattice friction on the prismatic plane is probably lowered. Indeed the lattice friction is related to the gradient of the Gamma surface along the Burgers vector, and this gradient is also probably lowered by the presence of H. Furthermore, it is likely that the increase of prismatic spread is concomitant to a reduction of the basal spread. In this case, the core structure with hydrogen should be more planar and therefore undergo a lower Peierls barrier. On the other hand, the enhanced planar dislocation spread probably hinders cross slip, and therefore reduces the out of plane dislocation mobility. This interpretation accounts for a number of experimental observations, such as the H induced decrease of recovery rates in cold worked materials and the increase of creep rates in fully annealed samples containing hydrogen in solid solution [1]. In the previous interpretation, it is implicitly assumed that H atoms are always located in the lower energy sites. This assumes that H atoms move fast enough to follow the dislocations cores.

A completely different scenario is also possible if as a starting point, the H atoms are arranged in a basal plane. In this case a similar behavior should be observed, with basal slip, but this situation has not been detected experimentally as far as we know. One point however makes the above assumptions plausible : H atoms tend to adopt planar geometric configurations in ZrH cubic hydrides. The planar configuration in ZrH (which is the most stable) is very close to the

local configuration of H and Zr atoms that can be found in the prismatic fault plane with $\Theta = 2$. This indicates H atoms probably adopt a planar configuration, at least in the neighborhood of a dislocation core in hcp Zr.

CONCLUSION

The influence of hydrogen in solid solution in zirconium on the screw dislocation structure has been studied by means of atomic scale simulations using the Density Functional Theory methodology. Our results show that there is a strong attraction of hydrogen to the screw dislocation cores and that the presence of hydrogen strongly decreases the energies of the basal and prismatic stacking faults. These facts may result in a hydrogen induced modification of the screw dislocations core structure, which in turn may lead to a dislocation mobility change with possible implications on the macroscopic mechanical properties.

ACKNOWLEDGEMENTS

This work is part of the REVE (virtual reactor) project which aims to simulate the irradiation effects in structural materials. It has partially benefited from the computational facilities of the French organizations IDRIS and CINES as well as those of CRI –USTL supported by the Fonds Européens de Développement Régional.

REFERENCES

- [1] P. Bouffieux and N. Rupa, ASTM STP **1354**, 399–421, Proceedings of the 12th international meeting of zirconium in the nuclear industry, Toronto, June (1998). P. Bouffieux and L. Legras, ANS, Proceedings of International Topical Meeting on Light Water Reactor Fuel Performance, Park City, Utah Apr 10–13 2000. N. Rupa, PhD Thesis : "Effets de l'hydrogène et des hydrures sur le comportement viscoplastique du zircaloy-4 recristallisé " UTC-France, April 2000.
- [2] S. Farenc, D. Caillard and A. Couret, Acta. Metall. Mater. **41**, 2701–2709 (1993); *ibid*, Acta. Metall. Mater. **43**, 3669–3678 (1995).
- [3] MRS Symp. Proceedings **491** 1–3 dec 1997, "Tight Binding Approach to Computational Materials Science".
- [4] P. Hohenberg and W. Kohn, Phys. Rev. **136**, 864 (1964); W. Kohn and L. Sham, Phys. Rev. **140**, 1133 (1965).
- [5] C. Domain and A. Legris, in preparation.
- [6] M. S. Duesbery and V. Vitek, Acta. Mater. **46**, 1481 (1998).
- [7] G. Kresse and J. Hafner, Phys. Rev. B **47**, 558 (1993); *ibid*. **49**, 14251 (1994); G. Kresse and J. Furthmüller, Phys. Rev. B **55**, 11169 (1996); *ibid*, Comput. Mat. Sci. **6**, 15 (1996).
- [8] D. Vanderbilt, Phys. Rev. B **41**, 7892 (1990); G. Kresse and J. Hafner, J. Phys.: Condens. Mater. **6**, 8245 (1996).
- [9] J. P. Perdew, J.A. Chevary, S.H. Vosko, K.A. Jackson, M.R. Pederson, D.J. Singh and C. Fiolhais, Phys. Rev. B **46**, 6671 (1992).
- [10] G. Jomard, T. Petit, A. Pasturel, L. Magaud, G. Kresse and J. Hafner, Phys. Rev. B **59**, 4044 (1999); G. Jomard, T. Petit, L. Magaud and A. Pasturel, Phys. Rev. B **60**, 15624 (1999).
- [11] S.R. MacEwen, C.E. Coleman and C.E. Ells, Acta Metall. **33**, 753–757 (1985).
- [12] B. Legrand, Phil. Mag. B **49**, 171–184 (1984).

**Bond-Order Potentials with Analytic Environment-Dependent Tight-Binding Integrals:
Application to BCC Molybdenum**

Matous Mrovec¹, Duc Nguyen-Manh², David G. Pettifor² and Vaclav Vitek¹

¹ Department of Materials Science and Engineering, University of Pennsylvania,
Philadelphia, PA 19104-6272, U.S.A.

² Department of Materials, University of Oxford, Parks Road, Oxford OX1 3PH,
United Kingdom.

ABSTRACT

We present a new Screened Bond-Order Potential (SBOP) for molybdenum in which the environmental dependence of two-center tight-binding bond integrals has been implemented via a recently developed analytic expression. These bond integrals reproduce very well the numerical ab-initio values of screened LMTO bond integrals. In particular, they display the large discontinuity in $dd\pi$ between the first and second nearest neighbor of the bcc lattice whereas they do not show any discontinuity in $dd\sigma$. This dependence can be traced directly to the angular character of the analytic screening function and is shown to be critical for the behavior of the second nearest neighbor force constants. The new BOP eliminates the problem of the very soft T2 phonon mode at the N point that is found in most two-center tight-binding models. Preliminary study of the core structure of $1/2\langle 111 \rangle$ screw dislocations performed using SBOP indicates that the core is narrower and less asymmetric than structures found in previous studies, in agreement with recent ab-initio calculations.

INTRODUCTION

Tight-binding (TB) methods are a reliable approach for determination of total energies for materials in which covalent character of bonding plays an important role [1]. They comprise fundamental quantum mechanics, ensuring correct account of the angular character of bonds [2]. Atomistic calculations employing these methods are fast enough to treat systems of particles that are much larger than those attainable in ab-initio DFT based calculations. In recent years the tight-binding method with the orthogonal basis and two-center bond (hopping) integrals has been reformulated in terms of Bond-Order Potentials (BOP) [3]. This linear scaling TB scheme does not require use of periodic boundary conditions and all the calculations are performed in the real space. This is particularly expedient for studies of extended crystal defects, such as dislocations.

The key point in all TB schemes is to develop a suitable parametrization, which not only reproduces experimental and theoretical data for ideal lattice structures, but is transferable to configurations not included in the fitting. This is especially important when the method is to be used in studies of extended defects with structures very different from that of ideal lattices. However, this is a daunting task considering approximations and simplifications implicit in the TB scheme. One of the crucial approximations, embodied in the two-center orthogonal TB method, is the assumption of orthogonality of the underlying basis set. This, of course, can never be exact since the atomic-like orbitals centered at different sites overlap. Several studies have shown that the effects of non-orthogonality can be to a good approximation accounted for by environmental dependence of the two-center TB parameters [4, 5]. For this reason a new

screened bond-order potential (SBOP) formalism, which includes non-orthogonality via analytic concept of a screening function, has recently been developed [6].

In this paper we present a first application of this scheme for the case of molybdenum for which it has been found that the transferability of the unscreened bond integrals is limited. The unscreened BOP potentials were quite successfully employed in modeling of both pure transition metals [7, 8] and certain alloys, such as TiAl [9]. However, several problems have been encountered, in particular for molybdenum. Specifically, in some parts the calculated phonon spectra deviate significantly from the experimental observations; the acoustic phonons near the N point are too soft. Furthermore, the vacancy formation energy was generally found to be too low. We will demonstrate in this paper that the new scheme is able to remedy these problems and thus provide even more reliable predictions for complex configurations of atoms.

In the following section we briefly summarize the introduction of the screening function, S , into the BOP scheme. We then demonstrate improvements of predicted properties of molybdenum within the screened model (SBOP). Finally, we present calculations of γ -surfaces and atomic structures of the $1/2\langle 111 \rangle$ screw dislocation, which we compare with previous studies employing central-force potentials as well as with recent ab-initio calculations.

THEORY

The derivation of the SBOP formalism starts from the non-orthogonal two-center TB representation, whose secular equation is given as

$$[\mathbf{H} - \epsilon_v(\mathbf{I} + \mathbf{O})] = 0 \quad (1)$$

where \mathbf{H} and \mathbf{O} are the Hamiltonian and overlap matrices, respectively; \mathbf{I} is the unit matrix. The intersite elements of the Hamiltonian matrix are given as usually in terms of the radial bond integrals and Slater-Koster angular functions. The elements of the screening function $\mathbf{S} = (\mathbf{I} + \mathbf{O})^{-1}$ can be obtained analytically using the same formalism as that employed in the original BOP theory [3]. Analytical expression for the elements of the screening function $S_{\ell\ell'\tau}^{ij}$ for an orbital $\ell\ell'\tau$ ($\ell, \ell' = s, p, d$; $\tau = \sigma, \pi, \delta$) between atoms i and j , can be obtained by inverting $(\mathbf{I} + \mathbf{O})$ using Green's function method and Lanczos recursion [10] up to the third level [6]. This function reflects the fact that the two-center bond integral between atoms i and j is altered due to the environment of the i - j bond, so that its screened value is given as

$$\hat{\beta}_{\ell\ell'\tau}^{ij} = \beta_{\ell\ell'\tau}^{ij}(\mathbf{R}_{ij})(1 - S_{\ell\ell'\tau}^{ij}) \quad (2)$$

where $\beta_{\ell\ell'\tau}^{ij}$ is the corresponding unscreened bond integral. The screening function can be expressed in terms of second and third moments, μ_2 and μ_3 , of the overlap matrix \mathbf{O} , interference contribution c_I , defined in [6], and elements of the overlap matrix, $O_{\ell\ell'\tau}$, namely

$$S_{\ell\ell'\tau}^{ij} = \frac{(c_I^{ij})_{\ell\ell'\tau} - (\bar{\mu}_2)_{\ell\ell'\tau} + (\bar{\mu}_3)_{\ell\ell'\tau}}{1 + O_{\ell\ell'\tau}^2(\mathbf{R}_{ij}) - 2(\bar{\mu}_2)_{\ell\ell'\tau} + (\bar{\mu}_3)_{\ell\ell'\tau}} \quad (3)$$

This formula has been derived in [6] assuming that the screening is due to the s valence electrons only, and is exact up to three-member rings of s valent atoms; the screening by more localized p and d valence electrons is much weaker.

In order to increase computational efficacy, we have employed a simplified version of the formula (3) in our calculations. Since the third moment and $O_{\ell\ell\tau}^2$ are both very small they can be neglected in the denominator. The simplified formula for the screening function is then

$$S_{\ell\ell\tau}^{ij} = \left[c_i^{ij} \right]_{\ell\ell\tau} - (\bar{\mu}_2)_{\ell\ell\tau} \sqrt{1 - 2(\bar{\mu}_2)_{\ell\ell\tau}} \quad (4)$$

Both c_i and μ_2 are functions of overlap and bond integrals between atoms i, j and their neighbors as well as of angular functions of Slater-Koster type which depend on mutual positions of atoms and orbital types. Hence, this concept of screening function introduces into the BOP scheme only a small number of additional parameters. Specifically, these are $ds\sigma$ interactions and the overlap integrals; the latter have the same scaling dependence as the corresponding bond integrals albeit a different magnitude. All these parameters can be extracted by analyzing ab-initio calculations and are not fitted to any particular physical property.

Figure 1 shows a comparison of $dd\sigma$ and $dd\pi$ bond integrals in bcc molybdenum calculated by three methods: The BOP with unscreened bond integrals, new SBOP and ab-initio screened LMTO method. We do not present $dd\delta$ bond integrals since their behavior is analogous to that of $dd\pi$ bond integrals. The important feature of SBOP is its ability to reproduce the values of $dd\pi$ for the second nearest neighbors that, unlike $dd\sigma$, are environment dependent. As shown in the following section, this is crucial for certain phonon modes.

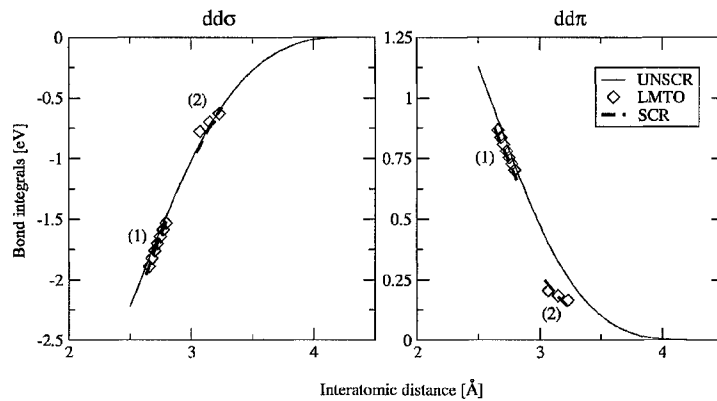


Figure 1. $dd\sigma$ and $dd\pi$ bond integrals for molybdenum: Full curves: analytical unscreened BOP; Dashed curves: SBOP; Symbols: Ab-initio screened LMTO. (1) and (2) label first and second nearest neighbors of the bcc structure, respectively.

The SBOP differs from the original BOP only by addition of the screening function and, therefore, fitting of other parts of the potential is done in the same way as in the unscreened case [7]. The remaining repulsive contributions, which represent electrostatic and orbital-orbital interactions, are fitted to reproduce the basic properties of the ground state structure (lattice parameter, cohesive energy, elastic constants). Forces due to the bond part can be calculated using Hellmann-Feynman theorem provided the bond order is computed sufficiently accurately. The repulsive parts are given as analytical functions of distance between atoms and their differentiation is, therefore, straightforward.

RESULTS

We have constructed the SBOP for molybdenum and here we present a brief compilation of results documenting the validity and importance of the implemented screening concept. After constructing the potentials we have performed several tests contrasting SBOP calculations with ab-initio LDF based calculations. Specifically, comparison of energies of competing structures and calculations of deformation paths [7, 8]. In all cases the introduction of screening led to the improvement of the agreement between the two types of calculations. An exception is the A15 structure the energy of which calculated using SBOP deviates from that calculated ab-initio more than in the unscreened case. We believe that this is caused by dependence of unscreened two-center bond integral, $\beta_{\sigma\sigma}^u$ in (2), on the local atomic density or effective coordination about the bond. Details of these tests and values of the potential parameters will be published elsewhere.

The vacancy formation energy was calculated using both the unscreened BOP and SBOP. The results are 2.3eV and 2.6eV, respectively. The experimental and ab-initio calculated values range from 2.9 to 3.1eV. It is apparent that SBOP leads to a more accurate value than the unscreened BOP.

However, a major problem encountered in previous studies was a too soft T2 phonon mode close to the zone boundary in the [110] direction, the N-point phonon [8]. This problem is common to all TB methods and can be traced to the behavior of the second nearest neighbor force constants. When screening is included, the energy associated with the $dd\pi$ bond integral at second nearest neighbors is decreased, in accordance with results of ab-initio calculations, and the frequency of the T2 mode of the N-point phonon increases. This is seen in Fig. 2, which demonstrates that this increase is more than three-fold. It is further seen from Fig. 2 that changes of the remaining two modes, while not so dramatic, are in the correct directions, towards experimental values.

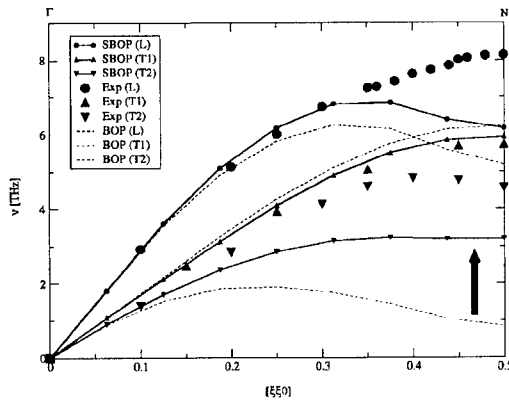


Figure 2. Improvements in the phonon spectra of molybdenum for [110] direction. Full lines with symbols show the new SBOP results, dashed lines correspond to unscreened BOP and filled symbols are experimental data. The arrow shows the major improvement in the T2 mode.

It has been generally accepted that the plastic behavior of bcc metals is governed by the special properties of $1/2\langle 111 \rangle$ screw dislocations, in particular by their non-planar core structure

[11, 12]. A number of atomistic studies employing central-force potentials have, indeed, revealed structures, spread into three $\{110\}$ planes of the $\langle 111 \rangle$ zone [11, 13]; similar results were obtained in calculations that included the directional covalent character of bonding in bcc transition elements [14].

As a prelude to dislocation simulations, we have investigated the γ -surface for the $\{110\}$ slip plane which provides some insight into the shape and extension of the dislocation cores [12]. The contour plot of the $\{110\}$ γ -surface for molybdenum calculated by SBOP is shown in Fig. 3a. Qualitatively, its shape is similar to that obtained for the unscreened BOP [8] but the maximum energy is about 40% higher and thus the surface is generally steeper. This suggests a narrower core since spreading of the dislocation into $\{110\}$ plane becomes energetically less favorable.

As shown in previous studies [13], cores of screw dislocations in bcc transition metals always spread into three $\{110\}$ planes but may possess either a three-fold or a six-fold symmetry. In the case of molybdenum studies employing central force potentials [13] as well as MGPT potentials including directional bonding [14] suggest the core with the three-fold symmetry. However, recent calculations employing ab-initio LDF based methods suggest cores with six-fold [15] or almost six-fold symmetry [16]. The differential displacement map [12] of the core structure calculated the present SBOP is shown in Fig 3b. This core displays three-fold symmetry but is much narrower and closer to the six-fold symmetry than the cores found in studies employing central force and MGPT potentials [14, 13]. This reflects, of course, the steepness of the γ -surface mentioned above. However, more importantly, this structure is close to that found in ab-initio calculations of Rao and Woodward [16] indicating again that the SBOP represents very correctly the bonding in molybdenum even in the highly distorted structures. Notwithstanding, the present calculations are only preliminary. They have been made using a relatively small block containing only 200 relaxed atoms and 500 atoms in the border region which interact with the relaxed atoms. Furthermore, investigation of the consequences of the core structure for plastic deformation requires detailed study of the effect of applied stresses on the core and eventual dislocation motion, similarly as it was done using central-force potentials [17, 18]. These studies are presently in progress.

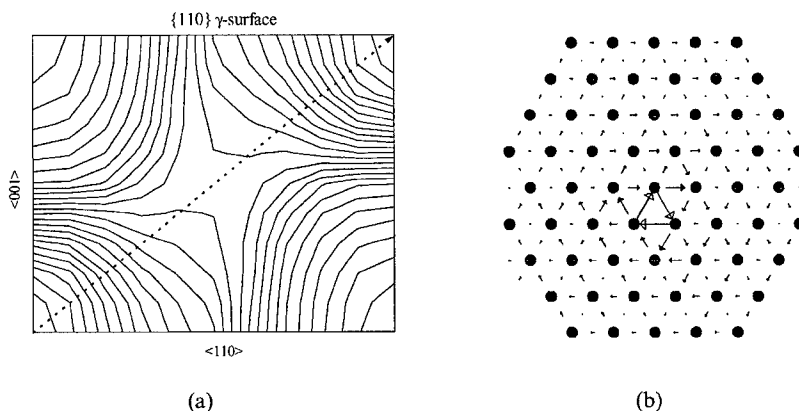


Figure 3. (a) Contour plot of $\{110\}$ γ -surface for molybdenum; the diagonal arrow is pointing in the $[111]$ direction. (b) Core structure of the $1/2\langle 111 \rangle$ screw dislocation in Mo; arrows show mutual displacement of atoms parallel to the dislocation line.

CONCLUSIONS

We have demonstrated that the recently developed concept of screening of bond integrals which results in their environmental dependence [6] substantially improves their transferability. Constructed SBOP for molybdenum then predict much less soft T2 phonon in the [110] direction than the unscreened model and give vacancy formation energies closer to the experimental values. Results of screw dislocation core calculations are close to those found in recent ab-initio studies and while they are not principally different than those obtained using simpler schemes, they suggest appreciably narrower and less asymmetric cores. However, the implication for the glide of screw dislocations requires study of the effect of applied loads that are presently in progress.

ACKNOWLEDGMENTS

This work was supported by the U.S. Department of Energy, BES Grant no. DE-PG02-98ER45702 and by the Advanced Strategic Computing Initiative of the U.S. Department of Energy through LLNL, Grant no. B501663.

REFERENCES

1. D. G. Pettifor, *Bonding and Structure of Molecules and Solids*, (Oxford University Press, Oxford, 1995).
2. M. Aoki and D. G. Pettifor, *Mat. Sci. Eng. A* **176**, 19 (1994).
3. A. P. Horsfield, A. M. Bratkovsky, M. Fearn, D. G. Pettifor and M. Aoki, *Phys. Rev. B* **53**, 12694 (1996).
4. M. S. Tang, C. Z. Wang, C. T. Chan and K. M. Ho, *Phys. Rev. B* **53**, 979 (1996).
5. H. Haas, C. Z. Wang, M. Fähnle, C. Elsässer and K. M. Ho, *Phys. Rev. B* **57**, 1461 (1998).
6. D. Nguyen-Manh, D. G. Pettifor and V. Vitek, *Phys. Rev. Lett.* **85**, 4136 (2000).
7. M. Mrovec, V. Vitek, D. Nguyen-Manh, D. G. Pettifor, L. G. Wang and M. Sob, *Multiscale Modelling of Materials*, edited by V. Bulatov, T. D. de la Rubia, R. Phillips, E. Kaxiras and N. Ghoniem (Pittsburgh, Materials Research Society), Vol. 538, p. 529 (1999).
8. M. Mrovec, V. Vitek, D. Nguyen-Manh, D. G. Pettifor, L. G. Wang and M. Sob, *Multiscale Phenomena in Materials: Experiments and Modeling*, edited by D. H. Lassila, I. M. Robertson, R. Phillips and B. Devincere (Pittsburgh, Materials Research Society), Vol. 578, p. 199 (2000).
9. S. Znam, PhD Thesis, University of Pennsylvania (2001).
10. C. Lanczos, *J. Res. Natl. Bur. Stand.* **45**, 225 (1950).
11. M. S. Duesbery, *Dislocations in Solids*, edited by F. R. N. Nabarro (Amsterdam, North Holland), Vol. 8, p. 67 (1989).
12. V. Vitek, *Prog. Mater. Sci.* **36**, 1 (1992).
13. M. S. Duesbery and V. Vitek, *Acta Mater.* **46**, 1481 (1998).
14. W. Xu and J. A. Moriarty, *Phys. Rev. B* **54**, 6941 (1996).
15. S. Ismail-Beigi and T. A. Arias, *Phys. Rev. Lett.* **84**, 1499 (2000).
16. S. Rao and C. Woodward, *Philos. Mag. A* to be published (2001).
17. K. Ito and V. Vitek, *Multiscale Modelling of Materials*, edited by V. Bulatov, T. D. de la Rubia, R. Phillips, E. Kaxiras and N. Ghoniem (Pittsburgh, Materials Research Society), Vol. 538, p. 87 (1999).
18. K. Ito and V. Vitek, *Philos. Mag. A*, to be published (2001).

Lattice Trapping of Cracks in Fe Using an Interatomic Potential Derived from Experimental Data and *Ab Initio* Calculations

D. Farkas,¹ M. J. Mehl,² and D. A. Papaconstantopoulos²

¹Department of Materials Science and Engineering, Virginia Polytechnic Institute and State University, Blacksburg, VA, USA 24061-0237

²Center for Computational Materials Science, Naval Research Laboratory, Washington, DC, USA 20375-5345

ABSTRACT

A recent approach which combines first-principles and experimental data to produce highly accurate and reliable interatomic potentials is tested for the case of bcc and fcc Fe. The Embedded-Atom-like potential accurately reproduces the basic equilibrium properties of bcc Fe, including elastic constants, phonon properties, and vacancy formation energies, as well as the correct relative stability of structures with coordination numbers ranging from 12 to 4. This potential was used in a simulation study of lattice trapping effects during the cleavage fracture of bcc Fe. A strong directional anisotropy for crack propagation was observed due to lattice trapping effects. The strongest trapping effects were observed for cleavage along the {110} planes and it was found that lattice trapping strongly favors cleavage along the {100} planes.

INTRODUCTION

Body-centered cubic metals are difficult to describe using the Embedded Atom Method (EAM)[1]. A possible work-around to this problem is the addition of angular-dependent terms[2]. However, a recent paper[3] describes a new approach to the development of EAM potentials, which includes fitting to a large database of experimental and first-principles data, including both the fcc and bcc phases. This was highly successful in describing defect structures in the FCC metals Al and Ni. In the present work we attempt to apply this technique to the case of a bcc metal, iron, that is known to be very difficult to describe within the EAM framework. It is our intention to treat the EAM as an entirely empirical formalism and explore the possible accuracy that can be obtained, even if the good fit is not a result of an accurate theoretical description of the bonding. We fit the potentials to experimental data and first-principles calculations, including the magnetic contribution, even though such a contribution is not included in the EAM formalism.

AB INITIO CALCULATIONS

Ab initio structural energies were computed using the first-principles, all-electron, general-potential Linearized Augmented Plane Wave (LAPW) method[4, 5], using spin-polarization[6, 7], the Perdew-Wang[8] Generalized Gradient Approximation (GGA), and the "special" k-point set of Monkhorst and Pack[9]. In order to understand the importance of the magnetic contribution in the various phases, calculations were performed with and without the magnetic contributions (spin-polarization) to the energy. The *ab initio* lattice parameters and cohesive energies were rescaled[3] so that the calculated equilibrium bcc phase coincides with the experimental values.

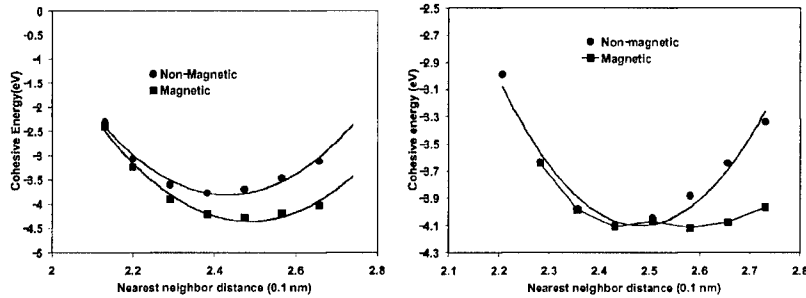


Figure 1: Results of *ab initio* calculations for the energies of bcc (left) and fcc (right) Fe. The results have been scaled to the experimental cohesive energy, as explained in the text.

Figure 1 shows the results obtained for the bcc and fcc phases, including the energies obtained for both the non-magnetic and magnetic calculations. We see that the bcc phase is stabilized by the magnetic interactions. Magnetism is even more significant in the lower coordination diamond and simple cubic structures. We therefore used the spin-polarized GGA energies in the database for EAM potential development, effectively including magnetic effects in the EAM. Two interesting features need to be pointed out in the *ab initio* results. One is the double minimum obtained for the fcc phase. This cannot be reproduced in the EAM formalism and we have used a best fit of the data to a parabolic curve. The other interesting point is that the hcp phase in our calculations is predicted to have a lower energy than the fcc phase. We did require the potential to reproduce this feature of the *ab initio* results.

PARAMETERIZATION AND FITTING PROCEDURE FOR THE INTERATOMIC POTENTIAL

In the present work we apply a similar strategy to that used in previous work by Mishin *et al.*[3] for the development of the potential. The experimental part of the database used includes the following physical properties of bcc Fe: the equilibrium lattice parameter, the cohesive energy, the elastic constants, and the vacancy formation energy. These experimental values coincide with those employed by Harrison, Voter and Chen [10] and Simonelli *et al.*[11] in the development of their EAM potentials for Fe.

Additionally, our database includes the experimental values of the vacancy migration energy E_v^m [12], which is underestimated by most EAM potentials[13], and the experimentally measured phonon dispersion relations [14]. Another experimental property included in the database was the bcc surface energy γ_s . As reliable estimates of the specific energies of low-index surfaces are not available, we only required that $\gamma_s(111) > \gamma_s(100) > \gamma_s(110)$, with all being slightly lower than the average measured value [15]. This is very important in the case of Fe, since its cleavage plane is experimentally $\{100\}$ and in the present work we wanted to explore the role of lattice trapping in this choice of cleavage plane. The equation of state, i.e., the crystal energy as a function of the lattice parameter, was taken into account in the form of the universal empirical EOS of Rose *et al.*[16].

Table I: Properties of Fe predicted by EAM potentials. Items marked “*” are fitted with high weight and those marked “†” are fitted with low weight.

	Experiment or <i>ab initio</i>	Present work
bcc a_0 (Å)*	2.87	2.87
bcc E_0 (eV/atom)*	-4.28	-4.28
bcc B (10^{11} Pa)*	1.73	1.73
bcc c_{11} (10^{11} Pa)*	2.52	2.56
bcc c_{12} (10^{11} Pa)*	1.38	1.36
bcc c_{44} (10^{11} Pa)*	1.22	1.13
bcc Phonon frequency $\nu_L(H)$ (THz)†	8.50	8.53
$E(\text{hcp})$ (eV/atom)*	-4.16	-4.15
$E(\text{sc})$ (eV/atom)*	-3.45	-3.33
$E(\text{diamond})$ (eV/atom)†	-2.84	-2.99
bcc vacancy formation E_v^f (eV)*	2.00	1.95
bcc vacancy migration E_v^m (eV)*	0.90	0.89
bcc E_1^f ([111]-dumbbell) (eV)		7.29
bcc E_1^f ([110]-dumbbell) (eV)		6.29
bcc E_1^f ([100]-dumbbell) (eV)		6.18
bcc {111} {110} γ_{us} (mJ/m ²):		1100
bcc $\gamma_s(110)$ (mJ/m ²)†	2452	1530
bcc $\gamma_s(100)$ (mJ/m ²)†	2452	1890
bcc $\gamma_s(111)$ (mJ/m ²)†	2452	2027

Since we are interested in studying structures far from equilibrium, the database also includes first-principles equations of state for the fcc phase of iron, as well as the hypothetical simple cubic and diamond structures, all using the spin-polarized GGA functional. Thus our database contains information about iron in environments with coordination numbers between 4 and 12.

The parameterization procedure used produces an exact fit for the lattice parameter, bulk modulus and cohesive energy. For all other properties we minimized the sum of relative squared deviations from the desired values assigning a chosen weight to each property, fitting according to the simplex algorithm of Nelder and Mead [17]. Larger weights were used for the elastic constants, vacancy formation energy and the energies of the hcp and fcc structures. The phonon frequency, the surface energies, and the energies of the lower coordinated structures were included with lower weights. The empirical EOS of Rose and co-workers [16] was also included, with a lower weight.

In Table I we compare the data included in the fitting database to the values predicted by the potentials. We see a generally good fit of the properties with the experimental and *ab initio* data.

Another important quantity listed in Table I is the unstable stacking fault energy γ_{us} , which was determined by rigidly shifting half of the bcc crystal above a {110} plane in a {111} direction of a typical Burgers vector, and then relaxing the atomic displacements normal to this plane. The unstable stacking fault energy, γ_{us} , determines the activation barrier for dislocation nucleation and is a critical quantity influencing the ductile/brittle behavior in the fracture of many kinds of materials [18]. The values of γ_{us} predicted by our potentials are notably higher than those predicted by other potentials [19], and are

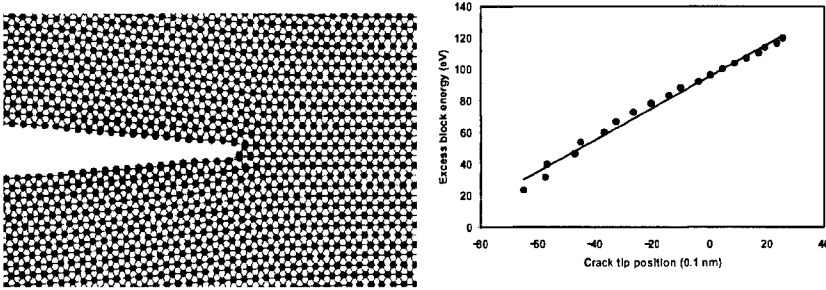


Figure 2: *Left:* Configuration of the crack tip region for a $\{110\}\langle 111 \rangle$ crack, showing an atomically sharp crack tip and no dislocation emission. *Right:* Excess block energy versus crack tip position for the $\{100\}\langle 011 \rangle$ configuration, showing negligible lattice trapping.

expected to be more realistic. Previous work[19] underestimated γ_{us} . Our value of 1.1 J/m^2 is more reliable because of the *ab initio* data included in the fit.

MOLECULAR STATICS SIMULATIONS OF FRACTURE BEHAVIOR

The crack is embedded in a simulation cell with rigid boundary conditions imposed along the directions perpendicular to the crack front and periodic boundary conditions parallel to the crack front. In the simulation, the crack may: emit a dislocation on an inclined slip plane, if one is available; cleave directly ahead; deflect and propagate on an inclined plane; or close.

The displacement field predicted by elasticity theory [20] is used to prescribe displacements for atoms located in the two different areas in the simulation cell (free and fixed). When applied to atoms located in the free region near the crack tip, the displacement field serves to generate an initial configuration, which is then relaxed using a conjugate gradient technique. Atoms located far away from the tip are kept fixed at positions obtained by displacing atoms according to the elastic displacement field. Fixing atoms at the boundary of the simulation cell imposes a stress intensity on the crack.

A finite crack growing under constant load would be subject to an increasingly higher stress intensity factor as it grows. In our simulations this is imposed through the boundary conditions, and we study the response of the crack tip to this increasing load. For the simulations at the atomistic scale, the displacements due to a stress intensity field can be approximated by that of an infinite crack, representing crack lengths of macroscopic sizes. Our simulations can be considered as snapshots of the quasi-equilibrium crack tip region as the macroscopic crack grows. The simulations we report at relatively low stress intensities correspond to the initial stages of crack propagation and the ones at higher stress intensities to later stages. The semi-infinite crack is incrementally loaded to higher stress intensities and the system is subsequently relaxed for each value of applied loading. The technique cannot address high temperature or dynamic effects or propagation at high values of applied strain rate where the crack tip is not permitted to attain a stable configuration.

We observed no dislocation emission from the crack tip at any of the tested orientations. This is in contrast to the results obtained with other EAM potentials[21], such as the one developed by Simonelli *et al.*[11] According to Rice[18], this can be related our predicted

unstable stacking fault energy, which is significantly higher than the one predicted by the Simonelli potential. Experimentally, Fe fails in a brittle fashion at low temperatures, with cleavage fracture typically occurring in the $\{100\}$ planes. The $\{100\}$ plane is not the most compact plane in the bcc structure and we used the present potential to study cleavage in the $\{100\}$ and $\{110\}$ planes.

To illustrate the brittle behavior, the left side of Figure 2 shows the crack tip configuration for a $\{110\}\langle 111 \rangle$ crack with no evidence of dislocation emission. This orientation is the one that is most likely to present slip planes available for emission as it does for the empirical EAM Simonelli potential[11]. We also studied the $\{110\}\langle 001 \rangle$, $\{110\}\langle 110 \rangle$, $\{110\}\langle 111 \rangle$, $\{100\}\langle 011 \rangle$, and $\{100\}\langle 001 \rangle$ configurations and found no dislocation emission. We studied the energy necessary for crack advance in each of these cases and obtained a detailed picture of the lattice trapping effects in each case. We found that there is a marked anisotropy in the lattice trapping effects, ranging from negligible to very significant.

The right side of Figure 2 shows the energy related to crack advance for the $\{100\}\langle 011 \rangle$ case. This case presents negligible lattice trapping and the slope of the plot can be related simply to the surface energy. This slope is 3.95 J/m^2 , while twice the value of the $\{100\}$ surface energy is 3.78 J/m^2 . In this simple case the crack starts propagating at the Griffith stress intensity. In contrast, the $\{100\}\langle 001 \rangle$ case presents significant lattice trapping. Lattice trapping in this orientation is very significant, with $K_+/K_G = 2$. We studied three different orientations of the $\{110\}$ plane crack front, all of which presented lattice trapping. Ranging from $K_+/K_G = 1.1$ for the $\{110\}\langle 111 \rangle$ orientation, to $K_+/K_G = 1.8$ for the $\{110\}\langle 110 \rangle$ orientation, to $K_+/K_G = 2.4$, for the $\{110\}\langle 001 \rangle$ case. The later is shown in Figure 3.

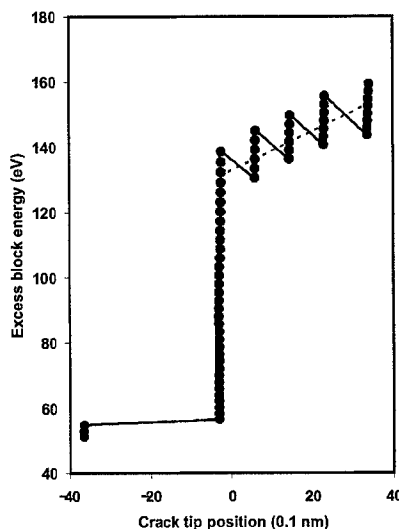


Figure 3: Excess block energy versus crack tip position for the $\{110\}\langle 001 \rangle$ configuration, showing lattice trapping.

DISCUSSION AND SUMMARY

In developing potentials for Al and Ni[3] it was shown that many EAM potentials are less accurate than they could be within the intrinsic limitations of the EAM model. These limits are more serious for the bcc metals, but we have used the improved procedure to develop a potential that is a significantly better description of Fe than previous EAM potential for this important bcc metal. The intrinsic limitations of the EAM still require caution in the use of this potential. The potential reproduces the basic features of the first principle calculations. Nevertheless, there are still weaknesses, in particular the areas of describing the configuration of self interstitials and details of crystallographic dependence of the surface properties.

The potential predicts brittle fracture of Fe in both the {110} and {100} type planes, and was used to study the effects of lattice trapping. Significant lattice trapping effects were found for some orientations, particularly for the crack front orientation, whereas other orientations showed negligible effects of lattice trapping. This creates a marked anisotropy in the fracture behavior for cracks in the same plane but with different crack fronts. The results show that the large lattice trapping effects favor cleavage in the {100} plane over the {110} plane. These effects could result in the observed cleavage plane being of the {100} type, even if the independently of which plane presents the lowest surface energy.

ACKNOWLEDGEMENTS

This work was supported by the Office of Naval Research, U.S. Department of Defense. We also thank Yuri Mishin for help with codes used in the present work.

REFERENCES

1. M. S. Daw and M. I. Baskes, *Phys. Rev. B* **29**, 6443 (1984).
2. R. Pasianot, D. Farkas and E. Savino, *Phys. Rev. B* **43**, 6952 (1991).
3. Y. Mishin, M. Mehl, D. Farkas and D. Papaconstantopoulos, *Phys. Rev. B* **59**, 3393 (1999).
4. O. K. Andersen, *Phys. Rev. B* **12**, 3060 (1975).
5. S. H. Wei and H. Krakauer, *Phys. Rev. Lett.* **55**, 1200 (1985).
6. W. Kohn and L. J. Sham, *Phys. Rev.* **140**, A1133 (1965).
7. U. von Barth and L. Hedin, *J. Phys. C* **5**, 1629 (1972).
8. J. P. Perdew and Y. Wang, *Phys. Rev. B* **45**, 13244 (1992).
9. H. J. Monkhorst and J. D. Pack, *Phys. Rev. B* **13**, 5188 (1976).
10. R. J. H. A. F. Voter and S. P. Chen, in: *Atomistic Simulation of Materials*, edited by V. Vitek and D. Srolovitz, 219, Plenum, New York and London (1989).
11. G. Simonelli, R. Pasianot and E. Savino, in: *Materials Research Society Symposium Proceedings*, volume 291, 567 (1993).
12. C. J. Smith, editor, *Metal Reference Book*, Butterworth, London, fifth edition (1976).
13. Y. Mishin and D. Farkas, *Phil. Mag. A* **75**, 169 (1997).
14. G. Simonelli, R. Pasianot and E. J. Savino, *Phys. Rev. B* **55**, 5570 (1997).
15. L. E. Murr, *Interfacial Phenomena in Metals and Alloys*, Addison-Wesley, Reading, MA (1975).
16. J. H. Rose, J. R. Smith, F. Guinea and J. Ferrante, *Phys. Rev. B* **29**, 2963 (1984).
17. W. H. Press, S. A. Teukolsky, W. T. Vetterling and B. P. Flannery, *Numerical Recipes in FORTRAN*, Cambridge University Press (1992), p. 402.
18. J. R. Rice, *J. Mech. Phys. Solids* **40**, 239 (1992).
19. D. Farkas, S. Zhou, C. Vailhé, B. Mutasa and J. Panova, *Journal of Materials Research* **12**, 93 (1997).
20. G. C. Sih and H. Liebowitz, in: *Fracture - An Advanced Treatise*, edited by H. Liebowitz, volume II, 69-189, Academic Press, New York (1968).
21. V. Shastry and D. Farkas, *Modeling and Simulation in Materials Science and Engineering* **4**, 473 (1996).

**Hybrid electronic-density-functional/molecular-dynamics simulation
on parallel computers: oxidation of Si surface**

Shuji Ogata,¹ Fuyuki Shimojo,² Aiichiro Nakano,³ Priya Vashishta,³ and Rajiv K. Kalia³

¹Department of Applied Sciences, Yamaguchi University, Ube 755-8611, Japan

²Faculty of Integrated Arts and Sciences, Hiroshima University, Higashi-Hiroshima 739-8521, Japan

³Concurrent Computing Laboratory for Materials Simulations, Louisiana State University, Baton Rouge, LA 70803-4001, U.S.A

ABSTRACT

A hybrid quantum mechanical/molecular dynamics simulation scheme is developed by embedding a quantum mechanical system described by the real-space density-functional theory in a classical system of atoms interacting via an empirical interatomic potential. A novel scaled position method for handshake atoms coupling the quantum and the classical systems is introduced. Hybrid simulation run for oxidation of Si (100) surface is performed to demonstrate seamless coupling of the quantum and the classical systems.

INTRODUCTION

Simulation of chemical reactions in materials such as oxidation and fracture requires that inter-atomic interaction in the reactive region needs to be calculated by a quantum mechanical (QM) method that can describe breaking and formation of bonds. Heat produced by the reaction should be correctly transferred to surrounding regions. Large-scale atomistic simulations described with a reliable QM method are therefore required. There have been growing interests in developing hybrid QM/MD simulation schemes, in which a reactive region treated by a QM method is embedded in a classical system of atoms interacting via an empirical interatomic potential.

Various hybrid schemes combining a quantum-mechanical molecular orbital method and a classical molecular mechanics method have been proposed to simulate chemical processes in solution [1-4]. Recently Broughton *et al.* [5] developed a hybrid simulation scheme for materials simulations. In Ref. [5], a cracked silicon system is partitioned into three regions corresponding to the semiempirical tight-binding (TB) method, the MD method, and the finite element (FE) method. Handshake Hamiltonians are introduced to link the TB/MD and the MD/FE boundaries [5]. Hybrid TB/MD/FE simulation of the system demonstrated seamless couplings of the methods.

Accurate QM calculations are possible based on the density-functional theory (DFT) [6,7]. An efficient parallel implementation of the DFT calculations has been proposed, in which wave functions and pseudopotentials [8] are represented on uniform real-space mesh points in Cartesian coordinates [9]. The real-space DFT calculations can be accelerated further [10] by the multigrid method [11]. The real-space multigrid-based DFT is effective for QM atomic-clusters in QM/MD schemes, since it is free from the periodic boundary conditions.

In this paper we describe a novel hybrid QM/MD scheme [12] for dynamic simulations of materials on parallel computers using a real-space multigrid-based DFT for QM calculations of

atomic clusters. The hybrid simulation scheme is implemented on massively parallel computers by first dividing compute nodes into the QM and the MD calculations, and then using spatial decomposition in each task. To partition the total system into the cluster and its environmental regions, we use the modular approach by Svensson *et al.* [2] and Eichler *et al.* [3] that is based on a linear combination of QM and MD potential energies and consequently requires minimal modification of existing QM and MD codes. Termination atoms are introduced in both calculations for the cluster. Handshake atoms linking the cluster and the environment regions are treated by a novel scaled-position method, in which different scaling parameters are used in those calculations to relate the handshake atoms to the termination atoms.

HYBRID QM/MD SIMULATION SCHEME

Present hybrid scheme allows us to simulate chemical reactions of the material with external atoms or molecules or in itself. An insulator material such as ceramics or semiconductors whose microscopic structures at equilibrium are known is assumed. Atoms in the total system are classified into three types: (i) cluster atoms forming an atomic cluster to which QM calculations apply; (ii) environment atoms described by an empirical interatomic potential; and (iii) handshake atoms at the cluster/environment boundary. Chemical reactions are assumed to occur only within the cluster. Figure 1 shows an example of the atomic classification in the oxidation simulation of Si (100) surface (see below). In Fig. 1, the cluster atoms (Si or O) are drawn as black spheres, while the environment atoms (Si) as white spheres. The handshake atoms (Si), shown as gray spheres in Fig. 1, link between the cluster and the environment atoms. Small black spheres in Fig. 1 represent virtual H atoms to terminate dangling bonds, which will be explained below.

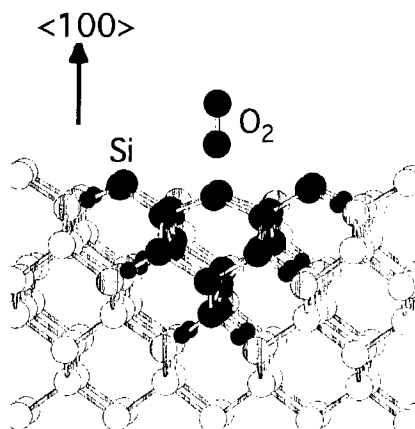


Figure 1. Initial configuration in the present hybrid simulation. Black spheres represent the cluster atoms (Si or O); gray, the environment Si atoms; small black, termination H atoms; gray, handshake Si atoms.

Assuming that the system comprises N atoms with masses $\{m_i\}$ at positions $\{\vec{r}_i\}$, the Hamiltonian of the total system is written as

$$H = \sum_{i=1}^N \frac{m_i}{2} \vec{v}_i^2 + E_{\text{pot}}(\vec{r}_i \in \text{system}) . \quad (1)$$

Following the modular approaches [2,3], we approximate that the potential energy, E_{pot} , in Eq. (1) as a sum of a classical (CL) potential-energy $E_{\text{CL}}^{\text{system}}$ of the total system and a difference between QM and CL potential-energies for the QM cluster:

$$E_{\text{pot}}(\vec{r}_i \in \text{system}) = E_{\text{CL}}^{\text{system}}(\vec{r}_i \in \text{system}) + E_{\text{QM}}^{\text{cluster}}(\vec{r}_i \in \text{cluster} + \text{handshake}) - E_{\text{CL}}^{\text{cluster}}(\vec{r}_i \in \text{cluster} + \text{handshake}) . \quad (2)$$

Stabilizing atomic configuration of the cluster cut from a bulk system necessitates termination of its dangling bonds by H atoms [1-5]. We relate the termination H atoms to the handshake atoms in the calculation of $E_{\text{QM}}^{\text{cluster}}$ in Eq. (2) as follows. Let us denote $\vec{r}_{j(i)} \in \text{cluster}$ as a bonding counterpart of $\vec{r}_i \in \text{handshake}$; $n_c(i)$, as the number of different j for each i . To terminate a dangling bond, a termination H is placed at $\vec{x}_{i,j}^{\text{H}} = \beta \vec{r}_i + (1 - \beta) \vec{r}_{j(i)}$ for each (i, j) with a control parameter β [4]. Total number of termination H atoms for the cluster hence equals the number of dangling bonds, i.e., $\sum_i n_c(i)$. We then regard $E_{\text{QM}}^{\text{cluster}}$ as the potential energy of the cluster with termination H atoms: $E_{\text{QM}}^{\text{cluster}} = E_{\text{QM}}^{\text{cluster}}(\vec{r}_i \in \text{cluster}; \vec{x}_{i,j}^{\text{H}})$.

For the calculations of $E_{\text{CL}}^{\text{cluster}}$ in Eq. (2), we similarly introduce classical atoms (= termination atoms) on the cluster surface to minimize surface effects on atomic forces in the cluster. In the present formulation, a handshake atom in the original system corresponds to a single termination atom. Position $\vec{x}_{i,j}^{\text{cl}}$ of the termination atom i is obtained by shifting its original position (\vec{r}_i) slightly with a parameter α depending on the empirical interatomic potential: $\vec{x}_{i,j}^{\text{cl}} = \alpha \vec{r}_i + (1 - \alpha) \langle \vec{r}_{j(i)} \rangle_j$, where $\langle \cdots \rangle_j$ denotes taking average over different j . The $E_{\text{CL}}^{\text{cluster}}$ is obtained as a classical potential energy of the terminated cluster: $E_{\text{CL}}^{\text{cluster}} = E_{\text{CL}}^{\text{cluster}}(\vec{r}_i \in \text{cluster}; \vec{x}_{i,j}^{\text{cl}})$. Values of the parameters, β and α , are determined to minimize mean square forces on the cluster atoms in the QM and the CL calculations, respectively.

For the QM calculations, we use the real-space multigrid-based DFT, in which electronic wave-functions are represented on a uniform real-space mesh in Cartesian coordinates [9,10]. We use norm-conserving pseudopotentials [8] with the generalized gradient approximation [13]. The second derivative of the wave function in each direction, which is related to the kinetic energy operator, is calculated by the sixth-order finite difference method [9]. The multigrid (MG) method [10,14] is adopted to calculate the Hartree potential corresponding to a given density of electrons and to obtain the Kohn-Sham wave functions [6,14,15] with the Hartree potential. In each self-consistency field (SCF) iteration cycle, electronic eigenstates are determined band-by-band using the conjugate gradient (CG) method [14,15].

PARALLEL IMPLEMENTATION

In the present parallel implementation, compute nodes are grouped into MD and QM [12,16]. Figure 2 shows a flowchart of parallel computations. First spatial decomposition is used to decompose the total system into subdomains, each of which is mapped onto an MD compute node. The classical potential energy, E_{CL}^{system} , and corresponding atomic forces are calculated in the MD nodes using the empirical interatomic potential. Second, atomic data for the cluster and the handshake atoms that are necessary to create the H-terminated cluster are transferred to the QM nodes. Third, the QM nodes perform DFT calculations to obtain $E_{QM}^{cluster}$ and atomic forces for the H-terminated cluster, while the MD nodes calculate $E_{CL}^{cluster}$ and atomic forces for the classical terminated-cluster using the empirical interatomic potential. The real-space multigrid-based DFT code is parallelized by decomposing the mesh points to subdomains and then distributing them into the QM compute nodes [14]. The energy and forces from both QM and MD calculations are collected in the MD nodes. Finally, the total potential energy, $E_{pot} = E_{CL}^{system} + E_{QM}^{cluster} - E_{CL}^{cluster}$, and atomic forces are calculated in the MD nodes, which in turn are used for time integration of the equations of motion using the velocity-Verlet algorithm [18].

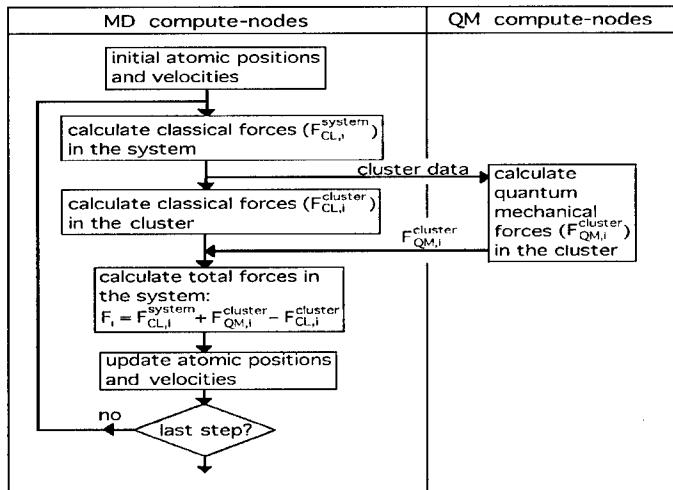


Figure 2. A flowchart of parallel computations in the present hybrid simulation code.

APPLICATION TO OXIDATION OF Si (100) SURFACE

The hybrid QM/MD simulation code is applied to oxidation of Si (100) surface, to demonstrate seamless coupling of the cluster and the environment atoms. The reaction energy is transferred to surrounding atoms, and affects subsequent dynamic processes significantly. It is

therefore important in dynamic simulations of oxidation of Si surface to include a large number of environmental Si atoms in addition to reacting atoms.

We use the Stillinger-Weber (SW) potential [19] for classical description of Si atoms. The SW potential consists of two-body and three-body terms between nearest-neighbor atoms. The SW potential reproduces dimer reconstruction observed experimentally on (100) surface of Si [20]. For the hybrid simulation, a slab with dimensions (65.2Å, 65.2Å, 34.5Å) in ($\langle 001 \rangle$, $\langle 010 \rangle$, $\langle 100 \rangle$) directions is cut from bulk Si. Periodic boundary conditions are applied in $\langle 001 \rangle$ and $\langle 010 \rangle$ directions.

Value of β for termination H is chosen to 0.625 through comparison between Si-H and Si-Si distances in the DFT calculations. We set $\alpha = 1.0$ for termination Si in the classical calculations since a SW Si atom interacts only with its nearest-neighbors. We select 20 Si atoms in the slab as the cluster atoms (see Fig. 1). No handshake or classical atoms are found within interaction ranges of O in the present settings. The inter-atomic potential formulas for O-O and Si-O pairs may be arbitrary in the classical calculations since the MD potential energy terms for O-O and Si-O pairs in $E_{\text{CL}}^{\text{cluster}}$ cancel with the corresponding terms in $E_{\text{CL}}^{\text{system}}$ in Eq. (1).

Initial configuration for the hybrid simulation of oxidation is obtained by placing an O₂ molecule above a well-relaxed, reconstructed Si (100) surface of the slab. An O₂ molecule oriented along $\langle 100 \rangle$ direction with zero velocity is placed 2.0 Å above the center of the dimer (see Fig. 1). Total number of atoms treated in the DFT calculations is 37 that includes 20 Si atoms, 2 O atoms, and 15 H atoms for termination.

We perform a hybrid QM/MD simulation using 9 nodes on SGI Origin 2000; 8 nodes are assigned to the QM calculations of the cluster. The unit MD time step is 1.0 fs. Figure 3 shows time evolution of spherically-averaged local temperatures at 50 fs and 250 fs. Here origin of the system (*i.e.*, $r = 0$) is set at the center of the dimer at the initial (*i.e.*, the position below the lower O by 2Å). Radial depth of each bin is $\Delta r = 3\text{Å}$. Vertical lines in Fig. 3 represent the cluster atoms connecting to the handshake atoms. No apparent discontinuity is observed at the cluster/environment boundaries at all times.

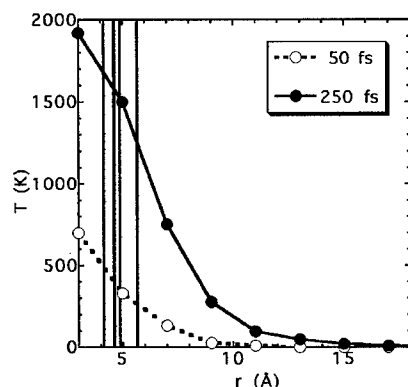


Figure 3. Spherically-averaged temperatures at 50 fs and 250 fs in the present simulation. The r denotes the distance from the center of the Si-Si dimer at the initial, which is the closest to the O₂. Vertical lines represent the cluster atoms at the cluster/environment boundary.

SUMMARY

We have developed a hybrid QM/MD simulation scheme (Eqs. 1 and 2) by embedding a quantum-mechanical cluster calculated by the real-space multigrid-based DFT in a classical system of atoms interacting via an empirical potential. We have performed a hybrid QM/MD simulation of oxidation of Si (100) surface, which demonstrates seamless coupling of the quantum and the classical systems (Fig. 3).

ACKNOWLEDGEMENT

This work was supported by U.S. DOE, AFOSR, ARO, USC-LSU Multidisciplinary University Research Initiative, NSF, and NASA.

REFERENCES

1. A. Warshel and M. Levitt, *J. Mol. Biol.* **103**, 227 (1976).
2. M. Svensson, S. Hymbel, R.D.F. Froese, T. Matsubara, S. Sieber, and K. Morokuma, *J. Comp. Chem.* **100**, 19357 (1996).
3. U. Eichler, C. M. Kölmel, and J. Sauer, *J. Comp. Chem.* **18**, 463 (1996).
4. S. Dapprich, I. Komáromi, K. S. Byun, K. Morokuma, and M.J. Frisch, *J. Mol. Struc. (Theochem)* **461-462**, 1 (1999).
5. J.Q. Broughton, F.F. Abraham, N. Bernstein, and E. Kaxiras, *Phys. Rev. B* **60**, 2391 (1999).
6. P. Hohenberg and W. Kohn, *Phys. Rev.* **136**, B864 (1964); W. Kohn and L. J. Sham, *Phys. Rev.* **140**, A1133 (1965).
7. See, e.g., M.C. Payne, M.P. Teter, D.C. Allan, T.A. Arias, and J.D. Joannopoulos, *Rev. Mod. Phys.* **64**, 1045 (1992).
8. N. Troullier and J.L. Martins, *Phys. Rev. B* **43**, 1993 (1991).
9. J.R. Chelikowsky, N. Troullier, and Y. Saad, *Phys. Rev. Lett.* **72**, 1240 (1994).
10. E.L. Briggs, D.J. Sullivan, and J. Bernholc, *Phys. Rev. B* **54**, 14362 (1996).
11. A. Brandt, *Math. Comp.* **31**, 333 (1977).
12. S. Ogata, F. Shimojo, A. Nakano, P. Vashishta, and R.K. Kalia, *Comp. Phys. Comm.*, in press
13. J.P. Perdew, K. Burke, and M. Ernzerhof, *Phys. Rev. Lett.* **77**, 3865 (1996).
14. F. Shimojo, T.J. Campbell, R.K. Kalia, A. Nakano, S. Ogata, P. Vashishta, and K. Tsuruta, *Future Generation Comp. Sys.*, accepted for publication.
15. G. Kresse and J. Furthmüller, *Phys. Rev. B* **54**, 11168 (1996).
16. W. Gropp, E. Lusk, and A. Skjellum, *Using MPI* (MIT Press, Cambridge, 1994).
17. A. Nakano, R. K. Kalia, and P. Vashishta, *Comp. Phys. Comm.* **83**, 197 (1994); A. Nakano, *Concurrency: Practice and Experience* **11**, 343 (1999).
18. M.P. Allen and D. Tildesley, *Computer Simulation of Liquids* (Clarendon, Oxford, 1987).
19. F.H. Stillinger and T.A. Weber, *Phys. Rev. B* **31**, 5262 (1985).
20. K.E. Khor and S. Das Sarma, *Phys. Rev. B* **36**, 7733 (1987).

Parallel Tight-Binding Simulations of Nanophase Ceramics: Atomic and Electronic Transport at Grain Boundaries

Kenji Tsuruta, Hiroo Totsuji, and Chieko Totsuji

Department of Electrical and Electronic Engineering, Okayama University,

3-1-1 Tsushima-naka, Okayama 700-8530, JAPAN

Email: tsuruta@elec.okayama-u.ac.jp, URL: <http://www.mat.elec.okayama-u.ac.jp>

ABSTRACT

We report on tight-binding molecular dynamics (TBMD) of neck formation processes and atomic and electronic diffusivity at grain boundaries of nanocrystalline silicon carbide. The TBMD simulations are based on an $O(N)$ algorithm (the Fermi-operator expansion method) for calculating electronic contributions to energy and forces. The code has been fully parallelized on our PC-based parallel machines. The TBMD simulations of collision of SiC nanospheres show that the processes of neck formation depend strongly on contact angles between the two grains. Atomic diffusions are quite different in the necks formed with different angles. Also, the electronic transport property at grain boundary is investigated via a TB representation of an electronic diffusivity. A preliminary result on the diffusivity at a $\Sigma=9$ grain boundary of SiC indicates significant enhancement of electron mobility along the grain boundary.

INTRODUCTION

Nanophase ceramics [1] have gained rapidly a great deal of attention due to their unique properties such as larger fracture toughness and higher sinterability than conventional ceramics. Also some of them have shown superplastic behavior at elevated temperatures [2]. High chemical reactivity and enhanced catalytic behavior, presumably due to large surface-to-volume ratio in the system, have also been observed in some nanophase ceramics such as n-TiO₂ [1]. Silicon carbide (SiC) is a well-known high-temperature ceramic, and SiC-based nanophase materials (n-SiC) are very promising for both structural and electronic applications under extreme conditions, including radar/microwave applications and gas/irradiation sensors [3]. Understanding the atomic organizations and the electronic properties of grain boundaries in n-SiC is very important for designing and optimizing material performances in these industrial applications. A theoretical investigation of these material properties requires methods for multi-level descriptions of the physical hierarchy in nanophase systems—from local electronic/atomic structures to mesoscopic grain dynamics. Recent efforts in developing efficient order- N methods for semi-empirical tight-binding molecular dynamics [4] have made a realistic quantum/atomistic simulation of nanophase materials possible.

In this paper, we report on tight-binding molecular-dynamics (TBMD) simulations of neck formation of SiC nanospheres (diameter ~ 27 Å), and atomic and electronic diffusivity at grain-boundary regions. The Fermi-operator expansion method (FOEM) [4, 5] has been employed to calculate efficiently the electronic part of the energy and forces in the TBMD simulations, and it has been run on our sixteen-node parallel PC cluster. Using the parallel

TBMD, we investigate the processes of neck formation (a) between aligned nanospheres, and (b) between misaligned nanospheres, and atomic diffusions at intergranular necks formed in these simulations. Electron mobility at a coincidence grain boundary has been evaluated by a moment-based calculation of electronic diffusivity.

TIGHT-BINDING MOLECULAR DYNAMICS FOR SILICON CARBIDE

For a system consisting of N atoms, the tight-binding total energy model is defined as

$$E_{\text{tot}} = E_{\text{kin}} + E_{\text{bs}} + E_{\text{rep}}, \quad (1)$$

where E_{kin} stands for the kinetic energy of ions, E_{bs} is the band-structure energy of valence electrons, and E_{rep} represents the repulsive term that takes into account the core-core interactions between ions and neglected contributions in E_{bs} to the true electronic energy, such as a correction for double counting of electron-electron interactions. In semi-empirical TB methods, the repulsive energy is modeled by the sum of short-range 2-body interaction. The band-structure energy is calculated by diagonalizing the effective one-electron Hamiltonian matrix. Each off-diagonal element of the TB Hamiltonian involves interactions between valence electrons within the two-center hopping approximation. The electronic contribution to interatomic forces, *i.e.*, derivatives of E_{bs} with respect to the atomic coordinates, can be obtained through the Hellmann-Feynman (HF) theorem.

In semi-empirical TB methods, the parameterization of matrix elements in the TB Hamiltonian is an essential ingredient for TBMD simulations. Among a number of TB models for SiC systems [6], we have chosen Mercer's parameterization of the TB Hamiltonian [7], which is based on an sp^3 orthogonal basis. It also includes environment-dependent contributions to the onsite energies through intra-atomic terms. These terms give important contributions to variation of the electron transfer between Si and C atoms, especially for inhomogeneous systems, although it does not include explicitly the Coulomb interaction between ions. The original parameterization by Mercer, however, involves some discrepancies with experimental data such as the lattice constant and the interfacial energies. Minor modifications of the parameters have therefore been made so that magnitudes of these discrepancies are reduced [8].

Diagonalization of the TB Hamiltonian matrix, involved in conventional TB methods, takes the computational cost proportional to N^3 , where N is the number of atoms in a simulation cell. This quickly becomes overwhelming when the system size of simulation exceeds a few hundred atoms, which is too small for realistic simulations of nanophase materials. Several new methods have been proposed recently to resolve this problem [4]. Among them we have adopted the Fermi-operator expansion method, proposed originally by Goedecker and Colombo [5]. This algorithm is based on a moment expansion of a pseudo-density matrix (the Fermi operator) of the TB Hamiltonian by Chebyshev polynomials. Combining an appropriate truncation at a finite order of the expansion and a truncation in the multiplication between each element of the matrix at a physical cut-off distance, the computational complexity in evaluating the band-structure energy and the HF forces is reduced to that proportional to N .

Since the truncation at the physical distance between atomic sites can make the data structures localized, a scalable parallelization can easily be achieved in the present algorithm. We employed a spatial domain-decomposition technique for calculating matrix-matrix multiplication. In this algorithm, data transmission between neighboring nodes is performed only for near-boundary atoms and matrix elements because of the spatially localized nature of the density matrix.

Although it has been reported [9] that the method does not surpass other $O(N)$ TB methods such as the bond-order potential method and the density-matrix method in the efficiency and accuracy, the present method has advantages in its simplicity of the algorithm and, hence, in the suitability for massive parallelism. Scalability of the present algorithm has been tested on massively paralleled architectures: It has been reported [10] that using thousand-node Cray T3E machine one can simulate very large systems (up to million atoms) by the present TBMD algorithm.

In the present study, we have performed the parallel TBMD simulations on our sixteen-node parallel PC cluster: It consists of Dual-Pentium III based personal computers. Data transmissions between nodes were done through a network connected by a gigabit-switching hub (Myrinet). The communication overhead in the TBMD simulations was approximately 20% of the total CPU time.

COLLISION BETWEEN SILICON-CARBIDE NANOSPHERES

Dynamics of neck formation at high temperatures is an important issue because it may determine not only mechanical stability of the grain boundaries but also carrier transport properties. We have investigated effects of grain orientation on the neck formation processes between SiC nanospheres at 1500 K via the parallel TBMD simulations.

We used a velocity-Verlet algorithm [11], with the time step of 1 femto-second, for molecular dynamics (MD) simulations. In calculations of the band-structure energy and the HF forces on each atom, the Chebyshev order in the moment calculation and the pseudo-electronic temperature were set to be 50 and 0.1 eV, respectively. These values give a reasonable accuracy (of the order of 10^{-3} eV/atom for the energy conservation) and numerical stability in the course of our simulation.

Figure 1(a) shows xy projection of the initial configuration of nanocrystallites 'aligned' along a $\langle 100 \rangle$ direction: The nanocrystallites are prepared by removing a spherical system with a radius 13.6 Å from a β -crystalline bulk SiC. The number of atoms involved in the cluster is 1008 (504 Si atoms and 504 C atoms). Initially the system was relaxed by the steepest-descent method. Then the system was heated to 1500 K using the Nose-Hoover's thermostat chain [11], and was subsequently thermalized for 3000 time steps.

Two configurations of the cluster at different time steps in the thermalization process were copied into an MD cell with a separation 32 Å between their centers of mass, and they were aligned along their $\langle 100 \rangle$ crystal axis, as in Fig. 1(a). Subsequently, thermal velocities of 1500 K were added to each cluster with directions opposite to each other, so as to have the clusters being colliding. Within 2 ps (pico-seconds), the clusters began to make some bonds between Si atoms on one cluster and C on the other. After collision (at 6 ps), as in Fig. 1(b), we

find that their orientations were changed slightly after collision and the intergranular neck has some distorted bonds. There is however no unsaturated bond formed in the neck region.

In addition to the collision between aligned clusters, we have performed TBMD simulation of nanocrystallites with a tilt angle. Figure 2(a) shows the initial configuration of the ‘misaligned’ clusters. The tilt angle corresponds to a coincidence grain boundary ($\{122\}\Sigma=9$) found typically in experiments [12]. After the same thermal process as in the previous case, the clusters were made to collide with each other. Figure 2(b) depicts the configuration after collision. In contrast with the previous case, we find that they changed relative orientation significantly by both tilting and twisting their orientations. The structure in the intergranular neck formed in this collision is rather disordered.

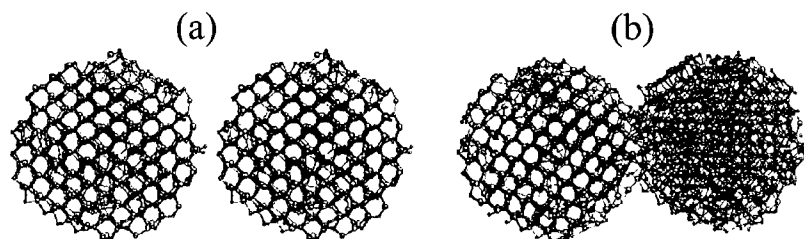


Figure 1. Neck formation between aligned SiC nanospheres: (a) initial configuration, (b) configuration after collision (6 ps) at $T = 1500$ K. Large and small spheres represent Si atom and C atom, respectively.

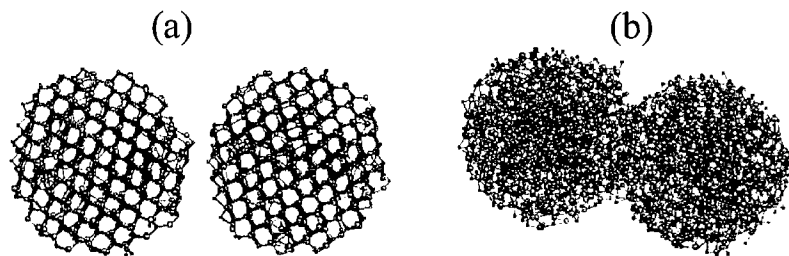


Figure 2. Same as in Fig. 1, but for neck formation between misaligned SiC nanospheres: (a) initial configuration, (b) configuration after collision (8 ps) at $T = 1500$ K.

ATOMIC DIFFUSION AT INTERGRANULAR NECK

After the collisions were completed between aligned and misaligned nanocrystallites, we estimated atomic self-diffusion constants through the local mean-square-displacement analysis. At the temperature of 1500 K, however, no significant diffusion at intergranular neck regions were found in both cases. We therefore raised the temperature to 2000 K, and monitored the atomic diffusion. We then found a significant increase of self-diffusion constant ($\sim 10^{-5}$ cm²/s) at the grain boundary formed between misaligned clusters, whereas no significant change was

observed in the case of aligned clusters. The temperature dependence observed in the present study agrees with a recent work [13], which has found that the onset of sintering in nanophase SiC occurs at temperatures above 1600 K.

ELECTRONIC DIFFUSIVITY

We have investigated the electronic transport properties in a coincidence grain boundary through an analysis of an electronic diffusivity defined by

$$D_{i\alpha} \equiv \lim_{t \rightarrow \infty} \frac{1}{t} \langle \Psi_{i\alpha}(t) | \hat{X}^2 | \Psi_{i\alpha}(t) \rangle, \quad (2)$$

where \hat{X} denotes a position operator of an electron, and

$$|\Psi_{i\alpha}(t)\rangle \equiv e^{-i\hat{H}t/\hbar} |i\alpha\rangle \quad (3)$$

is a time-dependent state vector of the electron located initially ($t = 0$) at an α orbital on i th atom. Evaluation of Eq. (2) was done by a method derived by Roche and Mayou [14], originally for an efficient calculation of dc conductivity in quasiperiodic systems. The method is based on a moment expansion of the vector in Eq. (3) with orthogonal polynomials of the TB Hamiltonian, and it involves very similar procedure to the Chebyshev expansion of the density matrix in our TBMD simulation.

Figure 3 shows a preliminary result on the electronic diffusivity near a $\{122\}\Sigma=9$ non-polar grain boundary; (a) an atomic configuration of the grain boundary, (b) distribution of relative diffusivity of electrons, calculated by the formula described above. We find a significant increase of the diffusivity in the grain boundary, as compared with that in the bulk.

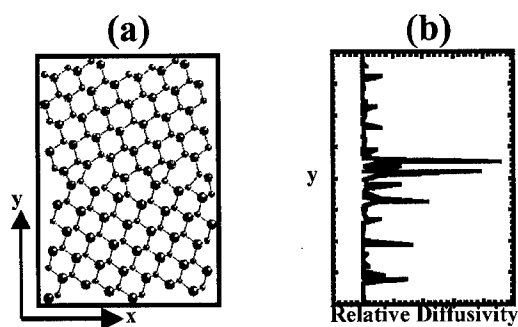


Figure 3. (a) Atomic configuration of a $\{122\}\Sigma=9$ coincidence grain boundary, and (b) distribution (along the y direction) of relative electronic diffusivity.

CONCLUSIONS

We have performed large-scale TBMD simulations for the neck formations between nanosphere of diameter $\sim 27\text{\AA}$. The $O(N)$ algorithm has been implemented for efficient computation of the band-structure energy and the electronic force. The code has been fully parallelized on PC-based parallel machines. We have found that the neck formation at 1500 K

occurs without large change of crystallographic orientation between aligned nanospheres, whereas initially tilted nanospheres form a disordered structure in the intergranular neck. The atomic diffusion at the disordered grain boundary increases significantly at 2000 K. A preliminary analysis on an electronic diffusivity shows significant enhancement of the diffusivity at a $\Sigma=9$ coincidence grain boundary. An application of the diffusivity analysis to the nanophase SiC systems is in progress.

ACKNOWLEDGMENTS

This work was supported by the Grants-in-Aid for Scientific Research (B) 11480110 and for Encouragement of Young Scientists 12750604 from the Ministry of Education, Science, Sports, and Culture of Japan.

REFERENCES

1. *Nanophase and Nanocomposite Materials III*, edited by S. Komarneni, J. C. Parker, and H. Hahn, Mater. Res. Soc. Symp. Proc. vol. 581 (MRS, Warrendale, PA, 2000).
2. *Superplasticity: Current and Future Potential*, edited by P. B. Berbon *et al.*, Mater. Res. Soc. Symp. Proc. vol. 601 (MRS, Warrendale, PA, 2000).
3. E.g., IEEE Trans. Electron Devices (Special Issue) Vol. 46 (1999); *Silicon Carbide Ceramics - I: Fundamental and Solid Reaction*, edited by S. Somiya and Y. Inomata (Elsevier Applied Science, London and New York, 1991).
4. *Tight-Binding Approach to Computational Materials Science*, edited by P. Turchi, A. Gonis, L. Colombo, Mater. Res. Soc. Symp. Proc. vol. 491 (MRS, Warrendale, PA, 1998).
5. S. Goedecker and L. Colombo, Phys. Rev. Lett. **73**, 122 (1994).
6. M. Kohyama, S. Kose, M. Kinoshita, and R. Yamamoto, J. Phys. Condens. Matter **2**, 7791 (1990); *ibid.* **2**, 7809 (1990); J. Robertson, Phil. Mag. B **66**, 615 (1992); D. Sanchez-Portal, E. Artacho, J. M. Soler, Solid State Comm. **95**, 685 (1995).
7. J. L. Mercer, Phys. Rev. B **54**, 4650 (1996).
8. K. Tsuruta, H. Totsuji, C. Totsuji, Phil. Mag. Lett. (to be published).
9. D. R. Bowler, M. Aoki, C. M. Goringe, A. P. Horsfield, D. G. Pettifor, Modelling Simul. Mater. Sci. Eng. **5**, 199 (1997).
10. F. Shimojo, T. J. Campbell, R. K. Kalia, A. Nakano, P. Vashishta, S. Ogata, and K. Tsuruta, Future Generation Computer Systems **17**, 279 (2000).
11. G. J. Martyna, M. E. Tuckerman, D. J. Tobias, and M. L. Klein, Mol. Phys. **87**, 1117 (1996).
12. M. Kohyama and K. Tanaka, Mater. Sci. Forum Vols. 294-296, 231 (1999).
13. A. Chatterjee, R. K. Kalia, A. Nakano, A. Omeltchenko, K. Tsuruta, P. Vashishta, C.-K. Loong, M. Winterer, and S. Klein, Appl. Phys. Lett. **77**, 1132 (2000).
14. S. Roche and D. Mayou, Phys. Rev. Lett. **79**, 2518 (1997).

Coupling of Length Scales: Hybrid Molecular Dynamics and Finite Element Approach for Multiscale Nanodevice Simulations

Eleftherios Lidorikis¹, Martina E. Bachlechner¹, Rajiv K. Kalia¹, George Z. Voyiadjis², Akihiro Nakano¹, and Priya Vashishta¹

¹Concurrent Computing Laboratory for Materials Simulations and Biological Computation & Visualization Center, Department of Physics & Astronomy and Department of Computer Science Louisiana State University, Baton Rouge, LA 70803, USA

²Advanced Computational Solid Mechanics Laboratory, Department of Civil and Environmental Engineering, Louisiana State University, Baton Rouge, LA 70803, USA

ABSTRACT

A hybrid molecular-dynamics/finite-element simulation scheme is applied to describe multiscale phenomena in nanodevices. The quality of both static and dynamic coupling between atomistic and continuum regions is studied. The hybrid scheme is used for the Si/Si₃N₄ interface problem (static coupling), and for the projectile impact on Si problem (dynamic coupling). Excellent agreement is found between hybrid and full molecular dynamics simulation results in the static case, and no wave reflections are found at the atomistic/continuum hand-shake in the dynamic case. The hybrid scheme is thus validated a powerful and cost effective method for performing multiscale simulations of nanodevices.

INTRODUCTION

Scaling the size of mechanical structures and electronic devices down to the nanometer scale, in order to achieve enhanced mechanical and electro-optical properties, has been of great importance in recent years. In this regime, atomistically-induced stress and strain inhomogeneities, originating at surfaces and interfaces, become increasingly important due to the large surface-to-volume ratio [1-3]. A theoretical description for rational design and accurate lifetime prediction of mechanical structures [4,5] in this regime, that goes beyond the traditional continuum approach [3,6,7], is thus necessary [9,10].

Atomistic simulations utilizing the molecular dynamics (MD) method through use of suitable interatomic potentials can provide the necessary atomic level information [11], but cannot reach the desired length scales due to high computational cost. A multiscale scheme, that will efficiently combine atomistic and continuum simulations, is thus needed. The serial multiscale approach is to use atomistic simulations to re-construct the constitutive equations for continuum in regions where atomic resolution is required [12-14]. The concurrent multiscale approach is to spatially decompose the system into an atomic and a continuum region, use atomistic and continuum simulations respectively for their study, and establish a seamless hand shaking (HS) between the two schemes [15-17]. In this work, we use the concurrent multiscale approach and study the quality of the hand shaking in the static coupling between atomistics and continuum (atomistically-induced stress patterns that extend into the continuum) as well as their dynamic coupling (stress waves that propagate from the atomistics region into the continuum).

COMPUTATIONAL PROCEDURE

In the MD method, Newton's equations of motion are integrated in time for a N -atom system subjected to suitable interatomic potentials, consisting of two- and three-body terms:

$$H_{MD} = \frac{1}{2} \sum_i^N m_i v_i^2 + \sum_{i < j}^N V_{ij}^{(2)}(\mathbf{r}_{ij}) + \sum_{i < j < k}^N V_{ijk}^{(3)}(\mathbf{r}_{ij}, \mathbf{r}_{ik}) \quad (1)$$

In this work, the materials we study are crystalline silicon and α -crystalline silicon nitride, as well as their interface. For silicon we use the Stillinger-Weber (SW) interatomic potential [18]. For silicon nitride, the two-body terms account for steric repulsion, Coulomb, and charge-dipole interactions, while the three-body terms account for covalent bond bending and stretching [19]. For interactions at the silicon/silicon nitride interface we use a variation of the silicon nitride potential in order to account for the correct charge transfer across the interface obtained from self-consistent LCAO electronic structure calculations [20].

In the continuum region, we utilize the finite element (FE) method in which the continuum linear elasticity equations are solved on a computational grid. The displacement field is discretized on the grid points (nodes) and interpolated within the grid cells (elements). The Hamiltonian can then be pre-calculated as a function of the nodal displacements \mathbf{u}

$$H_{FE} = \frac{1}{2} \sum_l \sum_{i,j}^{N_e, N_n} (\mathbf{u}_i^T \mathbf{K}_{ij} \mathbf{u}_j + \dot{\mathbf{u}}_i^T \mathbf{M}_{ij} \dot{\mathbf{u}}_j) \quad (2)$$

where N_e, N_n are the number of elements and nodes per element respectively, and \mathbf{K}, \mathbf{M} are the elemental stiffness and mass matrices respectively. In this work, we use 8-node brick and 6-node prism elements for the atomic-size FE grid close to the HS (see Fig.1) and 20-node brick elements for larger elements far from the HS. 8- and 6-node elements use linear interpolation for the displacement field, while 20-node elements use quadratic interpolation. We also use the lumped mass approximation where the mass is collapsed on the nodes instead being uniformly distributed (*i.e.* \mathbf{M} is diagonal), which is more appropriate for the small, atomic size elements close to the HS.

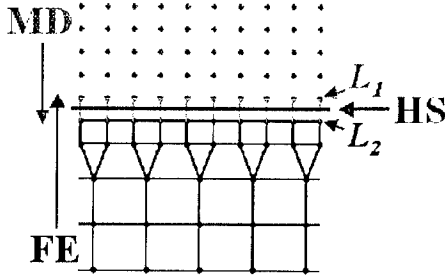


Figure 1. A 2D schematic of the hybrid scheme. On the top is the MD region (spheres represent atoms), and on the bottom is the FE region (spheres and lines represent nodes and element boundaries). The HS region consists of the two lattice planes L_1 and L_2 , and the line between them marks the HS surface.

MD and FE regions merge together in the HS region. In both applications we perform the HS is in crystalline silicon parallel to the (111) plane. The FE grid is fine-grained to atomic size and distorted so as to follow the silicon diamond lattice, and some portion of it overlaps with a portion of the MD region. These hybrid atom/nodes constitute the HS region. For the case of silicon, due to the short range of the SW interactions, only two (111) lattice biplanes (denoted L_1 and L_2 in Fig. 1) are enough to make up the HS. The total Hamiltonian is now defined as [17]

$$H = \frac{1}{2} \sum_i^N m_i v_i^2 + \sum_{i,j}^N w_{ij} V_{ij}^{(2)}(\mathbf{r}_{ij}) + \sum_{i,j,k}^N w_{ijk} V_{ijk}^{(3)}(\mathbf{r}_{ij}, \mathbf{r}_{ik}) + \frac{1}{2} \sum_l \sum_{i,j}^{N_e, N_n} w_l \mathbf{u}_i^T \mathbf{K}_{ij} \mathbf{u}_j \quad (3)$$

where the MD potential terms are weighted with w_{ij} (w_{ijk}) by 1 if i and j (ijk) are within or below $L_1, 1/2$ if they cross the HS surface, and 0 if they are within or above L_2 . Similarly, the FE terms

are weighted with w_i by 1 if element 0 is above the HS surface, 1/2 if it crosses it, and 1 if it below it. This averaging scheme of the two Hamiltonians at the HS was proposed by Abraham, Broughton, Bernstein and Kaxiras [17], and it smoothly couples the MD and FE regions.

The computational efficiency of this scheme is very large. Grid generation for the FE region is done in a way so that only a small number (10 to 20) of different elements is used (see Fig. 1), so we can pre-calculate and store their stiffness matrix (in linear elasticity the stiffness matrix does not change with time). The time then spend on the force computation for one node is less than 75% of that spend on one atom, therefore expanding the system size with finite elements comes practically for free. This is shown in Fig. 2 where we plot the computational efficiency of this scheme when expanding the system size with FE from L_0 to L . Time stepping is done with the velocity-Verlet algorithm and the same time step for both MD and FE systems. The code was parallelized through spatial decomposition and run on a 166-node PC-cluster at the Concurrent Computing Laboratory for Materials Simulations at LSU.

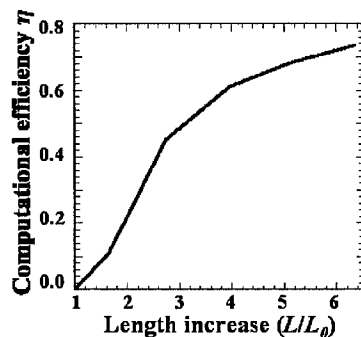


Figure 2. Computational efficiency as a function of the length increase L/L_0 . Assume an initial system of size L_0 . If $\tau_{MD}(L)$ is the time spent on the force computation at each time step, when the enlarged system L is modeled solely by MD, and $\tau_{FE/MD}(L)$ is the corresponding time if the initial system part L_0 is modeled by MD and the rest $L-L_0$ is modeled by FE, then the computational efficiency η is defined as $\eta = 1 - \tau_{FE/MD}(L) / \tau_{MD}(L)$.

RESULTS AND DISCUSSION

The first simulation we perform is to study the quality of the static coupling between MD and FE. The system we chose for this study is a realistic application of the interface problem between dissimilar materials: a $25 \times 25 \times 1$ nm Si(111) mesa covered with a $25 \times 25 \times 5$ nm Si_3N_4 (0001) film, on a $50 \times 50 \times 15$ Si(111) substrate [11] (see Fig. 3).

The lattice mismatch of about 1.1% between Si and Si_3N_4 at their interface creates deformations and stress patterns that extend throughout the Si substrate. With our hybrid scheme, we model with MD the Si_3N_4 film, the Si/ Si_3N_4 interface and the top part of the Si substrate, while with FE we model the rest of the Si substrate. The HS is placed 3 nm below the top of the Si substrate. A second simulation, with the whole system modeled by MD, is also performed for comparing results. The simulation schedule is as follows: the system is initially relaxed at zero temperature, then heated and thermalized at 300 K with Langevin dynamics, and finally cooled down back to zero temperature.

A vertical slice of this system, at the end of the hybrid simulation, is depicted in Fig. 3. Displacements from equilibrium have been magnified so that the deformations that take place are seen clearly. There are large deformations in the Si_3N_4 pixel and at edges with the Si substrate. Si_3N_4 is 1.1% larger than Si, and so it gets compressed at the Si/ Si_3N_4 interface (accompanied by a small curvature), while Si below the interface gets expanded (accompanied with large compressions at the edges). Deeper in the Si substrate, however, deformations remain relatively small, therefore linear elasticity describes them satisfactorily.

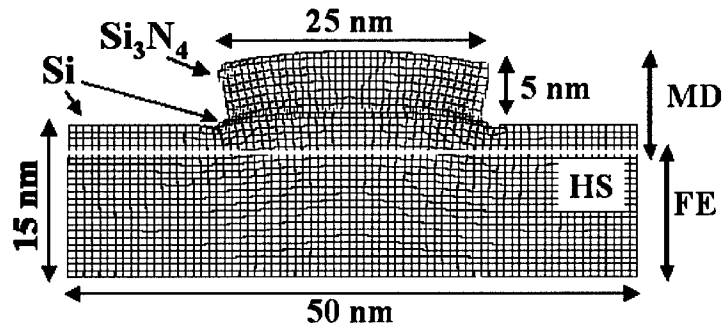


Figure 3. A vertical slice of the Si/Si₃N₄ nanopixel on top of the Si substrate, after the hybrid simulation. Displacements from equilibrium have been magnified by a factor of two in order to picture more clearer the deformations taking place. HS is 3 nm below the top of the Si substrate.

Figure 4 compares the displacement and stress distributions for the hybrid FE/MD and full MD simulations. These are averaged over the corresponding unit cells and are plotted as a function of depth from the top of the Si₃N₄. The lattice mismatch is well reflected in both displacement and stress curves. The corresponding effect is the creation of a parabolic tensile stress well in the Si substrate, accompanied by compressive stresses in the larger Si₃N₄ pixel.

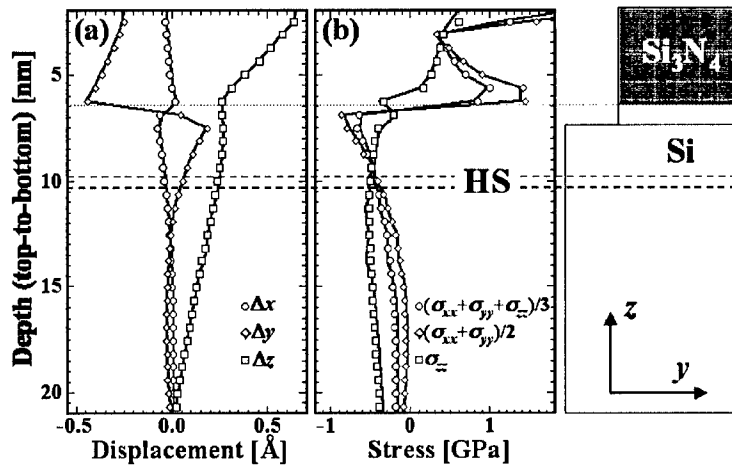


Figure 4. (a) Displacements from equilibrium and (b) stresses as a function of the depth (along z) from the top of the nanopixel. The directions denoted here are x : $[-211]$, y : $[0-11]$, z : $[111]$. Displacements and stresses are plotted on a vertical line that passes through $x=0$, $y=d/4$ and $x=0$, $y=0$ respectively, where $d=25$ nm is the pixel width and its center is at $x=y=0$. The hand shake region (dashed lines) is about 3 nm below the top of the Si substrate, or, about 4 nm below the Si/Si₃N₄ interface (dotted line).

The agreement between the hybrid FE/MD and full MD simulations is very good. Small deviations are only found in the stress curves in the form of three small "bumps" in the hybrid results. One is centered on the HS and is due to the inevitable differences between MD and FE. The other two are deeper in the FE region and are centered on the regions where the FE grid is coarsened, i.e., where larger FE elements are connected with smaller ones. Overall, all features and multiscale phenomena involved in this interface system are faithfully reproduced by the hybrid simulation scheme.

In the second simulation we study the quality of the dynamic coupling between MD and FE. The system here consists of a block of silicon, one-third of it modeled with MD and two-thirds of it modeled by FE, and the simulation involves a projectile impact. The silicon block has dimensions of $11 \times 6 \times 30$ nm with the HS parallel to the (111) plane 10 nm below the top Si surface. Periodic boundary conditions are imposed on the sides. The top Si surface in the MD region is free and the nodes at the bottom Si surface in the FE region are fixed. The projectile is approximated by an infinite-mass hard sphere of radius 1.7 nm, from which the silicon atoms scatter elastically. A harmonic motion of the projectile along the [111] direction close to the top Si surface in the MD creates small-amplitude waves in the silicon crystal. Figure 5 shows snapshots at three different times, in which only a thin slice is plotted for the clarity of presentation. The gray-scale denotes the absolute displacement from the equilibrium positions measured in Å. The induced waves in the MD region propagate through the HS into the FE region without reflection demonstrating seamless dynamic hand-shaking between MD and FE.

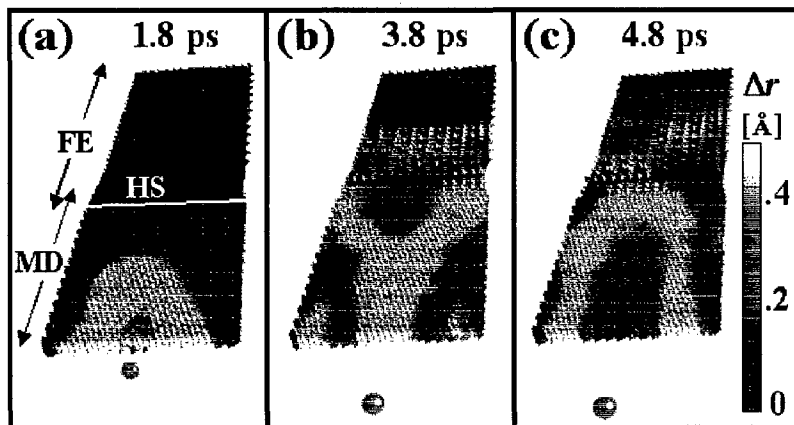


Figure 5. Time evolution of FE nodes and MD atoms in a hybrid FE/MD simulation of projectile impact on a silicon crystal. Absolute displacement of each particle from its equilibrium position is gray-scale-coded. The figure shows a thin slice of the crystal for the clarity of presentation.

CONCLUSIONS

We have investigated the quality of the hand-shaking between atomistics and continuum in a concurrent hybrid FE/MD simulation scheme. The first test involved Si/Si₃N₄ nanopixels on a Si substrate where the nanopixel was modeled by MD and the substrate by FE. No discontinuity is found along the atomistics/continuum HS and comparison with standard full MD simulations shows excellent agreement. The second test involves projectile impact on a block of silicon where part of the block is modeled by MD and the other part of it by FE. The impact occurs on

the MD region and excited waves propagate seamlessly through the HS into the FF region with no visible reflections at the HS. Overall, the HS provides a seamless coupling between atomistics and continuum for both static and dynamical problems.

ACKNOWLEDGMENTS

This work was supported by DOE, NSF and AFOSR and BCVC (Louisiana Board of Regents). Simulations were performed on parallel machines at the CCLMS.

REFERENCES

1. F. Liu, F. Wu, and M.G. Lagally, Chem. Rev. **97**, 1045 (1997).
2. S. Di Fonzo *et al.*, Nature **403**, 638 (2000).
3. Y. Zhuang *et al.*, *Strain relaxation in period arrays of Si/SiGe quantum wires determined by coplanar high-resolution x-ray diffraction and grazing incidence diffraction* (IOP Publishing, 1999) p. 224.
4. Z. Zhang and M. G. Lagally, Phys. Rev. Lett. **72**, 693 (1994).
5. Madhukar, J. Crystal Growth **163**, 149 (1996).
6. S. C. Jain *et al.*, J. Appl. Phys. **78**, 1630 (1995).
7. T. Johnson and L. B. Freund, J. Appl. Phys. **81**, 6081 (1997).
8. P. H. Geubelle and J. R. Rice, J. Mech. Phys. Solids **43**, 1791 (1995); J. W. Morrissey and J. R. Rice, J. Mech. Phys. Solids **46**, 467 (1998).
9. Needleman, Acta mater. **48**, 105 (2000).
10. G. Z. Voyiadjis and B. Deliktas, Mech. Research Comm. **27**, 295 (2000).
11. M. E. Bachlechner *et al.*, Appl. Phys. Lett. **72**, 1969 (1998); A. Omeltchenko *et al.*, Phys. Rev. Lett. **84**, 318 (2000).
12. E. B. Tadmor, M. Ortiz and R. Phillips, Philos. Mag. A **73**, 1529 (1996).
13. O. A. Shenderova, D. W. Brenner, A. A. Nazarov, A. E. Romanov, and L. H. Yang, Phys. Rev. B **57**, R3181 (1998).
14. R. E. Rudd and J. Q. Broughton, Phys. Rev. B **58**, R5893 (1998); Phys. Stat. Sol. (b) **217**, 251 (2000).
15. M. Mullins and M. A. Dokainish, Philos. Mag. A **46**, 771 (1982).
16. S. Kohlhoff, P. Gumbsch and H. F. Fischmeister, Philos. Mag. A **64**, 851 (1991).
17. F. F. Abraham, J. Q. Broughton, N. Bernstein, and E. Kaxiras, Computers in Physics **12**, 538 (1998).
18. F. H. Stillinger and T. A. Weber, Phys. Rev. B **31**, 5262 (1985).
19. P. Vashishta *et al.*, in *Amorphous Insulators and Semiconductors*, edited by M. F. Thorpe and M. I. Mitkova, NATO ASI, Vol. 23 (Kluwer, Dordrecht, 1997).
20. G. L. Zhao and M. E. Bachlechner, Phys. Rev. B **58**, 1887 (1998).

Atomically-based Field Formulations for Coupled Problems of Composition and Mechanics

Krishna Garikipati[†] and Lori C. Bassman[‡]

[†] Dept. of Mechanical Engineering, University of Michigan, Ann Arbor, MI 48109, USA

[‡] Engineering Dept., Harvey Mudd College, Claremont, CA 91711, USA

ABSTRACT

Preliminary ideas are presented on developing coupled, continuum field formulations for composition and mechanics with applications to microelectronic materials. A thermodynamic basis is constructed, reflecting atomic-level transport mechanisms and the associated mechanics. Formal arguments lead to constitutive field relations, and specification of balance laws completes the coupled field description. Early numerical results are also presented.

INTRODUCTION

Compositional phenomena play a prominent role in semiconductor and microelectronic materials. Examples include (i) the self-diffusion of metal atoms in interconnect lines [1, 2], (ii) transport of oxygen molecules during thermal oxidation of silicon [3], (iii) dopant diffusion in silicon [4] and (iv) precipitation of separate phases in patterned structures [5, 6]. In each of these cases, composition and mechanics are, in fact, tightly coupled. Models for the coupled description of composition and mechanics exist to a lesser (thermal oxidation and dopant diffusion) or greater extent (metal self-diffusion and phase precipitation). While the richness of the work cited above (and references therein) is indisputable, a bidirectionally coupled continuum field formulation accounting for atomic mechanisms of exchange, defect creation and the associated stress/strain, is not yet in place. Such a formulation would enable one to pose very general, coupled, initial and boundary-value problems and eliminate simplifying assumptions such as regularly shaped domains and known, constant external stress states. The development of such a class of formulations and the methods for their computational implementation is our goal.

THERMODYNAMIC FORMULATION

To fix ideas we consider the two-dimensional lattice of Figure 1. It consists mostly of atoms marked A in substitutional sites with B atoms (dopants or impurities) and vacancies, V, at lower concentration. We also assume A and B interstitials, and that all species are electrically neutral.

The Gibbs free energy density is expressed, pointwise, as a sum of the densities of internal energy, e , work done, w_{ext} and entropy, η : $\phi = e - w_{\text{ext}} - \eta\theta$, where θ is the absolute temperature. The Gibbs free energy density as defined by this relation and Equations (1-3) below is the cornerstone for developments to follow. We have,

$$\hat{e}(\boldsymbol{\varepsilon}, \varepsilon_Z, \varepsilon_\theta, \varepsilon_C, C_Z, \eta) = \hat{e}_\eta(\eta) + \sum_Z e_Z^F C_Z + \frac{1}{2} \boldsymbol{\varepsilon}^e : \mathbb{C} : \boldsymbol{\varepsilon}^e \quad (1)$$

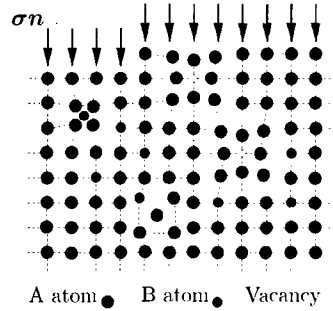


Figure 1: The two-dimensional lattice: substitutional/interstitial species and vacancies.

The first two contributions to e come from an entropic term, $\hat{e}_\eta(\eta)$ and an energy density of formation, $e_Z^F C_Z$, with the index, Z , running over substitutional and interstitial species, whose concentrations are denoted, C_Z . The third term represents the contribution of the elastic strain energy density involving the fourth order elasticity tensor, \mathbb{C} , which can be anisotropic, and the elastic strain, $\boldsymbol{\varepsilon}^e = \boldsymbol{\varepsilon} - \frac{1}{3}(\sum_Z \varepsilon_Z + \varepsilon_\theta) \mathbf{1} - \frac{1}{3}\varepsilon_C \mathbf{n} \otimes \mathbf{n}$. Here, $\boldsymbol{\varepsilon}$ is the total strain, $\varepsilon_Z \mathbf{1}$ is the inelastic, isotropic strain of relaxation or expansion at a point defect (Figure 1, with the index, Z , running over point defect types), $\varepsilon_\theta \mathbf{1}$ is the isotropic thermal strain and $\varepsilon_C \mathbf{n} \otimes \mathbf{n}$ is the creep strain, due to atomic flux, and acting through the rank-one tensor, $\mathbf{n} \otimes \mathbf{n}$, at locations such as the free surface in Figure 1.

The incremental work density is written as

$$\delta w_{\text{ext}} = \boldsymbol{\sigma} : \boldsymbol{\varepsilon}_V^F \Omega \delta C_V + \frac{1}{3} \boldsymbol{\sigma} : \mathbf{1} (f_V - f_i) \Omega \delta C_Z - q^* V \delta C_V + \boldsymbol{\sigma} : \delta \boldsymbol{\varepsilon} \quad (2)$$

The first term is the work done by the local stress, $\boldsymbol{\sigma}$, in increasing the vacancy concentration (δC_V) at the free surface. It involves a non-isotropic strain tensor, $\boldsymbol{\varepsilon}_V^F$. The second term is the work done by the stress acting through an isotropic strain in creation of a vacancy-interstitial pair or their recombination. The third term is the work done by an applied electrostatic potential field, V , via vacancy transport (the phenomenon of electromigration), where q^* is the apparent charge on a vacancy. The mechanical work done by the stress acting through the strain is seen in the fourth term.

The entropy has thermal and configurational terms. For substitutional (S) sites, $C_A + C_B + C_V = C_S$, and for interstitial spaces (i), $C_i + C_{Ai} + C_{Bi} = \alpha C_S$, α being a geometric factor. From elementary statistical considerations:

$$\hat{\eta}(C_Z, \theta) = \hat{\eta}_{\text{vib}}(\theta) - k \left[\sum_Z C_Z \log\left(\frac{C_Z}{C_S}\right) + C_i \log\left(\frac{C_i}{\alpha C_S}\right) \right] \quad (3)$$

COUPLED FIELD EQUATIONS

The electrochemical potential corresponding to each species is obtained as

$$\mu_Z = \mu_{Z_0} + \frac{\partial \phi}{\partial C_Z} + \sum_{Y \neq Z} \frac{\partial \phi}{\partial C_Y} \frac{dC_Y}{dC_Z}. \quad (4)$$

The first term is a uniform reference potential. The third term arises from coupled mechanisms of exchange, defect creation and annihilation such as creation of an A interstitial-vacancy pair: $\delta C_A = -\delta C_{A_i} = -\delta C_V = -\delta C_i$. From μ_Z , follows the flux

$$\mathbf{j}_Z = -\frac{D_Z C_Z}{k\theta} \nabla \mu_Z, \quad (5)$$

where D_Z is the diffusivity corresponding to species Z. The fluxes satisfy continuity equations of the type:

$$\frac{\partial C_Z}{\partial t} = -\nabla \cdot \mathbf{j}_Z + k_{Z_i,V}(C_{Z_i}C_V - C_{Z_i}^{\text{eq}}C_V^{\text{eq}}). \quad (6)$$

If Z represents a substitutional species, the recombination of Z interstitials (Z_i) and vacancies is a source term, with $k_{Z_i,V}$ being the recombination rate constant. For Z interstitials, Z_i , the recombination source term has its sign reversed (a sink). In the continuity equation for vacancies recombination with both types of interstitials (A_i, B_i) acts as a sink. An additional source term, $-\frac{1}{\tau_V}(C_V - C_V^{\text{eq}})$ acts due to the creation of vacancies at grain boundaries and free surfaces. The effective time constant of this process is τ_V . The construction of the Gibbs free energy density ensures that the electrochemical potentials, Equation (4), reflect the influence of the mechanics. The fluxes, \mathbf{j}_Z , obtained from the corresponding electrochemical potentials via Equation (5) are also directly influenced by the mechanics. The continuity equations for various species are coupled through the recombination terms.

Formal thermodynamic arguments can be advanced for the derivation of Equations (4–5) and extended to the following general constitutive relation for stress: $\boldsymbol{\sigma} = \partial e / \partial \boldsymbol{\varepsilon}$. Ignoring inertia, the stress is governed by the quasistatic equilibrium equation: $\nabla \cdot \boldsymbol{\sigma} + \mathbf{b} = 0$, \mathbf{b} being the body force. The coupling of composition and mechanics that underlies the thermodynamic description ensures that the mechanics reflects the influence of composition of various species. The coupled continuum field description of the problem is thus complete. Details of the arguments alluded to in this section and the previous one have been presented elsewhere [7] for the more limited problem of self-diffusion.

EXAMPLES

The formulation, restricted to self-diffusion, is applied to an electromigration problem in aluminum. The composition problem is posed in terms of vacancies. Figure 2 shows the contours of vacancy concentration in a polycrystalline line of width $1\mu\text{m}$. Numerical solutions were obtained using finite element methods developed for the present formulation [7]. Details are avoided here. The distribution shown is obtained by solving the initial boundary value problem with an initial condition of uniform vacancy concentration, $C_V = C_V^0$, boundary conditions of vanishing normal flux of vacancies, $\mathbf{j}_V \cdot \mathbf{n} = 0$ on the horizontal boundaries and periodic boundary conditions on concentration on the vertical boundaries. The vacancy



Figure 2: Initial vacancy distribution.

formation energy, e_V^F , has been specified to be lower in grain boundaries, here modelled as regions of finite width. As a result, when transients disappear, the obtained vacancy concentration is higher over grain boundaries. An electric field, \mathbf{E} , directed to the right is then imposed, and the vacancies drift parallel to \mathbf{E} . Due to their higher diffusivity, grain boundaries act as fast diffusion paths. Focusing attention upon the grain boundaries in the middle of the line, it is argued that vacancies accumulate at the right end, where the fast diffusion path terminates while depleting from the left end. The result is an increasing hydrostatic tension at the right end and hydrostatic compression at the left end of the diffusion path (Figure 3). While no external tractions or non-zero displacement boundary conditions are imposed, a local stress arises as electromigration proceeds and is coupled into the composition problem. The stress equilibrium problem is also solved, and it is influenced by the composition. The fully coupled problem is thus treated as discussed above. When a tensile thermal stress is superimposed upon the line, the relatively higher tensile stress at the locations on the line where C_V is highest (numerical results not shown here) could result in void nucleation as discussed below.

The conditions for void nucleation under the proposed formulation are investigated as a special case of phase separation. For the latter, a ternary A,B,V mixture is considered with composition-dependent moduli. For simplicity, we restrict ourselves to one dimension. We have Young's moduli for pure A and B satisfying the relation $E_B = 0.1 \times E_A$. A hypothetically high stress, of the order of 10 GPa is considered. Volume fractions $f_A = 1.5$, $f_B = 0.5$ and $f_V = 0.8$ are assumed relative to the average atomic volume, $\Omega = 125 \text{ \AA}^3$ and the temperature $\theta = 300K$. A necessary condition for phase separation is a non-convex Gibbs free energy density, ϕ as a function of composition. Figure 4a demonstrates that such a structure is indeed a property of ϕ under the assumed condition. Furthermore, a sufficient condition is the existence of a "double-welled" structure from a second local minimum in ϕ . Such an additional local minimum is observed corresponding to almost pure B and is revealed upon closer examination of ϕ in the limit of high C_B (Figure 4b). Thus, the formulation proposed here does possess the ingredients for phase separation. The relevance of this investigation to void nucleation is that examination of the Gibbs free energy density for a binary A,V mixture (self-diffusion) reveals a similar non-convexity for $0.75 \leq f_V \leq 1$.

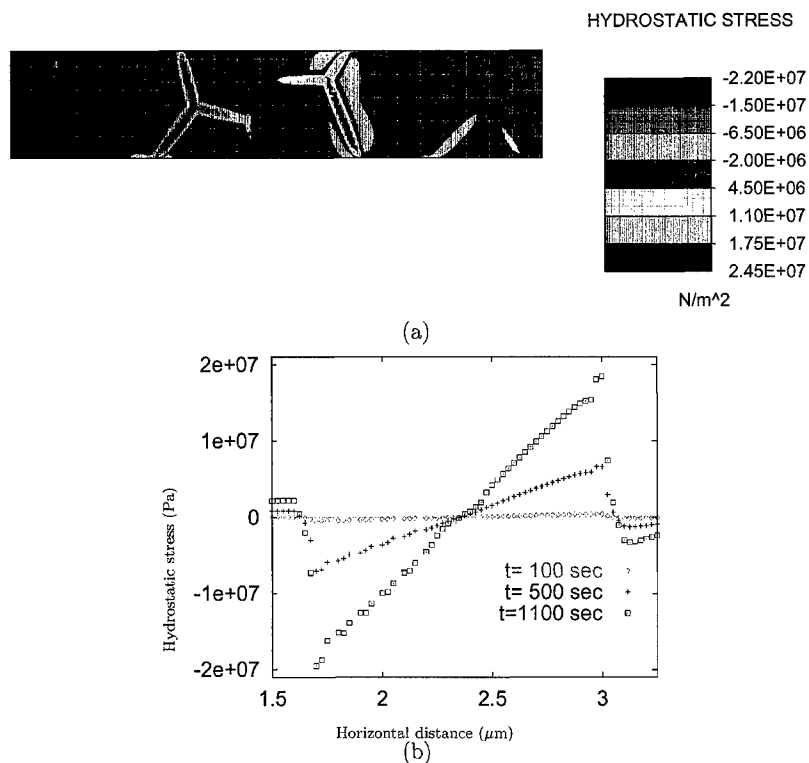


Figure 3: (a) Hydrostatic stress. (b) Evolution of hydrostatic stress.

A minimum observed at high high vacancy concentration in this case corresponds to the conditions for void nucleation.

CONCLUSIONS

The approach presented here forms the basis for a broad effort to study and model the coupling of composition and mechanics in microelectronic and semiconductor materials. While promising early results are available, much remains to be done. The problem of dopant diffusion, even without the influence of mechanics is rich and complex in its own right. The same holds for self-diffusion and phase precipitation, including the influences of surface energies, moving grain and phase boundaries, grain growth and microstructure evolution. In the case of thermal oxidation, it is hoped that the approach advocated here will help to improve process models currently in use.

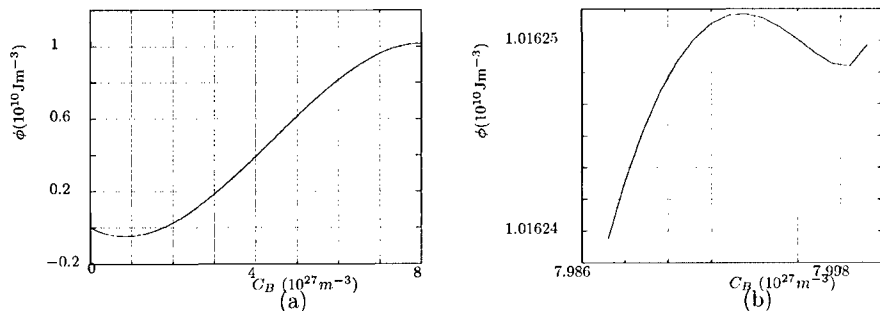


Figure 4: (a) Non-convex Gibbs free energy density. (b) Existence of a second local minimum.

ACKNOWLEDGEMENTS

This work is supported by the NSF through grant #0075989. Earlier support from MARCO and DARPA is also acknowledged.

References

- [1] F. Y. Génin. *J. App. Phys.*, 77(10):5131–5137, 1995.
- [2] Y. W. Zhang, A. F. Bower, L. Xia, and C. F. Shih. *J. Mech. Phys. Solids*, 47:173–199, 1999.
- [3] K. Garikipati, V. S. Rao, M. Y. Hao, E. Ibok, I. DeWolf, and R. W. Dutton. *Comp. Model. Engrg. Sci.*, 1(1):63–80, 2000.
- [4] M. J. Aziz. *App. Phy. Lett.*, 70(21):2810–2812, 1997.
- [5] F. C. Larché and J. W. Cahn. *Acta Mechanica*, 33 no. 3:331–357, 1985.
- [6] M. E. Gurtin and M. T. Lusk. *Physica D*, 130:133–154, 1999.
- [7] K. Garikipati, L. C. Bassman, and M. D. Deal. to appear in *J. Mech. Phys. Solids*, 2000.

Features of Vacancy Interaction with Interstitial Clusters in BCC Metals

Marta Pelfort⁽¹⁾, Yuri N.Osetsky⁽²⁾ and Anna Serra⁽¹⁾

⁽¹⁾ Dept. Matemàtica Aplicada III, E.T.S. Eng. Camins, UPC, Barcelona, Spain

⁽²⁾ Materials Science and Engineering, Dept. of Eng., The University of Liverpool, UK

ABSTRACT

Recent theoretical calculations and atomistic computer simulations have shown that one-dimensional (1D) glissile clusters of self-interstitial atoms (SIAs) play an important role in the evolution of the microstructure in metals and alloys under cascade damage conditions. Theoretical treatments based on the production bias model (PBM) and cascade-induced source hardening clarify many features of materials behaviour under irradiation by considering 1D glissile SIA clusters. However, further progress in understanding irradiation phenomena demands a detailed knowledge of different reactions where glissile SIA clusters take part. The latest version of the PBM has demonstrated that there is a significant lack of knowledge on mechanisms such as the interaction between mobile clusters and other microstructure components, changes on glide directions or the reduction of cluster mobility. Some aspects of interactions have been recently studied and the formation of immobile complexes of glissile clusters in the bulk and near dislocations has been shown. However, in addition to the cluster - clusters and cluster - dislocation interactions, the interactions of clusters with point defects should be considered. Here we present the first results on interaction between a SIA cluster and vacancy in bcc-iron. The interactions were studied by both atomistic simulations and elasticity theory. Some qualitative differences between the results obtained by these two methods were found, thereby demonstrating the need for the atomistic approach. It is shown that the interaction with vacancies can reduce and, in some cases, suppress the mobility of SIA clusters. The results are discussed in the light of both experimental data and theoretical predictions.

INTRODUCTION

During the last years a significant attention was paid to clusters of self-interstitial atoms formed in metals irradiated with energetic particles. The main reason is the recognition of the important role of SIA clusters in the evolution of the microstructure under irradiation. The successful application of PBM [1] and its further development [2] in the explanation of many peculiarities of radiation induced microstructures such as the mechanism of void lattice formation, swelling inhomogeneity near grain boundaries, rafts of dislocation loops and decoration of dislocations by interstitial clusters and dislocation loops [3-9] suggested to perform extensive studies of properties of SIA clusters in different metals. Thus, the structure and mobility properties of SIA clusters were studied in bcc, fcc and hcp lattices and the results have corroborated fast one-dimensional mobility in all structures, thereby confirming the basic suggestion of PBM [1]. However, the later version of PBM [2] has shown that there is a significant lack of knowledge on the mechanisms of interaction between mobile clusters and other microstructure components, the change in cluster glide directions and the reduction in clusters mobility. Some aspects of interactions have been recently studied [11] and formation of immobile complexes of glissile clusters in bulk and near dislocations has been demonstrated. However, in addition to cluster-cluster and cluster-dislocation interaction another type of reaction, namely with point defects, has to be considered. Traditionally,

'point defect – cluster' interactions are treated like 'point defect – dislocation' interactions; clusters are considered as dislocation loops and a conventional elastic bias factor is used [12,13]. An important feature of cluster – point defect interactions, as they appear in rate theory calculations, is related to the total balance of defects in the system. For example, when a vacancy interacts with a cluster of N SIAs it is supposed that the result will be another cluster of $N-1$ SIAs. This is based on the supposition that vacancy-SIA cluster reaction is of annihilation type. Qualitatively the same description is used for SIA – vacancy cluster interaction. The results of an intensive atomistic study of SIA cluster properties allows us to expect that the mentioned phenomena could be not as simple as described above. This encouraged us to launch a special study aiming to clarify features of point defects interactions with clusters and small dislocation loops. In this paper we present some results related to the interaction between glissile SIA clusters and vacancies in bcc-iron. The choice of bcc-Fe for this study is based on several reasons. Some are related to the peculiarities of experimental results such as the low density of the observed matrix defects, the low swelling and a recent positron annihilation observation showing that a significant number of vacancies is stored in the bulk of neutron-irradiated iron in the form of tiny clusters invisible by electron microscopy [14]. Others are related to the fact that glissile SIA clusters in iron are commonly observed in cascades studies and their properties are well studied by atomistic simulation and, then, a wide range of static and dynamic properties is available for comparison [10].

CALCULATION MODEL

Atomistic simulation

The interaction between vacancy and SIA cluster in bcc crystallite was studied by molecular static technique using an interatomic potential for alpha-iron constructed within the Finnis-Sinclair many-body approach [15]. Interstitial planar clusters were initially created in the central (111) plane of a rectangular crystallite oriented along $[1\bar{1}0]$, $[11\bar{2}]$ and $[111]$ directions. Usual fixed boundary conditions were applied. The system was relaxed using a combination of conjugate gradients and quasi-dynamics methods. A previous study has shown that the most stable clusters are hexagons with sides along $\langle 112 \rangle$ directions, which is equivalent to the most stable edge dislocation $\frac{1}{2}[111]\langle 112 \rangle$ [16]. Thus, hexagonal clusters in the form of $\langle 111 \rangle$ crowdions distributed over three adjacent (111) planes represent perfect dislocation loops with Burgers vector $\frac{1}{2}[111]$. Such hexagons containing 19, 61, 91 and 127 SIAs were simulated in a crystallite containing about 400,000 mobile atoms.

Once a SIA cluster was created and relaxed, a vacancy was placed in a certain position in the cluster vicinity and the crystallite was relaxed again. After relaxation the crystallite energy was calculated and the configuration was analysed. The SIA cluster – vacancy interaction energy was estimated through previously calculated formation energies of both an individual cluster and a vacancy. The vacancy positions studied are in rows of sites along the Burgers vector direction. Three types of rows crossing the cluster habit plane in the hexagon centre, vertex and centre of the $\langle 112 \rangle$ edge were considered. Some positions within the cluster perimeter were also investigated.

For some clusters we also performed molecular dynamics (MD) simulations at temperature $T=260\text{K}$. This was done in a crystallite consisting of about 95,000 atoms with periodic boundary conditions, a period of time of about 5ns , e.g. approximately 4,000,000 time steps. The aim of this simulation is to compare the mobility of SIA clusters with and without vacancies by comparing the atomic displacements. Note that all SIA clusters

considered here were studied earlier and being isolated they performed a fast thermally-activated one-dimensional glide along the Burgers vector direction e.g. $\langle 111 \rangle$ [10].

Continuum calculations

A simple continuum model based on the isotropic elasticity theory was used to describe the interaction energy (E_v^I) between a vacancy at the position $\vec{r} = (X, Y, Z)$ in the stress field of an extended defect :

$$E_v^I(\vec{r}) = P(\vec{r}) \delta V_v(\vec{r}) \quad (1)$$

where $P(\vec{r})$ is the hydrostatic pressure and $\delta V_v(\vec{r})$ is the vacancy dilatation volume which, in general, is a function of the vacancy position. This expression is commonly used in the approximation that a vacancy is an isotropic defect with a constant volume equal to that in the bulk. The vacancy dilatation volume in the bulk of a perfect crystallite $\delta V_v = 0.18 \Omega_0$ (Ω_0 is equilibrium atomic volume) was estimated using the force dipole method described in [17] and this value was used in eq.1. Two approaches were used to estimate the pressure distribution near the SIA cluster. The first evaluates the hydrostatic pressure in the terms of the isotropic elasticity through the trace of the dislocation loop stress tensor $\sigma_{ij}(\vec{r})$:

$$P(\vec{r}) = -\frac{1}{3}(\sigma_{xx}(\vec{r}) + \sigma_{yy}(\vec{r}) + \sigma_{zz}(\vec{r})) \quad (2)$$

The components of the stress field created by the dislocation loop can be easily evaluated adding the contribution of the dislocation segments forming the loop e.g. in the present case 6 segments along $\langle 112 \rangle$ directions [18]. The dislocation line energy and core radius used here were obtained in [11] for the $\frac{1}{2}\langle 111 \rangle \{110\}$ edge dislocation simulated with the same potential. In the second approach, the pressure near the SIA cluster was directly calculated by atomistic simulation using the virial theorem :

$$P(\vec{r}) = -\frac{1}{6N\Omega_0} \sum_{i=1}^N \sum_{j=1}^N \frac{d\phi(r_{ij})}{dr} \frac{\vec{r}_{ij} \cdot \vec{r}_{ij}}{|\vec{r}_{ij}|} \quad (3)$$

where N is the number of atoms in the simulated crystallite, $\phi(\vec{r})$ is the interatomic potential and \vec{r}_{ij} is the radius-vector between the i^{th} and j^{th} atoms.

RESULTS

The results for clusters of 19 and 127 SIAs interacting with a vacancy along rows through either the cluster centre or the middle of the edge are presented in Fig. 1 and 2. In general the comparison of the atomistic simulation results with the theoretical estimations is rather poor since the theory significantly underestimates the interaction energy. Though the estimation based on the pressure obtained from simulation shows a slightly better picture, the interaction energy is still significantly lower than that estimated from simulation. Few reasons can be presented to explain this difference. The first is the inaccuracy of the theory calculating stress field and, therefore, the pressure near such small dislocation loops which

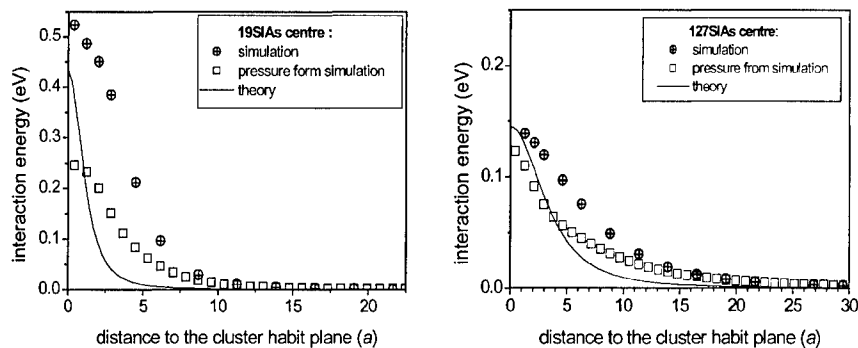


Figure 1. Vacancy interaction energy versus distance to the 19 and 127 SIA cluster habit plane along the line through the cluster centre. Note the difference in energy scale for 19 and 127 SIA clusters.

causes poor results of theoretical estimations. The second is the inaccuracy of using the vacancy dilatation volume calculated for bulk perfect crystallite. This is the reason of the disagreement when the pressure obtained from simulation of individual SIA clusters is used in eq.1. Actually, the pressure increases significantly near the clusters and this should affect the local dilatation volume of the vacancy, which should be increased. This can be only taken into account in full atomistic simulations. Finally, the approach on the basis of eq.1 is in general poor and more accurate approaches must be used to evaluate the interaction energy near clusters e.g. in regions with a high stress field gradient. The fact that the difference between the theory and simulation results for the centre is much lower for the larger cluster, where the stresses are lower, is consistent with all the reasons presented.

Besides the different values of the interaction energy, more significant qualitative differences between simulation and theory appear for a vacancy near the edge of SIA clusters. This difference is related to the annihilation of a vacancy by the SIAs belonging to the cluster edge observed in simulations. The regions where annihilation occurs are indicated in Fig.2. This annihilation was observed only for vacancy positions above (or below) the cluster edge.

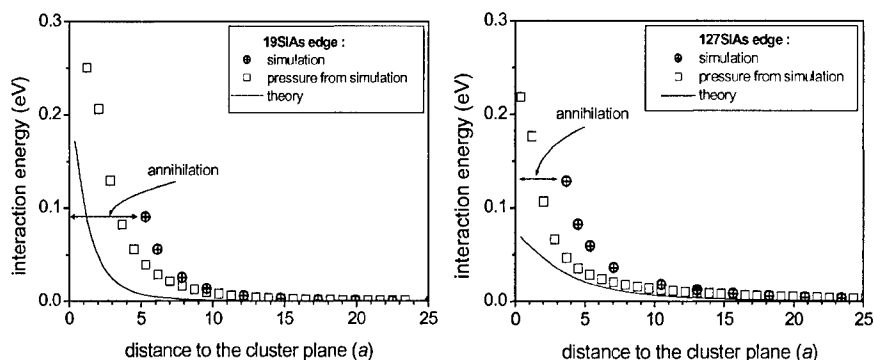


Figure 2. Vacancy interaction energy versus distance to the 19 and 127 SIA cluster habit plane along the line through the centre of cluster edge. Regions where vacancy annihilated are indicated.

Next positions towards the cluster centre were not annihilated. The annihilation region is larger for smaller clusters, which reflect the higher value of the pressure. The limit case of the large loop is the straight dislocation where only the vacancy in the nearest lattice site was observed to be annihilated from simulations with the same Fe potential [19].

Vacancies interacting with SIAs within the cluster/loop perimeter do not annihilate but affect very much to the dynamic properties of SIA clusters. The main effect is a significant reduction of clusters mobility. At low temperature, the vacancies are immobile and they can completely suppress the cluster motion. An example is presented in Fig.3 where the temporal evolution of the atomic square displacements (SD) along the $\langle 111 \rangle$ direction for both a regular isolated cluster of 91 $\langle 111 \rangle$ crowdions and the same cluster with a vacancy in the next to the cluster centre site is shown. It can be seen that the motion of a cluster without a vacancy causes significant SD whereas that with a vacancy does not produce displacements.

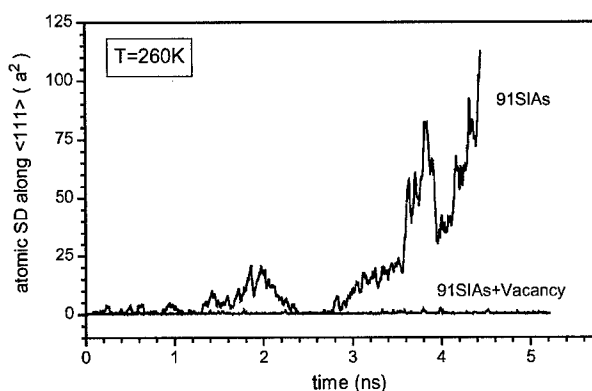


Figure 3. Temporal evolution of atomic squared displacements obtained by MD simulation of an isolated 91SIAs cluster and the same cluster with vacancy in the next to the centre site.

CONCLUSIONS

Vacancy interaction with SIA cluster was studied by atomistic simulation and two theoretical approaches based on the interaction of a dilatation centre with a stress field from an extended defect within the isotropic elasticity theory. It is found that the theoretical approaches underestimate the interaction energy and the disagreement between theory and simulation increases for small clusters and near the cluster edge.

Vacancies can annihilate only with the cluster edge and the annihilation distance in the direction perpendicular to the cluster habit plane increases for small clusters, e.g. up to about $5a$ for 19SIAs cluster.

Vacancies inside the cluster perimeter do not annihilate but strongly affect to the dynamic properties of SIA clusters reducing or, even, preventing their mobility.

It is concluded that, in general, the isotropic elasticity theory cannot describe accurately the point defect – cluster interactions especially for the case of small clusters. Instead, atomistic simulation should be used.

ACKNOWLEDGEMENTS

The computations were carried out at the C⁴ (CEPBA) under the 'Access to Supercomputing Facilities for European Researches', a project of the Large Scale Facilities programme (contract ERBCHGE-CT92-0009) and the research was supported by the Engineering and Physical Sciences Research Council (UK).

REFERENCES

- [1] C.H.Woo and B.N.Singh, *Philos. Mag.*, A **65**, 889 (1992) ; B.N.Singh and A.J.E.Foreman, *Ibid*, A **66**, 975 (1992) ; B.N.Singh, S.I.Golubov, H.Trinkaus, A.Serra, Yu.N.Osetsky and A.V.Barashev, *J. Nucl. Mater.*, **251**, 107 (1997).
- [2] S.I.Golubov, B.N.Singh and H.Trinkaus, *J. Nucl. Mater.*, **276**, 78 (2000).
- [3] H.Trinkaus, B.N.Singh and A.J.E.Foreman, *J.Nucl.Mater.*, **199**, 1 (1992) ; B.N.Singh, *Rad. Effects and Defects in Solids*, **148**, 383 (1999).
- [4] J.O.Stiegler and E.E.Bloom, *Rad. Effects*, **8**, 33 (1971).
- [5] B.N.Singh, A.Horsewell, P.Toft and D.J.Edwards, *J. Nucl. Mater.*, **224**, 131 (1995).
- [6] J.L.Brimhall and B.Mastel, *Radiat.Eff.*, **3**, 325 (1970).
- [7] B.N.Singh, J.H.Evans, A.Horsewell, P.Toft and D.J.Edwards, *J. Nucl. Mater.*, **223**, 95 (1995).
- [8] B.N.Singh, J.H.Evans, A.Horsewell, P.Toft and G.V.Müller, *J.Nucl.Mater.*, **256-263**, 865 (1998).
- [9] A.J.E.Foreman, Harwell Report, AERE R-7135 (1972) ; P.Hähner and W.Frank, *Solid State Phenomena*, **23-24**, 203 (1992).
- [10] Yu.N.Osetsky, A.Serra, V.Priego, F.Gao and D.J.Bacon, *Mat. Res. Soc. Symp. Proc.*, **527**, 69 (1998) ; Yu.N.Osetsky, A.Serra and V.Priego, *Mat. Ibid* , **527**, 59 (1998) ; Yu.N.Osetsky, D.J.Bacon and A.Serra, *Ibid* , **538**, 649 (1999) ; A.V.Barashev, Yu.N.Osetsky and D.J.Bacon, *Ibid*, **540**, 697 (1999) and *Philos. Mag.*, A **80** (2000) 2709 ; Yu.N.Osetsky, D.J.Bacon and A.Serra, *Philos.Mag.Lett.*, **79**, 273 (1999) ; Yu.N.Osetsky, D.J.Bacon, A.Serra, B.N.Singh and S.I.Golubov, *J.Nucl.Mater.*, **276**, 65 (2000).
- [11] Yu.N.Osetsky, A.Serra and V.Priego, *J.Nucl.Mater.*, **276**, 202 (2000); Yu.N.Osetsky, D.J.Bacon, F.Gao, A.Serra and B.N.Singh, *J.Nucl.Mater.*, **283-287** (2000) 784.
- [12] N.Meissner, E.J.Savino, J.R.Willis and R.Bullough, *Phys.Stat.Sol. (b)* **63**, 39 (1974); C.H.Woo, *J.Nucl.Mater.*, **98**, 279 (1981).
- [13] R.Bullough, B.L.Eyre and K.Krishan, *Proc.R.Soc.Lond.A.*, **346**, 81 (1975).
- [14] M.Eldrup and B.N.Singh, *J.Nucl. Mater.*, **276**, 269 (2000).
- [15] G.J.Ackland, D.J.Bacon, A.F.Calder and T.Harry, *Philos.Mag.*, A **75**, 713 (1997).
- [16] Yu.N.Osetsky, A.Serra, B.Singh and S.Golubov, *Philos. Mag.*, A **80**, 2131 (2000).
- [17] H.R.Schober and K.W.Ingle, *J.Phys.F*, **10**, 575 (1980).
- [18] J.P.Hirth and J.Lothe, *Theory of Dislocations*, (1982), Wiley.
- [19] F. Gao, 1999. Unpublished work

Al Grain Boundary Embrittlement Promoted by Na Impurity: An *ab initio* Study

Guang-Hong Lu, Masanori Kohyama¹, Ryoichi Yamamoto

Institute of Industrial Science, University of Tokyo, 7-22-1 Roppongi, Minato-ku, Tokyo 106-8558, Japan

¹Department of Materials Physics, Osaka National Research Institute, AIST, 1-8-31 Midorigaoka, Ikedashi,

Osaka 563-8577, Japan

ABSTRACT

We calculate the electronic structure of $\Sigma 9$ tilt grain boundary with substitutional Na impurity atoms by first principles pseudopotential method. Results show that by Na segregation Al grain boundary expands and the valence charge density decreases significantly along the boundary. There is no stronger bond than metallic bond in the boundary even with Na impurity. We therefore conclude that the mechanism of Na-promoted Al grain boundary embrittlement should be one kind of 'decohesion model'.

Introduction

It seems that theoretically there are two kinds of mechanism of impurity-promoted embrittlement of metal grain boundaries. One is called 'decohesion model'. In this model, the metal-impurity or metal-metal cohesion is weakened by impurity segregation in metal grain boundary and thus induces embrittlement. A typical one is presented by Losch[1], which indicates that the metal-metal bonds neighboring to the impurity-metal bonds are weakened by the embrittling element in group IV-VI. Supporting calculations are carried out by Briant and Messmer[2-3] on a nickel cluster with sulfur impurity, and a iron cluster with phosphorus impurity, respectively. The other is 'bond mobility model' proposed by Haydock[4]. In this model segregated non-metallic impurities at the metal grain boundary bind with the neighboring metal atoms. This increases the covalent character of the bonds and reduces their mobility. Under stress, the bonds between grains cannot slide smoothly and thus stress concentration is generated. Goodwin et al. [5-6] carried out the supercell calculation based on the density functional theory (DFT) on the embrittlement by Ge and As impurities in the host Al[111], supporting 'bond mobility model'.

Until now the embrittling elements seemed to be limited to group III-IV. However, recently it has been experimentally found that elements in group I and II have also the embrittling effect on Al alloys. For example, it was reported that as for Al-Mg alloy, Na atoms tend to segregate on Al boundary thus induces the embrittlement[7]. In this paper we therefore carry out the supercell calculation to investigate the effects of Na segregation on Al grain boundary.

Because of the limited computational ability, we don't consider the lattice vibration and only carry out the calculations at absolute 0 K. Hence the calculation results probably can't compare directly with the experimental ones. However, our results still will be very helpful to understand the effects of segregated Na impurities.

COMPUTATIONAL METHOD

The unit cell is constructed as shown in figure 1. There include 84 atoms in the unit cell.

Al $\Sigma 9(2-21)/[110]$ tilt grain boundary is formed by rotating grain by 38.94° along the $[110]$ axis, and $(2-21)$ is set as boundary plane. The coincidence site lattice (CSL) unit cell on the boundary plane is defined by $3\sqrt{2}/2 a_0[1-1-4]$ and $\sqrt{2}/2 a_0[110]$. The size in the $[110]$ direction is set twice that of the CSL, i.e., $\sqrt{2} a_0$, in order to isolate 4 impurity atoms and keep symmetry. In the $[2-21]$ direction two symmetric grain boundaries are introduced to make periodicity. The distance between the grains is determined by that atom density in the boundary is the same as that by Mills and Daw[8].

The first principles plane-wave pseudopotential method[9] is used based on the DFT[10-11] with local density approximation (LDA)[12]. The electronic ground state is obtained using the conjugate-gradient technique proposed by Bylander, Kleinman and Lee[13]. The plane wave energy cutoff is 13Ry, and 32 k points in the Brillouin zone is used. The electronic structure is determined on a real space grid of $128 \times 64 \times 32$ points. All the atoms are

relaxed according to the Hellman-Feynman forces until all the forces are less than 0.10eV/Å.

We construct the TM-type pseudopotential[14] for Al[15] and the HSC-type pseudopotential[16-17] for Na[18]. For Na we used partial core correction developed by Louie, Froyen and Cohen[19]. The separable form by Kleinman and Bylander[20] with the p as the local component is used. Then we calculate the equilibrium lattice parameter using the present pseudopotentials. Results are listed in table 1.

Table 1 Experiment and calculation values of the lattice constant

lattice constant (Å)		Al (fcc)	Na (bcc)
		Exp. 4.02(0K) ^a	4.225(5K) ^b
	Cal.	3.95	3.98

Exp.: experimental values Cal.: calculation values ^a Ref.[21] ^b Ref.[22]

RESULTS AND DISCUSSIONS

We choose the 4 equivalent sites of the impurity substitution in the boundary supercell as shown in figure 1. In this configuration, the Na atoms can be isolated without neighboring to each other and the symmetric property can be kept.

The relaxed atomic configurations are shown in figure 2. Only the left half parts of A and B layer are shown due to the symmetry. E is the position of the impurity atom (Na) in

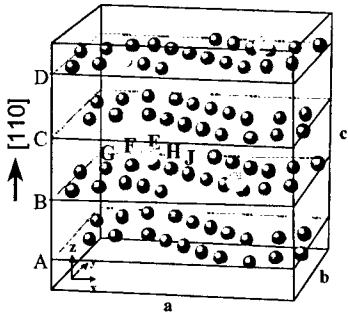


Figure 1. Supercell of Al $\Sigma 9(2-21)/[110]$ tilt grain boundary. A, B, C and D indicate four (110) layers. The length of side a, b, c are 28.469Å, 8.379Å and 5.586Å, respectively, but the model isn't showing the real proportion of them. There are 84 atoms in the unit cell. Four big-sized light-gray spheres indicate the Al atoms in grain boundary replaced by Na atoms. G, F, E, H and J are the atom positions marked for later discussions.

the substitutional cases. The interatomic distances between the five atoms (G, F, E, H and J) are calculated and listed in table 2. It is shown that Al atoms around the Na atom (E) are away from Na atom compared with the relaxed configuration without any impurity (as in table 2: $EF_{Na}=2.719>EF_{Al}=2.622$, about 3.7% increase; $EH_{Na}=2.919>EH_{Al}=2.764$, about 5.6% increase). This makes the distance between the adjacent Al atoms smaller (as in table 2: $FG_{Na}=2.639<FG_{Al}=2.736$, about 3.5% decrease; $HJ_{Na}=2.704<HJ_{Al}=2.748$, about 1.6% decrease). According to periodic condition of CSL the displacement in y and z direction will not contribute to boundary volume change. Because the size in x direction in unit cell is fixed, the present boundary volume change should be different from that of the real case. However, from the distance enlargement between Al and Na atoms in the boundary, it can be concluded that even in real case the boundary volume should be enlarged by Na segregation.

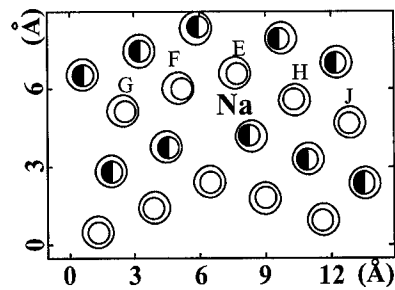


Figure 2. The relaxed configuration of the left half part of layer B and A in the unit cell. G, F, E, H and J correspond to the atoms marked in figure 1. Atom positions without impurity segregation are represented by smaller circles, in which the unfilled and the half-filled ones represent the atom positions of B and A layer, respectively. Bigger circles indicate atom positions with Na segregation.

Table 2 The interatomic distance (Å) between Al atoms, or Al and Na atoms

	FG	EF	EH	HJ
Al ^a	2.736	2.622	2.764	2.748
Na ^b	2.639	2.719	2.919	2.704

^a pure Al boundary ^b Na segregation

The reason of the boundary expansion by Na segregation should be due to the different atomic radii or atomic volumes of Al and Na. Because the interaction between Al and Na atom are not so significant, Na atom in Al boundary tends to have a similar atomic radius to that in pure Na metal. Atomic radius can be considered as half of the nearest neighbor distance of atom. According to our calculated results, the nearest-neighbor distance of fcc-Al (2.79Å) is shorter than that of fcc-Na (3.56Å). This should be the main reason that Al atoms are away from Na atom.

Figure 3(a) shows the calculation range of local density of states (LDOS). The figure shows cross section of z direction of the unit cell, which is perpendicular to the boundary plane (2-21). The calculation range is the sum of two symmetric parts: I and II near the two boundaries. Figure 3(b) shows the results of LDOS near the two boundaries. The figure indicates that LDOSs around the Al boundaries with and without Na segregation both have the characteristic of free electrons, which means that the atomic bonding at the boundary is mainly metallic bond for both systems and there exist no significant ionic or covalent interactions even in the systems with Na impurity. But Na segregation makes LDOS

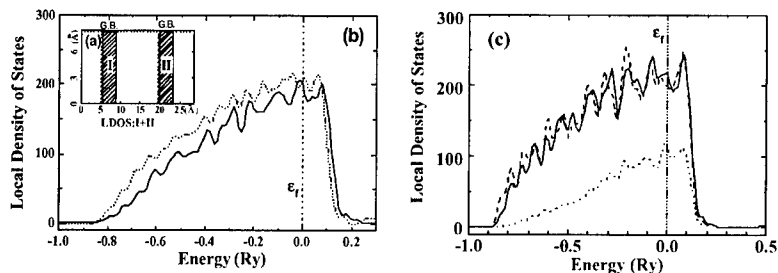


Figure 3. (a) The calculation range of local density of states (LDOS). The figure shows the cross section of z direction of the unit cell, which is perpendicular to the grain boundary plane (2-21). The calculation range is the sum of two symmetric parts: I and II near the two grain boundaries. (b) LDOS of the range above. The dotted line and the solid line are the LDOS result of pure boundary and with Na segregation, respectively. (c) LDOS around the atom E (the dotted line), H (the solid line) and J (the dashed line). Fermi energy is set as zero.

decrease over the whole energy region. This is shown more clearly in figure 3(c), which shows LDOS around the atom indicated E, H and J. LDOS is much lower around Na atom (E) than that around Al atom H and J, and that around J (in the bulk) is a little higher than that around H.

The results of integrated valence charge density on the y - z plane parallel to the boundary plane (2-21) is plotted again x axis, as shown in figure 4. The charge density at the boundary is much lower comparing with the pure boundary, and there is a small increase of charge density in the bulk region. Figure 5 are contours of the valence charge density. Only the left

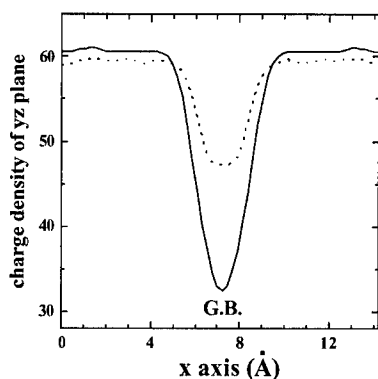


Figure 4. Integrated valence charge density on the y - z plane parallel to the grain boundary plane (2-21), in the left half part of the unit cell. (the dotted line: pure boundary, the solid line: Na segregation)

half part of the layer B is shown due to the symmetry. Comparing figure 5(b) with (a), it can be noted that the charge density decreases significantly near the substituted Na atom E, and the range of the lower charge density region extends largely along the boundary. There is an increase of the charge density between Al atoms in the bulk region, especially along the most-closely-packed lattice direction of fcc Al, i.e., $[1-10]$ direction, for example, between G and F, H and J.

The changes in the charge density distribution by Na segregation should be due to the following reasons. First, Al atom has 3 valence electrons while Na atom has one. The difference of the valence electrons should be the main reason for a decrease of the valence charge in the boundary. Secondly, the boundary expands because of Na segregation, which causes a further

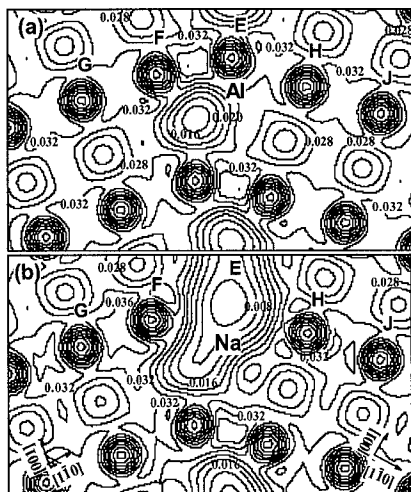


Figure 5. Contours of the valence charge density of the left half part of layer B in unit cell, in which Al atoms are replaced by Na atoms. The interval of the contours is 0.004/a.u. 3. F, G, E, H and J correspond to the atoms marked in figure 1. [1-10] and [001] indicated in the figure are lattice directions in the grains that the grain boundary is made up of. (a) no impurity (b) Na segregation

decrease of charge density in the boundary. The distance decrease between Al atoms in the bulk region causes the charge density between these Al atoms higher especially along [1-10] direction. Thirdly, the increase of the charge density in the bulk region of the unit cell is mainly caused by the contraction of Al layers due to the boundary expansion by Na segregation. Here it should be noted that the present contraction of the bulk Al layers is affected by the present condition of the fixed cell size. The size of x direction is fixed in order to save the computing time. If the size of x direction is relaxed, there will be a charge density increase only near the boundary but not the whole bulk region.

CONCLUSIONS

Na segregation in Al grain boundary causes the boundary expansion and the significant decrease of valence charge density around the impurity atoms and along the boundary plane. The significant decrease of the valence charge in the boundary means the formation of the weak bonding region between Al-Na atom at the boundary and between grains. Such weak bond regions may act as the origin of the crack or the preferential path of the cracks under stress. This should be the impurity-promoted embrittlement mechanism by Na segregation. It can be said that this is one kind of 'decohesion model'. However, as discussed above, there are some new features which is quite different from the previous examples of the 'decohesion model'. The low charge density part is between Al atoms and impurity atoms, and also between grains. It is different from Losch's model, for example, that the decohesion part is between the neighbor metal-metal atoms by the elements of IV, V and VI groups. Further calculation of 'First principles tensile test' based on Nielsen-Martin scheme[23] is being carried out.

ACKNOWLEDGEMENTS

The research is supported by the Science and Technology Agency of Japan as the joint research with National Research Institute for Metals (NRIM), and also partly supported by the Science and Technology Promotion of Japan.

REFERENCES

1. W. Losch, *Acta Metallurgica*, **27**, 1885 (1979)
2. C.L. Briant and R.P. Messmer, *Phil. Mag. B*, **42**, 569 (1980)
3. R.P. Messmer and C.L. Briant, *Acta. Metall.*, **30**, 457 (1982)
4. R. Haydock, *J. Phys. C: Solid State Phys.*, **14**, 3807 (1981)
5. L. Goodwin, R.J. Needs and V. Heine, *Phys. Rev. Lett.*, **60**, 2050 (1988)
6. L. Goodwin, R.J. Needs and V. Heine, *J. Phys: Condens. Matter*, **2**, 351 (1990)
7. H. Okada and M. Kanno, *Scripta Materialia* **37**, 781 (1997)
8. M.J. Mills and M.S. Daw, *Mat. Res. Soc. Symp. Prov.*, **183**, 15 (1990)
9. For example, W.E. Pickett, *Comput. Phys. Rep.*, **9** 115 (1989)
10. P. Hohenberg and W. Kohn, *Phys. Rev.* **136B**, 864(1964)
11. W. Kohn and L.S. Sham, *Phys. Rev.* **140A**, 1133 (1965)
12. J.P. Perdew and A. Zunger, *Phys. Rev. B*, **23**, 5048 (1981)
13. D.M. Bylander, L. Kleinman and S. Lee, *Phys. Rev. B*, **42**, 1394 (1990)
14. N. Troullier and J.L. Martins, *Phys. Rev. B*, **43**, 1993 (1991)
15. J. Hoekstra and M. Kohyama, *Phys. Rev. B*, **57**, 2334 (1998)
16. D.R. Hamann, M. Schluter and C. Chiang, *Phys. Rev. Lett.*, **43**, 1494 (1979)
17. G.B. Bachelet, D.R. Hamman and M. Schluter, *Phys. Rev. B*, **26**, 4199 (1982)
18. M.M. Dacorogna and M.L. Cohen, *Phys. Rev. B*, **34**, 4996, (1986)
19. S.G. Louie, S. Froyen and M.L. Cohen, *Phys. Rev. B*, **26**, 1738 (1982)
20. L. Kleinman and D.M. Bylander, *Phys. Rev. Lett.*, **48**, 1425 (1982)
21. P.K. Lam and M.L. Cohen, *Phys. Rev. B*, **24**, 4224 (1981)
22. Kittel C. *Introduction to Solid Physics*, seventh edition, (John Wiley & Sons, INC., 1996) pp. 23
23. O.H. Nielsen and R.M. Martin, *Phys. Rev. B*, **32**, 3780 (1985)

EFFICIENT TREATMENT OF FIXED AND INDUCED DIPOLAR INTERACTIONS

Celeste Sagui^(1,2) and Thomas Darden⁽¹⁾

⁽¹⁾Laboratory of Structural Biology, National Institute of Environmental Health Sciences,
Research Triangle Park, NC 27709

⁽²⁾ Department of Physics, North Carolina State University, Raleigh NC 27695

ABSTRACT

Fixed and induced point dipoles have been implemented in the Ewald and Particle-Mesh Ewald (PME) formalisms. During molecular dynamics (MD) the induced dipoles can be propagated along with the atomic positions either by iteration to self-consistency at each time step, or by a Car-Parrinello (CP) technique using an extended Lagrangian formalism. The use of PME for electrostatics of fixed charges and induced dipoles together with a CP treatment of dipole propagation in MD simulations leads to a cost overhead of only 33% above that of MD simulations using standard PME with fixed charges, allowing the study of polarizability in large macromolecular systems.

INTRODUCTION

Despite the unprecedented growth of computer power and algorithms in the last two decades, the accurate simulations of biologically active macromolecules remains a formidable challenge. The two main problems are the sheer size of the simulations (hundreds of thousands of atoms that need to be simulated for a few nanoseconds at least) and the limitations due to the accuracy of the empirical force fields. In classical MD, the description of the atoms is based on empirical potentials that combine short-range *n-body* terms, *intermediate-range* dispersive van der Waals forces, and *long-range* electrostatic interactions.

Since quantum mechanical approaches are prohibitively expensive for relevant simulations of biological systems, quantum mechanics (QM) methods have been combined with classical molecular mechanics (MM) in the so-called QM/MM methods in order to achieve an accurate quantum description of the biological active part and a computationally feasible but realistic description of the rest of the molecule and the solvent. An accurate treatment of electrostatics is crucial for the successful merging of QM and MM approaches. In fact, one of the major sources of errors in hybrid QM/MM methods is due to the presence of point charges in the QM/MM interface and in the MM region near the interface [1].

Electrostatic interactions outside the van der Waals surface of the molecule have traditionally been modeled using an atomic point charge representation of the molecular charge density. These charges are usually obtained by optimizing the fit to the molecular electrostatic potential. However, the error in the electrostatic interaction energy, due to the atomic point charge approximation, is now known to be significant. In fact, it has been pointed out that convergence to the quantum electrostatic potential requires the inclusion of higher order multipoles—up to hexadecapoles, (*i.e.*, the fourth-order expansion of the electrostatic potential) at the nuclear positions [2]. In addition to the permanent charge distribution, one also has to consider induction effects or polarization, caused by the distortion of the electron distribution of a particle in the electric field of all its neighbors. As in the case of permanent multipoles, accurate intermolecular interactions need high rank polarizabilities. The method of distributed multipole moments introduced by Stone [3] gives a multipolar representation

of the wavefunction valid outside the van der Waals surface, where each atom is assigned – apart from a point charge – a hierarchy of multipoles and polarizabilities. Currently many groups are seeking to incorporate some form of polarization into empirical macromolecular force fields. Usually these attempts involve either re-arrangement of point charges or induction of point dipoles or both, although some attempts in smaller systems include quadrupolar responses. Ultimately, the success of these methods depends on the availability of methods for efficient evaluation of the new terms in macromolecular systems.

In our work [4], we have implemented the dipolar interactions in the Ewald model [5] and in the PME method [6]. We have also included induced dipoles via two computational methods: the traditional iterative method, where the constitutive equation for the induced dipoles is iterated until convergence; and the CP method, which is an efficient dynamical scheme where the induced dipoles are treated as additional dynamical variables [7]. We have compared the relative accuracy and efficiency of these methods, and studied the long-time behavior for a system of waters governed by a representative polarizable water-water potential (RPOL) [8] having charges and induced dipoles at all three atomic sites.

THEORY

Suppose there are N point charges q_i and N point dipoles \mathbf{p}_i at positions \mathbf{r}_i , with $i = 1, 2, \dots, N$, within the unit cell, with $q_1 + q_2 + \dots + q_N = 0$. The edges of the unit cell are denoted by vectors \mathbf{a}_α , $\alpha = 1, 2, 3$, which need not be orthogonal. The conjugate reciprocal vectors \mathbf{a}_α^* are defined by the relations $\mathbf{a}_\alpha^* \cdot \mathbf{a}_\beta = \delta_{\alpha\beta}$, for $\alpha, \beta = 1, 2, 3$. The charges and dipoles interact with each other, and with their periodic images at positions $\mathbf{n} = n_1 \mathbf{a}_1 + n_2 \mathbf{a}_2 + n_3 \mathbf{a}_3$, for all such triples with n_1, n_2, n_3 not all zero. The electrostatic energy of the unit cell is:

$$E(\mathbf{r}_1, \dots, \mathbf{r}_N) = \frac{1}{2} \sum_{\mathbf{n}}' \sum_i \sum_j (q_i + \mathbf{p}_i \cdot \nabla_i)(q_j - \mathbf{p}_j \cdot \nabla_j) \left(\frac{1}{|\mathbf{r}_i - \mathbf{r}_j + \mathbf{n}|} \right) \quad (1)$$

where the prime in the outer sum indicates that terms with $i = j$ and $\mathbf{n} = 0$ are omitted.

As in the usual Ewald or PME treatment of Coulombic interactions under periodic boundary conditions, this sum is split into a short-range term which is handled in the direct sum, plus a long-range, smoothly varying term, handled in the reciprocal sum by means of Fourier methods. In molecular systems, corrections are introduced to account for the “masked pairs”, which are atom pairs whose nonbond interactions should not be calculated, since they are accounted for by other terms in the potential. For simplicity, we will omit these corrections in this presentation. Similarly the self-energy, which is the reciprocal part of the interactions of the charge, dipole pairs with themselves, must be removed. The electrostatic energy can then be written as a sum of three terms, the direct, the reciprocal, and the self terms: $E = E_{dir} + E_{rec} + E_{self}$. These are given by:

$$\begin{aligned} E_{rec} &= \frac{1}{2\pi V} \sum_{\mathbf{m} \neq 0} \frac{\exp(-\pi^2 \mathbf{m}^2 / \beta^2)}{\mathbf{m}^2} \sum_{i=1}^N \sum_{j=1}^N (q_i + \mathbf{p}_i \cdot \nabla_i)(q_j + \mathbf{p}_j \cdot \nabla_j) \exp(2\pi i \mathbf{m} \cdot (\mathbf{r}_j - \mathbf{r}_i)) \\ E_{dir} &= \frac{1}{2} \sum_{\mathbf{n}}' \sum_{i,j=1}^N (q_i + \mathbf{p}_i \cdot \nabla_i)(q_j - \mathbf{p}_j \cdot \nabla_j) \frac{\text{erfc}(\beta |\mathbf{r}_j - \mathbf{r}_i + \mathbf{n}|)}{|\mathbf{r}_j - \mathbf{r}_i + \mathbf{n}|} \\ E_{self} &= -\frac{\beta}{\sqrt{\pi}} \sum_i^N \left(q_i^2 + \frac{2\beta^2}{3} |\mathbf{p}_i|^2 \right) \end{aligned} \quad (2)$$

where the structure factor $S(\mathbf{m})$ is given by:

$$S(\mathbf{m}) = \sum_{j=1}^N [q_j + \mathbf{p}_j \cdot \nabla_j] \exp(2\pi i \mathbf{m} \cdot \mathbf{r}_j) = \sum_{j=1}^N [q_j + 2\pi i \mathbf{p}_j \cdot \mathbf{m}] \exp(2\pi i \mathbf{m} \cdot \mathbf{r}_j) \quad (3)$$

In these equations, the reciprocal lattice vectors are defined by $\mathbf{m} = m_1 \mathbf{a}_1^* + m_2 \mathbf{a}_2^* + m_3 \mathbf{a}_3^*$ with m_1, m_2, m_3 integers not all zero and the volume of the unit cell is $V = \mathbf{a}_1 \cdot \mathbf{a}_2 \times \mathbf{a}_3$. To make the sum in E_{dir} in Eq. (2) more tractable, Smith [5] defines generalized source functions which satisfy a recursion relation. These functions are very useful for the efficient computation of higher order multipoles and the corresponding fields and forces [4]. The electrostatic field and force on atom i at position \mathbf{r}_i are computed as $\mathbf{E}(\mathbf{r}_i) = -\nabla_i \phi(\mathbf{r}_i)$ and $\mathbf{F}(\mathbf{r}_i) = -\nabla_i E(\mathbf{r}_i) = -(q_i + \mathbf{p}_i \cdot \nabla_i) \nabla_i \phi(\mathbf{r}_i)$. An important difference with the monopolar case is that, for non-zero dipoles, the force is no longer necessarily parallel to the field. The electric field has a self term or “self field”, given by $\mathbf{E}_{self}(\mathbf{r}_i) = (4\beta^3/3\sqrt{\pi})\mathbf{p}_i$.

The PME method [6] approximates the electrostatic structure factors by replacing the complex exponentials appearing in the structure factor by appropriate linear combinations of their values at nearby grid points. The resulting trigonometric sums over grid points can be rapidly evaluated by the Fast Fourier Transform (FFT). The method uses Cardinal B-splines to interpolate the complex exponentials. This leads to approximate structure factors and hence approximate reciprocal energies E_{rec} which can be analytically differentiated to give the reciprocal forces and stress tensors. Since this method has been described in detail in the literature [6] and the mathematical formalism resulting from the addition of dipolar interactions is somehow complex, we refer the reader to ref. [4] for mathematical details.

Polarization is generally introduced into empirical force fields through inducible point dipoles. Each total dipole \mathbf{p}_i can be written as the sum of a *permanent* dipole \mathbf{s}_i and an *induced* dipole \mathbf{d}_i , $\mathbf{p}_i = \mathbf{s}_i + \mathbf{d}_i$. The induced polarization is a many-body problem, where the induced dipoles all depend on each other. If α_i is the polarizability of site i , the induced dipole \mathbf{d}_i at position \mathbf{r}_i is given by $\mathbf{d}_i = \alpha_i \mathbf{E}_i^T = \alpha_i [\mathbf{E}_i^0 + \sum_{j=1, j \neq i}^N \mathbf{T}_{ij} \cdot \mathbf{d}_j]$, where \mathbf{E}_i^T is the total electric field at \mathbf{r}_i , which is the sum of an “external” field \mathbf{E}_i^0 (due to charges, permanent dipoles and any other applied field) at \mathbf{r}_i , and an interaction field that describes, through the dipole interaction tensor \mathbf{T}_{ij} , the net effect of all the other induced dipoles \mathbf{d}_j on dipole \mathbf{d}_i . Since direct matrix inversion is too expensive for macromolecular simulations, a common approach is to solve the equation iteratively until self-consistency is achieved for each time step. We have implemented this approach for both Ewald and PME methods. In our algorithm, an initial guess for the dipole i at time t is provided using a Taylor’s expansion and then iteration in the computation of fields is applied until convergence in the induced dipoles is achieved. In the simulations of water reported below, we find that a very small tolerance, of at most $10^{-6}D$, is required for energy conservation. Once the water is equilibrated, an average of 6 iterations is necessary to achieve such a tolerance.

As a cheaper alternative to the iteration procedure, we have implemented a Car-Parrinello (CP) method. The original CP method [9] is used in electronic density-functional MD, where the system is assumed to be in its electronic ground state, while the electrons follow the nuclear motion adiabatically. The fluctuations of the electronic density around the minimum energy do not exert a systematic drag force on the nuclei. The CP method can be extended to classical systems to replace the expensive iterative procedure by a much more efficient

dynamical method [7]. The method consists of defining an extended Lagrangian, where the induced dipoles are treated as additional dynamical variables:

$$L = \frac{1}{2} \sum_{i=1}^N m_i |\dot{\mathbf{r}}_i|^2 + \frac{1}{2} \sum_{i=1}^N M_i |\dot{\mathbf{d}}_i|^2 - \left[U_0(q^N, \mathbf{s}^N) - \sum_{i=1}^N \mathbf{d}_i \cdot \mathbf{E}_i^T + \frac{1}{2} \sum_{i=1}^N \frac{|\mathbf{d}_i|^2}{\alpha_i} \right] \quad (4)$$

Here, the first two terms are the kinetic energy (M_i is the mass associated with the dipoles), and the expression in brackets is the electrostatic potential energy; $U_0(q^N, \mathbf{s}^N)$ only depends on the N charges q_i and N permanent dipoles \mathbf{s}_i , and the last term represents the polarization energy. Application of the Lagrangian equations of motion leads to $M_i \ddot{\mathbf{d}}_i = -\mathbf{d}_i/\alpha_i + \mathbf{E}_i^T$. The object of the CP scheme is to keep the dipoles near the minimum energy configuration (which changes as the nuclei evolve). Thus the dipoles must be at a low temperature but able to move rapidly to adjust to the new minima. These conditions are met in the limit of zero dipolar mass. In practice the dipole mass is an adjustable parameter of the model. This mass should be chosen low. For time steps of 1 fs, we have chosen $M \sim 0.3 \text{ kcal} \cdot \text{ps}^2 / \text{Debye}^2$. Decreasing the mass after a certain value may produce instabilities. Increasing the dipole mass increases stability, but also increases the effective temperature of the dipoles and hence the coupling with the atomic degrees of freedom. We have tested the energy conservation of this scheme (see below) and find that a very slow heating, over tens to hundreds of picoseconds, appears inevitable. Thus for production runs we recommend separately and loosely coupling the dipoles and atomic degrees of freedom to external baths.

RESULTS

We have incorporated the algorithmic formalism described in the previous section into the sander module of AMBER6 and tested the implementation with several simulations of RPOL [8] waters. We have also utilized a number of other polarizable models including polarizable DNA and proteins in water. The results assessing the relative performance of PME versus Ewald and of CP versus the self-consistent iteration procedure are consistent with those obtained using the other models and thus appear generally applicable.

The relative rate of convergence of the direct and reciprocal sums, E_{dir} and E_{rec} depends on the cutoff for the direct sum and on the constant β . Increasing β speeds up the convergence of E_{dir} and slows down the convergence of E_{rec} . It is customary to choose a fixed β independent of the system size which allows a fixed cutoff (e.g. 9 Å) in E_{dir} , thereby reducing its computation to order N . This choice forces the number of reciprocal vectors in the Ewald method to grow linearly with simulation cell volume (i.e. as N) in order to meet the requirement on the reciprocal space tolerance so that the cost of the E_{rec} grows as N^2 . In the PME method, however, the use of 3DFFT's on a grid reduces this calculation to order $N \log(N)$. We have carried out extensive accuracy tests of the PME method against the Ewald method by comparing the errors in the reciprocal force, field and energy. The accuracy of the PME method depends on the mesh size for the computation of the 3DFFT's and on the order of interpolation p for the B-splines. For instance, after equilibration of a 38.56 Å cubic box of 1916 RPOL waters with a standard value $\beta = 0.35 \text{ Å}^{-1}$ and grid side L the relative root-mean-square force errors were 2.1×10^{-4} ($L = 40 \text{ Å}$, $p = 4$); 4.4×10^{-5} ($L = 40 \text{ Å}$, $p = 5$); 1.0×10^{-5} ($L = 40 \text{ Å}$, $p = 6$); and 1.2×10^{-6} ($L = 54 \text{ Å}$, $p = 6$).

We have investigated the energy conservation along an MD trajectory as a function of the method used to calculate the induced dipoles. A box of size 18.67 Å containing 216

waters was equilibrated at 300 K using the iterative method for the induced dipoles. The equilibrated configuration was then taken as the initial configuration for 1 ns microcanonical ensemble simulations using the sander module of AMBER 6. Figure 1 (left) shows the results of a series of simulations using the PME method with an $(18 \text{ \AA})^3$ grid and 6th order interpolation. From the figure it is clear that a tight convergence (10^{-6} Debye or below) must be employed with the iterative method to prevent catastrophic results on the nanosecond timescale. Even with a tolerance of $10^{-6}D$, there is a drift in the total energy, of about 4 kcal at the end of the 1 ns simulation. Next, we assessed the results of applying the CP method. At the end of the 1 ns simulation, time steps of 1 fs and 0.5 fs produce an increase in energy of approximately 6.5 and 5 kcal, respectively. The results were the same for both Ewald and PME methods. Thus we recommend the use of weak thermostating for the CP method, with separate thermostats for nuclear and dipolar degrees of freedom.

Finally, we have plotted the CPU time (on an SGI Octane, 225 MHz R10000, 2MB secondary cache, 128 MB memory) required to perform the Ewald and the PME calculations as a function of system size, which was varied to keep a density of 0.99 g/cm^3 at 300 K. The tolerance for the iterative method was set at $10^{-6}D$, while the mass of the dipoles in the CP method was 0.33. Figure 1 (right) shows the average CPU time (in seconds) needed for one step of a microcanonical MD simulation, using the Sander module of AMBER6. The time includes the cost of updating the extended Verlet list, as well as that for constraining the rigid water geometry. The CPU time for the Ewald method grows as N^2 , and therefore the cost becomes prohibitive for large systems. On the other hand, the time needed for the PME method grows as N over this range of sizes. Finally, we notice that the iterative method is about 6 times more expensive than the CP method. The CP method is 1.25-1.30 times more expensive than the PME method for charges alone. The direct sum, including dipoles, is about 1.4 times more expensive than the direct sum for charges alone, whereas the cost overhead of including dipoles in the reciprocal sum is negligible.

CONCLUSIONS

The PME method, combined with a CP propagator using a 1 fs time step in MD was able to reproduce the properties calculated by full Ewald summation with converged dipole iteration. The energy conservation for the PME-CP method was excellent over the multi picosecond time scale, however a slow heating occurred on the nanosecond time scale, and therefore a gentle, separate thermostating of dipolar and nuclear degrees of freedom is recommended. The computational overhead in the PME method due to the dipoles is mainly manifested in the direct sum, whereas there is a negligible overhead in the reciprocal sum calculation. Overall the calculation of electrostatic energies, fields and forces due to a system of point charges and dipoles at each atom costs about 33% more than that of atomic charges alone at a similar level of accuracy. Since the overhead of the CP propagation is negligible, the combination of an PME treatment of electrostatics and a CP propagation of dipoles allows MD simulations using force fields that include dipole polarizability with only a modest cost overhead over those using a fixed atomic charge representation of the molecular electrostatics. At present we are working on extending this formalism all the way to hexadecapoles. We believe that this accurate treatment of electrostatics will play a crucial role for the smooth merging of the QM and MM regions in a multiscale approach.

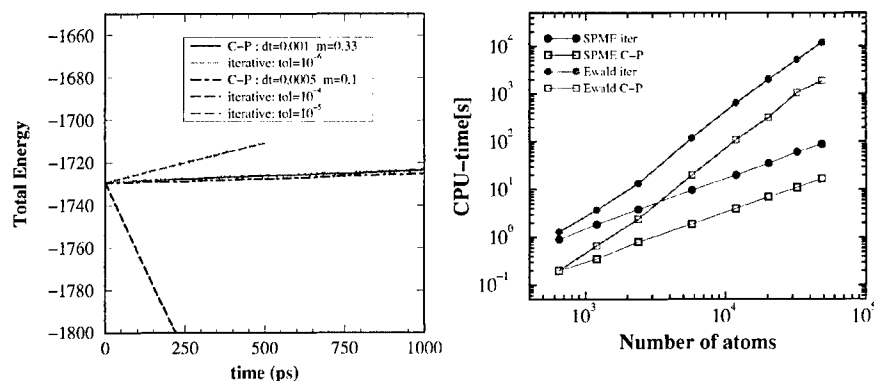


Figure 1. Left: Total energy as a function of time in NVE simulations with the PME method. Dipoles are propagated by either iterating to convergence below a tolerance, or by using the CP method. Right: CPU time (225MHz R10000 1proc) per MD time step as a function of system size, sum method (PME or Ewald), and method of dipole propagation (iteration to 10^{-6} Debye or CP).

REFERENCES

1. N. Reuter, A. Dejaegere, B. Maigret, and M. Karplus, *J. Phys. Chem. A* **104**, 1720 (2000).
2. S. Price, in *Reviews in Computational Chemistry* **14**, K. Lipkowitz and D.B. Boys editors, 225 (2000).
3. A. J. Stone, *The Theory of Intermolecular Forces* (Clarendon Press-Oxford, New York, 1996).
4. A. Toukmaji, C. Sagui, J. Board, and T.A. Darden, *J. Chem. Phys.*, in press December 2000.
5. W. Smith, *CCP5 Information Quarterly* **4**, 13 (1982).
6. U. Essmann, L. Perera, M.L. Berkowitz, T. Darden, H. Lee, and L.G. Pedersen, *J. Chem. Phys.* **103**, 8577 (1995).
7. M.-L. Saboungi, A. Rahman, J. W. Halley, and M. Blander, *J. Chem. Phys.* **88**, 5818 (1988); M. Sprik and M. Klein, *J. Chem. Phys.* **89**, 7556 (1988).
8. L. Dang, *J. Chem. Phys.* **97**, 2659 (1993).
9. R. Car and M. Parrinello, *Phys. Rev. Lett.* **55**, 2471 (1985).

**Mesoscopic Studies:
Thin Films and Layers**

Unstable Motion of an Edge Dislocation in a Solute Atom Atmosphere Studied by Kinetic Monte Carlo Simulations

X. M. Gu and Y. Q. Sun

Department of Materials Science and Engineering
University of Illinois, Urbana, IL 61801, USA

ABSTRACT

The discontinuous yielding of a model material, which contains an edge dislocation moving in the atmosphere of solute atoms, is studied by Kinetic Monte Carlo (KMC) simulations. The stress-strain curves for a constant strain rate were obtained at different temperatures. The dislocation moves discontinuously, producing three types of serrated yielding behavior at intermediate temperatures for different imposed strain rates. Positive dependence of flow stress on temperature and negative strain rate sensitivity were observed in the regime of discontinuous motion. The present model, though highly simplified and not taking into account the collective behaviors of dislocations in real materials, does exhibit some of the basic features observed in experiments.

INTRODUCTION

Discontinuous yielding, commonly referred to as the Portevin-Le Chatelier (PLC) effect, occurs in many dilute alloys within certain regimes of temperature and strain rate. Such an effect, characterized by temporal and spatial inhomogeneity in slip, has been investigated extensively by both theoretical and experimental studies [1-9]. One of the most successful theories, first proposed by Penning [1] and later developed by Kubin, Estrin and their coworkers [2-3], explains the temporal inhomogeneity by phenomenological descriptions of deformation with a constitutive equation. A condition for temporal inhomogeneity, according to this theory, is the existence of negative strain rate sensitivity. The physical mechanisms of the negative strain rate sensitivity are based on the dynamic interaction between diffusing solute atoms and mobile dislocations that are temporarily arrested by localized obstacles [6-7]. Later developments have taken into account the effect of strain softening by using the second derivative of local strain as an additional term in the constitutive equation [3,8], and further progress has been made by introducing a non-linear theory [5,9].

In the present paper, Kinetic Monte Carlo simulation is used to study the motion of an edge dislocation moving in a solute atmosphere without explicit assumptions about strain rate sensitivity, work hardening or work softening. Nor are there strong localized obstacles in the simulation. The Monte Carlo method has been used recently by Wang *et al.* [10] to study the behavior of an edge dislocation interacting with solute atoms under a constant stress. We study a more relevant situation, where the net machine strain rate, consisting of elastic and plastic contributions, is kept constant, and the stress and dislocation velocity are both allowed to vary under the constraint of the constant net strain rate. The approach therefore mimics the usual tensile test. Although the model is a highly simplified one, it is shown to possess some of the basic features found in experiments.

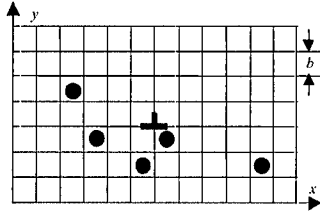


Figure 1. A schematic illustration of the simulation system consisting of an edge dislocation moving in a square lattice containing solute atoms. The lattice constant is equal to Burgers vector h

SIMULATION MODEL

The simulation system, Fig. 1, consists of a two-dimensional square lattice, an edge dislocation jumping on lattice sites in the x direction, and solute atoms that move between the interstitial sites. The Burgers vector h is equal to the lattice constant. A randomization procedure is applied, where once a solute atom moves out of the simulation box from one side it reenters randomly from the opposite side. This randomization process maintains a random distribution of solute atoms outside the stress field of the dislocation.

The interaction between solute atoms and the dislocation is only via the stress field of the dislocation, giving an interaction energy [11]:

$$E_d(x_i, y_i; x_d, y_d) = \mu b^4 \beta (y_i - y_d) / [(x_i - x_d)^2 + (y_i - y_d)^2] \quad (1)$$

where μ is the shear modulus, β is a dimensionless constant, and $\{x_i, y_i\}$, $\{x_d, y_d\}$ are the coordinates of the i th solute atom and the dislocation respectively. Thus the total interaction energy between the dislocation and the solute atoms is:

$$E_d(x_d, y_d) = \sum_i^N E_d(x_i, y_i; x_d, y_d) \quad (2)$$

where N is the number of solute atoms in the stress field of the dislocation. Under a constant machine strain rate $\dot{\gamma}_m$, the machine condition equation at time t is:

$$\dot{\gamma}_m \cdot t = \tau(t) / \mu + \Delta\gamma \cdot x_d(t) \quad (3)$$

where $\tau(t)$ is the applied shear stress, $x_d(t)$ is the x coordinate of the dislocation, and $\Delta\gamma$ is the plastic strain due to the dislocation jumping across one lattice site. The stress on the dislocation, from equation (3), is:

$$\tau(t) = \mu(\dot{\gamma}_m \cdot t - \Delta\gamma \cdot x_d(t)) \quad (4)$$

A main objective of this work is to test a major premise in the literature, namely the dislocations must be arrested at strong permanent obstacles in order to produce discontinuous yielding. Both deterministic and probabilistic modes of dislocation motion can be used, though probabilistic movement is deemed closer to reality. The key element is the effects of diffusing solute atoms on the movements of dislocations; the differences between deterministic and probabilistic modes would not change the final results. In this paper, the dislocation moves in the x direction of the lattice probabilistically. The dislocation jump probabilities may be calculated based on several different mechanisms that would operate in real systems, but their choice would not affect qualitatively the conclusions. For the sake of simplicity, we assume that the dislocation moves through nucleating a double kink with a critical width l_c . The critical width of the kink pair depends on stress via [11]:

$$l_c = (8\pi\tau/\mu)^{-1/2} b \quad (5)$$

Thus, the rate of dislocation jumping in the direction of the applied shear stress is:

$$\Gamma_{d+} = \frac{1}{2} \nu_d \exp\left(-[(\tau_{p-n} - \tau)b^2 l_c - \frac{1}{2} \cdot \Delta E_d^+]/kT\right) \quad (6)$$

where τ_{p-n} is the Peierls-Nabarro stress, ν_d is the attempt frequency of dislocation, and ΔE_d^+ is the change of interaction energy with solute atoms due to the jumping of the dislocation. This equation implicitly assumes that the interstitial sites along dislocation line are not completely segregated by solute atoms. In order to prevent equation (5) from diverging at low stresses, we assume a maximum value for l_c at $20b$, a reasonable value for low stress condition [11].

Similarly, the jumping rate of dislocation against the applied shear stress is:

$$\Gamma_{d-} = \frac{1}{2} \nu_d \exp\left(-[(\tau_{p-n} + \tau)\mu b^3 l_c - \frac{1}{2} \cdot \Delta E_d^-]/kT\right) \quad (7)$$

Following the standard Monte Carlo n-fold way procedure [13] (also known as the residence time algorithm), the average time for dislocation to make a successful jump is:

$$\Delta t_d = 1/(\Gamma_{d+} + \Gamma_{d-}) \quad (8)$$

The solute atoms are allowed to move in four directions. Let ΔE_j^i be the energy change for the j th solute atom jumping one step in the i th direction. The jumping rate in that direction is:

$$\Gamma_j^i = \frac{1}{4} \nu_a \exp\left(-[Q_a - \frac{1}{2} \cdot \Delta E_j^i]/kT\right) \quad (9)$$

where Q_a is the activation energy for the diffusion of solute atoms, and ν_a is the attempt frequency of solute atoms. Therefore, the average time for solute atoms to make one successful jump is:

$$\Delta t_a = 1 / \sum_{j=1}^N \sum_{i=1}^4 \Gamma_j^i \quad (10)$$

The simulation is organized as follows: First, Δt_a and Δt_d are calculated from the jumping rates of solute atoms and the dislocation; t_a and t_d are respectively the sums of the time taken by successful dislocation jumps and solute atoms jumps. Second, if $t_a + \Delta t_a < t_d + \Delta t_d$, a solute atom, selected by the residence time algorithm, makes a jump, and then $t = t_a$, with t being the system time; or if $t_a + \Delta t_a > t_d + \Delta t_d$, the dislocation makes one jump, and $t = t_d$. Third, dislocation coordinate $x_d(t)$, system time t and equation (4) are used to calculate the shear stress τ , then return to first step.

Before imposing a constant strain rate, the system is annealed at the test temperature to allow a full relaxation and formation of a solute atom atmosphere. All the simulation results are obtained for $\mu b^3 = 7.8eV$, $\tau_{p-n} = 5 \times 10^{-4} \mu$, $\beta = 0.071$, $Q_a = 0.5eV$, $\nu_a = 10^{13} s^{-1}$, and $\nu_d = 10^{10} s^{-1}$. These parameters, though reasonable, are not meant to represent a particular material.

RESULTS

A stress-strain curve with discontinuous yielding is shown in Fig. 2. We define point A and B as upper and lower yielding points respectively. Since there is no overall work hardening

mechanism in the simulation, we define the flow stress as the average stress after the lower yielding point.

The effects of temperature on stress-strain curves at a constant strain rate are shown in Fig. 3. At low and high ends of the temperature range studied, the stress-strain curves are smooth after the yielding point. But at intermediate temperatures, discontinuous yielding occurs as manifested by serrated stress-strain curves. As shown in Fig. 3, three types of serration can be distinguished. We make use of the traditional taxonomy of PLC bands that classifies them into types A, B and C [13].

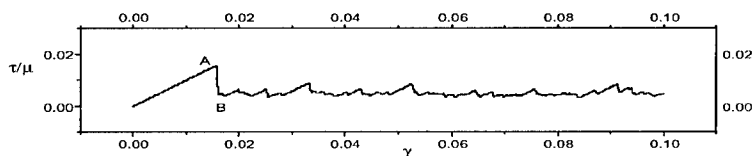


Figure 2. A stress-strain curve with serration ($\dot{\gamma}_m = 10^{-1.5} s^{-1}$, $T=344$ k)

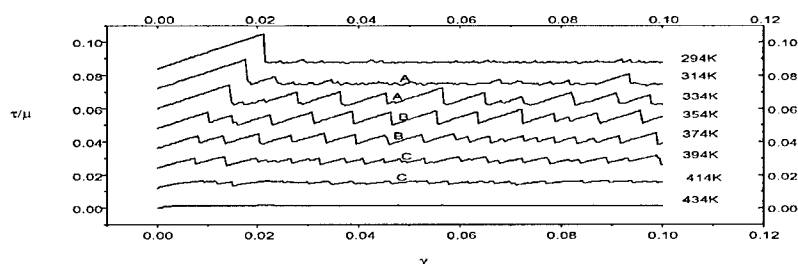


Figure 3. Stress strain curves at different temperatures ($\dot{\gamma}_m = 10^{-3} s^{-1}$). The offset of the curves in the ordinate direction is 70%.

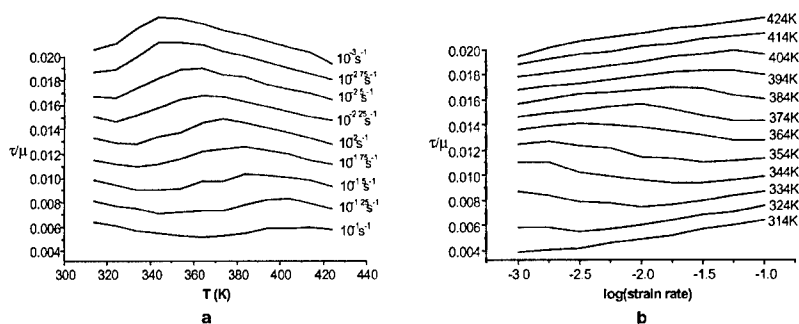


Figure 4. Temperature and strain rate dependence of the flow stress. The domain of abnormal flow stress is identical with that of negative strain rate sensitivity. The offset of curves in the ordinate direction is 100%.

As shown in Fig. 4, besides the three types of serration, positive temperature dependence of flow stresses and negative strain rate sensitivities are also found in the strain rate and temperature regimes where Type-B serration occurs. The region with abnormal flow stress, which is identical with that of negative strain rate sensitivity in temperature and strain rate domains, shifts to higher strain rate with increasing temperature.

Compared with experimental data [13], some of the basic features of serrated yielding in experiments are exhibited by the present simple model. The usual explanation for the experimentally observed serrated yielding relies on the presence of both diffusing solute atoms and permanent obstacles, such as particles or forest dislocations [6-7]. The role of the permanent obstacles is to temporarily arrest the dislocation in order for the solute atoms to diffuse back to the dislocation and pin the dislocation. The present simple model contains diffusing solute atoms, but there are no strong obstacles to the dislocation. The simulation results show that the motion of an edge dislocation in the presence of fast diffusing solute atoms is intrinsically discontinuous.

An advantage offered by the present simple model is that the plastic strain rate can be directly correlated with the motion of the dislocation. The stress-strain curves in Fig. 3, including the three types of serration, can be understood on the basis of the machine equation (4). According to equation (4), the rises and falls of the stress result from the plastic strain relative to the imposed constant machine strain rate. The stress on the dislocation drops when the plastic strain rate due to dislocation motion is greater than the machine strain rate. If the plastic strain rate due to dislocation motion is less than the machine strain rate, the stress increases. If the dislocation is stationary, the stress increases linearly with a gradient equal to the shear modulus. When the plastic strain-rate due to dislocation motion is equal to the machine rate, the stress is constant.

As shown in Type-B serration in Fig. 3, one stress peak follows another immediately, meaning that the dislocation switches between total stoppage and fast motion. While in Type-A, the peaks are separated by regions where the stress is constant, meaning that the dislocation moves at a constant speed (equal to the imposed machine rate) between the switches. When the temperature is increased, the region of constant stress in Type-A becomes progressively shorter, leading to Type-B when the regions of constant stress disappear completely. This shows that at low temperatures, where type-A serration occurs, the dislocation first slows down to and moves at the velocity imposed by machine rate before it is pinned by the solute atoms. With increasing temperature, where Type-B occurs, the dislocation is captured by solute atoms before it slows down to the velocity imposed by machine rate. Therefore, the occurrence of types A and B serration and their mutual transition with temperature change are consistent with the effect of temperature on the diffusion of solute atoms. At the temperature region of Type-B serration, the higher the temperature the earlier the dislocation is captured by the solute atoms. So, the stress-strain curve will be shifted up by increasing temperature, leading to a flow stress that increases with increasing temperature in serration B.

The uphill slope of the stress-strain curves with Type-C serration is less than the shear modulus, meaning, according to equation (4), the dislocation begins to move before it is fully released from the solute atmosphere. This is due to the high mobility of solute atom at high temperatures. At still higher temperatures when the thermal energy is comparable with the binding energy between solute atoms and the dislocation, a stable atom atmosphere can no longer exist, and then serration C disappears from stress-strain curves.

As shown above, the temporal inhomogeneity can be studied by the present simple model. Some of the experimental features can in this model be accounted for by the simple process of dislocation breaking away from, and recaptured by, the solute atoms without involving strong permanent obstacles. It is obvious that the present simulation is unable to take into account the collective dislocation phenomena that lead to the formation of strain localization and PLC bands. However, the types of serration obtained within the present simulation bear some analogy with the types of PLC bands found in bulk specimens. The reason for this is simply that if the motion of dislocations is strongly correlated in time, the collective behavior may look like that of a single 'super-dislocation'. The situation corresponding to spatial inhomogeneity or strain localization has also been studied by introducing more dislocations into the simulation system. Preliminary results, to be presented in a future paper, show that, in the temperature and strain rate regime of serrated yielding, only one of the multiple dislocations present moves at a given time.

CONCLUSIONS

The motion of a single edge dislocation in the presence of diffusing solute atoms under the constraint of a constant machine strain-rate is intrinsically discontinuous. This result is shown in this work by Kinetic Monte Carlo simulations of a simple system without strong local obstacles. With increasing temperature three types of serration are observed on stress-strain curves. Negative strain rate sensitivity and positive temperature dependence of flow stress were found in the regime of discontinuous flow.

ACKNOWLEDEMENTS

We thank the National Science Foundation (grant DMR 98-74854 CAR) and the Air Force Wright Laboratory (grant AF UES S-157-000-004) for support.

REFERENCES

1. P. Penning, *Acta metall.*, **20**, 1169 (1972).
2. L. P. Kubin and Y. Estrin, *Acta metall.*, **33**, 295 (1985).
3. M. A. Lebyodkin, Y. Brechet, Y. Estrin and L. P. Kubin, *Phys. Rev. Lett.*, **74**, 4758 (1995).
4. Z. S. Basinski, M. S. Szczerba and J. D. Embury, *Phil. Mag., A*, **76**, 743 (1997).
5. S. Rajesh and G. Ananthakrishna, *Phys. Rev. E*, **61**, 3664 (2000).
6. P. G. McCormick, *Acta metall.*, **20**, 351 (1972).
7. A. H. Cottrell, *Dislocations and Plastic Flow in Crystals*, Clarendon Press, Oxford (1953).
8. H. M. Zbib and E. C. Aifantis, *Scripta. metall.*, **22**, 1331 (1988).
9. G. Ananthakrishna and D. Sahoo, *J. Phys. D*, **15**, 2081 (1981).
10. Y. Wang, D. J. Srolovitz, J. M. Rickman and R. Lesar, *Acta mater.*, **48**, 2163 (2000).
11. J. P. Hirth and J. Lothe, *Theory of Dislocations*, 2nd ed. (Kridger Publishing Company, Malabar, Florida, 1982).
12. A. B. Bortz, M. H. Kalos and J. L. Lebowitz, *J. Comput. Phys.*, **17**, 10 (1975).
13. A. S. Keh, Y. Nakada and W. C. Leslie, *Dislocation Dynamics*, ed. Alan R. Rosenfield, McGraw-Hill New York, 1968.

Coarse Slip Bands in a Single-Crystalline Aluminum Alloy

Seung-Yong Yang, Xianghong Li and Wei Tong¹

Department of Mechanical Engineering, Yale University, New Haven, CT 06520-8284, USA

ABSTRACT

The effect of crystal orientation on the discontinuous deformation and coarse slip bands in aluminum single crystals has been investigated by finite element simulation. The numerical analysis is based on a rate-dependent crystal plasticity model recently formulated by us with modifications made here that explicitly accounts for the *three* strain hardening stages and the effect of the interaction of dislocations and alloying elements on setting the hardening rules on the *individual* slip systems of the aluminum alloy crystal. The dependence of the magnitude of the serrations of tensile stress-strain curves on orientation and its evolution over the three strain hardening stages of Al-0.3%Mg single crystals observed experimentally has been successfully explained in this investigation.

INTRODUCTION

Plastic deformation in crystals is inherently nonuniform in a microscopic sense. It is common for plastic flow in crystals deformed to finite plastic strains to become localized macroscopically also in the form of a shear band. Such local deformations influence the mechanical properties and lead to poor surface finishing.

Various experiments have been carried out on different materials in an attempt to explore the relation between the characteristics of moving deformation band and the experimental conditions and material properties. Propagating deformation bands on specimen surfaces and serrations in the force-displacement curves were observed in steel and aluminum alloys [1, 2]. Estrin and Kubin investigated discontinuous yielding and the propagation of bands of localized plastic strain (the Portevin-Le Chatelier effect). It is accepted that PLC effect is consequence of dynamic strain ageing (DSA) [3]. An increase in the flow stress is caused by the local concentration of solute atoms at temporarily arrested dislocations.

A high accuracy whole-field strain measurement technique was developed to directly measure the whole-field localized deformation band patterns of the aluminum sheet metals during uniaxial tensile test [4]. A crystal plasticity model [5] and a dynamic strain-aging model [3] were recently combined to account for the interaction between solute atoms and mobile dislocations on crystal slips in a continuum perspective [6] to explain the formation of the coarse slip bands in aluminum alloys. As a continuation of our constitutive modeling and finite element simulation efforts, the model has been further modified here in terms of two important aspects: namely, the dynamic strain aging effect on each *individual* slip system and the *three* strain hardening stages are explicitly incorporated for Al-Mg crystals. A summary of the modified crystal plasticity model is given and numerical simulation results of the serrated plastic flows of single crystals of Al-Mg alloys are discussed and compared with experimental observation [8] in this paper.

CONSTITUTIVE EQUATIONS

The corotational Cauchy stress rate on axes rotating with the material is given by

$$\overset{\nabla}{\boldsymbol{\sigma}} = \mathbf{C} : \mathbf{D}^e - \boldsymbol{\sigma}(\mathbf{I} : \mathbf{D}^e) + \boldsymbol{\sigma}(\mathbf{W} - \mathbf{W}^e) - (\mathbf{W} - \mathbf{W}^e)\boldsymbol{\sigma} \quad (1)$$

where \mathbf{C} is the tensor of elastic moduli, \mathbf{I} is the identity tensor, \mathbf{D}^e is the elastic stretching rate, and \mathbf{W} , \mathbf{W}^e are the total and elastic spins, respectively [5].

We assume that there are N slip systems in a single crystalline solid. Based on the Schmid law, the slipping rate $\dot{\gamma}^\alpha$ of the α slip system in the rate dependent solid is determined by the corresponding resolved shear stress in the reference configuration, τ^α , and dislocation-solute interaction as

$$\dot{\gamma}^\alpha = \dot{\alpha}_0 \frac{\tau^\alpha}{g^\alpha} \left| \frac{\tau^\alpha}{g^\alpha} \right|^{n-1} P(C_s^\alpha), \quad (2)$$

where the constant $\dot{\alpha}_0$ is the reference strain rate, g^α is the yield strength of slip system α , and P is a function describing the effect of point defects on the motion of dislocations in the slip system α . C_s^α is the solute concentration on the mobile dislocations in the slip system α (the same solute concentration that is the sum of the solute concentration on all active slip systems is used in our previous crystal plasticity model, see [6]). We assume an Arrhenius equation for the expression of $P(C_s^\alpha)$ to describe plastic flow resulting from thermally activated dislocation motion, i.e.

$$P(C_s^\alpha) = e^{-\frac{\Delta H(C_s^\alpha)}{kT}} \quad (3)$$

where $H(C_s^\alpha)$ is the activation enthalpy for dislocation motion. Using Taylor expansion for ΔH , the resolved shear stress can be expressed as

$$\ln \left| \frac{\tau^\alpha}{g^\alpha} \right| = \frac{1}{n} \ln \left| \frac{\dot{\gamma}^\alpha}{\dot{\alpha}} \right| + \frac{1}{n} \beta C_s^\alpha \quad (4)$$

where $1/n$ is the conventional strain rate sensitivity associated with the localized obstacles (always positive), and β is a coefficient characterizing the strength of the dislocation-solute interaction.

Unlike our previous crystal plasticity model formulation that assumes isotropic hardening behavior similar to a stage III strain hardening in single crystals [6], the strain hardening is here characterized by the anisotropic evolution of the strength g^α through the incremental relation:

$$\dot{g}^\alpha = \sum_{\beta=1}^N h_{\alpha\beta} |\dot{\gamma}^\beta| \quad (5)$$

where $h_{\alpha\beta}$ are the slip hardening moduli. To describe the three-stage hardening of single crystalline materials we use

$$h_{\alpha\alpha} = \left\{ (h_0 - h_s) \operatorname{sech}^2 \left[\frac{(h_0 - h_s) \bar{\gamma}^\alpha}{\tau_I - \tau_0} \right] + h_s \right\} G(\bar{\gamma}^\beta; \beta \neq \alpha), \quad (\text{no sum on } \alpha) \quad (6)$$

$$h_{\beta\alpha} = q h_{\alpha\alpha}, \quad (\beta \neq \alpha) \quad (7)$$

where τ_0 is the initial yield strength, τ_I is the Stage I stress, h_0 is the hardening modulus just after initial yield, h_s is the hardening modulus during easy glide and $\bar{\gamma}^\alpha = \int_0^t |\dot{\gamma}^\alpha| dt$. G is associated with interactive (cross) slip hardening and given by

$$G(\bar{\gamma}^\beta; \beta \neq \alpha) = 1 + \sum_{\beta \neq \alpha} f_{\alpha\beta} \tanh(\bar{\gamma}^\beta / \gamma_0) \quad (8)$$

where γ_0 is the amount of slip after which the interaction between slip systems reaches the peak strength and $f_{\alpha\beta}$ represents the magnitude of the strength of a particular slip interaction. In general, the hardening modulus during Stage I easy glide is distinct from that in Stage III, and we assume

$$h_s = h_s^I + (h_s^{III} - h_s^I) \tanh(\bar{\gamma} / \gamma_0^{III}) \quad (9)$$

where $\bar{\gamma} = \sum_{\alpha} \bar{\gamma}^\alpha$ and γ_0^{III} is approximately the accumulated slip at the onset of Stage III. [5]

The solute concentration at temporarily arrested dislocations is related to the aging time t_a^α on α slip system by the equation including saturation:

$$C_s^\alpha = C_m - C_m e^{-\left(\frac{t_a^\alpha}{\tau}\right)^{\frac{3}{2}}}, \quad (10)$$

where τ , a characteristic time, is assumed to be $\tau = \frac{(C_m / C_0)^{\frac{3}{2}}}{KD}$ [3]. C_m is the maximum solute concentration, C_0 is the nominal solute concentration a long way from the dislocation. It follows from the Orowan equation relating the plastic strain rate to the average velocity and the density of mobile dislocations that the waiting time for a dislocation to be unpinned is inversely proportional to the plastic strain rate [7]:

$$t_w^\alpha = \frac{b \rho_m^\alpha \bar{x}}{|\dot{\gamma}^\alpha|} = \frac{C_1 \rho_m^\alpha / \sqrt{\rho_f^\alpha}}{|\dot{\gamma}^\alpha|}, \quad (11)$$

where ρ_m^α is the density of mobile dislocations on the α slip system, ρ_f^α is the density of forest dislocations, and \bar{x} is the average distance moved by a dislocation. We assume that $\rho_m^\alpha \propto \bar{\gamma}^\alpha$

and $\rho_f^\alpha \propto \sum_{\beta \neq \alpha} \bar{\gamma}^\beta$. Instead of using an aging time and a waiting time defined as an average over all active slip systems [6], individual aging times and waiting times are introduced in the current model formulation for each active slip system. The solute concentration is a growing function of the waiting time that is the average time a dislocation spends at a localized obstacle to its glide. An increase in strain rate reduces the solute concentration to lead to a negative strain rate sensitivity of the flow stress, which gives rise to discontinuous yielding and coarse slip bands. In the numerical simulation we assumed $t_w^\alpha = t_a^\alpha$.

NUMERICAL INTEGRATION

The tangent modulus method for rate dependent solid is used in our numerical integration scheme. The increment of plastic strain in slip system α within the time increment Δt is given by

$$\Delta \gamma^\alpha = \Delta t [(1-\theta) \dot{\gamma}_t^\alpha + \theta \dot{\gamma}_{t+\Delta t}^\alpha] \quad (12)$$

where the subscript is the time at which the slipping rate is evaluated. The parameter θ ranges from 0 to 1. Approximating slipping rate at time $t + \Delta t$ by Taylor expansion at time t , we can get the following incremental relation:

$$\Delta \gamma^\alpha = \Delta t \left[\dot{\gamma}_t^\alpha + \theta \frac{\partial \dot{\gamma}^\alpha}{\partial \tau^\alpha} \Big|_t \Delta \tau^\alpha + \theta \frac{\partial \dot{\gamma}^\alpha}{\partial g^\alpha} \Big|_t \Delta g^\alpha + \theta \frac{\partial \dot{\gamma}^\alpha}{\partial C_s^\alpha} \Big|_t \Delta C_s^\alpha \right] \quad (13)$$

The increments $\Delta \tau^\alpha$, Δg^α , and ΔC_s^α are functions of $\Delta \gamma^\alpha$. Then the above equation is solved for $\Delta \gamma^\alpha$ by writing a user defined material model (UMAT) for the finite element code ABAQUS/Standard.

NUMERICAL RESULTS

The effect of crystal orientation on the discontinuous deformation in aluminum single crystals has been investigated by finite element simulation. Tabata *et al.* [8] reported experimental results on the evolution of serrated plastic flows using Al-0.3%Mg single crystals with three various tensile axes. Three different tensile axes similar to the ones used in their experiments (see Fig.1 in [8]) were examined for the single crystal bar in the finite element simulation. The global strain rate was $0.1 \times 10^{-3} \text{ s}^{-1}$. The numerical parameters are listed in Table 1. For the values of $f_{\alpha\beta}$ of FCC crystals, refer to Table II in [5]. One three-dimensional 20-node element was used. Stress-strain curves are shown in Figs. 1, 2 and 3 for the three different uniaxial loading axes: multiple-, double- and single-slip orientations respectively. The magnitude of the serration increases with increasing strain up to the end of stage II and then decreases in stage III to a roughly steady-state level in all specimens irrespective of specimen orientation. These results agree well with the experimental observations (for details, see the Fig.2, Fig.4 and Fig.6 in [8], respectively).

The magnitude of the serration decreases for large strain (stage III) because the dynamic strain aging effect is not strong at the large strain for the value of the material parameters in the simulations. Large serration is observed in stage II because many slip systems are activated at the same time so that the dynamic strain aging effects are superposed. That is, in the framework of our crystal plasticity modeling, if there are m active slip systems in two-dimensional symmetric loading with the symmetry angle ϕ , then the tensile stress is related to the deformation rate D_{11} by

$$\left(\frac{\sigma_{11}}{2g} \right)^n = \frac{2D_{11}}{m \dot{a}_0 (\sin 2\phi)^{n+1} e^{-\Delta H/kT}} \quad (14)$$

where elastic deformations are neglected and the same yield strength g and activation enthalpy ΔH are assumed for all active slip systems. Defining $\dot{\alpha}_0^{eff} = m\dot{\alpha}_0$ as a new reference strain rate for an effective slip system, the activation enthalpy increases as the number of the active slip systems, m , increases for the same deformation rate, D_{11} , and σ_{11}/g . Large activation enthalpy will cause bigger serration.

CONCLUSIONS

A dynamic strain aging crystal plasticity model has been modified to incorporate explicitly the effect of the interaction between solute atoms and mobile dislocations on each individual slip system and the three stages of anisotropic strain hardening for an Al-Mg crystal. Tensile stress-strain curves were obtained by finite element simulations for three different tensile loading axes with respect to the crystal orientation. The dependence of magnitude of serrations in stages I, II and III of strain hardening of the crystals found in the simulations agreed with experimental observation. The results of this investigation indicate that the formation of coarse slip bands on the crystal surfaces can be explained consistently in terms of dynamic strain aging.

REFERENCES

1. H. Cimenoglu, E. S. Kayali and F. Dikec, *Scripta Metall.*, **23**, 1543 (1989).
2. A. Inagaki, T. Komatsubara and H. Inagaki, *Z. Metall.*, **90**, 6 (1999).
3. Y. Estrin, L. P. Kubin, Spatial coupling and propagative plastic instabilities, in: H. -B. Muhlhaus (Ed.), *Continuum Models for Materials with Micro-Structure*, John Wiley & Sons (N.Y.), 395 (1995).
4. X. Li, Ph.D. Thesis, Yale University, New Haven, Connecticut (December, 2000).
5. J. Bassani, *Adv. App. Mech.*, **30**, 191 (1994).
6. S. Yang and W. Tong, *Mat. Sci. Engng. A*, in print (2000).
7. D. Hull, D. Bacon, *Introduction to Dislocations*, Pergamon Press, 1984.
8. T. Tabata, H. Fujita and N. Ueda, *Mat. Sci. Engng.*, **44**, 81 (1980).

Table 1: Numerical parameters of single crystalline aluminum.

Parameter	Value	Parameter	Value
Young's modulus	69 GPa	β	800.0
Poisson's ratio	0.3	KD	4.0
h_0	0.1 GPa	C_1	0.03
h_s^I	2.0 MPa	C_0	0.00095
h_s^{III}	0.2 MPa	γ_0	0.001
τ_l	6.1 MPa	γ_0^{III}	0.3
τ_0	6.0 MPa	q	0
$\dot{\alpha}$	0.0001	n	30
θ	0.5	N	12

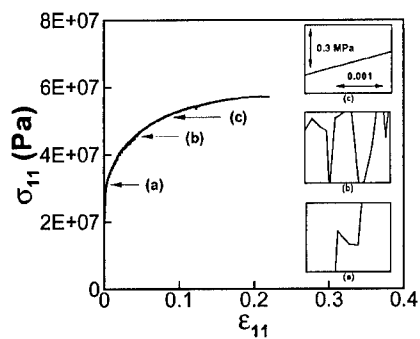


Figure 1: Computed stress-strain curve for multiple-slip. The tensile axis is along [111].

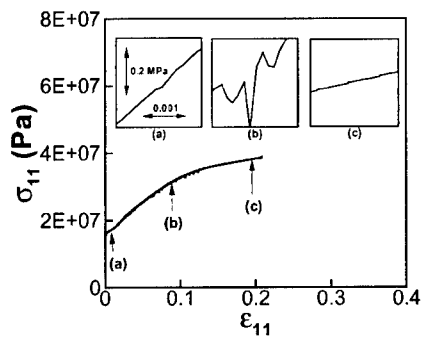


Figure 2: Computed stress-strain curve for double-slip. The tensile axis is along [112].

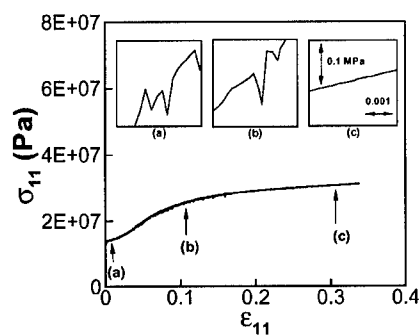


Figure 3: Computed stress-strain curve for single-slip orientation. The tensile axis is along [632].

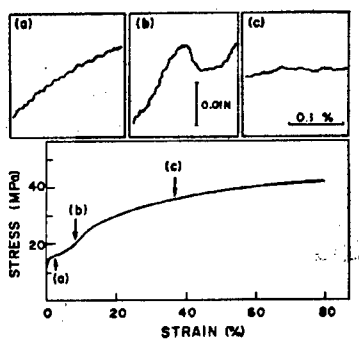


Figure 4: Experimental stress-strain curve for single-slip orientation. Picture is taken from reference [8].

Dynamics and Patterning of Screw Dislocations in Two Dimensions

Robin L. B. Selinger, Brian B. Smith, and Wei-Dong Luo

Physics Department, Catholic University

Washington, DC 20064

selinger@cua.edu

ABSTRACT

To understand how dislocations form ordered structures during the deformation of metals, we perform computer simulation studies of the dynamics and patterning of screw dislocations in two dimensions. The simulation is carried out using an idealized atomistic model with anti-plane displacements only; we show that this system is an analog of the two-dimensional XY rotor model. Simulation studies show that under a constant applied shear strain rate, the flow of dislocations spontaneously coalesces to form narrow dislocation-rich channels separated by wide dislocation-free regions, so that the applied strain is localized into slip bands. We argue that this pattern formation represents a phase separation into low/high defect density phases associated with the XY model, and conjecture that thermodynamic forces drive strain localization.

INTRODUCTION

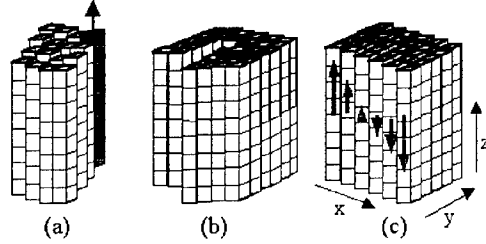
Much research and indeed much of the work presented in this symposium have been directed at understanding the evolution of dislocation microstructures and the mechanical response of metals. While many insights can be found from mesoscale models, the problem remains essentially unsolved: the elastic-plastic response of metals under arbitrary temperature and deformation history remains impossible to predict from first principles. Many researchers treat dislocation dynamics and patterning as a complex non-equilibrium reaction-diffusion process and focus on enumerating the list of potential dislocation reactions, sometimes relying on atomistic simulation to extract rules and parameters for use in mesoscale simulations.

Here we take a rather different approach, and study the dynamics and patterning of screw dislocations under a constant applied shear strain rate in two dimensions, using a simplified atomistic simulation. Although the 2-d geometry neglects dislocation entanglement and a host of other 3-d phenomena, the simulation shows formation of slip bands with a spacing that depends on the shear strain rate. We map the atomistic model onto a statistical physics model, the XY rotor model, to gain insight into the thermodynamic forces that drive the localization of strain. By understanding the mechanisms for strain localization in this highly idealized 2-d system, we hope to make progress toward a solution of the more complex 3-d problem.

MODEL

Consider a simple cubic lattice of particles, where each vertical column moves as a unit and can be displaced only along the column axis, as shown in Fig. 1(a). This system can contain straight parallel screw dislocations, as shown in Fig. 1(b), but cannot contain edge dislocations, as there are no in-plane displacements. The deformation can be represented as a scalar field $z(x,y)$.

Fig. 1 (a) Displacement z_i of each column is a dynamic variable.
(b) Straight screw dislocations are allowed in this restricted geometry, but no edge dislocations.
(c) Driving boundary conditions maintain constant shear strain rate.



Neglecting any surface effects, the Hamiltonian (per unit length) of this system is:

$$H = -K \sum_{\langle i,j \rangle} \cos[2\pi(z_i - z_j)/a_o] + \frac{1}{2} \sum_i m \left(\frac{dz_i}{dt} \right)^2 \quad (1)$$

Here z_i is the out-of-plane displacement of column i , K is an energy per unit length (closely related to the unstable stacking energy), a_o is the lattice spacing, m is the mass per unit length of each column, and the first sum is over nearest neighbor columns $\langle i,j \rangle$. The cosine term represents the energy per unit length associated with each pair of neighboring columns as they slide in and out of registry with one another, with an energy barrier of $2K$ to cross from one local energy minimum to the next. The second term represents the kinetic energy per unit length associated with the motion of the columns.

Deterministic equations of motion are derived from the Hamiltonian, just as in classical molecular dynamics (MD) simulations, and are integrated forward in time with a finite time step. Typical system size studied is $1,000 \times 200$ and simulations are run up to 2×10^6 discrete time steps, for total duration of $10^5 t_o$. Here $t_o = a_o (m/K)^{1/2} \approx 10^{-12}$ sec is the natural time unit.

We use this model to study the homogeneous nucleation, motion, and pattern formation of screw dislocations under a constant shear strain rate $\dot{\epsilon}$ at temperature T . In the initial conditions, each column starts with zero displacement and a small randomized z -velocity appropriate for the chosen temperature. A velocity gradient is then superimposed along the x direction as shown in Fig. 1(c). Periodic boundary conditions are applied with a z -offset across the boundary in the x direction. The offset increases linearly with time, and this "driving" boundary condition maintains the total shear strain rate $\dot{\epsilon}$ at a fixed value. Regular periodic boundary conditions are used in the y -direction. The driving boundary conditions do work on the system, so a thermostat algorithm is used to maintain constant T .

To make the model more realistic, the cosine term in Eqn. 1 could be replaced with an appropriate Embedded Atom Method potential, and a slice of a suitably oriented FCC lattice could replace the square lattice. However the highly idealized version of the model is of particular interest because of its close analogy to the XY rotor model. The 2-d XY rotor model consists of a lattice of spins as shown in Fig. 2. Each spin lies in the x - y plane and has an angular orientation θ_i with respect to the x axis, with $0 < \theta_i < 2\pi$. The Hamiltonian is:

$$H = \sum_{\langle i,j \rangle} -J \cos(\theta_i - \theta_j) + \sum_i \frac{1}{2} I \left(\frac{d\theta_i}{dt} \right)^2 \quad (2)$$

Here J is the (positive) exchange coefficient, and I is the moment of inertia of each spin, treated as a rigid rotor.

Fig. 2: (a) Positive vortex, analog of a positive screw dislocation. (b) The XY rotor model under "twisting" boundary conditions, analogous to the applied shear strain shown in Fig. 1(c).



The mapping between the two models involves the transformation, $\theta_i = 2\pi z_i / a_0$. A screw dislocation in the atomistic model maps to a vortex in the XY rotor model, as shown in Fig. 2(a). Applied shear strain in the crystal is analogous to applied twist in the XY rotor model, shown in Fig. 2(b). The sign and "charge" of a vortex can be calculated by making the equivalent of a Burgers circuit around the defect core. If the result is $\pm 2\pi$, the vortex is positive/negative, respectively. If the result is 0, there is no defect. See Chaiken and Lubensky [1] for a detailed discussion of topological defects in the XY model.

The XY model in 2-d lacks true long-range order at low temperature due to thermal fluctuations. The system has only a small density of thermally activated vortices, and these are bound in closely-spaced pairs. At a critical temperature of approximately $k_B T/J = 0.89$, the system undergoes a phase transition, known as the Kosterlitz-Thouless (K-T) transition [2]. This is a second-order melting transition that occurs via cooperative homogeneous nucleation and unbinding of vortex dipoles. The high T phase has a high density of unbound vortices.

The addition of driving boundary conditions changes the phase behavior of the XY rotor model, because stress drives the nucleation and unbinding of vortex pairs even at low temperature. Reduction of the effective transition temperature due to stress was predicted theoretically by Khantha et al [3] in their theory of the ductile-brittle transition. We find that the critical temperature for defect nucleation drops linearly with increasing stress [4] in agreement with their predictions.

RESULTS

We carry out simulations at $T=0.2$, well below the K-T transition, with the system initially vortex-free. The shear strain rate is applied, and at a critical value of the stress, dislocation pairs nucleate and unbind in roughly constant density, as shown in Fig. 3(a). Positive and negative screw dislocations are driven in opposite directions by the stress and undergo more or less constant motion, with frequent nucleation/annihilation, and the structure is in continuous evolution. Dislocation flow then spontaneously localizes into a nearly periodic array of narrow channels separated by wide defect-free regions, as shown in Fig. 3(b). The initial spacing of the channels depends on the strain rate; higher strain rate produces more closely spaced channels.

Once coalesced into channels, dislocations continue to flow in opposite directions with frequent nucleation/annihilation events. As there is no pinning mechanism, there are no immobile dislocations. Fig. 4 displays the $z(x,y)$ displacement field for a larger system, showing that the dislocation-rich channels represent localization of the shear strain into a series of nearly periodic slip bands.

The channel pattern coarsens, as channels diffuse laterally and occasionally merge. Channel number drops as $t^{-\alpha}$ where $\alpha < 0.5$ depends on the strain rate. The overall dislocation density remains roughly constant over time; channel width increases as the pattern coarsens. Equilibrium dislocation density scales with strain rate with an exponent of 0.75 ± 0.05 , as shown in Fig. 5. Since scaling exponents generally depend sensitively on dimensionality, this exponent cannot be usefully compared with experimental results for three-dimensional materials.

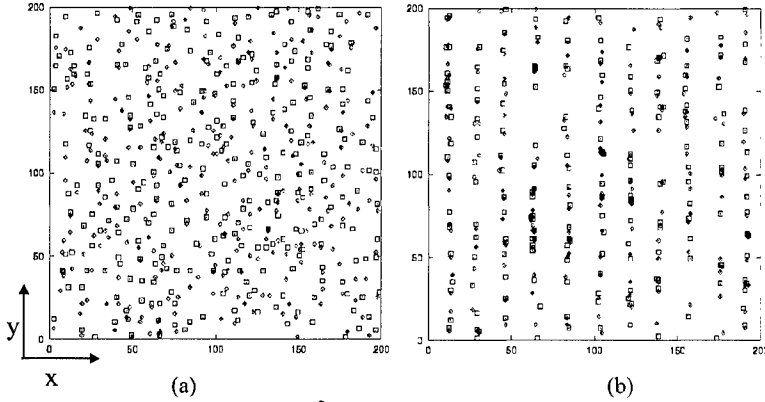


Fig. 3: Simulation with $T=0.2$ and $\dot{\epsilon}=3.2 \times 10^{-3}$, showing topological defects in the x - y plane. (Note that the strain rate is defined per natural time unit t_0 .) Screw dislocations of opposite signs are displayed as \blacklozenge and \blacksquare . (a) Initial density is uniform. (b) Dislocation channels form. Defects of opposite sign travel in opposite directions along each channel.

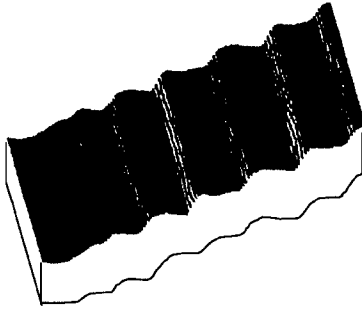


Fig. 4: Three-dimensional displacement field $z(x,y)$ for a system of size 1000×200 . Dislocation channeling produces localization of the applied shear strain into a series of slip bands.

DISCUSSION

The close analogy between anti-plane deformation of a crystal and the XY rotor model provides a useful theoretical framework for understanding the coalescence of dislocation flow into channels and the localization of strain. In the absence of driving boundary conditions, the XY model has no unbound vortices at low temperature. The imposition of driving boundary

conditions imposes a non-zero density of free topological defects, because $\dot{\epsilon} = \rho b v$, where ρ is the total defect density ($\rho_- + \rho_+$), v is the average speed of defect motion, and b is Burgers vector. In principle the induced defect density could remain uniform, but the system is not stable at arbitrary defect density and divides into a nearly defect-free phase and a defect-rich phase.

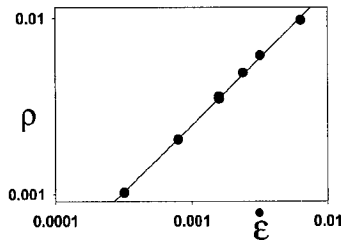


Fig. 5: Dislocation density $\rho = \rho_+ + \rho_-$ scales with strain rate as $\rho \propto (\dot{\epsilon})^{3/4}$.

We conjecture that the system lowers its free energy by phase separating, that is, two-phase coexistence is lower in free energy than the homogeneous phase. The defect-free phase is stiff with a well-defined elastic modulus, while the defect-rich phase yields with a viscous response. The coarsening process we observe can thus be interpreted as a simple phase separation and coarsening of a system in two-phase coexistence. The driving force for later channel coalescence is surface tension associated with the boundary between the two phases. In future work we hope to complete an analytical calculation of the free energy density associated with the two phases and derive analytical results for the thermodynamic forces driving phase separation. Such a result would greatly clarify the role of equilibrium thermodynamics in the pattern formation process, a matter of some controversy since the system is dissipative and driven by external forces, and is not in thermal equilibrium in the usual sense.

Holt [5] argued that a gas of +/- screw dislocations in 2-d is unstable to the formation of cell structure through spinodal decomposition. In the absence of an applied stress or strain, the defects would annihilate, but Holt rather unphysically assumed fixed density. In our simulations, we find that patterning occurs only in the presence of an applied strain rate, a more physical way to impose non-zero defect density. Further analysis of the thermodynamics of slip band formation and coarsening may also explain the ubiquitous scaling behavior seen by Hughes et al [6] in dislocation microstructures.

APPLICATIONS

Besides providing a novel theoretical viewpoint on dislocation patterning, the two-dimensional deformation model presented here can be used to investigate a variety of phenomena related to the elastic-plastic response of crystalline solids. A crack may be introduced into the model by allowing the coefficient K in Eqn. [1] (equivalently J in Eqn. [2]) to vary as a function of position, setting it equal to zero along part of a row of nearest-neighbor bonds. Stress intensification occurs at the crack tips in the normal way and heterogeneous screw dislocation nucleation is observed under shear, which loads the crack in mode III. We introduce a bond-breaking rule that sets K on a bond to zero when the local stress exceeds a threshold value. Preliminary studies indicate that with this modification, the system displays a brittle-ductile transition with temperature and strain rate. This model will allow direct calculation of fracture toughness as a function of temperature and strain rate in two dimensions, and should provide a useful test for comparison with the predictions of the theory by Khantha et al [3].

This model may also have use in the study of both size effects and strain-gradient effects in plasticity. Even in a simple geometry like the one explored here, one can expect size effects if the sample is comparable in size to the equilibrium channel spacing. Strain gradients can be introduced by changing from simple shear to more complex geometries. For example, we have

started initial studies on the shear of a thick-walled cylindrical shell between its inner and outer surfaces, and of simple torsion of a beam.

As discussed above, the model can also be altered to include realistic potentials and lattice structure and to include both in-plane and out-of plane displacements. At that stage the model becomes essentially a molecular dynamics simulation, but with a particular 2-d geometry that could display dislocation patterning at accessible time and length scales. Even in its simplest form, the present model has advantages over discrete dislocation dynamics techniques. Pair nucleation, defect motion, and annihilation occur spontaneously through the dynamics of the model with no need for arbitrary rules or extra parameters. Since it is an atomistic model, though a simplified one, dislocations interact through a dynamic strain field. They have appropriate effective mass, velocity-dependent damping, and relativistic effects.

CONCLUSIONS

We have carried out simulation studies of screw dislocation dynamics and patterning in two dimensions using a simplified atomistic model. The simulations show the formation of distinct dislocation channels, or slip bands, with accompanying localization of applied shear strain. The initial spacing between slip bands drops with increasing strain rate. Total dislocation density appears to scale with strain rate with a characteristic exponent of approximately $\frac{3}{4}$.

We use the close analogy between anti-plane shear deformation of a crystal and the XY rotor model to gain new insight into the mechanisms driving dislocation patterning and strain localization in two dimensions. We argue that the mechanism driving this pattern formation is a phase separation into two phases characterized by low and high defect densities. The simulation model shows promise for further investigation of elastic-plastic response of solids, including size effects and strain gradient effects in plasticity and the brittle-ductile transition.

ACKNOWLEDGMENTS

This work was supported by The National Science Foundation NSF-DMR-9702234.

REFERENCES

- [1] Chaikin, P. M. and Lubensky, T., *Principles of Condensed Matter Physics*, Cambridge Univ. Press (1995).
- [2] J. M. Kosterlitz and D. J. Thouless, *J. Phys.* **6**, 1181 (1973).
- [3] Khantha, M., Pope, D. P., and Vitek, V., *Phys. Rev. Lett.* **73**, 684 (1994).
- [4] Smith, B. B. and Selinger, R. L. B., in preparation.
- [5] Holt, D., *J. Appl. Phys.* **41**, 3197 (1970).
- [6] A. Godfrey and D. A. Hughes, *Acta. Mater.* **48**, 1897 (2000).

Dislocation Multiplication in Germanium Single Crystals

Corinne Charbonnier, Tomas Kruml and Jean-Luc Martin

Département de Physique, Ecole Polytechnique Fédérale (EPFL), CH-1015 Lausanne
(Switzerland)

ABSTRACT

Thermal activation of $\langle 123 \rangle$ germanium single crystal deformation is studied by using stress-relaxation experiments. These exhibit a non logarithmic dependence of stress as a function of time. The athermal component of stress and the apparent activation volume are determined. The role of dislocation multiplication is discussed in terms of specific features of the monotonic and transient deformation behaviour.

INTRODUCTION

Although the plasticity of semiconducting covalent materials with the diamond cubic structure has been studied during the last forty years (see e.g [1,2]), some questions remain unanswered. In particular, the interpretation of the multiplication yield point has been recently revisited: for germanium, Siethoff et al. [3], by reanalyzing former data, distinguish two (or even three) temperature regimes corresponding to different mechanisms with given activation energies. For silicon, Moulin et al. [4] question the dynamics of dislocations and associated multiplication processes at the early stages of plasticity by performing 3 dimensional computer simulations of dislocations sources.

In the present work, the role of dislocation multiplication in deformation at constant strain-rate is studied in germanium by using conventional transient tests such as stress-relaxation experiments. The first results of this ongoing work are presented below, while a full report will be found in reference [5].

EXPERIMENTAL PROCEDURE

$\langle 123 \rangle$ intrinsic germanium single crystals (kindly provided by Prof. Louchet, University of Grenoble, France) were cut using a diamond wheel. Prismatic specimens had dimensions $3 \times 3 \times 9$ mm³ and $\langle 154 \rangle$ and $\langle 111 \rangle$ respective lateral faces. To limit surface damage on the lateral faces, these were polished mechanically using several types of sand papers and diamond paste. While the original single crystal was almost dislocation-free, the preparation process inevitably induced defects on the superficial layers of the specimen. Etching of these by a solution containing HF (25% HF, 50% HNO₃, 25% CH₃COOH) revealed rows of dislocations parallel to the polishing direction. This dislocation-rich surface layer was removed by using the above HF solution for 20 minutes.

Specimens were then deformed in compression in a RMC 100 Schenck machine equipped with a furnace, under a helium flux. Imposed strain-rate tests combined with stress-relaxation experiments were performed in the temperature range 700-920K at a nominal strain-rate of 4.10^{-5} s⁻¹, up to a shear strain of about 15 %.

EXPERIMENTAL RESULTS

Compression tests

Typical stress-strain curves are shown in figure 1 as a function of temperature. Most stress-relaxation experiments were performed after the lower yield point. A few tests were made before the upper yield point as discussed later.

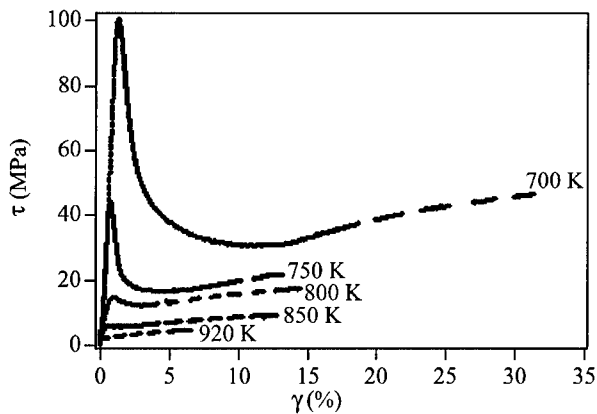


Figure 1. Stress-strain curves for various temperatures. $\langle 123 \rangle$ orientation, $\dot{\gamma} = 4 \cdot 10^{-5} \text{ s}^{-1}$. Stress-relaxation experiments are performed where the stress-strain curves are interrupted.

The well known multiplication yield point is pronounced for low temperatures (700K) and gradually disappears as the temperature increases. At the strain-rate used in this study, the crystals are brittle below 700K so that the yield point cannot be observed anymore under such conditions.

At given temperatures, the stress corresponding to the upper yield point is found to be constant within $\pm 9\%$.

Transients tests

The first stress-relaxation experiments were performed after the lower yield point in order to measure activation parameters related to dislocation mobility. These experiments will be compared with similar ones made before the upper yield point, where intense dislocation multiplication takes place, so as to get new information on dislocation source activity.

The procedure used to perform single as well as repeated stress-relaxation experiments and the assumptions made for their interpretation can be found in references [6] and [7]. Stress-relaxation curves can be divided into two classes in which the stress decrease as a function of

time exhibits respectively a logarithmic and a non logarithmic dependence [6]. For the deformation conditions used in this study and for relaxation duration of 30s or more, non logarithmic relaxations are observed as a rule. An example is shown in figure 2 of the dependence of $\ln(-\dot{\tau})$ on the stress decrease $\Delta\tau$ (a negative quantity). $\dot{\tau}$ is the stress-rate during relaxation, a quantity proportional to the plastic strain-rate $\dot{\gamma}_p$. The slope of the corresponding curve is proportional to the apparent activation volume V_a defined as:

$$V_a = kT \frac{\partial \ln \dot{\gamma}_p}{\partial \tau}$$

where k is the Boltzman constant, T the absolute temperature. This activation volume is similar to the one measured in strain-rate jump experiments during a constant strain-rate test or a stress change experiment during a creep test. It includes the changes of mobile dislocation densities during the transients and therefore is different from the microscopic volume V of the dislocation velocity [6-7]. Figure 2 shows that V_a is not constant during the stress-relaxation experiment. Consequently, the latter is not logarithmic. The procedure used here to measure V_a considers the onset of the curve in figure 2 over a range of 3 MPa where it is approximately linear. This corresponds to a relaxation time of 10 s. An example of variation of V_a along the stress-strain curve (after the lower yield point) is shown in figure 3. V_a is expressed in b^3 units, b being the Burgers vector of the total dislocation ($b=0.401$ nm). V_a appears to be almost constant as a function of strain. This can be understood as follows: V_a depends on the effective stress $\bar{\tau}$ which is constant at a given temperature. Accordingly, the increase of stress along the stress-strain curve reflects the increase of the athermal stress τ_i . This interpretation is fully supported by the results of the following section.

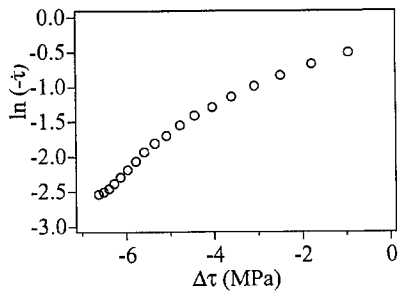


Figure 2. Curve corresponding to a stress-relaxation experiment performed at $T=700K$, $\dot{\gamma}_p=8\%$ and $\tau=38$ MPa, after the lower yield point. (see text).

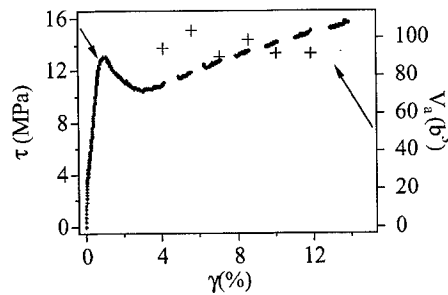


Figure 3. Stress-strain curve and apparent activation volume as a function of strain at 800K.

Determination of the stress components

The internal stress τ_i corresponding to a given plastic strain was determined using two methods which are conventionally used in the case of thermally activated dislocation motion [8]: i) by plotting the stress measured at constant strain-rate which is known to decrease and stabilize at τ_i as the temperature rises and ii) under the same conditions, the volume as a function of stress reaches high values as τ decreases to τ_i . Because of the presence of the multiplication yield point, the plastic strain corresponding to the above parameters is measured taking the plastic strain of the lower yield point γ_{plyp} as the origin. An example of such a determination is shown in figures 4 and 5 for a plastic strain equal to $\gamma_{plyp} + 3\%$.

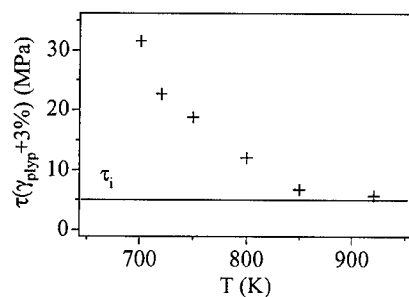


Figure 4. Stress corresponding to a plastic strain of $\gamma_{plyp} + 3\%$ for various temperatures (see text).

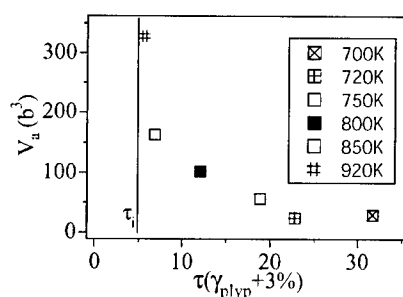


Figure 5. Activation volume as a function of stress at $\gamma_{plyp} + 3\%$ (see text).

The values obtained for τ_i using both methods are in fair agreement, $\tau_i \approx 5$ MPa in figures 4 and 5. By performing these measurements for various amounts of plastic strain, τ_i can be plotted along the stress-strain curves as illustrated in figure 6. Figure 6 shows that at 800 K, the internal stress is about half of the total stress. The thermal part of the stress $\tau^* = \tau - \tau_i$ is approximately constant as a function of strain, within the uncertainty of measurement. This result confirms the above interpretation of the volume dependence on strain in figure 3. In addition, this result complies with previous estimations by Sumino and Kojima [9]. In their study, the stress components were determined by analyzing the data of strain-rate change experiments along a stress-strain curve, another type of transient test. They used high purity germanium single crystals deformed in tension in the 10^{-4} s^{-1} range and also found the thermal part of the stress to be constant along the stress-strain curve.

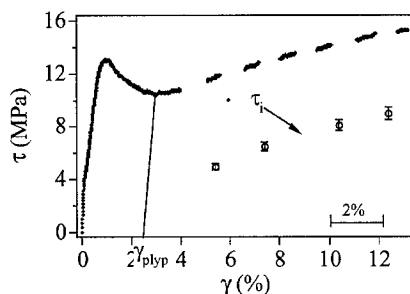


Figure 6. Deformation curve and internal stress τ_i at 800K.

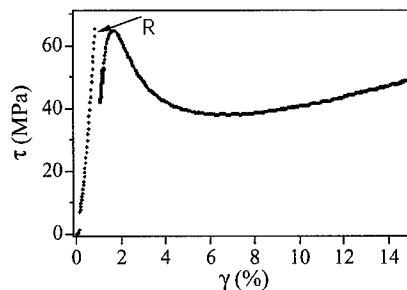


Figure 7. Stress-strain curve at 700K while a stress-relaxation experiment of 300 s duration (R) is performed before the upper yield point (at 65 MPa).

Stress-relaxation and dislocation multiplication

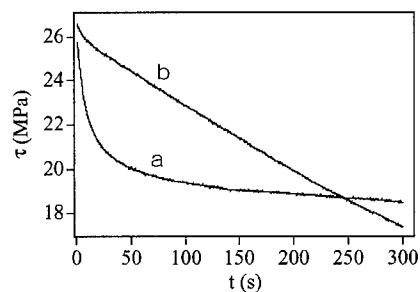


Figure 8. Two stress-relaxation curves performed at the same stress (26 MPa) along the monotonic curve after the lower yield point a) and before the upper yield point b) respectively. $T=750K$.

Some single stress-relaxation experiments of 300 s duration were performed before the upper yield point (UYP). Such experiments are time (and specimen) consuming since a new specimen is needed for each test. Preliminary results are presented below.

An example of stress-strain curve is shown in figure 7 for a test performed at 700K. When the specimen is reloaded after relaxation, a yield point is indeed observed. Its amplitude (about 65 MPa in the present case) is much smaller than that of the UYP of the monotonic curve (about 100 MPa), the latter being visible in figure 1 at the corresponding temperature.

Furthermore the comparison of the two relaxation curves in figure 8, corresponding to the same stress respectively before the UYP and after the LYP, clearly shows that the relaxation-rates are different. In the former case (curve b), the stress-rate is approximately constant. After the lower yield point (curve a), the initial rate is fast as compared to the previous curve, due to a large number of mobile dislocations (during the first 25 s). Then it slows down because of dislocation exhaustion. As a rule, it was observed that the shape of the relaxation curves depends on stress and temperature.

DISCUSSION AND CONCLUSION

The first set of stress-relaxation results presented here shows that germanium single crystal behaviour is quite different from other materials studied under similar conditions [6]: stress relaxes following a non logarithmic dependence on time (figure 2) and the total amount of relaxed stress is quite large (7 MPa over 300 s in figure 8 as compared to a 26 MPa onset stress). Some reasons for this are analyzed in reference [6]: i) a more intense dislocation multiplication takes place in germanium, ii) the microscopic activation volume is strongly stress dependent. Another aspect of the importance of dislocation multiplication as stress relaxes is clearly illustrated by the above results. During a monotonic test at 750 K, dislocation multiplication takes place at the onset of deformation and is responsible for the UYP (figure 1). If a stress-relaxation experiment is performed before the UYP (curve b in figure 8), the UYP is either no longer present on the stress-strain curve, or is considerably reduced. This emphasizes the activation of dislocation sources during relaxation. Moreover, the comparison of the two stress-relaxation curves in figure 8 shows that before the UYP (curve b) the slower deformation-rate during the transient is very likely due to the low available mobile dislocation density, as compared to the conditions of curve a.

Work is in progress to distinguish between two effects on the stress-relaxation: dislocation multiplication on the one hand and stress dependence of the activation volume on the other hand. For this purpose, creep transients are performed instead of stress-relaxation tests. Since the stress is kept constant in the former experiments, the observed change in creep-rate as a function of time can be directly connected with the evolution of the mobile dislocation density [7]. Transmission electron microscope observations are underway to characterize dislocation structures and measure dislocation densities as a function of the deformation conditions.

ACKNOWLEDGEMENTS

The authors wish to acknowledge fruitful discussions with Dr. Caillard and Dr. Spätig. They are grateful to Fonds National Suisse for the financial support.

REFERENCES

1. H. Alexander, *Journal de Physique* **35-C7**, 173, (1974)
2. A. George and R. Rabier, *Revue de Physique Appliquée* **22**, 941, (1987)
3. H. Siethoff, K. Ahlborn and W. Schröter, *Phys. Stat. Sol. (a)* **174**, 205, (1999)
4. A. Moulin, M. Condat, and L-P. Kubin, *Acta Mater.* **47**, 2879, (1999)
5. C. Charbonnier, PhD thesis, Ecole Polytechnique Fédérale de Lausanne, in preparation
6. O. Couteau, C. Charbonnier, T. Kruml and J-L. Martin, this volume
7. J-L. Martin, B. Lo Piccolo, T. Kruml and J. Bonneville, *Mater. Sc. Eng. A.*, in print
8. P. Groh, in *Dislocations et déformation plastique*, ed. P.Groh, L-P. Kubin and J-L. Martin (les Editions de Physique, Paris, 1980), p.67
9. K. Sumino and K-I. Kojima, *Crystal Lattice Defects* **2**, 159, (1971)

FACET: a two dimensional simulator of polycrystalline thin film growth

Jie Zhang, James B. Adams
Department of Chemical and Materials Engineering, Arizona State University, Tempe, AZ,
85287, USA

ABSTRACT:

We present FACET: a two dimensional simulator to model polycrystalline thin film growth, which links atomic scale processes to macroscopic phenomena. The model is based on the concept of describing the crystal surface in terms of preferred facets. Line segments were used to depict the profile of the grain and grain boundaries. Multiple nuclei are semi-randomly distributed along the textured or non-textured surface, and crystallographically appropriate facets are created in the nucleation simulation. We use a Kinetic Lattice Monte Carlo (KLMC) method to calculate the inter-facet diffusion rates and use a continuum approach to grow the facets, hence the multiple grains. The software is Windows(95/98/2000/NT) based and has an integrated Graphical User Interface, within which a user can input deposition conditions and experimental and simulation data, visualize the nucleation and growth of the grains, and obtain the final grain structure and texture.

INTRODUCTION

It would be extremely useful to be able to predict the profile and the microstructure (grain size, grain shape, grain orientation, texture, voids, dislocation density, and roughness) of polycrystalline thin films as a function of their deposition conditions (temperature, flux distribution, deposition method, substrate geometry, materials).

For example, the semiconductor industry is moving towards using copper interconnect lines due to their decreased resistivity and increased resistance to electromigration[1]. Experiments by Ryu et al. have shown that the electromigration lifetime of (111)-textured Cu films is about four times longer than that of (100)-textured Cu films[2]. As line widths become comparable to the grain size, a 'bamboo' structure can eliminate the high diffusivity grain boundary transport paths, which can result in slower vacancy diffusion.[3] Therefore, the need to gain control over the microstructures of interconnect materials is becoming more important, and computer simulations can decrease the overall development cycle time.

Because of the importance of understanding the basic mechanisms of thin film growth, a variety of models have been developed in recent years. Some typical ones are: atomic level simulations[4,5], a micron scale model based on solving continuum equations numerically[6,7], a facet model with application in diamond simulation[8,9], and a model using "discs" to represent thousands of atoms[10,11].

In this work, we describe a model to simulate thin film growth, including deposition, nucleation, surface diffusion, grain growth and grain interaction. With some approximations, this model is capable of predicting, in two dimensional space, the thin film structure, such as the grain size, grain shape, grain orientation, and surface roughness.

In addition, we intend for the code to be “user-friendly”. We designed an open software package, which has an integrated Graphic User Interface (GUI). No third-party software is needed to interpret results, so that users can design and run simulations according to their own research interests.

MODEL DESCRIPTION

Assumptions

In order to get a model with reasonable simplifications that still represents the most important physical processes, we made the following assumptions:

- 1) This is a two dimensional simulation;
- 2) We describe facets & grain boundaries with line segments. Each facet will be described by one line segment, while grain boundaries are described by multiple line segments in order to depict the proper grain shape and film structure.
- 3) Each nuclei has its own orientation, which affects facet growth rates; because we only allow 0, 1, -1 as the index of zone axes, we only allow 26 zone axes in the 3D space. But each grain is allowed to rotate by any angle around the zone axis.
- 4) The nuclei density, initial size and texture are input parameters.

These assumptions limit the accuracy of the code, but they greatly reduce the computational cost, allowing the model to be run on a desktop PC and yield qualitative and semi-quantitative results for large systems within minutes.

Description of thin film structure in two-dimensional space

In reality, under a non-epitaxial growth condition, there are an infinite number of possible ways a grain can orient to the surface, with infinite possible zone axes perpendicular to the cross section plane. To simplify the model, we allow 0, 1, -1 as the index number for the zone axis, which contribute to a total of 26 directions in real space, namely the $\langle 100 \rangle$, $\langle 110 \rangle$, $\langle 111 \rangle$ families. A sophisticated mathematical algorithm has been developed to create the profile by selecting crystallographically correct facets, then rotate it around the zone axis randomly to create a nucleus with proper orientation.

Figure 1a shows one possible shape of a whole grain with $[0, -1, 1]$ zone axis. By cutting and rotating it through different angles, nuclei of different sizes and shapes can be formed, as shown in Figure 1b.

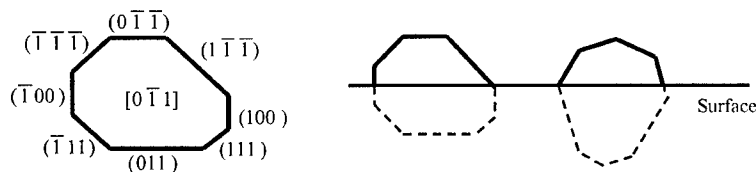


Figure 1. (a) A possible shape of a whole grain with $\langle 110 \rangle$ type zone;
(b) Two nuclei generated from the whole grain in (a)

One dimensional KLMC calculation

After atoms land on a surface, they will diffuse around. The diffusion rates determine the growth rate of each grain, and thus control the morphology and final texture of the film. Knowing the diffusion activation energies, it is possible to calculate the atomic flow rates between adjacent facets by a Kinetic Lattice Monte Carlo method. The results from a sophisticated three dimensional KLMC calculation can be put into our facet model as an input, but because of the complexity of the full scale KLMC methods, only the rates for Cu atoms diffusing from {100} to {110} and {111} have been achieved in the previous[10] 3D KLMC calculation.

In order to be able to simulate most of the FCC and BCC structure materials without involving complex three dimensional calculations, we developed a new one dimensional KLMC model to estimate the flow rates between facets. The major approximation we made in the 1D KLMC model is that we assume only atoms near the edge would be likely to diffuse to adjacent facets, whereas the adatoms landing in the center region will only contribute to the vertical growth of the facet. We define the length of the region, in which atoms can diffuse out, as the average step length. By our 1D KLMC model, we can calculate a statistical average of the percentage of deposited atoms which diffuse to the adjacent facet as a function of temperature.

Two dimensional facet model

Many factors can affect the nucleation rate of islands, such as temperature, gas pressure, deposition rates, contamination, defects, etc. At present, there is no good model for heterogeneous nucleation, therefore, the nucleation rate, nuclei size, and texture are treated as user-input parameters, as shown in Figure 2.

Experimental data	
Deposition flux (Atoms/nm.Sec)	10
Lattice Constant (Angstroms)	3.615
Calculate the flow rate	

Surface Preference	
<input checked="" type="radio"/> No Preference	
<input type="radio"/> (100)	<input type="radio"/> (110)
<input type="radio"/> (111)	
0 %	0 %
0 %	0 %

Simulation Limits	
Number of Nuclei	50
Total Length (nm)	1000
Facet Length (nm)	5
Facet Angle (degree)	70

Magnification	
Nucleation (times)	5
Grow I (times)	3

Render Facets	
<input checked="" type="radio"/> Yes	
<input type="radio"/> No	

Advanced settings OK

Figure 2. The main input window of the software package: FACET

After nucleation is finished, FACET determines facet growth rates based on deposition and diffusion between the facets, and diffusion from surface to the nuclei, as illustrated in Figure 3.

Deposition flux is defined by the user, in units of Atoms/nm·sec, i.e., the number of atoms landed on the surface per nanometer per second.

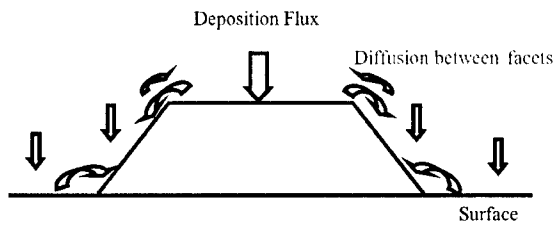


Figure 3. Deposition and diffusion events in the model

At every simulation time step, computer with FACET calculates the length of each facet, the number of atoms dropped on that facet, the number of atoms diffusing to and from the facet to adjacent facets and surfaces. Then, it calculates the net change of atoms on each facet, and translates that into the growth rate.

Many kinds of scenarios may happen during grain growth and interaction, Figure 4 shows how we generate a grain boundary, and how the grain boundary grows. Basically, we detect the approaching of two facets, and when they contact each other, we merge them and start a new grain boundary from that merging point. In the following growth steps, we calculate the position of the merging point dynamically, and use many small line segments to describe the track of the merging point, and thus form the grain boundary.

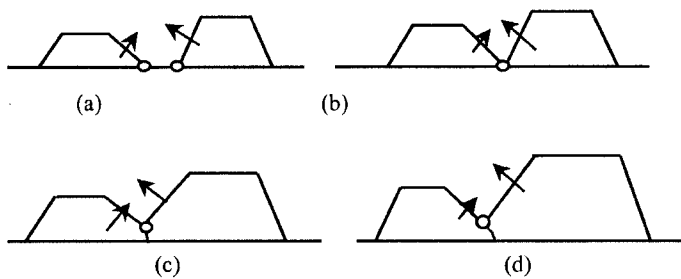


Figure 4. Two grains approaching to each other and forming a grain boundary

DISCUSSION

Figure 5 shows the results of 3D[10] and 1D KLMC calculations. As we can see, the shape of the fitted curves are the same, and the fitted function are very close too: the 3D model has the fitted function of $4X^{-1}$, while the 1D model provide $4.1X^{-1}$. More comparison will be conducted in the future work.

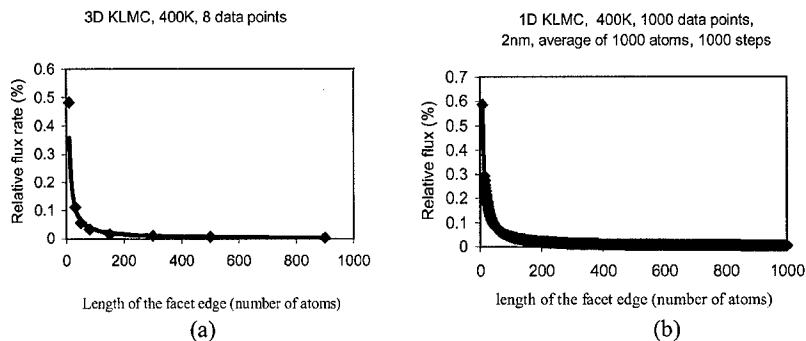


Figure 5. Percentage of atoms landing on (100) facet that diffuse to adjacent (110) facets as a function of facet size. The temperature is 400 K, and the deposition rate is 300 monolayer/s. (a) 3D calculation[10]; (b) 1D calculation with the average step length set to 2nm.

Figure 6a shows the results of deposition with a purely vertical flux, which means that all the atoms are coming in the direction normal to the surface. Figure 6b shows the results for a different flux condition, where each facet receives the same flux density. As we can see, the final structure in Figure 6b exhibits more grain coarsening phenomena, while Figure 6a exhibits a purely columnar, non-coarsening growth.

Most of the important experimental and simulation inputs were displayed in the upper section of the window; the middle section provides an overview of the film under investigation, and the lower section is the “zoom-in” of the overview, where users can choose a magnification, and browse the whole film by horizontal and vertical scroll bars. Simulation time indicators and length markers are also available in the main window. Different colors represent different type of facets: red for {100}, green for {110}, blue for {111}, thus the user can not only see the orientation directly, but also get the zone axes by calculating the dot product of any two facets of the interested grain.

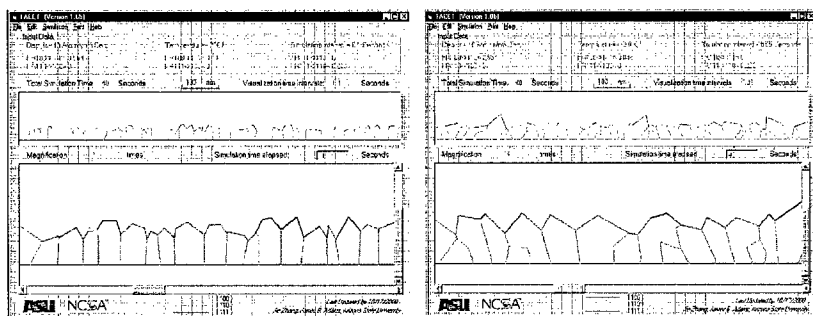


Figure 6. Final structure of deposited film with (a) direct bombarding flux (b) each facet has the same flux density. The fine prints in the frame explained the experimental data: Deposition rate 10 atoms/nm-sec.; Temperature 298K; Total simulation time 40 sec.; Magnification 3 times. Calculation results of integrated 1D KLMC simulator are also embedded in the frame.

CONCLUSION

We have constructed a new model to simulate thin film growth, combined with a visualization package with an easy-to-use Graphical User Interface. The beta version of FACET, Ver. 1.0b, has been put up on our web site for free download. <http://ceaspub.eas.asu.edu/cms/>

ACKNOWLEDGEMENTS

The authors wish to thank Zhiyong Wang and Youhong Li for useful discussions. We also thank Dr. Len Borucki of Motorola for many helpful discussions. We thank NSF for funding this work through grant ASC97-40300.

REFERENCES

- [1] J.M.E. Harper, K.P. Rodbell, J. Vac. Sci. Technol. B 15 (4), (1997), p.763
- [2]. C. Ryu, A.L.S.Loke, T.Nogami, S.S.Wong, Proceedings of IEEE International Reliability Physics Symposium(1997), p.201
- [3]. F.M. d'Heurle, I. Ames, Appl. Phys. Lett. 16 (1970) p.80
- [4]. Z.Wang, Y. Li, J.B. Adams, Surface Sci., 450, (2000), p. 51
- [5]. H.Huang, G.H.Gilmer, T.D. de La Rubia, J.Appl. Phys. 84(1998), p. 3636
- [6]. T.S. Cale, G.B. Raupp, J.Vac.Sci.Technol.B8(6), Nov/Dec (1990), p.1242
- [7]. T.S.cale, M.K.Jain, G.B.Raupp, J.Electrochem. Soc. (1990), p.1526
- [8]. Paritosh, D.J.Srolovitz, C.C.Battaile, X.Li, J.E.Butler, Acta mater. Vol. 47, No. 7, (1999), p. 2269
- [9]. Srolovitz, D. J., J. Vac. Sci. Technol., A4, (1986), p.2925.
- [10]. T.Smy, R.N.Tait, K.L.Westra, M.J.Brett, June12-13, 1989 VMIC conference p.292
- [11]. S.K.Dew, T.Smy, M.J.Brett, IEEE transactions on electron devices, Vol.39, No.7, July, (1992), p.1599

Calculation of Intrinsic Stresses and Elastic Moduli in Nonhomogeneous Thin Films

Pedro C. Andia, Francesco Costanzo, Gary L. Gray, and Thomas J. Yurick
Laboratory for Parallel and Computational Mechanics
Engineering Science and Mechanics Department, The Pennsylvania State University
University Park, PA 16802, USA

ABSTRACT

An approach is presented for the determination of the residual stresses and elastic moduli of particle systems resulting from computer simulations of particle or atomic deposition. The proposed technique is based on fundamental concepts of elasticity and is capable of capturing the variation of stresses and moduli as functions of position within the system. Application to a simple particle system consisting of a deposited thin film is demonstrated.

INTRODUCTION

One of the goals of nanotechnology is to design thin films with a desired set of properties. Therefore, it has become increasingly important to understand how the nanostructure of a thin film impacts its properties at all length scales. Relating the nanostructure of the TF to its mechanical properties is the goal of this work and is necessary for the model-based design of structurally stable TFs with complicated morphologies.

Different approaches have been developed to determine the mechanical properties of TFs. In general, previous work that has focused on evaluating residual stresses of TFs can be divided in two categories: experimental techniques and theoretical models. But this division is not completely distinct as each of them relies on the other and both assume that the TF is a plate-like structure.

The most popular experimental techniques perform curvature measurements. They are used independent of the work temperature and the nature of the stresses in the film (*i.e.*, compressive or tensile) [1, 2]. They relate the curvature of the TF to its internal stress state using a simple theoretical model that, in general, assumes an isotropically elastic material with a state of plane stress and small deflections.

Theoretical models have been developed to account for anisotropy and more general stress states [3]. Other theoretical approaches eliminate the assumption of small deflections by developing a geometrically nonlinear stress-deflection relation for TFs [4].

The methods discussed above are not immediately applicable to our objective. The reason is that they do not take into account the morphology of the film deposited on the substrate.

BASIC DEFINITIONS AND THEORETICAL FRAMEWORK

The derivations presented in this paper presuppose that the configuration of a system of particles is known (*e.g.*, via a simulation, such as a kinetic Monte Carlo (KMC) or a molecular dynamics (MD)). This configuration is assumed to be that of a solid system and is assumed to be consistent with the various input parameters necessary to perform the aforementioned simulation. It is important to note that no assumptions are made here concerning the spatial

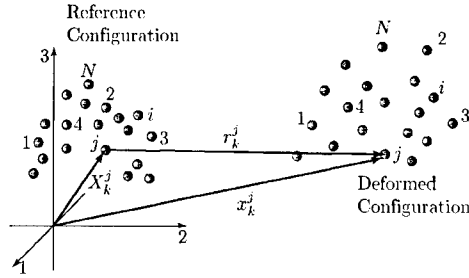


Figure 1. A particle system in its reference and deformed configurations.

arrangement of the system's particles, that is, the system can be crystalline, amorphous, or have any other microstructure.

With reference to Fig. 1, the system configuration provided by the aforementioned simulation will be referred to as a reference configuration. As discussed later, the calculation of the intrinsic stresses and elastic moduli requires that the system be subjected to a deformation. The configuration resulting from said deformation will be referred to as the deformed or current configuration. The various particles in the system are referred to by an index ranging from 1 to N , the total number of particles. The position of the j -th particle in the reference and deformed configurations will be denoted by X_k^j and by x_k^j , respectively, where the superscript ($j = 1, \dots, N$) denotes the particle number and the subscript ($k = 1, \dots, 3$) denotes the component of vectors along the corresponding coordinate direction. The position vector of a particle i relative to that of a particle j will be denoted by R_k^{ij} and r_k^{ij} for reference and deformed configurations, respectively.

The particles interact with one another by exerting inter-particle forces which represent the inter-particle bonds. These bonds are described via a potential energy function which will be denoted by f and which, in general, is a function of the particle positions. For the sake of simplicity, and without loss of generality, the potential energy of the bond between two particles i and j will be assumed to be only a function of the distance between the particles $f = f(r^{ij})$, $r^{ij} = \sqrt{r_k^{ij} r_k^{ij}}$, where r^{ij} denotes the distance between particles i and j and the summation convention has been used. We note here that our method allows other forms of the potential energy, for example, an f in which the orientation of one particle relative to another is important. It is understood that the bond potential to be used in the calculations described later *must* be the same as that used in the simulation which generated the reference configuration.

Constitutive Theory of an Isothermal Hyperelastic Material

Until the reference configuration is altered by bond breaking, the N particles form a conservative system whose total potential energy is the sum of all the bond potentials. From

a continuum viewpoint, such a system would behave like a hyperelastic material*. Furthermore, if the temperature of the system is not changed with respect to that assigned by the MD or KMC simulation, the material can also be considered to be isothermal. The constitutive theory for this class of materials is very well established (see, *e.g.*, Gurtin [5]). Therefore, only the results relevant to the present discussion will be reported herein.

The residual or intrinsic stress in a material is the stress that the material experiences in the absence of deformation. Hence, viewing a particle system as if it were a continuous body, elasticity theory indicates that the residual (or intrinsic) stress at a location X_m is given by

$$\sigma_{ij}^R(X_m) = \left. \frac{\partial W(E_{kl}, X_m)}{\partial E_{ij}} \right|_{E_{kl}=0}, \quad (1)$$

where $W(E_{kl}, X_m)$ is the strain energy density per unit volume and E_{ij} is the Lagrangian strain tensor. Formally, the Lagrangian strain tensor is defined as $E_{ij} = \frac{1}{2}(F_{ki}F_{kj} - \delta_{ij})$, where δ_{ij} is the identity second order tensor, F_{ij} is the deformation tensor, defined as $F_{ij} = \partial x_i / \partial X_j$, and $x_i(X_j)$ is the deformation function.

As far as the elastic moduli are concerned, these will be denoted by C_{ijkl} and are given by the second derivative of the strain energy function with respect to the strain:

$$C_{ijkl}(X_m) = \left. \frac{\partial^2 W(E_{pq}, X_m)}{\partial E_{ij} \partial E_{kl}} \right|_{E_{pq}=0}. \quad (2)$$

Thus, the residual stresses and elastic moduli of a system are easily computed if the strain energy density function is known as a function of the deformation gradient. Hence, in order to compute the residual stresses and elastic moduli in a particle system, one needs to translate the discrete information consisting of positions and bond potentials into a strain energy function which depends on a continuum notion of deformation. The *translation* from discrete-type information to continuum-type information is discussed in the next section.

From a Discrete System to an Equivalent Continuum Body

This section summarizes a strategy for the determination of a continuous function of position expressing the strain energy per unit volume of the particle system. That is, we outline how to determine a continuous body which is mechanically equivalent to the discrete system. The approach presented herein is not entirely new in that it has been proposed by Martin [6] and more recently used by Alber *et al.* [7]. An important element of novelty is represented by the fact that the approach outlined herein is generalized for use in particle systems which are amorphous instead of crystalline. Details of our approach can be found in [8].

It can be shown that the strain energy per unit volume of a continuum body, equivalent to the given particle system (evaluated at the centers of the selected subvolumes), is given by

$$W(E_{ij}, X_k^{\text{Center of } \Omega_i}) = \frac{1}{\text{Vol}(\Omega_i)} \sum_{p=1}^{N_{\Omega_i}} \left[\sum_{q=1}^{M_p} c^{n_p m_q} f \left(\sqrt{R_v^{n_p m_q} (2E_{vw} + \delta_{vw}) R_w^{n_p m_q}} \right) \right]. \quad (3)$$

*In simple words, a hyperelastic material is an elastic material whose mechanical behavior is dictated by a potential energy function of the deformation.

Equation (3), which can be explicitly computed if one knows particle positions and interparticle potentials, allows one to easily determine the intrinsic stresses and elastic moduli at the center of each subvolume. In fact, using Eqs. (1), (2) and (3) one obtains

$$\sigma_{ij}^R(X_k^{\text{Center of } \Omega_i}) = \frac{1}{\text{Vol}(\Omega_i)} \sum_{p=1}^{N_{\Omega_i}} \left(\sum_{q=1}^{M_p} c^{n_p m_q} \frac{1}{R^{n_p m_q}} \frac{\partial f}{\partial r} \Big|_{r=R^{n_p m_q}} R_i^{n_p m_q} R_j^{n_p m_q} \right), \quad (4)$$

and

$$C_{ijkl}(X_k^{\text{Center of } \Omega_i}) = \frac{1}{\text{Vol}(\Omega_i)} \sum_{p=1}^{N_{\Omega_i}} \left(\sum_{q=1}^{M_p} c^{n_p m_q} (A) R_i^{n_p m_q} R_j^{n_p m_q} R_k^{n_p m_q} R_l^{n_p m_q} \right). \quad (5)$$

where $A = [(\partial^2 f / \partial r^2 - r^{-1} \partial f / \partial r) / r^2]_{r=R^{n_p m_q}}$. Examples of the application of Eqs. (4) and (5) are presented in the next section.

RESULTS AND DISCUSSION

Intrinsic Stresses and Moduli of a Lennard-Jones Material

In this section, results are obtained from the analysis of a true molecular dynamics simulation. The potential used in this simulation is the celebrated Lennard-Jones potential (LJP) and has been nondimensionalized in the standard way (see, *e.g.*, Haile [9]). In the results that follow, the particles were deposited onto a substrate composed of a material with the same LJP as that of the incoming species and then the simulation was run for 1000 additional time steps during which time the average position of each particle was computed for use in the stress and moduli computations. We note that since the potentials for the substrate and for the deposited species are the same, we do not expect stresses due to misfit between the film and the substrate. That is, intrinsic stresses are only expected to arise from morphological features associated with those regions in which the perfect crystal is disrupted.

Figure 2 shows a planar thin film consisting of 2040 particles deposited via a MD simulation. The particles were introduced at random horizontal positions with an angle of incidence of 0° with respect to the vertical. Figure 2(a) shows the particle positions on a substrate 150 units wide. Figures 2(b)–(d) show the results of the application of Eqs. (4) and (5) to the particles whose positions are shown in Fig. 2(a). The size of the subvolumes used to compute the stresses and moduli are 0.5 units on a side. Figure 2(b) shows the 11-component of the elasticity tensor (according to engineering convention), clearly illustrating the nonuniformity of the moduli throughout the film. Figures 2(c) and (d) show the first two principal components of residual stress, σ_{11} and σ_{22} , respectively, within the thin film. Again we see the method capturing the *distribution* of residual stresses within the film and note that the resolution of stresses and moduli is dependent only on the size of the subvolumes used to compute the strain energy of the material.

Figure 3 shows a planar thin film grown under the same conditions as that shown in Figure 2, except that there are 2550 particles and the deposition angle is 80° with respect to the vertical instead of 0° . All of the comments made about Fig. 2 also apply here, but in addition we see that our method easily captures variations in stresses and moduli of very porous columnar thin films.

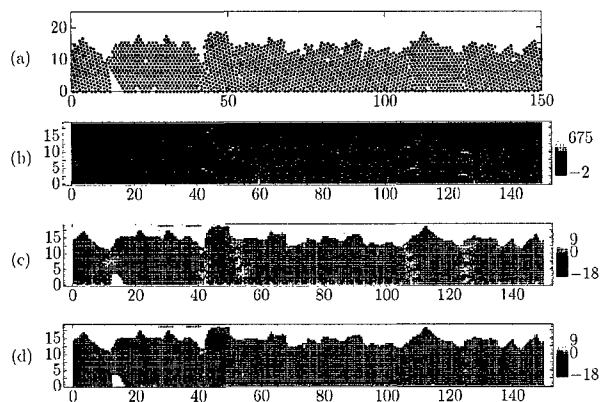


Figure 2. For the 0° deposition: (a) Particle positions, (b) 11-component of the elastic moduli, (c) first principal stress, and (d) second principal stress.

We note that in the principal stress plots in Figs. 2 and 3 most of the stresses are zero or nearly so. As discussed earlier and as expected, it is only in those locations in which the perfect crystal lattice has been disrupted that we see stresses which deviate significantly from zero.

CONCLUSIONS

We have developed a variational approach for the determination of elastic moduli and residual or intrinsic stresses in heterogeneous media. This method can be readily adapted for the determination of both the residual stresses as well as the elastic moduli of continuum media which are mechanically equivalent to the discrete media of interest. During the development, no assumptions were made concerning the spatial arrangement of the system's particles. The only information that the method requires is the location of each particle or group of particles in the system and the inter-particle or inter-group potential or potentials. We apply our approach to the results of two molecular dynamics simulations of a Lennard-Jones material with 2040 and 2550 particles to determine the residual stresses and elastic moduli.

ACKNOWLEDGMENTS

This research was supported, in part, by a grant from the National Science Foundation through the NSF grant no. CMS-9733653.

REFERENCES

- [1] W. D. Nix, Metallurgical Transaction A **20**, 2217 (1989).
- [2] E. D. Nicholson and J. E. Field, Journal of Hard Materials **5**, 89 (1994).

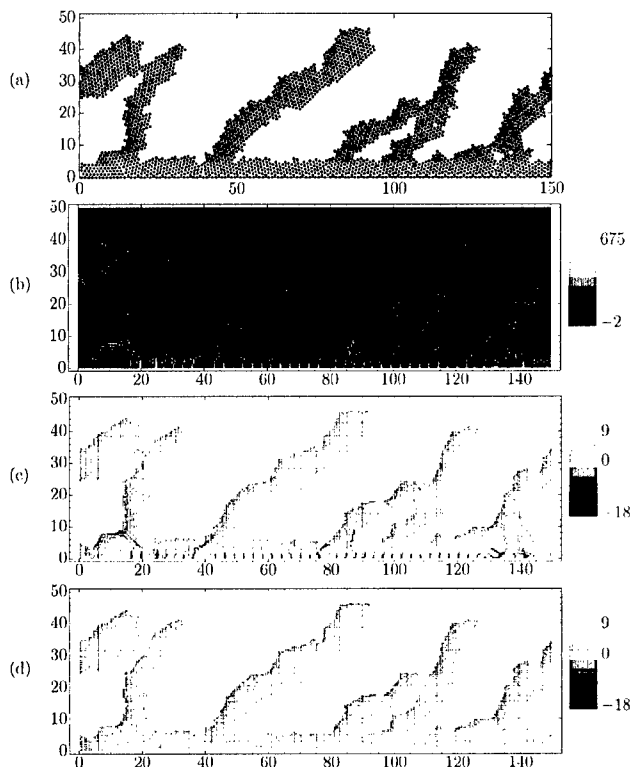


Figure 3. For the 80° deposition: (a) Particle positions, (b) 11-component of the elastic moduli, (c) first principal stress, and (d) second principal stress.

- [3] L. B. Freund, *Journal of the Mechanics and Physics of Solids* **44**, 723 (1996).
- [4] D. E. Fahnline, C. B. Masters, and N. J. Salamon, *Journal of Vacuum Science and Technology A* **9**, 2483 (1991).
- [5] M. E. Gurtin, *An Introduction to Continuum Mechanics*, Vol. 158 of *Mathematics in Science and Engineering* (Academic Press, Inc., San Diego, California, 1981).
- [6] J. W. Martin, *Journal of Physics C: Solid State Physics* **8**, 2837 (1975).
- [7] I. Alber *et al.*, *Philosophical Transactions of the Royal Society of London A* **339**, 555 (1992).
- [8] P. C. Andia, F. Costanzo, and G. L. Gray, in *Complex Mediums*, edited by A. Lakhtakia, W. S. Weiglhofer, and R. F. Messier (Proceedings of SPIE's 45th Annual Meeting, San Diego, CA, 2000), Vol. 4097, pp. 280–290.
- [9] J. M. Haile, *Molecular Dynamics Simulation: Elementary Methods* (John Wiley & Sons, New York, 1992).

Stresses in Thin Coatings from Curvature Measurements on Non-Planar Substrates

A. Wikström and P. Gudmundson

Department of Solid Mechanics, Royal Institute of Technology (KTH), SE-100 44
Stockholm, Sweden

ABSTRACT

Mechanical elastic and inelastic properties of thin coatings are often studied by means of the curvature measurement technique in combination with the Stoney formula. It is then implicitly assumed that the elastic substrate is initially flat which implies that the curvatures theoretically remain constant over the substrate. If the substrate has a slight initial curvature, a different situation arises. In this case, the curvatures will vary over the substrate. It has recently been shown that in spite of this, the stresses that appear in the thin coating will remain constant over the surface of the substrate. Therefore, measured curvatures can generally not be used to extract layer stresses without a proper compensation for the initial curvature. A general method for the extraction of mechanical properties from curvature measurements on non-planar substrates is outlined. The method is valid for linear as well as non-linear shell theories. The compensation needed to evaluate a coating on a circular substrate with spherical initial curvature is studied for all relevant parameters. The results are particularly discussed in relation to curvature measurements on silicon wafers.

INTRODUCTION

The curvature measurement technique in conjunction with the Stoney formula [1] is used extensively to obtain material properties of thin layers deposited on initially flat elastic substrates. This technique is commonly used in the microelectronics industry to obtain elastic and plastic properties of thin films and lines [2] as well as for many other applications such as thermal-barrier coatings, wear resistant coatings and organic paints. Curvature measurements may also under certain circumstances be used to obtain average stresses in passivated lines [3]. While there exists considerable information on the mechanics of flat substrates, the mechanics of initially curved substrates appears to be relatively unexplored. By treating the substrate/coating system as an anisotropic homogenized shell (see [4] for flat plates) it becomes clear that there is a close connection between certain material properties of the shell and average stresses in the thin coating. Recently, a correction applicable to circular substrates with spherical initial curvatures under the assumption of small deformation shell theory has been proposed [5]. With this correction, measured curvatures may be used in conjunction with the Stoney formula to obtain average stresses in the possibly inelastic coating. In this paper, the method is extended such that large deformations and arbitrary shallow initial curvatures may be treated. Furthermore, the correction for circular substrates with spherical initial curvatures and small deformation theory [5] is revisited and investigated for all relevant parameter combinations. Those parameters are the initial curvature, Poisson's ratio of the substrate and the scanning length used in the curvature measurements.

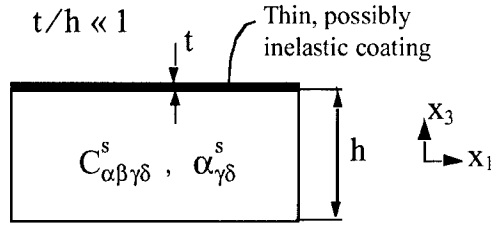


Figure 1. Representative volume element of a flat or initially curved shell. $C_{\alpha\beta\gamma\delta}^s$ and $\alpha_{\gamma\delta}^s$ represent the substrate plane stress stiffness tensor and coefficients of thermal expansion respectively. A cartesian coordinate system is defined by x_1 , x_2 and x_3 .

THEORY AND RESULTS

Consider the in-plane view of a representative cell of an elastic possibly non-flat substrate with a thin coating deposited on one side (Figure 1). From now on, the summation convention is utilized for Greek subscripts which range from 1 to 2. Let the whole system be subjected to a homogeneous temperature change ΔT . Consider a series expansion in terms of the small parameter $\delta = t/h$. It is clear that $\delta = 0$ represents a substrate without coating. Hence, the terms of order 0 and 1 may be defined by superscripts S and 1. The leading non-zero terms in the homogenized stiffness ($C_{\alpha\beta\gamma\delta}$), total middle surface strain ($\epsilon_{\alpha\beta}$) and curvature ($\kappa_{\alpha\beta}$) may be expressed as:

$$C_{\alpha\beta\gamma\delta} = C_{\alpha\beta\gamma\delta}^S \quad \epsilon_{\alpha\beta} = \alpha_{\alpha\beta}^S \Delta T \quad \kappa_{\alpha\beta} = \delta \kappa_{\alpha\beta}^1 \quad (1)$$

It is observed from eq. (1) that the average in-plane strain in the thin coating is governed by the in-plane strain of the substrate, therefore, stresses and strains in the thin coating are virtually unaffected by (small or moderate) curvatures and may therefore be modeled as a coating deposited on an elastic half plane. Hence, stresses in the coating may be treated as a surface tension and moment equilibrium may be utilized to derive a generalized Stoney formula. The constitutive law that describes the mid-surface bending response of a shallow shell with small ([6]) or large ([7]) deformations reads

$$M_{\alpha\beta} = \frac{h^3}{12} C_{\alpha\beta\gamma\delta}^S (\kappa_{\gamma\delta} - \beta_{\gamma\delta} \Delta T) \quad (2)$$

where $\beta_{\gamma\delta} \Delta T$ represents the curvature of a flat substrate that is subjected to a temperature change ΔT . Moment equilibrium and free boundaries give a Stoney type formula for a shallow shell:

$$\langle \sigma_{\alpha\beta} \rangle = - \frac{h^2}{6t} C_{\alpha\beta\gamma\delta}^S \beta_{\gamma\delta} \Delta T \quad (3)$$

where $\langle \sigma_{\alpha\beta} \rangle$ represent the average stresses in the coating. It is observed in eqs. (2-3) that $\beta_{\gamma\delta} \Delta T$ are constitutive parameters that characterize the effect of the thin coating on the elastic initially

curved substrate, therefore any material behavior of the thin coating is reflected solely in $\beta_{\gamma\delta}\Delta T$. Note that $\beta_{\gamma\delta}\Delta T$ represent homogenized material properties of the substrate/coating system and are thus independent of x_α . For an initially non-flat substrate there is a coupling between the bending and membrane state, therefore $\kappa_{\alpha\beta}$ is generally not equal to $\beta_{\gamma\delta}\Delta T$ as would be the situation for a flat plate. It is thus clear from eq. (3) that also for an initially curved substrate/coating system where the curvature varies from point to point, the stresses in the thin coating remain virtually unaffected by this curvature variation. Hence, useful data may be obtained from curvature measurements on non-flat substrates by solving for $\beta_{\gamma\delta}\Delta T$ which control average stresses through eq. (3). Consider a shell with an undeformed middle surface given by $z = -\tilde{\kappa}_{\alpha\beta}x_\alpha x_\beta / 2$, where $\tilde{\kappa}_{\alpha\beta}$ represent the initial curvature, that is subjected to a temperature change ΔT . The out-of-plane displacement perpendicular to the middle surface (w) may be expressed as

$$w = w(x_\alpha, C_{\alpha\beta\gamma\delta}^S, \alpha_{\alpha\beta}^S \Delta T, h, t, \tilde{\kappa}_{\alpha\beta}, \beta_{\gamma\delta} \Delta T) \quad (4)$$

Suppose curvature measurements are performed on an initially curved shell before and after a temperature change (ΔT) is applied. Let the scanning be performed on evenly spaced points along three directions denoted by s_i with the scanning length defined by $-c_i \leq s_i \leq c_i$. The output from each scan is a curvature that originates from a least squares fit of a straight line to the measured surface slope versus position along s_i [2]. The curvature changes that result from the change in temperature (ΔT) are denoted κ_i^{LS} . Assume for a moment that $\beta_{\gamma\delta}\Delta T$ are known in advance, then the measured curvatures (κ_i^{LS}) may be predicted theoretically by a proper continuous least squares minimization. By an extension of the results in [5], the measured curvatures along the direction s_i would be predicted as:

$$\kappa_i^{LS} = -\frac{3}{2c_i^3} \int_{-c_i}^{c_i} s_i \frac{\partial w}{\partial x_\alpha} \frac{\partial x_\alpha}{\partial s_i} ds_i \quad (\text{no sum over } i) \quad (5)$$

By replacing the predicted curvatures with the measured ones, eq. (5) represents three equations for the three unknowns $\beta_{\gamma\delta}\Delta T$. The analysis so far is valid for small and large deformation shell theory. A particularly simple case appears if small deformation shell theory is considered, then the solution becomes linear in the unknown material properties $\beta_{\gamma\delta}\Delta T$ such that:

$$w = \Delta T \beta_{\gamma\delta} F_{\gamma\delta}(x_\alpha, C_{\alpha\beta\gamma\delta}^S, \alpha_{\alpha\beta}^S \Delta T, h, t, \tilde{\kappa}_{\alpha\beta}) \quad (6)$$

and eq. (5) represents a linear system in the unknown material properties. Hence, for a given coating thickness and known substrate properties, useful results may be extracted from curvature measurements. Once $F_{\gamma\delta}$ have been computed, the unknown material properties $\beta_{\gamma\delta}\Delta T$ may be extracted by solving a set of three linear equations (eq. (5)). The determination of $F_{\gamma\delta}$ requires the solution of the thermoelastic boundary value problem for the substrate. The solution must be computed for three load cases where different components of $\beta_{\gamma\delta}\Delta T$ are set to unity.

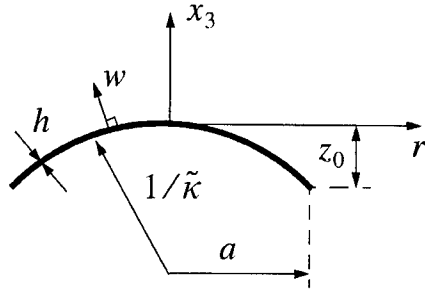


Figure 2. A circular shallow substrate/coating system. A nondimensional measure of the spherical initial curvature $\tilde{\kappa}$ is given by z_0/h .

For the particular case of a circular isotropic substrate with radius a and spherical initial curvature (see Figure 2), the problem has previously been solved analytically [5]. In this case $F_{\gamma\delta}$ may be expressed as:

$$F_{\gamma\delta} = \frac{1}{2}(a^2 f(\bar{r})\delta_{\gamma\delta} - x_\gamma x_\delta) \quad (7)$$

where $\delta_{\gamma\delta}$ represents the two-dimensional Kronecker delta and $\bar{r} = r/a$. The function $f(\bar{r})$ may be written as

$$f(\bar{r}) = C_1(\text{ber}_0(\xi\bar{r}) - 1) + C_2\text{bei}_0(\xi\bar{r}) + \frac{1}{2}\bar{r}^2 \quad \xi = \sqrt{48\left(\frac{z_0}{h}\right)^2(1-\nu^2)} \quad (8)$$

where $\text{ber}_n(x)$ and $\text{bei}_n(x)$ represent Kelvin functions, ν Poisson's ratio of the substrate and z_0 the initial deflection according to Figure 2. The constants C_1 and C_2 may be expressed as:

$$C_1 = \frac{1+\nu}{\xi\lambda} \{\text{ber}_1(\xi) + \text{bei}_1(\xi)\} \quad C_2 = -\frac{1+\nu}{\xi\lambda} \{\text{ber}_1(\xi) - \text{bei}_1(\xi)\} \quad (9)$$

$$\lambda = \sqrt{2}(1-\nu) \{\text{ber}_1^2(\xi) + \text{bei}_1^2(\xi)\} + \xi \{\text{ber}_0(\xi)(\text{ber}_1(\xi) - \text{bei}_1(\xi)) + \text{bei}_0(\xi)(\text{ber}_1(\xi) + \text{bei}_1(\xi))\}$$

By insertion of eq. (7) into eqs. (5-6), and solving the linear system, one obtains

$$\beta_{11}\Delta T = \frac{1}{\bar{g}(z_0/h, \eta, \nu)} \frac{(\kappa_1^{\text{LS}} + \kappa_2^{\text{LS}})}{2} + \frac{(\kappa_1^{\text{LS}} - \kappa_2^{\text{LS}})}{2} \quad (10)$$

where κ_1^{LS} and κ_2^{LS} are measured along x_α which has been chosen along the principal directions of measured curvatures. The nondimensional scanning length η is defined as $\eta = c/a$ where c is the scanning length. $\beta_{22}\Delta T$ is obtained by interchanging the subscript indices 1 and 2. The nondimensional function \bar{g} becomes:

$$\bar{g}(z_0/h, \eta, \nu) = \frac{3}{\eta^3} \int_0^\eta \bar{r} \left(\bar{r} - \frac{df(\bar{r})}{d\bar{r}} \right) d\bar{r} \quad (11)$$

The function \bar{g} is shown in Figure 3 for a fixed Poisson's ratio of 0.26 which corresponds to the in-plane Poisson's ratio of a Si wafer with the (111) direction perpendicular to the $x_1 - x_2$ plane. In Figure 4, the function \bar{g} is shown for a fixed scanning length of 0.75. Very often, the curvature is only measured in one direction, it is then commonly assumed that the layer is macroscopically isotropic. The second term in eq. (10) then vanishes and \bar{g} may be interpreted as the ratio between a measured curvature and the corresponding flat plate curvature. It is observed in Figure 3 that for a very small initial curvature, the correction \bar{g} is unity, and for a large initial curvature, the correction tends to zero. Hence, useful information can not be obtained from curvature measurements in this case. The reason for this is that when the initial curvature is large, the deformation becomes localized near the edge of the substrate. It is also observed that a compensation becomes necessary when $z_0/h > 0.5$. Note that the curvature near the center of the substrate ($\eta = 0$) changes sign when $z_0/h \approx 2$. It is seen in Figure 4 that the effect of Poisson's ratio on the correction \bar{g} may be important if $z_0/h \approx 1$.

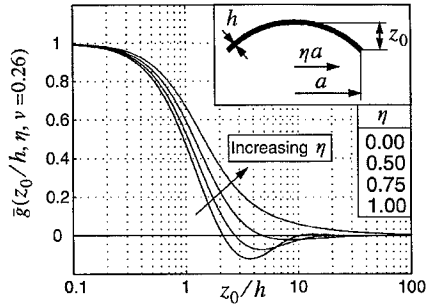


Figure 3. The correction $\bar{g}(z_0/h, \eta, \nu)$ (cf. eq. 10) for a Poisson's ratio of 0.26.

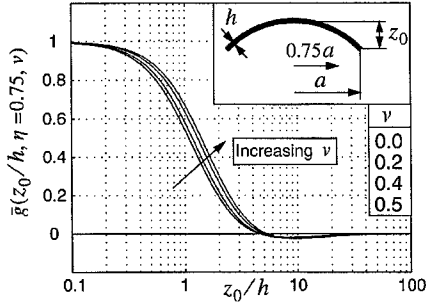


Figure 4. The correction $\bar{g}(z_0/h, \eta, \nu)$ (cf. eq. 10) for a relative scanning length of 0.75.

DISCUSSION AND CONCLUSIONS

It was first demonstrated (eq. 1) that stresses and strains in a thin coating during thermal cycling are primarily caused by substrate in-plane strains. Curvatures play a secondary role and may be viewed as an effect rather than a cause of stress build-up in the coating. Hence, it is meaningful to interpret curvature measurements also for situations when the curvatures vary over the substrate. This is exactly the situation when curvature measurements are performed on substrates which are initially non-flat. It has been shown (eq. 3) that the average stresses in the thin coating, and hence elastic as well as inelastic properties may be expressed in terms of coefficients of thermal curvature times temperature change ($\beta_{\gamma\delta}\Delta T$) for a homogenized thermoelastic shell. This is possible because the coating is thin as compared to the substrate which implies that the behavior of the whole substrate/coating system is predominantly elastic. A general method to correct measured curvatures in such a way that they can be used for the stress evaluation in thin coatings has been presented for small and large deformation shell theory. The method relies on a simulation of the curvature measurement technique in combination with thermoelastic solutions to linear or non-linear shell problems. Specifically, the correction required for curvature measurements on a circular substrate with spherical initial curvature [5] has been studied with respect to all relevant parameters. The general conclusions are: (a) It is meaningful and possible to extract stresses in thin coatings from curvature measurements on non-flat substrates. (b) The corrections are valid for elastic, inelastic and anisotropic coatings. (c) Corrections can be made for small and large deformation shell theory. Furthermore, for circular substrates with spherical initial curvature it is concluded that: (d) A compensation becomes necessary when the dimensionless initial curvature z_0/h is larger than about one half. (e) A large relative scanning length η makes it less urgent to correct the curvature measurements. (f) Since most materials have a Poisson's ratio in the range $0.25 < \nu < 0.35$, the influence on the correction becomes rather small.

REFERENCES

1. G. G. Stoney, "The tension of metallic films deposited by electrolysis", *Proc. Roy. Soc. Lond.*, **A82**, 172-175, (1909).
2. P. A. Flinn, S. Gardner and W. Nix, "Measurement and Interpretation of Stress in Aluminum-Based Metallization as a Function of Thermal History", *IEEE Transactions on Electronic Devices*, **ED-34**, No. 3, 689-699, (1987).
3. A. Wikström and P. Gudmundson, "Stresses in passivated lines from curvature measurements", *Acta Materialia*, **48**, 2429-2434, (2000)
4. A. Wikström, P. Gudmundson and S. Suresh, "Thermoelastic analysis of periodic thin lines deposited on a substrate", *J. Mech. Phys. Solids*, **47**, 1113-1130, (1999).
5. A. Wikström and P. Gudmundson, "Thermal deformation of initially curved substrates coated by thin inhomogeneous layers", *J. Appl. Mech.*, in press (2000).
6. A. W. Leissa and M. S. Qatu, "Equations of Elastic Deformation of Laminated Composite Shallow Shells", *J. Appl. Mech.*, **58**, 181-188, (1991).
7. Chen-Yuan Chia, "Nonlinear Analysis of Plates", McGraw-Hill Inc. p 96-99, (1980).

Modeling Stress and Failure in Shrinking Coatings

Herong Lei*, Lorraine F. Francis, William W. Gerberich, and L. E. Scriven

Department of Chemical Engineering & Materials Science

University of Minnesota, Minneapolis, MN 55455

ABSTRACT

Drying or curing of a coating after vitrification or gelation is accompanied by stress development. Evaporation of solvent, polymerization, cross-linking, and cooling all cause shrinkage, but adhesion of the coating to the substrate prevents shrinkage to a stress-free state. The interaction of shrinkage and restraint creates strain and stress. If the local stress grows above the local strength of the coating, it can produce cracking, delamination, or other defects.

A large deformation elastic model based on the Galerkin/finite element method is developed to analyze stress development in coatings subject to uniform shrinkage. The model is used to analyze effects of delamination and surface cracks. The strain energy release rates in both delamination and surface cracking are computed at different crack lengths. In both cases, results show that thicker coatings have larger energy release rates and are more vulnerable to cracking. A key conclusion of this modeling is that a crack can propagate only from an inherent flaw greater than a certain size. If the coating is thin enough so that the maximum energy release rate is less than the crack growth resistance, then no inherent flaws in the coating can grow into a crack, and so the coating remains crack-free. The model also shows how to calculate a critical coating thickness, i.e., the maximum thickness of a coating that can remain crack-free.

INTRODUCTION

Coatings produced by depositing liquid on a substrate can be solidified by solvent evaporation (drying), by polymerization and cross-linking reactions (curing), by cooling, and other means. Once they are solidified, evaporating more solvent, reacting further, cooling more, and so on, may cause considerable volume shrinkage. Because a coating is usually designed to remain anchored to its substrate, it can shrink only in the direction perpendicular to the substrate. Such restraint causes departure of the current state from the stress-free state. The departure is strain and is accompanied by stress that is greater the higher the current modulus of the coating.

The mechanisms of stress development in shrinking coatings have long been studied. Croll [1] was the first to develop a simple theory to estimate the "residual internal stress" in solvent-cast thermoplastic coatings. He assumed the drying was slow enough such that the concentration did not vary with depth in the coating. He took the stress to be solely in plane, uniform, and dependent on the decrease in volume fraction of solvent after it passed the level at which the coating solidified and thereby acquired an elastic modulus. Croll's predictions of final stress level matched fairly well with some measurements of final stress by the cantilever-deflection method.

* Current address: Eastman Kodak Company, Kodak Park, Rochester, NY 14652

In the coating process, contamination, suspended particles, and bubbles can all lodge at the coating/substrate interface. These sources can contribute small flaws that act as stress magnifiers. Cracks may form either at the interfacial plane between the coating and the substrate, causing delamination, or along the thickness, causing "mud cracking" [2]. Many experiments [3-6] show that there exists a critical cracking thickness for a given coating. Mud cracking and delamination can be avoided if the coating is thinner than this critical thickness.

In this paper, a nonlinear elastic model is developed in order to analyze stress development in coatings subject to uniform shrinkage. The Galerkin/finite element method is applied to the equations transformed to the domain of the original stress-free state. The solutions found in this way are used to analyze delamination and surface cracks. In order to take in account the relative large strains that usually exist in polymer coatings, the materials considered here are neo-Hookean rubber-like materials.

THEORY

To analyze stress development after solidification, the solidification point, which is stress free, is chosen as the original reference state. The positions of "particles" of nonvolatile material, most often polymer, that can support stress in this state are depicted by the vector field \mathbf{X} . Following further drying, cooling, and chemical reaction, these particles may be displaced to new positions \mathbf{x} , which define the current deformed state. The material deformation that accompanies displacement of particles from their positions in the original reference state to positions in the current state is described by the total deformation gradient

$$\mathbf{F} = \nabla_{\mathbf{X}} \mathbf{x} \quad (1)$$

Here $\nabla_{\mathbf{X}}$ is the divergence operator in the original reference state. The total deformation gradient tensor \mathbf{F} can be multiplicatively [7, 8] decomposed into the shrinkage deformation gradient \mathbf{F}^s and elastic deformation gradient \mathbf{F}^e

$$\mathbf{F} = \mathbf{F}^e \cdot \mathbf{F}^s \quad (2)$$

In isotropic materials the pure shrinkage from the original reference state to the intermediate state is isotropic, hence

$$\mathbf{F} = \alpha \mathbf{F}^e \quad (3)$$

The amount of shrinkage is measured by shrinkage ratio α , the cube of which is the ratio of the current volume to the original volume that occupied by the same amount of nonvolatile material. The elastic strain is conveniently represented by the left Cauchy-Green tensor [9]

$$\mathbf{B}^e = \mathbf{F}^e \cdot \mathbf{F}^{eT} \quad (4)$$

The coating generally achieves mechanical equilibrium much faster than solvent evaporation, cooling, or chemical reaction proceeding. Hence, shrinkage can be considered a quasi-static process. Then the appropriate form of the mechanical equilibrium equation is simply

$$\nabla \cdot \boldsymbol{\sigma} = \mathbf{0} \quad (5)$$

where $\boldsymbol{\sigma}$ is Cauchy stress, and the divergence operator ∇ is in the current state of the coating.

In this study, the coating, by hypothesis, follows the following constitutive equation

$$\boldsymbol{\sigma} = -\pi \mathbf{I} + G \mathbf{B}^e \quad (6)$$

in which G is the coating shear modulus and π is the hydrostatic pressure. Any material following the above constitutive equation is a neo-Hookean material. The condition of incompressibility in elastic deformation requires

$$\det(\mathbf{F}^e) = 1 \quad (7)$$

The situation considered is a shrinking coating on a rigid substrate. The boundary conditions are that at the interface between coating and rigid substrate, the nonvolatile material does not move, and at other boundaries, traction is zero.

Solutions of Eqs. (1-7) in terms of standard functions are available only for very special cases, such as shrinkage of a coating on a large flat substrate, shrinking spheres, and shrinking cylinders where the analysis can be simplified to one dimension [10]. For example, when the thickness is small compared with both width and length, the coating suffers only in-plane tensile stress σ_o , and that stress is related to the shrinkage ratio α by

$$\sigma_o = \frac{G}{\alpha^2} (1 - \alpha^6) \quad (8)$$

Plainly the stress level at a given degree of shrinkage is proportional to G , the shear modulus. When the volume change by shrinkage is small enough that the shrinkage ratio α is close to unity, this equation of in-plane stress reduces to Croll's relation [1] with Poisson's ratio $\nu = 0.5$ for an incompressible material.

As a coating dries, cools, or cures, the more its stress-free local state shrinks, the greater the strain and the greater the stress. Moreover, the greater the elastic potential energy stored in the coating. The existence of cracks, however, releases some stress and thus elastic energy. The total elastic energy P for a neo-Hookean material, according to Treloar [11], is the domain integral of the strain energy function,

$$P = \int \frac{G}{2} (I_{\mathbf{B}^e} - 3) dv \quad (9)$$

where $I_{\mathbf{B}^e}$ is the first invariant of \mathbf{B}^e . After elastic potential energy in the coating at different cracking area is evaluated, the energy release rate is just the negative derivative of the elastic potential energy on crack area.

RESULTS AND DISCUSSIONS

Delaminated coating. A rectangular coating with length l and thickness h on a rigid substrate is chosen to analyze the edge delamination. The coating considered is under plane-strain condition and has a plane of reflective symmetry so that only one-half needs to be considered. Figure 1(a) shows the contours of in-plane stress σ_{xx} for a coating $6 \mu m$ in total length and $1 \mu m$ in thickness, $1.5 \mu m$ from both ends of which are delaminated. The uniform shrinkage ratio (α) used is 0.9. As shown in the contour plot, stress is concentrated and magnified near the crack tip, and this may give rise to more delamination. The delaminated region that is not close to the crack tip, the stress is almost fully released.

In the calculation of elastic potential and energy release rate, the shrinkage ratio $\alpha = 0.98$ is used. This value is chosen because it is close enough to 1 so that strain is small and the neo-Hookean incompressible material should behave closely to linear elastic material. When the coating length is much larger than coating thickness an asymptotic solution of energy release

rate is available by considering the change in energy before and after the crack propagates a small amount. For an infinitely long coating after shrinkage α , its delamination energy release rate per unit width is [10]

$$\vartheta = \frac{G\alpha}{2}(1 + \alpha^6 - 2\alpha^3)h \quad (10)$$

When $\alpha = 0.98$, $\vartheta = 0.0016946Gh$, which is plotted in Figure 1(b) and marked as 'Solution from large deformation'.

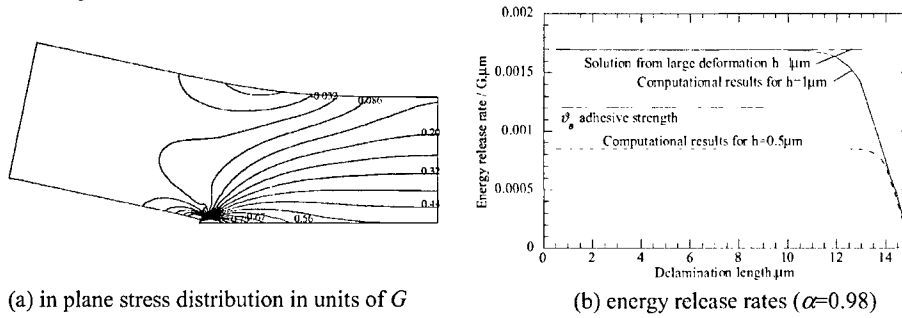


Figure 1. Edge

A sample of $30 \mu m$ in length and $1 \mu m$ in thickness is used to calculate elastic energy release rate. This example is symmetric about its mid-plane, and so it suffices to analyze just one half. The energy release rate calculated by virtual crack extension method [12] is shown in Figure 1(b). Result of energy release rate from Galerkin/finite element method is very close to the theoretical result from equation (10) except when the coating is close to complete delamination. Whenever the adhesive energy of the coating to the substrate is higher than the energy release rate at the plateau, the coating will not delaminate. If it is lower than the energy release rate at the plateau, once a crack starts, it will propagate until the energy release rate is lower than the adhesive energy, or at some point, which is close to complete separation of the coating from the substrate.

Figure 1(b) also shows the energy release rate if the coating thickness is $0.5 \mu m$. Compared with that of thickness $1 \mu m$, it has lower energy release rate. This agrees with Eq. (10), where the energy release rate for an asymptotic long crack is proportional to coating thickness. A thicker coating has more elastic energy to release than a thinner coating, and this makes the thicker coating more vulnerable to delamination. For instance, if the interface between coating and substrate has an adhesive strength, ϑ_a as marked in Figure 1(b), then the thicker coating will delaminate, but the thinner one will not. From Eq. (10), the critical coating thickness h_{CCT} for delamination is

$$h_{CCT} = \frac{2\vartheta_a}{G\alpha(1 + \alpha^6 - 2\alpha^3)} \quad (11)$$

Surface cracking. The in-plane stress distribution for a periodic cracking pattern is shown in Figure 2(a). Here, the periodicity is $l = 6 \mu m$ and the coating thickness $h = 1 \mu m$. The

shrinkage ratio is 0.9, and the coating is attached to a rigid flat substrate. Again, stress is magnified near crack tip, and once again high stress concentration near crack tip provides the driving force for further crack advance. Stress near the crack surface is partly released by the crack. Away from the crack tip, stress tends to be uniformly distributed.

The exact solution of the energy release rate for the periodic cracking of a coating on a rigid substrate is not available. When the coating thickness is much less than the periodicity and much larger than the crack length, or $a \ll h \ll l$, the influence of neighboring cracks and rigid substrate on the small crack is negligible. The energy release rate for a crack in an infinite sample, which has previously been solved, can be used. For incompressible material, $\nu=0.5$ and $E = 3G$, then

$$\dot{\vartheta} \approx \frac{G}{\alpha^4} (1 - \alpha^6)^2 a \quad , \quad (12)$$

in which the stress from Eq. (8) has been used. When, due to the symmetry, only half of the sample is considered, only half of the elastic energy in Eq. (12) needs to be taken into account. At shrinkage ratio of 0.98

$$\dot{\vartheta} / G \approx \frac{1}{2\alpha^4} (1 - \alpha^6)^2 a = 0.0070644a \quad . \quad (13)$$

The energy release rate is linearly related to crack length a and independent of coating thickness h . This estimation of energy release rate is plotted in Figure 2(b).

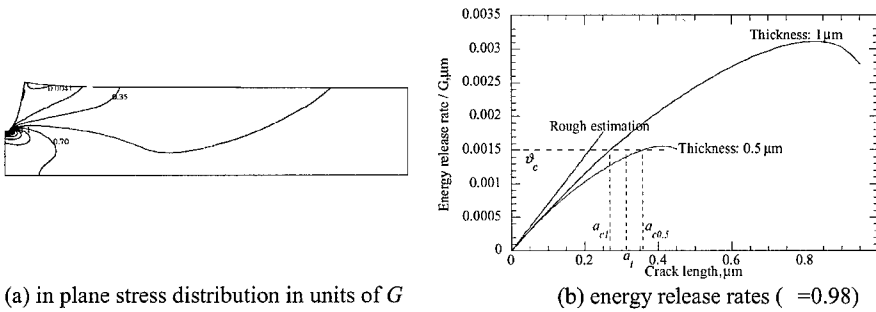


Figure 2. Periodic surface

Elastic energies for coatings subjected to a shrinkage ratio of 0.98 with periodic cracks having $30 \mu m$ spacing were calculated. Energy release rates from the virtual crack extension method are shown in Figure 2(b). Referring to Figure 2(b) when crack is small compared with coating thickness, energy release rates are nearly independent of coating thickness and linearly related to crack length. This is consistent with the rough estimation using Eq. (13). When the crack size is comparable to the coating thickness, the influence from the rigid substrate becomes important and the thickness effect becomes larger. The variation of energy release rate with crack length shows that the energy release rate rises in most of the crack depth. When the inherent flaw size a_i in a coating is large enough to make the energy release rate exceed the cohesive energy, $\dot{\vartheta}_c$, the flaw or crack grows, and it doesn't stop until it's close to the substrate. Comparing the energy release rate curves for a coating thickness of $1 \mu m$ and $0.5 \mu m$ shows that the thicker coating has a larger energy release rate and it is more vulnerable to cracking. As

schematically illustrated in Figure 2(b), the intersections of the coating cohesive strength ϑ_c and energy release rates are the critical crack lengths, $a_{c0.5}$ and a_{c1} for a $0.5\ \mu\text{m}$ and a $1\ \mu\text{m}$ coating respectively, where $a_{c1} < a_{c0.5}$. If the inherent flaw size of a_i in the coating falls between a_{c1} and $a_{c0.5}$, or $a_{c1} < a_i < a_{c0.5}$, then the flaw in the $1\ \mu\text{m}$ coating propagates and becomes a crack. For the $0.5\ \mu\text{m}$ coating it is crack-free since its energy release rate is not high enough to make inherent flaws to propagate.

Therefore, from the curve of the energy release rate and the cohesive energy ϑ_c , which is a material property, the critical flaw size to make cracking initiate can be estimated. The critical flaw size a_c in thinner coating is larger than that of thicker coating. The critical coating thickness (CCT) is the coating thickness when the inherent flaw size equals critical flaw size. A coating thickness above this critical thickness will crack because the size of inherent flaws exceeds the critical flaw size. The existence of critical coating thickness has been shown in many experiments, especially in ceramic coatings [3-6]. If a coating is so thin that the whole energy release rate curve is below the critical cohesive energy, no inherent flaw size can make a crack propagate and the coating remains free of cracks.

SUMMARY

An elastic model was developed to analyze stress and failure in shrinking coatings. The model was solved for plane-strain deformation by Galerkin/finite element technique. For delaminated coating, stress is highly magnified near the crack tip, but stress is almost completely released in the delaminated section. In surface cracking, stress near the crack surface is partially released, and high stress concentration near the crack tip provides the driving force for further cracking.

The virtual crack extension method was used to calculate energy release rates in delamination of a coating from a substrate and surface cracking. The variation of energy release rate with crack length suggests that a thicker coating has more energy to release than a thinner coating, thus the thicker coating is more vulnerable to delamination and surface cracks. The critical coating thickness (CCT), where the coating starts to delaminate or the surface starts to crack, can be evaluated.

REFERENCES

1. S. G. Croll, *J. Appl. Polym. Sci.*, **23**, 847 (1979).
2. H. Colina, L. de Arcangelis, and S. Roux, *Phys. Rev. B*, **48** 3666-3676 (1993).
3. T. J. Garino, *Mater. Res. Soc. Symp. Proc.*, **180**, 497-502 (1990).
4. R. C. Chiu, T. J. Garino, and M. J. Cima, *J. Am. Ceram. Soc.*, **76** 2257-2264 (1993).
5. F. F. Lange, *Science* **273** 903-909 (1996).
6. J. A. Payne, *Stress evolution in solidifying coatings*, Ph.D. Thesis, University of Minnesota (1998).
7. E. H. Lee, *J. Appl. Mech.*, **91** 1 (1969).
8. S. Y. Tam, L. E. Scriven, and H. K. Stolarski, *Mater. Res. Soc. Symp. Proc.*, **356**, 547 (1995).

9. L. E. Malvern, *Introduction to the mechanics of a continuous medium*, Prentice-Hall Inc., New Jersey (1969).
10. H. Lei, *Flow, deformation, stress and failure in solidifying coatings*, Ph.D. Thesis, University of Minnesota (1999).
11. L. R. G. Treloar, *Introduction to polymer science*, Wykeham, London (1970).
12. N. Miyazaki and T. Watanabe, *Eng. Fract. M.*, **22** 975-987 (1985).

A Method to Simulate the Interface-Diffusion in Solid-State Bonding-Processes Considering the Elastic Deformation

Takehiko Ito, Shigeki Saito, Kunio Takahashi and Tadao Onzawa

Department of International Development Engineering,
Faculty of Engineering, Tokyo Institute of Technology,
452, 1st Ishikawadai bldg., 2-12-1, O-okayama, Meguro-ku, Tokyo, Japan 152-8552

ABSTRACT

We propose a new method to simulate the interface diffusion in the solid-state bonding-process. This method is more significant under the condition of low pressure and low temperature. It is available for the bonding of two bodies which consist of the atoms of the same kind and have slight surface roughness. In a conventional method, the elastic deformation during the bonding process is considered. The interface diffusion is enhanced and the bonding time decreases when the external pressure changes at appropriate frequency. In order to clarify the enhancement effect of changing the pressure, we examine three cases, i.e., the 1st pressure type is constant pressure, the 2nd type is zero pressure, and the 3rd type is the on-off pressure. Our results suggest the on-off pressure decreases the required time for the perfect bonding if we choose on appropriate frequency.

INTRODUCTION

Conventional solid-state bonding-process is usually performed in vacuum at high temperature, at which the diffusion is activated. The rate of the bonding process is determined at least by four fundamental mechanisms; the plastic deformation, the creep deformation, the interface diffusion and the volume diffusion. A precise process is possible under the condition of low pressure and low temperature, under which the interface diffusion is dominant. Since the interface diffusion proceeds at a low rate, the bonding process requires an extremely long time under that condition. It is important to decrease the bonding time.

We calculate the stress distribution at the interface between the bodies based on Johnson's theory[1]. In the presence of the adhesion, Johnson showed the relation between the external pressure, the surface deformations and the contact width for the two elastic wavy surfaces, which have sinusoidal undulations.

The flux of the interface diffusion is proportional to the gradient of the stress distribution. The stress distribution changes dramatically and the interface diffusion becomes large in the transient state compared to the steady state. The diffusion could be enhanced when the external pressure is changed at appropriate frequency according to the transient behavior. This method examines the enhancement effect and the decrease of the bonding time. We define the external pressure changing at high frequency as 'on-off pressure type'. In a conventional method, the elastic deformation during the bonding process is not perfectly considered[2]. We discuss the advantage of the on-off pressure type considering the elastic deformation during the process.

THEORY

Model

We simulate the solid-state bonding-process for an ideal material in a two-dimensional model (Figure 1). We assume the bodies are represented by the elastic half-spaces and have

surface roughness. The amplitudes of the profiles are assumed extremely small compared to the wavelength. The external pressure f is applied to the bodies in the normal direction to the surfaces. The bonding process is performed under the condition of low temperature and low pressure. We assume the interface diffusion is dominant. Surfaces are assumed to have sinusoidal undulations before the surfaces contact. The surface profiles are assumed

$$y_{0a}(x) = h_a \left\{ 1 - \cos \left(\frac{2\pi x}{\lambda} \right) \right\}, \quad y_{0b}(x) = -h_b \left\{ 1 - \cos \left(\frac{2\pi x}{\lambda} \right) \right\} \quad (1)$$

where h_a and h_b are the amplitudes, and λ is the wavelength of each body. They have the relation of $h_a \ll \lambda$ and $h_b \ll \lambda$. The surface and interface profiles, defined as $y_a(x, t)$ and $y_b(x, t)$, change according to the progress of the interface diffusion and are superposed by two component parts:

$$y_a(x, t) = y_a^*(x, t) + u_a(x, t), \quad y_b(x, t) = y_b^*(x, t) + u_b(x, t) \quad (2)$$

where t is the bonding time, u_a and u_b are the elastic deformation, and y_a^* and y_b^* are the permanent deformation. We define y as $y = y_a - y_b$ in order to simplify the equations. We also define u as $u = u_a - u_b$ and y^* as $y^* = y_a^* - y_b^*$. Then $y = 0$ and $u = -y^*$ at the interface ($-a < x < a$).

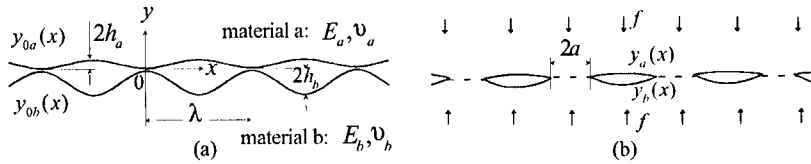


Figure 1. A two-dimensional model for the bonding process. (a) The surface profiles before the bonding, $y_{0a}(x)$ and $y_{0b}(x)$. (b) The partial contact on the strips of width $2a$ during the bonding process under the external pressure f .

Stress distribution and contact width

The external pressure $f(t)$ is written as the superposition of $f_1(t)$ and $f_2(t)$, $f(t) = f_1(t) + f_2(t)$. The stress distribution at the interface $p(x, t)$ is also written in the form:

$$p(x, t) = p_1(x, t) + p_2(x, t) \quad (3)$$

$p_1(x, t)$ is the stress distribution when the energy of the interface $\Delta\gamma$ is imaginarily reduced to 0, and the external pressure $f(t)$ is reduced to $f_1(t)$ while remaining the contact area ($-a < x < a$) adhered together[1]. $p_2(x, t)$ is the stress distribution when the pressure $f_2(t)$ is loaded to a plane which contains an array of equally spaced cracks, each of length $\lambda - 2a$. $p_2(x, t)$ is written as

$$p_2(x, t) = f_2(t) \left\{ 1 - \left(\frac{\cos \psi_a}{\cos \psi} \right)^2 \right\}^{-\frac{1}{2}}, \quad (-a(t) < x < a(t)) \quad (4)$$

where $\psi = \pi x / \lambda$, $\psi_a = \pi a / \lambda$ and $f_2(t) = -\{(2E_{ab}\Delta\gamma/\lambda) \tan \psi_a\}^{1/2}$. E_a and E_b are the elastic moduluses and $1/E_{ab} = 1/E_a + 1/E_b$ is formed. The differential of $u(x, t)$ is written as the integral equation[3]:

$$\frac{\partial u}{\partial x} = \frac{2}{\pi E_{ab}} \sum_{k=-n}^n \int_{L_k} \frac{p(s, t)}{s-x} ds \quad (5)$$

where $n \rightarrow \infty$ and L_k is the open interval $(-a + k\lambda, a + k\lambda)$. Since we can not solve the integral equation analytically, we approximate $n = N (\neq \infty)$ in the equation (5). Then the solution $p_1(x)$ is [4]:

$$p_1(x) = F_1(x) + F_0(x) \quad (6)$$

where $F_1(x)$ and $F_0(x)$ is written in the forms

$$F_1(x) = -\frac{E_{ab}}{2\pi} G(x) \sum_{j=-n}^n \int_{L_j} \frac{1}{G(s)} \frac{\partial u(s)}{\partial s} \frac{ds}{s-x}, \quad F_0(x) = G(x) \sum_{k=-n}^n \frac{c_k}{x+a-k\lambda} \quad (7)$$

where c_k is written in the form

$$\begin{pmatrix} c_{-N} \\ c_{-N+1} \\ \vdots \\ c_N \end{pmatrix} = \begin{pmatrix} W_{-N,-N} & W_{-N,-N+1} & \dots & W_{-N,N} \\ W_{-N+1,-N} & W_{-N+1,-N+1} & \dots & W_{-N+1,N} \\ \vdots & \vdots & \ddots & \vdots \\ W_{N,-N} & W_{N,-N+1} & \dots & W_{N,N} \end{pmatrix}^{-1} \begin{pmatrix} f\lambda - \int_{L_{-N}} F_1(x) dx \\ f\lambda - \int_{L_{-N+1}} F_1(x) dx \\ \vdots \\ f\lambda - \int_{L_N} F_1(x) dx \end{pmatrix} \quad (8)$$

$G(x)$ and $W_{j,k}$ are

$$G(x) = \prod_{k=-N}^N \left| \frac{x+a-k\lambda}{x-a-k\lambda} \right|^{\frac{1}{2}}, \quad W_{j,k} = \int_{L_j} \frac{G(x)}{x+a-k\lambda} dx \quad (9)$$

Since $p_1(x)$ is the stress distribution without the effect of the adhesion $\Delta\gamma$, the equation is formed:

$$\lim_{|x| \rightarrow |a| - 0} p_1(x) = 0 \quad (10)$$

We obtain the solution of $p(x)$ and a from above equations. When especially $N = 0$,

$$\lim_{|x| \rightarrow |a| - 0} F_1(x) = 0 \quad (11)$$

is formed at any value of f and a . Then $c_0 = 0$, $F_0(x) = 0$. $p_1(x)$ is written as

$$p_1(x) = -\frac{E_{ab}}{2\pi} \left(\frac{a+x}{a-x} \right)^{\frac{1}{2}} \int_{-a}^a \left(\frac{a-s}{a+s} \right)^{\frac{1}{2}} \frac{\partial u}{\partial s} \frac{ds}{s-x} \quad (12)$$

The correlation between $f_1\lambda$ and the integral of $p_1(x)$ is

$$f_1\lambda = \int_{-a}^a p_1(x) dx \quad (13)$$

We obtain the solution of a from the equation (13).

Permanent deformation

We define J as $J(x, t) = J_a(x, t) + J_b(x, t)$, where J_a and J_b are the flux of the interface diffusion of each body. Then J is assumed as $J(x, t) = -(D/k_0T)(\partial p/\partial x)$, where $D = D_a + D_b$, k_0 is the Boltzmann constant, and T is the absolute temperature of the atmosphere [2], [5]. D_a and D_b are the coefficients of the interface diffusion of the bodies. We assume the flux of the surface diffusion to be negligible compared to the flux of the interface diffusion.

Then the differential of the permanent deformation $\partial y^*(x)/\partial t = \text{constant}$ at the surface ($a < |x| < \lambda/2$). $\partial y^*(x)/\partial t$ is written as

$$\frac{\partial y^*}{\partial t} = \begin{cases} \omega \frac{\partial J(x)}{\partial x}, & (|x| < a) \\ -\frac{2\omega}{\lambda - 2a} \frac{\partial J(a)}{\partial x}, & (a < |x| < \frac{\lambda}{2}) \end{cases} \quad (14)$$

where $\omega = \delta_a \Omega_a + \delta_b \Omega_b$. δ_a and δ_b are the interface thicknesses. Ω_a and Ω_b are the atomic volumes.

Stress and permanent deformation of atoms

We consider the atomic size, which diameters are $d (= d_a = d_b)$. The equations $J_a = J_b$, $k_a = k_b$, $D_a = D_b$, $\delta_a = \delta_b$ and $\Omega_a = \Omega_b$ are formed because the bodies consist of the atoms of the same kind. Since we assume the atomic size at the interface (Figure 2), $a = (k + 1/2)d$, ($k = 1, 2, \dots, n_\lambda$) is possible. The stress at the atom of the interval $((k - 1/2)d, (k + 1/2)d)$ is defined as

$$\bar{p}[k] = \frac{1}{d} \int_{(k-1/2)d}^{(k+1/2)d} p(x) dx, \quad (k = 0, \pm 1, \pm 2, \dots, \pm n_a) \quad (15)$$

The differential of the permanent deformation $\bar{y}^{*'}[k]$ is also defined as

$$\bar{y}^{*'}[k] = \begin{cases} -\frac{D\omega}{k_0 T} \frac{\bar{p}[k+1] + \bar{p}[k-1] - 2\bar{p}[k]}{d^2}, & (k = 0, \pm 1, \dots, \pm(n_a - 1)) \\ 0, & (k = \pm n_a) \\ \frac{2D\omega}{k_0 T(\lambda - 2a)} \frac{p[n_a] - p[n_a - 1]}{r}, & (k = \pm(n_a + 1), \dots, \pm n_\lambda) \end{cases} \quad (16)$$

$\partial y^*/\partial t$ is found by the interpolation of $\bar{y}^{*'}$.

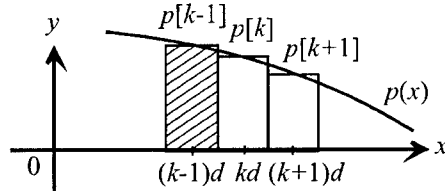


Figure 2. The model of the stresses on the atoms, $p[k]$, ($k = 0, \pm 1, \dots, \pm n_a$).

CALCULATED RESULTS AND DISCUSSION

We simulate the bonding process for an ideal material. Their material constants are showed on Table I. They are the same as those of Cu except the yield stress. In this study, the yield stress is assumed to be infinite because of the calculation time.

We adopt the approximation $N = 0$. Johnson showed the relation between a and f at the time of $t = 0$ which did not adopt the approximation. In order to examine the errors derived from the approximation $N = 0$, we compare our result with Johnson's result at $t = 0$ (Figure 3).

We calculate the required time for the perfect bonding in three cases of the external pressure $f(t)$ (Figure 4). When $f(t)$ is constant pressure or zero pressure, the contact width a increases at a high rate at the transient state immediately after starting the bonding process (Figure 5). By changing $f(t)$ at high frequency, the transient phenomena occurs at the moment of changing the pressure, and the bonding time decreases compared to the case of the constant pressure. As a result, we decrease the bonding time when we change $f(t)$ at appropriate frequency. In this study, an infinite yield stress is assumed in order to reduce the load of the calculation. The enhancement of the diffusion would be also possible for the small bonding pressure.

Table I. Material constants used in this analysis.

Constant	Dimension	Value	Constant	Dimension	Value
$E_a (= E_b)$	$(\times 10^{11} \text{ Pa})$	1.36	$h_a (= h_b)$	$(\times 10^{-9} \text{ m})$	2.56
$\nu_a (= \nu_b)$		0.35	$\delta_a (= \delta_b)$	$(\times 10^{-10} \text{ m})$	1.81
$d_a (= d_b)$	$(\times 10^{-10} \text{ m})$	1.28	$\Omega_a (= \Omega_b)$	$(\times 10^{-29} \text{ m}^3)$	1.19
$D_a (= D_b)$	$(\times 10^{-26} \text{ m}^2/\text{s})$	9.70	T	(K)	273.0
$\Delta\gamma$	(N/m)	1.0	σ_y		∞
λ	$(\times 10^{-8} \text{ m})$	2.56			

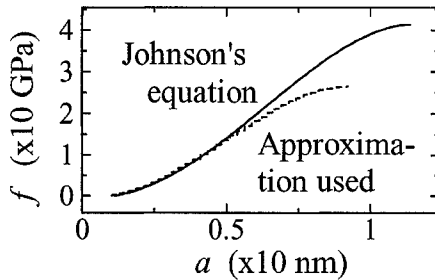


Figure 3. The correlation between the external pressure f and the half of the contact width a at the time of $t = 0$ (before the diffusion starting). This figure shows the errors derived from the approximation $N = 0$ compared to Johnson's equation.

CONCLUSIONS

This study suggests a new method to simulate the solid-state bonding-process under the condition of low pressure and low temperature. We examine the enhancement effect of changing the external pressure on the interface diffusion. We simulate the bonding process in three cases of the pressure; the constant pressure, the zero pressure and the on-off pressure. As a result, the on-off pressure decreases the required time for perfect bonding compared to the case of the constant pressure.

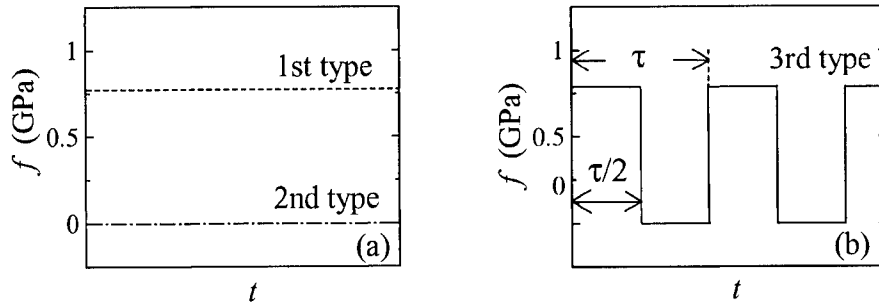


Figure 4. Three types of the external pressure f as a function of the bonding time t . (a) The 1st type is the constant pressure; the 2nd type is zero pressure; (b) the 3rd type is the pressure changed in the cycle, τ .

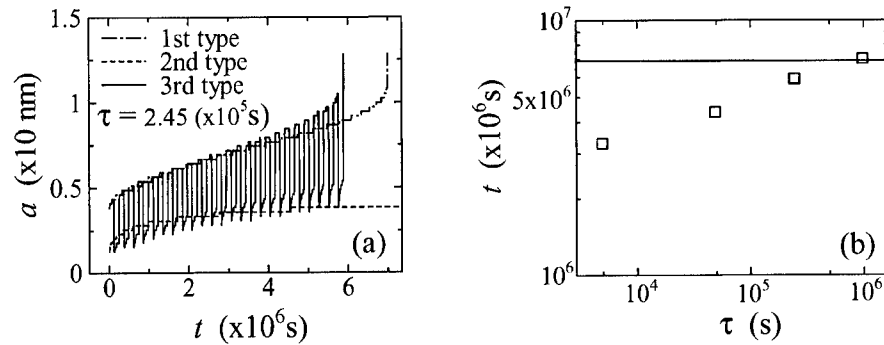


Figure 5. (a) The process of increasing the half of the contact width a . This figure shows the enhancement effect of changing the external pressure f ; the cycle of the 3rd pressure type is τ . (b) The correlation between the cycle of changing the pressure τ and the bonding time t ; — is the bonding time by the 1st pressure type.

REFERENCES

1. Johnson, K. L., The adhesion of two elastic bodies with slightly wavy surfaces, *Int. J. Solids Structures*, **32-3/4**, 423-430 (1995).
2. Nishiguchi, K., Takahashi, Y. and Takahashi, K., Transient behaviour of interface diffusion in solid state bonding and the enhancement effect, *J. Japan Welding Society*, **4-3**, 586-591 (1986), Japanese.
3. Johnson, K. L., *Contact mechanics*. (Cambridge University Press, London, 1985). p. 11-20.
4. Mikhlin, S. G., *Integral Equations*. (Pergamon Press), p. 126-133.
5. Raj, R., Transient behavior of diffusion-induced creep and creep rupture, *Metallurgical Transactions*, **6A**, 1499-1509 (1975).

Effective Determination of Coexistence Curves using Reversible-Scaling Molecular Dynamics Simulations

Maurice de Koning^{1,2}, Alex Antonelli³, and Sidney Yip¹

¹ Department of Nuclear Engineering, Massachusetts Institute of Technology, Cambridge, MA 02139-4307, U.S.A.

² Lawrence Livermore National Laboratory, University of California, Livermore, CA 94550-9234, U.S.A.

³ Instituto de Física Gleb Wataghin, Universidade Estadual de Campinas, Unicamp 13083-970, Campinas, São Paulo, Brazil

ABSTRACT

We present a simulation technique that allows the calculation of a phase coexistence curve from a single nonequilibrium molecular dynamics (MD) simulation. The approach is based on the simultaneous simulation of two coexisting phases, each in its own computational cell, and the integration of the relevant Clausius-Clapeyron equation starting from a known coexistence point. As an illustration of the effectiveness of our approach we apply the method to explore the melting curve in the Lennard-Jones phase diagram.

INTRODUCTION

One of the most challenging applications of computer simulation techniques concerns the determination of the phase behavior of a substance of interest. Given that the size of the systems studied in typical simulations is relatively small, a direct observation of phase coexistence in a single computational cell is problematic due to the interface dividing the coexisting phases. In order to avoid such problems one usually adopts an indirect route in which the coexistence conditions are determined by considering the thermodynamic properties of each phase individually. An effective methodology for the computation of phase equilibria using such an approach is the Clausius-Clapeyron integration (CCI) method introduced by Kofke [1-5], in which the relevant Clausius-Clapeyron differential equation is solved numerically. For coexistence in the pressure/temperature domain, for example, this equation has the well-known form

$$\frac{dP}{dT} = \frac{\Delta H}{T\Delta V}, \quad (1)$$

where ΔH and ΔV are, respectively, the molar enthalpy and volume differences between two coexisting phases A and B . In Kofke's implementation this equation is discretized and integrated numerically by conducting a series of equilibrium simulations along which the temperature (or pressure) varies on a discrete mesh. Each simulation considers both phases simultaneously, in separate computational cells, and measures the differences ΔH and ΔV corresponding to the current values of coexistence temperature and pressure. Given an initial coexistence condition, the rest of the coexistence curve is then mapped out by updating the coexistence pressure (or

temperature) according to Eq. (1) using a predictor-corrector integrator. In this fashion, each equilibrium simulation provides one new point on the coexistence curve.

In this paper we present an alternative implementation of the CCI concept which enables the determination of an *entire* coexistence curve from only one nonequilibrium simulation. The approach is based on the Reversible-Scaling free-energy method [6-8] and replaces the integration along a discrete series of equilibrium states by one along a quasi-continuous sequence of nonequilibrium states. We illustrate the effectiveness of our approach by exploring the melting curve in the Lennard-Jones phase diagram.

METHODOLOGY

Reversible Scaling

The Reversible-Scaling (RS) technique [6-8] is based on an equivalence relation between the partition functions of a given system of interest and its associated *scaled* system, whose potential energy function is constructed by scaling the original one by a positive factor λ :

$$U_{scaled}(\{\vec{r}_i\}; \lambda) \equiv \lambda U_{system}(\{\vec{r}_i\}), \quad (2)$$

where the \vec{r}_i denote the N particle positions. Considering the isobaric-isothermal partition functions [9] for both systems one finds that their configurational Gibbs free energies are related according to

$$G_{system}(N, P_0, T) = \frac{T}{T_0} G_{scaled}(N, \lambda P_0, T_0; \lambda), \quad (3)$$

where P_0 and T are the pressure and temperature in the system of interest, and $P_{scaled} = \lambda P_0$ and $T_0 = \lambda T$ are the corresponding values in the scaled system. This relation implies that the problem of computing the free energy of the system of interest as a function of temperature T is completely equivalent to the problem of evaluating the free energy of the scaled system as a function of the scaling parameter λ at a *constant* temperature T_0 .

The latter can be addressed very effectively within the framework of the coupling parameter formalism of thermodynamic integration (TI) [9], according to which the free energy of the scaled system may be written as

$$G_{scaled}(N, \lambda P_0, T_0; \lambda) = G_{scaled}(N, \lambda_{ref} P_0, T_0; \lambda_{ref}) + W_{rev}(\lambda), \quad (4)$$

where $G_{scaled}(N, \lambda_{ref} P_0, T_0; \lambda_{ref}) \equiv G_{system}(N, P_0, T_0 / \lambda_{ref})$ is a reference free-energy value assumed to be known beforehand, and where

$$W_{rev}(\lambda) \equiv \int_{\lambda_{ref}}^{\lambda} d\lambda' \left(\left. \frac{\partial G_{scaled}(\lambda)}{\partial \lambda} \right|_{\lambda'} \right) = \int_{\lambda_{ref}}^{\lambda} d\lambda' [P_0 \langle V \rangle_{\lambda'} + \langle U_{system} \rangle_{\lambda'}] \quad (5)$$

is the cumulative reversible work function associated with the scaling coordinate λ . Here, $\langle V \rangle$ and $\langle U_{system} \rangle$ denote ensemble averages of, respectively, the volume and potential energy over the $(N, \lambda P_0, T_0; \lambda)$ ensemble for the scaled system.

The function $W_{rev}(\lambda)$ can be estimated very efficiently using the adiabatic switching (AS) nonequilibrium method [8], in which the scaling parameter $\lambda = \lambda(t)$ is a function of time that varies continuously between initial and final values $\lambda(0) = \lambda_{ref}$ and $\lambda(t_s) = \lambda_f$, t_s being the switching time of the AS simulation. In this manner one obtains a *dynamical* estimator for the function $W_{rev}(\lambda)$ from a single AS simulation of duration t_s :

$$W_{dyn}[\lambda(t)] = \int_0^t dt' \dot{\lambda}(t') [P_0 V(t') + U_{system}(t')], \quad 0 \leq t \leq t_s, \quad (6)$$

where the ensemble averages of the volume and potential energy in Eq. (5) have been replaced by their instantaneous values during the AS simulation. Evidently, $W_{dyn}[\lambda(t)]$ is a biased estimator for $W_{rev}(\lambda)$ since the AS process is irreversible in nature and subject to dissipative entropy production. Accordingly, the dynamical estimator (8) will be rigorously equal to $W_{rev}(\lambda)$ only in the limit $t_s \rightarrow \infty$ when the process becomes ideally adiabatic. In practice, however, the convergence of $W_{dyn}[\lambda(t)]$ with increasing t_s is remarkably rapid, allowing an accurate determination of $W_{rev}(\lambda)$ and $G_{system}(N, P_0, T)$ (through Eqs. (4) and (3)), from a single and relatively short RS-AS simulation. Moreover, any small systematic errors caused by finite switching times can be eliminated using a simple hysteresis analysis procedure [10,11].

Clausius-Clapeyron Reversible Scaling

The RS approach can be extended in a manner that allows efficient and accurate integration of the Clausius-Clapeyron equation for two coexisting phases. In analogy to Eq. (4), the free energies of the scaled systems associated with the phases *A* and *B* can be written as

$$G_{scaled}^{A,B}(N, \lambda P_0(\lambda), T_0; \lambda) = G_{scaled}^{A,B}(N, \lambda_{ref} P_0(\lambda_{ref}), T_0; \lambda_{ref}) + W_{rev}^{A,B}(\lambda), \quad (7)$$

where the pressure P_0 in the systems of interest now varies explicitly as a function of temperature (and thus as a function of λ in the corresponding scaled systems). The corresponding cumulative reversible work functions for both phases are given by

$$W_{rev}^{A,B}(\lambda) = \int_{\lambda_{ref}}^{\lambda} d\lambda' \left[P_0(\lambda') + \lambda' \frac{dP_0}{d\lambda} \bigg|_{\lambda'} \right] \langle V \rangle_{\lambda'}^{A,B} + \int_{\lambda_{ref}}^{\lambda} d\lambda' \langle U_{system} \rangle_{\lambda'}^{A,B}. \quad (8)$$

Now, suppose the phases *A* and *B* are in coexistence at some temperature $T_{ref} = T_0 / \lambda_{ref}$ and pressure P_{ref} . In order to maintain the phases in coexistence upon an infinitesimal change $d\lambda$ in

the scaled systems, the associated reversible work increments for phases A and B must be equal. In order to satisfy this condition, the derivative $dP_0/d\lambda$ must obey

$$\lambda \frac{dP_0}{d\lambda} = -P_0(\lambda) - \frac{\langle U_{\text{system}} \rangle_{\lambda}^A - \langle U_{\text{system}} \rangle_{\lambda}^B}{\langle V \rangle_{\lambda}^A - \langle V \rangle_{\lambda}^B}, \quad (9)$$

which is simply the Clausius-Clapeyron equation within the RS formulation. Implementing Eq. (9) within the AS scheme then leads to a dynamical “equation of motion” for the evolution of the coexistence pressure:

$$\frac{dP_0[\lambda(t)]}{dt} = -\frac{\dot{\lambda}(t)}{\lambda(t)} \left(P_0[\lambda(t)] + \frac{U_{\text{system}}^A(t) - U_{\text{system}}^B(t)}{V^A(t) - V^B(t)} \right). \quad (10)$$

Given an initial coexistence condition, the integration of this equation then provides a dynamical estimator for an entire coexistence curve from a single RS-AS simulation in which both phases are considered simultaneously, in separate computational cells. At each instant, both cells are subjected to the same external pressure, given by Eq. (10). This relation describes an indirect coupling between the two coexisting phases, determining the evolution of the coexistence pressure in terms of the instantaneous potential energy and volume differences between both cells.

APPLICATION: MELTING CURVE IN LENNARD-JONES SYSTEM

As an illustration of the effectiveness of the Clausius-Clapeyron RS-AS technique, we computed the fcc solid-liquid coexistence boundary in the Lennard-Jones (LJ) system. For both phases we employed cubic computational cells containing 500 particles subject to standard periodic boundary conditions. The cut-off radius was selected at $r_c = 3.5\sigma$ and standard long-range corrections were applied to the measured energies and pressures [9]. The MD simulations were carried out using isobaric-isothermal dynamics based on a combination of the Nosé-Hoover thermostat and Andersen barostat. The corresponding equations of motion were integrated using the leapfrog algorithm with a time step $\Delta t = 0.002$ (LJ units).

First, we determined an initial point on the melting line by computing the Gibbs free energies of the LJ solid and liquid as a function of temperature at a pressure $P_0 = 1 \text{ } \epsilon / \sigma^3$ using the RS-AS technique. The functional form of $\lambda(t)$ was chosen to be linear in t . Figure 1 shows the converged results for the configurational Gibbs free energies per particle as a function of temperature, obtained using switching times of $t_s = 10$ ($5 \cdot 10^3$ MD steps) and $t_s = 50$ ($2.5 \cdot 10^4$ steps) LJ time units for the solid and liquid phases, respectively. As a check we conducted independent free-energy computations at the upper and lower limits of the temperature intervals covered by the RS-AS simulations. The results of these calculations, shown as the symbols in the plot, indicate an excellent agreement with the RS-AS data. From the crossing of both free-energy curves the coexistence condition for the pressure $P_0 = 1 \text{ } \epsilon / \sigma^3$ was found at a temperature $T_m = (0.777 \pm 0.001) \text{ } \epsilon / k_B$.

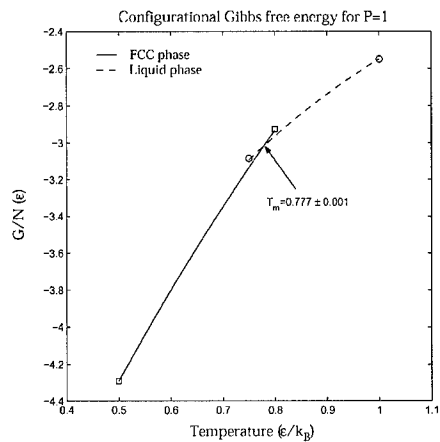


Figure 1. Configurational Gibbs free energy as a function of temperature for the Lennard-Jones FCC and liquid phases.

Starting from this initial coexistence point we applied the Clausius-Clapeyron RS-AS technique to extrapolate the melting line to the temperature $T = 7.777$. Figure 2 shows the results obtained for three values of the switching time: $t_s = 5$ (full curve, $1 \cdot 10^3$ MD steps), $t_s = 20$ (dotted curve, $1 \cdot 10^4$ MD steps), and $t_s = 200$ (dashed curve, $1 \cdot 10^5$ MD steps). For comparison, the equilibrium CCI results from [4] (obtained for 500 and 432 particles in the solid and liquid phases, respectively) are shown as the square symbols.

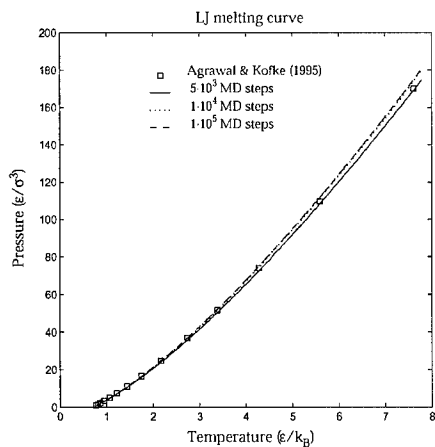


Figure 2. Clausius-Clapeyron RS-AS melting curves for the LJ system. Symbols represent data from [4].

The agreement between the Clausius-Clapeyron RS-AS results and those obtained in [4] is excellent for all temperatures below $T = 4.0$. For higher temperatures our results predict a slightly higher coexistence pressure, reaching a discrepancy of 2.5 % at $T = 7.61$. This discrepancy is possibly related to the fact that our calculations were carried out using a fixed cut-off radius for the potential, while the results in [4] were based on a variable cut-off radius. Considering the computational overhead associated with both methods, the Clausius-Clapeyron RS-AS technique is found to be considerably more efficient than the equilibrium method used in [4]. Given that each data point in the calculations of [4] required at least $4.2 \cdot 10^4$ Monte Carlo (MC) trials, the nonequilibrium implementation of CCI is about a factor 15 less expensive, showing a converged coexistence boundary using only $1 \cdot 10^4$ MD steps to cover the entire temperature range between $T = 0.777$ and $T = 7.777$.

SUMMARY

We presented a new implementation of the Clausius-Clapeyron integration procedure for the determination of phase coexistence boundaries using atomistic simulation techniques. Our approach is based on the Reversible-Scaling free energy method and allows the calculation of an entire coexistence curve from a single, relatively short nonequilibrium simulation. Application of the technique to the calculation of the melting curve in the Lennard-Jones phase diagram shows that the present nonequilibrium method is significantly less expensive than the original equilibrium implementation. Although further exploration of the technique's applicability is needed, the demonstrated efficiency suggests the method should be useful for the determination of coexistence curves using computationally demanding modeling approaches such as tight-binding and first-principles molecular dynamics.

ACKNOWLEDGMENTS

M.K. acknowledges support from the Brazilian agency FAPESP under Contract No. 97/14290-6, and from the U.S. Department of Energy through the University of California Lawrence Livermore National Laboratory under contract No. W-7405-Eng-48. A.A. gratefully acknowledges support from FAPESP, CAPES and CNPq, all of them Brazilian funding agencies. S.Y acknowledges support by Lawrence Livermore National Laboratory (ASCI-Level 2 grant), AFOSR (F49620-00-10082) and NSF (DMR-9980015).

REFERENCES

1. D.A. Kofke, *J. Chem. Phys.*, **98**, 4149 (1992).
2. R. Agrawal and D.A. Kofke, *Phys. Rev. Lett.*, **74**, 122 (1995).
3. R. Agrawal and D.A. Kofke, *Mol. Phys.*, **85**, 23 (1995).
4. R. Agrawal and D.A. Kofke, *Mol. Phys.*, **85**, 43 (1995).
5. E. J. Meijer and F. El Azhar, *J. Chem. Phys.*, **106**, 4678 (1996).
6. M. de Koning, A. Antonelli, and S. Yip, *Phys. Rev. Lett.*, **83**, 3973 (1999).
7. M. de Koning, A. Antonelli, and S. Yip, *J. Comp. Aid. Mat. Design*, **6**, 349 (1999).
8. M. de Koning, W. Cai, A. Antonelli, and S. Yip, *Comp. Sc. Eng.*, **2**, 88 (2000).
9. D. Frenkel and B. Smit, *Understanding Molecular Simulation From Algorithms to Applications*, Academic Press, San Diego (1996).
10. M. de Koning and A. Antonelli, *Phys. Rev. B*, **55**, 735 (1997).
11. J.E. Hunter III, W.P. Reinhardt, and T.F. Davis, *J. Chem. Phys.*, **99**, 6856 (1993).

MONTE-CARLO SIMULATION OF THREE DIMENSIONAL ION DYNAMICS IN POLYMERS

A. Wagner, H. Kliem, Institute of Electrical Engineering Physics, Saarland University, D-66041 Saarbruecken, Germany

ABSTRACT

Dynamic Monte-Carlo simulations of three dimensional ion motions are carried out based on a multi-well potential model. A parallel plate capacitor is modeled with an ionic conducting polymer having two ideal blocking electrodes. Positive ions (maximum 1000) are located on a cubic lattice with a maximum size of 100x100x100 locations. A negative background charge, constant in space and time, is used to provide charge neutrality. The positive ions can perform hops between neighboring sites with a probability corresponding to distributed energy barriers. To calculate the potentials due to an interaction of the ions the method of images is used. The steady state and the dynamic properties are studied after application of a voltage step in dependence on the sample thickness, the ion concentration and the voltage. A simulation of a space charge polarization yields an explanation for the experiments in the time and in the frequency domain.

INTRODUCTION

Electrical relaxation processes in dielectric materials as well as in solid ionic conductors often show a dispersed behavior in a wide range. In many cases this can be expressed in a power law $j \propto t^{-\alpha}$ of the response function in the time domain [1]. In the frequency domain we find a power law of the imaginary part of the permittivity $\epsilon''(\omega) \propto \omega^{\beta}$ respectively of the real part of the conductivity $\sigma'(\omega) \propto \omega^{\beta+1}$ with $\beta = \alpha - 1$ [2]. In the dielectrics this behavior can be explained with the aid of debye processes with distributed relaxation times due to an internal static energy barrier distribution. For solid polymer electrolytes several models are developed, which attribute the power law to the microscopic dynamic disorder in the material [3]. In this picture the ions can change their pathways through the electrolyte due to a rearrangement of the polymer host. For other classes of solid electrolytes similar assumption are made [4]. A model, which uses a combination of static disorder and interaction between the ions, is the counter-ion model [5]. In this model an energy distribution is caused by the coulomb interaction of counter-ions, which are fixed on lattice sites. In our model we use a constant negative background charge to provide charge neutrality. Furthermore, we introduce an intrinsic barrier energy distribution, which may be due to a disordered polymer host. Because the goal is to simulate thin structures, we have to consider the electrode effects due to image charges. The existence of blocking layers allows us to separate an injection of charges from a space charge polarization and the related accumulation of charges at the electrodes.

EXPERIMENTAL

Thin films (0.3 μm to 30 μm) of poly(ethylene oxide) (PEO) with molecular weights from 6×10^3 to 4×10^5 were prepared from aqueous solutions by a spin technique as Al-PEO-Al structures. Dielectric measurements (capacitance and loss angle) were carried out in a frequency

range $3 \text{ mHz} \leq f \leq 1 \text{ MHz}$ in atmospheres of different relative humidity (0% r.h. to 75% r.h.) and at different temperatures (293 K to 323 K) [6,7].

The capacitance $C_p(\omega = 2\pi f)$ exhibits a remarkable dependence on the sample thickness d in the high frequency range and is independent of d at low frequencies (Fig. 1). The relaxation frequency decreases with increasing thickness. The real part of the relative permittivity $\epsilon' \propto C_p d$ is not dependent on the sample thickness in the high frequency range and in the low frequency regime the permittivity increases linearly with increasing thickness. This can be explained by a true volume polarization in the high frequency range and a relaxation process due to an ion (hydrogen and lithium) movement in the low frequency range. The relaxation process is thermally activated and the time constant is shifted towards high frequencies with increasing relative humidity [7].

The ions move through the sample to the electrode interfaces and form an ionic space charge. We assume that at the PEO-Al interface an oxide layer is formed, which is impermeable for these ions. The imaginary part of the permittivity shows, that the relaxation process is not only due to a simple ionic conduction between the electrodes (Fig. 2). We find a dispersed imaginary part of the permittivity $\epsilon''(\omega) \propto \omega^{-0.7}$ respectively a conductivity $\sigma'(\omega) \propto \omega^{0.3}$.

MODEL

For the simulation of our system we use a model, in which the movement of the ions can be described by an ion hopping in a multi-well potential structure with thermally activated hopping rates. In the model it is assumed, that only the positive ions are mobile. A negative background charge, constant in space and time, is used to provide charge neutrality. Positive ions (maximum 1000) are distributed on a cubic lattice with up to 10^6 cells, which are separated by energy barriers W_0 . The intrinsic energy barriers can have different heights. A simple assumption is a box-like distribution function, which is used in the simulation besides a uniform height. To calculate the potentials between the electrodes due to an interaction of the ions we use the method of images. The potential of a test charge is the sum of the coulomb potentials of all original charges and the image charges. The potential of the charge itself is excluded from the sum. For the four sample surfaces not in contact with the electrodes, periodic boundary conditions are used. With the aid of this method it is possible to calculate the potential respectively the energy level for all lattice cells which contain ions and for their neighboring cells.

The influence of the energy distribution can be explained most clearly by a one-dimensional representation of the sample structure. The polymer electrolyte with thickness d is enclosed

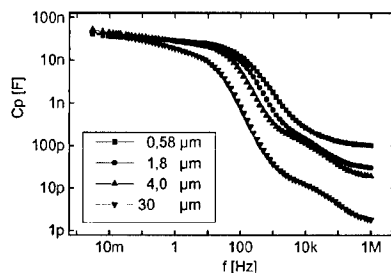


Fig. 1: Capacitance, 0 % r.h., 303 K

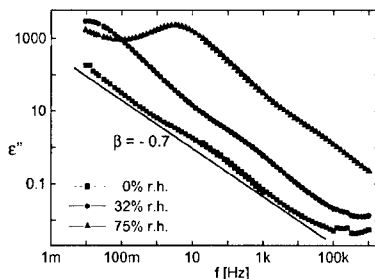


Fig. 2: Imaginary part of the nominal permittivity, 303 K, $d = 2.5 \mu\text{m}$

between two electrodes (Fig. 3). Between the dielectric and the electrodes an oxide layer is modeled, which is impermeable for ions. The dielectric can be subdivided in z_m layers or sites with a distance ℓ between them. The ions with a positive charge q are located on the sites, which correspond to minima in a multi-well energy structure. To jump from a well z to the neighboring well $z+1$ the ion has to surmount the energy barrier $W_{z,z+1}$ and the energy barrier $W_{z+1,z}$ in the opposite direction. The barrier height at the blocking oxide layer is infinite. Each energy barrier is the sum of three energy parts

$$W_{z,z+1} = W_0 - \Delta W / 2 - \delta W / 2 \quad (1)$$

The first term W_0 is the intrinsic energy barrier height, which may be distributed. The energy term $\Delta W / 2$ is due to the interaction of the ions and the last term $\delta W / 2$ is due to the external applied field E_a with $\delta W = q E_a \ell$. For a thermally activated hopping process between two layers we use the transition rates

$$w_{z,z+1} = v_0 \cdot \exp\left(-\frac{W_0}{kT} + \frac{\delta W}{2kT} + \frac{\Delta W}{2kT}\right) \quad (2)$$

$$w_{z+1,z} = v_0 \cdot \exp\left(-\frac{W_0}{kT} - \frac{\delta W}{2kT} - \frac{\Delta W}{2kT}\right) \quad (3)$$

The complement of the transition rate is the average transition time $\tau = 1/w$. For the one-dimensional model two possible directions of ion hopping must be considered. By expanding the model to three dimensions the layers are replaced by lattice cells, which can contain one single ion per cell. Then six possible hop directions to the nearest neighbors have to be considered. A Monte-Carlo algorithm can be formulated: For all ions i and all possible jump directions k the average transition times $\tau_{i,k}$ are calculated and a set of equidistributed random numbers x in the interval $[0,1]$ is generated. The random jump time t for all ions and all directions can be derived assuming an exponential time distribution of hopping events [8]. Using the distribution law we find $t_{i,k} = -\tau_{i,k} \ln x$. The ion with the minimum time $t_{\min} = \min[t_{i,k}]$ jumps in direction k . After the jump the system time is increased by t_{\min} and the interesting quantities: polarization, current density, charge distribution, etc., can be calculated. After that all $\tau_{i,k}$ must be recalculated. By repeating each step in a loop we are able to perform a simulation of the temporal evolution of the system. The loop is interrupted, if the maximum system time is reached.

SIMULATION

Basic properties of Ion Systems

The algorithm is implemented in a computer simulation. The basic configuration of the system is a lattice with $50 \times 50 \times 50$ lattice cells and 1000 ions, which are distributed randomly on the lattice. The hopping distance is 1 nm and the blocking layer thickness is 2 nm. Starting the simulation with an external voltage $V = E_a d = 0$, we find a fluctuation of the ions due to random hops in all directions. By application of an external voltage we find an average movement in the

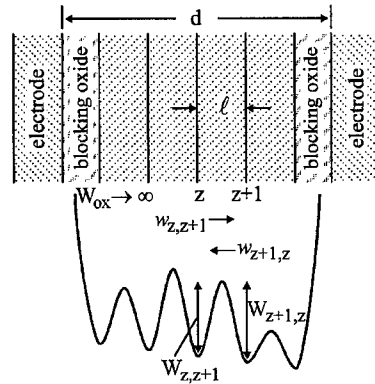


Fig. 3: One-dimensional representation of the sample structure

direction of the field until a new steady state is reached. In Fig. 4 the space charge density of positive ions is plotted versus the distance from the left electrode in the relaxed system. To reduce the noise from the data the space charge is averaged over the x- and the y-axis. For the zero voltage case the space charge is constant and equal to the negative value of the constant background charge. After application of a 4 V step the ions are moved from the positive (left) to the negative (right) electrode. A depletion of ions is generated at the positive electrode and an accumulation at the negative electrode. In addition to the external field the positive ions are attracted to the electrode by their negative image charges resulting in an increase of the transition times, i.e. a trapping of the ions at the electrode. Positive ions neighboring the accumulation layer are repelled because of their equal polarity and an additional depletion zone can be observed. The center of the positive charge is shifted by Δx out of the center of the electrolyte. Together with the negative background charge this yields a polarization of the sample.

The local electrical field, which is proportional to the integral of the space charge, has a finite value at the electrodes. There is no electrical field in the center of the electrolyte due to a shielding by the ions. Corresponding to the electrical field the potential in the center of the sample is a constant. After release of the external voltage the ions relax due to an interaction and due to diffusion.

Dynamic properties

The dynamic properties of the ionic systems are studied after application of an external voltage step. In Fig. 5 and Fig. 6 the current density versus the time is shown in a log-log plot for a voltage step of 0.5 V (linear regime). For one single transition time due to a constant energy barrier height of 27.6 kT, an exponential decay of the current density can be observed (Fig. 5). The system relaxation time constant is a multiple of a single transition time due to a jump over multiple wells and depends on the sample thickness. Considering a box-like distribution of energy barrier heights from 27.6 kT to 47.6 kT we find a current density $j \propto t^{-\alpha}$ with $\alpha = 0.6$ (Fig. 6). For a LTI-system in the frequency band a gradient β of the

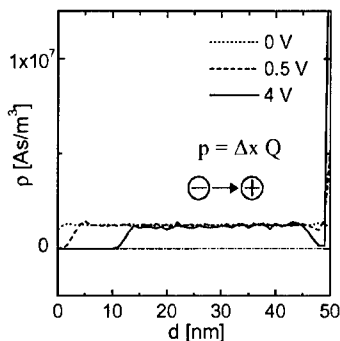


Fig. 4: Space charge distribution

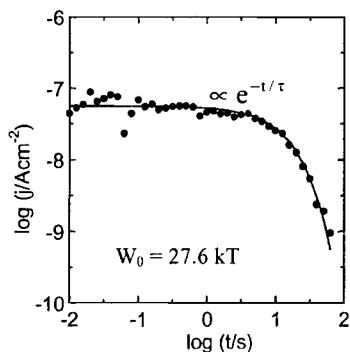


Fig. 5: Current response after a voltage step of 0.5 V for one single barrier height W_0

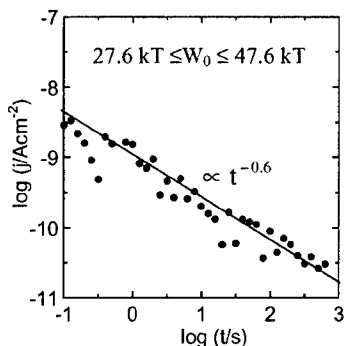


Fig. 6: Current response after a voltage step of 0.5 V for a box-like distribution of barrier heights W_0

imaginary part of the permittivity is found with $\beta = \alpha - 1 = -0.4$. Compared to the measurements (Fig. 2) this value is too high. But, by a variation of the energy distribution function it should be possible to adapt the experimental value. In the following simulations a constant barrier height $W_0 = 27.6$ kT is used.

Variation of the electrolyte thickness

From the low frequency capacitance the steady state polarization $P \sim C_s d$ is derived, which increases linearly with the sample thickness d (Fig. 1). In the simulation the thickness d was also varied with a constant density of ions and a constant applied field E_a . A linear increase of the polarization with increasing d is found (Fig. 7). The ions travel over longer distances and increase therefore the dipole moment p (Fig. 4). The experiment also shows a linear increase of the system relaxation time with increasing d . This is also found in the simulation. The system time constant in thicker samples is longer, because the ions have to travel over longer distances between the electrodes with multiple hops.

Variation of the ion density

The relaxation frequency of the measured process increases linearly with the dopant concentration n in a log-log scale. The simulated reciprocal system relaxation time also shows this behavior (Fig. 8), but with a lower slope. The increase can be explained by a long range displacement for lower ion concentrations and by a short range displacement for higher ion concentrations. Corresponding to the hop over less energy barriers a faster relaxation is found in the second case.

Variation of the external voltage

The static polarization is simulated in dependence on the applied voltage U (Fig. 9) for a $50 \times 50 \times 50$ lattice cells and 1000 ions corresponding to $n = 0.8 \times 10^{24} / \text{m}^3$. In the low voltage range the steady state polarization increases linearly with the applied voltage. The internal electrical field is zero nearly in the complete electrolyte. For larger values of U the slope of the curve decreases with increasing voltages. The non-linear behavior of the polarization is correlated with an increasing width of the depletion and the accumulation zones at the

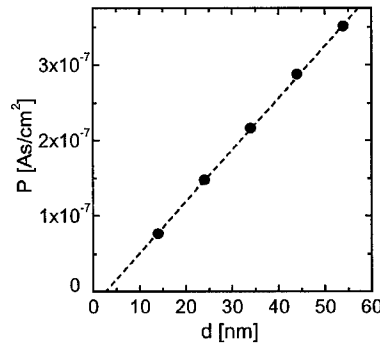


Fig. 7: Steady state polarization after a step of the electrical field $E_a = 9.3 \times 10^6$ V/m

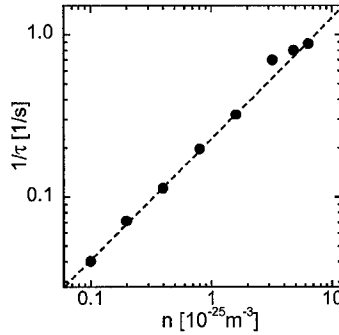


Fig. 8: Reciprocal relaxation time

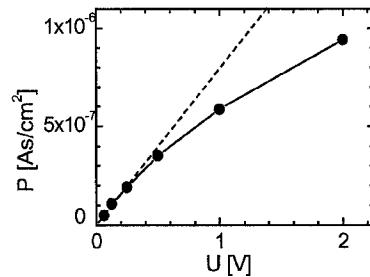


Fig. 9: Steady state polarization

electrodes (Fig. 4). The small signal permittivity $\epsilon_s \propto dP/dU$ decreases in the experiments with an increasing applied voltage U . This corresponds to the simulated behavior. To test the validity of the model in the static and small field limit, the polarization by the MC simulation can be compared to the polarization by the continuum equation assuming an ionic surface charge at the blocking layers (dashed line in Fig. 9). For small voltages ($U \rightarrow 0$) the results of the MC simulation and of the continuum model are in good agreement.

Thin blocking layers

An important parameter in the simulation is the thickness of the blocking oxide layers. For $d_{ox} = 0.1$ nm we find a polarization current density, which differs completely from the exponential decay observed for $d_{ox} = 2$ nm (Fig. 5). For longer times a current density $j \propto t^{-1.2}$ is found, which is due to an attraction of ions towards the electrodes by the image charges. This is the first time we find the $t^{-\alpha}$ -behavior without the need of any intrinsic distributed transition times. Measurements in the long time range show a current density $j \propto t^{-1.1}$. We assume that the thickness of the blocking layer and therefore the electrode material plays an important role for the behavior at long times.

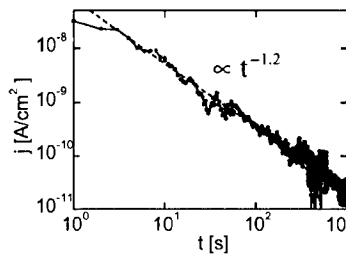


Fig. 10: Current density for one single transition time and a thickness of the blocking layer $d_{ox} = 0.1$ nm

CONCLUSION

Monte-Carlo simulations of the steady state and dynamic properties of a space charge polarization are performed. For an Al-PEO-Al thin film structure we find a qualitative agreement of experiment and simulation by a variation of the parameters thickness, ion density and applied voltage. Due to a shielding of the external field by the mobile ions the electrical field is zero in the center of the structure. For short time scales a polarization current $j \sim t^{-0.6}$ is found due to a box-like energy distribution. In the long time range a polarization current $j \sim t^{-1.2}$ is due to image charges in the electrodes.

REFERENCES

1. E. v. Schweidler, *Ann. Phys.* **24**, 711-770 (1907)
2. H. Kliem, G. Arlt, *Phys. Stat. Sol. (b)* **155**, 309 (1989)
3. Stephen D. Druger, *J. Chem. Phys.* **100** (5) 3979 (1994)
4. Jill E. Davidson, Malcolm D. Ingram, Armin Bunde, Klaus Funke, *J. Non-Cryst. Sol.* **203** 246-251 (1996)
5. W. Dieterich, D. Knödler, P. Penzig, *J. Non-Cryst. Sol.* **172-174** 1237-1242 (1994)
6. H. Kliem, K. Schröder, and W. Bauhofer, *CEIDP Ann. Rep.* pp. 12-15 (1996)
7. A. Wagner, H. Kliem, *MRS symp. proc.* **548**, pp.353-358 (1998)
8. Alexei Sinitzski, V. Hugo Schmidt, *Phys. Rev. B* **54** 842 (1996)

Self-Affinity Analysis of the Fracture Surfaces of Polypropylene and Opal Glass.

M. Hinojosa*, E. Reyes, C. Guerrero and U. Ortiz

Universidad Autónoma de Nuevo León, A.P. 149-F, S. Nicolás de los Garza, 66451 México.

*hinojosa@gama.fime.uanl.mx

ABSTRACT

In this work we report the self-affinity analysis of the fracture surfaces of a polymeric semicrystalline material and an opal glass. In the case of the plastic material, samples of isotactic polypropylene (i-PP) were prepared by varying the cooling rate from the melt; this resulted in different spherulite sizes. Samples were then broken in bend test after being immersed in liquid nitrogen. In the case of the opal glass, samples with different sizes of the opacifying particles, obtained by different thermal treatments, were broken in a punch test. In both cases the fracture surfaces were analyzed by both Scanning Electron Microscopy (SEM) and Atomic Force Microscopy (AFM) in the contact mode. Self-affinity analysis was performed by the variable bandwidth method, covering a range of length scales spanning from a few nanometers up to ten micrometers. The roughness exponents are found to be of similar values close to $\zeta = 0.8$ with the correlation length corresponding to the size of the spherulites in the plastic material and to the size of the opacifying particles in the opal glass. These results should be taken into account in the development of multiscale models and simulations of the fracture process of real heterogeneous materials.

INTRODUCTION

Fracture surfaces are natural anisotropic fractals, their self-affine character is now almost universally accepted. The first quantitative description of these irregular surfaces using fractal geometry were published in 1984 by Mandelbrot *et al*, his results suggested a correlation between the fractal dimension of the fracture surface of maraging steel with the impact energy in samples with different heat treatments [1]. Later on, refined experiments in a variety of materials did not corroborate this relationship between fractal dimension and mechanical properties [2,3,4]. It was accepted that the so-called roughness exponent, ζ , is a more appropriate parameter to describe fracture surfaces. Studying fracture surfaces obtained in rapid kinetic conditions and analyzed, mainly by SEM, Bouchaud proposed the idea of a *universal* roughness exponent, $\zeta \approx 0.78$, independent of the fracture mode, the microstructure and properties [2]. This universality was questioned by the finding of a self-affine regime with a low roughness exponent $\zeta \approx 0.5$ for fracture surfaces generated at low crack propagation speeds and/or analyzed at the nanometer scale using Scanning Probe Microscopy. At the present the co-existence of the two self-affine regimes has been reported in several materials. Both regimes are separated at a cut-off length, which appears to be dependent on the kinetic conditions [5]. Attempts have been made to correlate the cut-off length with microstructural parameters [6].

Hinojosa *et al* demonstrated that the correlation length was closely related to the grain size in a nickel superalloy [7]. This result supports the idea that the crack front, imagined as a

line, interacts with the different obstacles present in the microstructure and thus the largest heterogeneities should determine the correlation length. More recently, it was also reported that the correlation length is also related to the characteristic size of the dendrites in cast aluminum alloys [8]. In this work our aim is to provide more evidence to support the above mentioned hypothesis, i.e. that the correlation length is determined by the largest characteristic heterogeneities, and that this is valid not only for metals but for polymers and ceramics as well [9,10].

EXPERIMENT

The materials whose fracture surfaces were analyzed in this work are representative of the plastics and ceramic materials. The plastic material selected for our analysis was a semi-crystalline material, isotactic polypropylene (i-PP), which was chosen due to its facility to crystallize. Characterization of this material by Gel Permeation Chromatography showed that the number average molecular weight is 60,359, and the polydispersity index was 5.1. The melting temperature and the degree of crystallinity were 165.4°C and 46.7% respectively according to Differential Scanning Calorimetry measurements. Two samples in the form of small discs of about 10 mm in diameter and 1 mm thick were obtained and then melted and cooled at two different rates in order to alter the crystallization process. As a result two different spherulitic sizes were obtained, fine-spherulites and coarse-spherulites. The average spherulite diameter was measured by Optical Microscopy and image analysis techniques as well as by AFM in the contact mode. The specimens were immersed in liquid nitrogen for 15 minutes then broken in bending mode.

In the case of the glass materials, two samples of commercial opal glass were analyzed. As a result of different heat treatment during the manufacturing process, the samples had different sizes of the opacifying precipitates. Flat specimens were broken using a punch tester. The size of the opacifying particles was measured from SEM images as well as by AFM observations.

Fractographic analysis was performed by SEM, for this analysis, some samples of both materials were gold sputtered. The fractometric study was carried out with the AFM in contact mode for both materials. The maximum scan size in AFM was 10 micrometers and the best resolution of the 512 x 512 images was about 10 nm. Height profiles were extracted from these AFM images and at least 30 profiles were obtained for each specimen. The average roughness exponent and correlation length were then calculated by applying the self-affine analysis.

Self-affinity analysis was performed using the variable bandwidth method [11]. In this method we computed the quantities $w_2(r)$ and $Z_{max}(r)$. $Z_{max}(r)$ is calculated as follows:

$$Z_{max}(r) = \langle \max\{z(r')\}_{x < r' < x+r} - \min\{z(r')\}_{x < r' < x+r} \rangle_x \propto r^\zeta$$

where r is the width of the window, $Z_{max}(r)$ is the difference between the maximum and the minimum heights z within this window, averaged over all possible origins x of the window. $w_2(r)$ is the second moment or the standard deviation of the height distribution within the windows. This quantity also scales as a power law:

$$w_2(r) \propto r^\zeta$$

The second moment, $w_2(r)$, allows the most accurate determination of the self-affine correlation length. For each material, at least 30 individual self-affinity curves were averaged. The results were also compared with the Z_{max} method, but only the results for the second moment are presented.

RESULTS

Fractographic and fractometric analysis corroborate that the fracture surfaces of both i-PP and opal glass are self-affine objects.

i-PP

The average spherulitic diameter were estimated as 0.34 and 0.96 μm for the fine-spherulites and the coarse-spherulites samples, respectively.

Figure 1(a) and 1(b) show the fracture surface of the coarse-spherulite sample as observed by SEM and AFM respectively. Qualitative SEM observations, Figure 1(a), show irregular curved lines, named Chevron marks. These lines seem to depart from a point where the cracks started, and give the direction of crack propagation. These features were also observed in the fracture surface of the fine-spherulite samples. In all the analyzed SEM images, the fracture surfaces present similar morphologies at different magnifications. This can be considered a qualitative evidence of self-affinity.

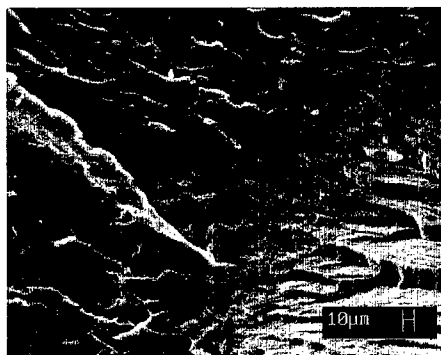


Figure 1(a). Fracture surface of i-PP, coarse-spherulites sample (SEM micrograph).

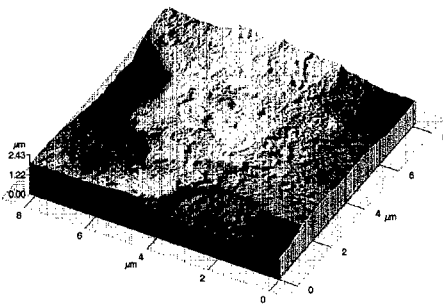


Figure 1(b). 3-D image of the fracture surface of coarse-spherulites of i-PP, constructed with the height profiles obtained by AFM.

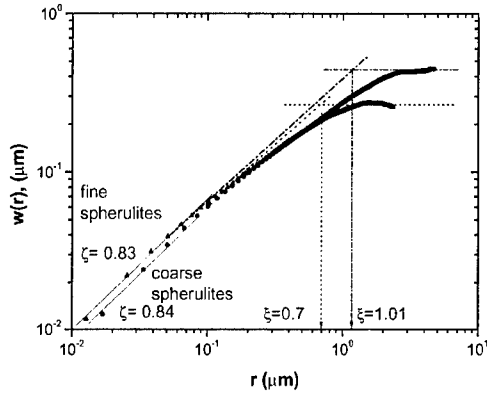


Figure 2. Self-affinity curves for the two samples of i-PP.

Results of the self-affinity analysis are shown in Figure 2. The self-affine curves are apparently disturbed, probably due to rheologic effects as the crack front causes some local viscoelastic deformation. The roughness exponent was $\zeta=0.83$ for fine-spherulites and $\zeta=0.84$ for coarse-spherulites. The correlation lengths are not clearly defined, but they were estimated as $0.7 \mu\text{m}$ and $1.1 \mu\text{m}$ for the fine-spherulites and the coarse-spherulites samples, respectively. These values are in good agreement with the estimated spherulite size.

OPAL GLASS

Two samples of opal glass with different size of the opacifying particles were broken with a punch tester and their fracture surfaces were analyzed by SEM and AFM in the contact mode. One of the sample had a homogeneous distribution of fine particles with an average size of $0.34 \mu\text{m}$, the other had a distribution of a coarse particles of about $4 \mu\text{m}$, together with fine particles of average size of $0.47 \mu\text{m}$.

Figure 3(a) shows a typical fracture surface observed by SEM, the mirror, mist and hackle zones are clearly seen. The AFM observations were concentrated in the mirror region for the two samples analyzed. Figure 3(b) is an AFM image showing coarse particles.

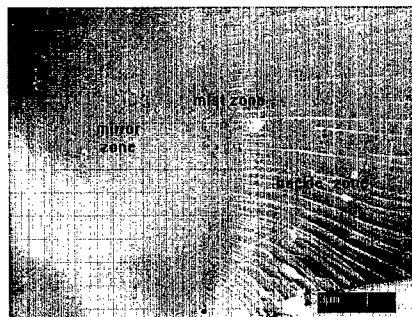


Figure 3(a). SEM image of the fracture surface of opal glass.

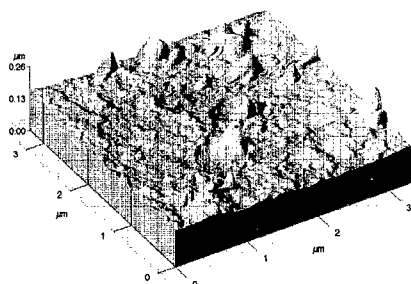


Figure 3(b). AFM image of mirror region showing opacifying particles.

The results of the self-affinity analysis are shown in Figure 4. In the case of the fine-particle sample the roughness exponent has a value of 0.8 and the correlation length is clearly seen at a value of around $0.3 \mu\text{m}$, which agrees with the size of the opacifying particles. For the sample with coarse particles, the self-affine regime is apparently disturbed by the presence of the two types of fine and coarse particles. The roughness exponent has a value of 0.78 and the correlation length is about $3.5 \mu\text{m}$, which again is of the order of the coarse opacifying particles. In figure 4 the arrow indicates the region where the self-affine regime corresponding to the coarse-particle specimen is disturbed presumably by the presence of the two distributions of particles with different size.

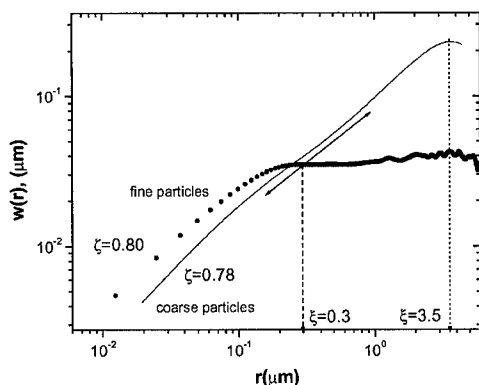


Figure 4. Self-affinity curves for the two samples of opal glass.

CONCLUSIONS

The qualitative and quantitative results shown in this work corroborate the self-affine character of the fracture surfaces of i-PP and opal glass. It is shown that the correlation length is determined by the size of the largest heterogeneities in the microstructure: the spherulites in the case of i-PP and the largest opacifying particles in opal glass. In all cases the roughness exponent was estimated to about 0.8, in good agreement with previously published result for similar propagation conditions.

ACKNOWLEDGMENTS

This work was supported by CONACYT and the PAICYT program of the University of Nuevo León. The help from L. Chávez, J. Aldaco, V. González, F. Garza and O. Garza is gratefully acknowledged.

REFERENCES

1. B.B. Mandelbrot, D.E. Passoja and A.J. Paullay, "Fractal Character of Fracture Surfaces of Metals", *Nature*, **308**, pp 721-722 (1984).
2. E. Bouchaud, "Scaling Properties of Cracks", *J. Phys.:Condens. Matter* **9** (1997) 4319-4344.
3. E. Bouchaud, G. Lapasset and J. Planés, *Europhys Lett.* , **13**, pp 73 (1990).
4. P. Daguiet, B. Nghiem, E. Bouchaud and F. Creuzet, "Pinning and Depinning of Crack Fronts in Heterogeneous Materials", *Phys. Rev Lett.* , **78**, pp 1062 (1997).
5. P. Daguiet, S. Hénaux, E. Bouchaud, and F. Creuzet, "Quantitative Analysis of a Fracture Surface by Atomic Force Microscopy", *Phys. Rev. E*, **53**, 5637 (1996).
6. P. Daguiet, Ph. D. thesis, Université Paris 6 (in french), November 1997.
7. M. Hinojosa, E. Bouchaud and B. Nghiem. Materials Research Society Symposium Proceedings, Volume 539, Materials Research Society, Warrendale Pennsylvania, pp. 203-208, 1999.
8. M. Hinojosa, J. Aldaco, U. Ortiz, and V. González, "Roughness exponent of the fracture surface of Al-Si Alloy". *Aluminum Transactions. An International Journal.* Volume 3. No.1. pp.53-57, 2000.
9. Edgar Reyes, Master Thesis, University of Nuevo Leon, Mexico (in spanish). 1999.
10. M. Hinojosa, and L. Chavez. "Self-affinity Analysis of Glass Fracture Surfaces-Natural Fractals". *The Glass Researcher.* Volume 9. pp. 23-24, USA 2000.
11. J. Schmittbuhl, J.P. Vilotte. S. Roux, "Reliability of self-affine measurements", *Phys. Rev. E*, **51** 131 (1995).

Mechanics of Plasticity and Fracture

A DISCRETE DISLOCATION APPROACH TO CRACK PROPAGATION

E.D. METSELAAR, J. Th. M. DE HOSSON, E. VAN DER GIESSEN

Department of Applied Physics, Materials Science Center and the Netherlands Institute of Metals Research, University of Groningen, Nijenborgh 4, 9747 AG Groningen, The Netherlands.

ABSTRACT

The propagation of cracks along homophase and heterophase interfaces is studied within the framework of discrete dislocation plasticity. The crack is described by a distribution of discrete interface dislocations and a mode II loading is exerted on the crack and surrounding lattice dislocations. In this paper special attention is paid to the ratio of the phonon viscosity between a running crack and a moving dislocation. It is shown that this ratio affects the possibility of screening the running interface crack to a great extent. Further, it was found that the shape and size of the dislocation structure around the crack depends critically on the actual distribution and value assumed for the nucleation strength of the dislocation sources.

INTRODUCTION

The objective of this work is aimed at examining the propagation of an interfacial crack surrounded by lattice dislocations within the framework of discrete dislocation plasticity (DDP). The modeling is essentially based on the superposition principle that can be found already in Bueckner's work¹. It involves a separation of the total stress fields in stress fields in an infinite medium and a complementary field to correct for the boundary conditions. The correction part is formulated as a boundary value problem and can be conveniently solved using a finite element method². When there are no free boundaries near a crack within a radius of, say, twice the crack length the crack problem can be solved to a good accuracy by assuming it embedded in an infinite medium. Otherwise the full integral approach or a numerical approach like DDP can be used. An excellent review of various approaches depending on the boundary conditions is presented in³. Here, we are interested in the description of the propagation of a crack on a meso-scale in multi-layer systems where the finite boundary conditions may affect the actual physical phenomena. A mode II loading is exerted on the simulated structure containing both an interfacial crack and surrounding dislocations.

COMPUTATIONAL METHODOLOGY

Because dislocations represent discontinuities in displacement, they can also be adopted to describe a crack, at least in a mathematical sense. Eshelby, Frank and Nabarro introduced the idea that a crack can be thought of as an array of discrete co-planar and parallel dislocations along the crack plane⁴. However, a much simpler method (at least in a numerical sense), first suggested by Leibfried⁵, is to make a continuum approximation right from the beginning. For a review on dislocation-based fracture mechanics reference is made to Weertman⁶. The stress field of a crack running from $-a$ to a can simply be related to the stress fields of individual dislocations. Using a dislocation distribution $B(\xi)$ on the crack plane (for $x_2 = 0$) the stress fields are given as:

$$\sigma_{ij}^{\text{crack}}(x_1, x_2) = \int_{-a}^a B(\xi) \sigma_{ij}^{\text{dis}}(x_1 - \xi, x_2) d\xi. \quad (1)$$

The boundary-value problem of a crack occupying $|x_1| < a$ with $-\infty < x_3 < \infty$ and subjected to either tensile or shear stresses turns out to be equivalent to a double pile-up of either edge or screw dislocations in the region $-a < x_1 < a$ caused by a dislocation source at $x_1 = 0$. Components of the stress show a square-root singularity close to the crack tip at $x_1 = \pm a$, $x_2 = 0$. The stress field for a Griffith-Inglis crack under mode-II loading condition, with κ Kolosov's constant, i.e. $3-4\nu$ in plane strain, μ the shear modulus and ν Poisson's ratio, is:

$$\tilde{\sigma}_{xy}(x, 0) = -\frac{2\mu}{\pi(\kappa+1)} \int_{-a}^a \frac{B_x(\xi)}{x-\xi} d\xi. \quad (2)$$

The function $B_x(\xi)$ describes the distribution function of the crack dislocation. The distribution function can be found by realizing that there is no tangential displacement between one end of the crack and the other. The dislocation density physically represents the negative slope at any point of the relative tangential shift between the upper and lower crack faces. Integrating the distribution function from the middle to the tip yields the number of dislocations needed to represent the crack as a function of materials constants and the external stress. This method was employed here to describe a crack shielded in the stress fields of surrounding dislocations. Nevertheless, the crack is described by discrete dislocations instead of using a distribution of infinitesimally small dislocations. This approximation has been validated by comparing the resulting stress fields with the corresponding stress field components of the analytical description. An advantage of this approach is that the interactions between the crack and surrounding lattice dislocations can be fully incorporated within the framework of the DDP method.

An important aspect in the description of moving defects in crystalline solids is the drag force during actual motion. The velocity of the dislocations is assumed to be proportional to the applied stress, that is to say the solid acts as a Newtonian viscous material and a drag force works in the direction opposite to the motion:

$$\mathbf{F}_{\text{Drag}} = -\eta_{\text{Drag}} \mathbf{v}, \quad (3)$$

where η_{Drag} represents the damping coefficient. Eq. 3 dates back to the original analyses by Leibfried⁷ and Eshelby⁸ in which phonon radiation and momentum transfer lead to a linear relationship between the drag force and a uniform velocity. It should be realized that this damping force becomes in particular relevant above $v \sim 10^{-2} C_T$ (C_T is the transversal velocity) whereas at lower velocities other processes, such as thermally activated glide and diffusive glide/climb, are rate controlling. The driving force of the dislocation motion is the Peach-Koehler force and the velocity can be solved from the force equilibrium of the Peach-Koehler force and the frictional force. In addition, a criterion is needed to describe the propagation of the crack as a function of the applied stress. From the previous section it is tempting to choose a criterion for crack propagation, which is based on the same rule as for the motion of a lattice dislocation, i.e. the 'Peach-Koehler' force is calculated on a super lattice dislocation. A crack can only expand if the potential energy exceeds the amount of energy it needs to create free surfaces (Griffith criterion). The critical stress associated with it is used as an offset of the 'Peach-Koehler' force of the crack.

It is necessary to understand the physics behind η_{Drag} both for the crack and surrounding dislocations because these might be significantly different. In a homogeneous isotropic solid the drag coefficient consists basically of two contributions $\eta_{\text{Drag}} = \eta_{\text{PII}} + \eta_{\text{L}}$.

where the subscripts refer to phonon viscosity and electron viscosity. When moving in a flux of phonons the dislocations and cracks experience frictional forces. This phonon viscosity is related to the density of phonon modes per unit frequency range, $D(\omega)$, i.e. inversely proportional to the group velocity $d\omega/dk$. Thermal phonons may excite vibrations in the dislocation line, which are then re-radiated around the dislocation line or the phonons are scattered by (an)harmonicities in the strain field. A moving dislocation and running crack encounter more phonons in the direction of motion than in other directions and it gives rise to a net force opposing the motion. Peculiar interactions may arise due to the deviation from linearity of the dispersion in a real crystal⁹. It is clear that there will be a singularity in $D(\omega)$ whenever the dispersion relation $\omega(k)$ becomes horizontal that is to say, whenever the group velocity becomes zero. In the case of fcc materials only small flat areas inside the Brillouin zone can be found, in sharp contrast to bcc materials. Therefore we anticipate that this peculiar behavior is of less importance for fcc materials compared to bcc materials and it will be ignored in the following.

Assuming only interactions of the moving defects via an elastic scattering process that accompanies momentum transfer, phonons are interchanged between the various modes which leads to a variation of the occupation number $N(k)$. The average retarding force is then

$$\mathbf{f}_{\text{phonon}} = -\sum \hbar \mathbf{k} \dot{\bar{N}}(\mathbf{k}). \quad (4)$$

The rate of change of the average numbers of phonons $\bar{N}(k)$ in mode $\{k\}$ can be expressed in a general form

$$\dot{\bar{N}}(\mathbf{k}) = \sum W(\mathbf{k}, -\mathbf{k}') [\bar{N}(\mathbf{k}') - \bar{N}(\mathbf{k})] + \dots \quad (5)$$

and according to Fermi's Golden Rule,

$$W(\mathbf{k}, -\mathbf{k}') = 2\pi \left[\frac{(2\pi)^3}{\Omega_0 \rho_0} \right]^2 \frac{|V(\mathbf{k}, -\mathbf{k}')|^2}{\omega(\mathbf{k}) \omega(\mathbf{k}')} \delta(\omega(\mathbf{k}) - \omega(\mathbf{k}')). \quad (6)$$

The delta function means that the energy of the phonons is conserved in collisions with the defects (only elastic interactions). W contains the basic physics of the description via V , which is the coupling between the vibrational modes, represented by $\{k\}$, their polarisation vectors and the defects, which are represented by the Fourier, transforms $\mathfrak{Z}(\epsilon)$ of their strain fields ϵ . We assume that the time the dislocation and crack need to travel a distance of the order of the phonon mean free path is large compared to the phonon relaxation time, i.e. the phonon distribution is, on average, equal to the distribution in thermal equilibrium. The phonon relaxation time τ_{phonon} can be estimated from the thermal conductivity yielding the relaxation time $\tau_{\text{phonon}} \cong 10^{-11}$ s in Al. η_{PH} can now be found by taking the Fourier transform of the strain fields. At 300K η_{PH} is calculated to be 43 $\mu\text{Pa s}$ for dislocation drag in Al.

The interaction of moving defects with conduction electrons is attributed to the interaction of propagating elastic waves with the electrons. η_{E} can be derived from standard perturbation theory or on the basis of the Boltzmann equation¹⁰. The latter leads to

$$\eta_{\text{E}} \approx \sum_{\mathbf{q}} A_{\mathbf{q}} |\Delta_{\mathbf{q}}|^2 \quad (7)$$

where $\Delta_{\mathbf{q}} = i^3 q \mathfrak{Z}(\mathbf{u})_{\mathbf{q}}$ is the Fourier component of the dilatation field of the defect. The summation can be replaced by an integral over the Debye sphere of radius. η_{E} (Al) is calculated to be 0.9 $\mu\text{Pa s}$. From the experimental values of Al at temperatures above 100 K,

ranging between 24 and 57 $\mu\text{Pa s}$ at room temperature, we may conclude that the principal contribution to the dislocation drag is due the phonon viscosity and the electronic contribution is far less in this temperature range.

The drag coefficient of a moving crack relative to that of a moving edge dislocation can be obtained by evaluating the Fourier transform of the strain fields of a mode II crack, Eqs. (6) and (7). Here we assume that the damping force is solely due to the phonon viscosity and not rate-controlled by the formation of steps, ledges, emitting dislocations etc, like in a ductile material. The leading term in the strain fields of the crack is the stress intensity factor K_{II} . With a total crack length of 1 μm and a far field stress of 150 MPa the drag coefficient of a moving crack is about equal to that of a dislocation at a distance of the order of the Burgers vector in Al. In Fig.1 the ratio of these drag coefficients are displayed as a function of distance to the defect in Fourier space. It is reasonable to assume that the effective area involved in the phonon viscosity of the running crack due to elastic scattering is much larger compared to a moving dislocation. In Dugdale's description the extent of the zone involved in elastic scattering scales with $(K/\tau_0)^2$, with τ_0 the effective yield stress. Assuming that the plastic zone remains fixed in size, i.e. corresponding to the size of the crack as it propagates, from Fig.1 we may conclude that drag term of the running crack is at least one order of magnitude larger than of a moving dislocation.

When the crack propagates along a heterophase interface a similar calculation can be executed. The stress intensity factors were calculated within the so-called contact model¹¹. It avoids the oscillatory stress fields and overlapping and wrinkling of the crack surfaces near the tips, which are all unphysical in the open crack model¹². Although there are ways to overcome the latter difficulties by defining a certain length scale¹³, essentially the problem remains because this length scale is totally arbitrary and the mode-mixity is fully dependent on this choice. An exact solution as far as the stress intensity factors are concerned was obtained by Gutesen and Dundurs¹⁴, in series form, for the contact model and the length of the contact zone can be calculated depending on the difference in elastic properties of the two materials. With the ratio of the shear moduli of the two elastic media $\mu_2/\mu_1=2$ and with identical Poisson's ratio of $\nu_1=1/3$ the stress intensity factor of the interfacial crack is found to be 1.4 higher than the stress intensity factor for the homogenous case, at equal values of the far-field stress state. This result was incorporated in the calculation of the drag of a moving crack along a dissimilar material and is also depicted in Fig.1. Here, we may conclude that the drag of a crack along a heterophase interface is even more enhanced compared to the drag exerted on a moving dislocation in a homogeneous material at larger distances. In this work velocity-dependent (i.e. non-Newtonian drag) and effects of accelerations are ignored. These aspects were treated elsewhere¹⁵.

COMPUTER SIMULATIONS AND DISCUSSION

The main part of the modeling is done in a computational 'plastic' cell in which edge dislocation can move on their glide plane. Obstacles and nucleation sources are randomly positioned on these glide planes. The initial lattice dislocations are generated by a pre-deformation step, where the pre-existing crack is kept stationary. The nucleation sources are a 2D representation of a Frank-Read source and it may generate new dislocation pairs if the local applied stress exceeds the nucleation stress for a certain period of time. The actual values of both obstacle stress and nucleation stress are chosen according to a Gaussian distribution. The mode II loading conditions are placed on the remote boundaries of the elastic cell, in which the plastic cell is contained. The elastic cell is much larger than the plastic cell. Throughout the simulation the loading is increased using a fixed loading rate. All

the elastic interactions are handled using the Discrete Dislocation method and the 'crack dislocations' are described analytically. The various parameters are listed in Table 1.

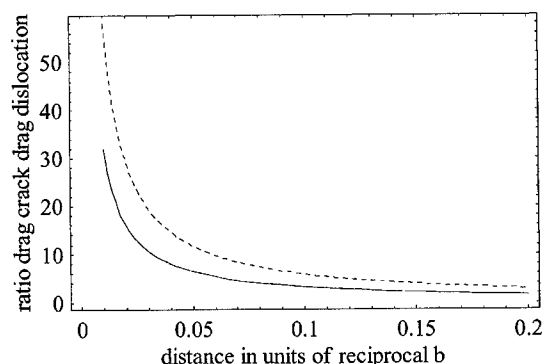


Figure 1. Ratio of the drag on a running crack and a moving dislocation as a function of the distance in Fourier space to the defect. Solid line refers to a homogeneous material whereas the dashed line illustrates the situation when the crack moves along a heterophase interface ($\mu_2/\mu_1=2$ and $v_1=v_2=1/3$).

Table 1

Property	Value	Property	Value
Young's modulus	70 GPa	Obstacle strength	450 MPa
Poisson ratio	0.33	Nucleation strength	140 ± 20 MPa
Material density	2.70 Mgm^{-3}	Nucleation time	$2 \cdot 10^{-10}$ s
Burgers vector	0.286 nm	Dislocation drag constant	40 μPas

The shape of the graph can be explained according to the Griffith criterion for a moving crack: the critical stress decreases with increasing crack size. It results in an increase of the effective stress and consequently in an increase of the crack tip velocity. An increasing drag value leads to an extension of the first linear region with a lower slope as can be seen in the unshielded crack result. Comparing the unshielded result with the shielded crack simulations the response looks roughly the same. Some striking differences can be seen, especially at higher values of the drag. These can be explained by looking at the surrounding dislocations in more detail. In all cases the initial dislocation structure is able to shield the crack tip but as soon as the stress inside the crack reaches the critical stress level the situation alters. At the lowest value of the drag coefficient the increase in velocity with increasing crack length is so fast that the dislocation structure cannot rearrange itself anymore so as to shield the crack. Nucleation is also a time-limited process and it also proves to be too slow to shield the crack. As soon as the crack breaks away it almost loses its interaction with the surrounding dislocation structure. A higher drag value, means a slower increase of the crack tip velocity, which in turn means that the shielding processes may longer stay effective. In the comparison of the graphs in Fig. 2, it is important to realize that the constant stress level of the unshielded stress is compared with a continuously increasing stress level in the shielded case, due to the fixed load rate. During various simulation runs it was also found that the shape and size of the dislocation structure depends critically on the actual value of the nucleation strength (see Fig.3). From the simulation with a non-uniform strength we see that the moving dislocations trigger the weaker sources and thus filling quickly the structure.

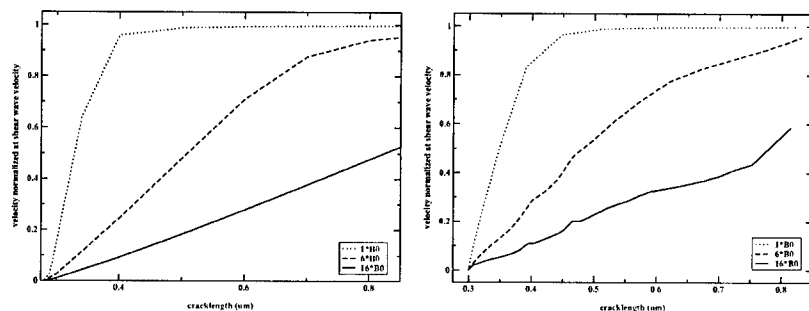


Figure 2. The crack tip velocity versus the crack length for various drag values for the crack. Left: an unshielded crack. Right: a crack shielded by dislocations.

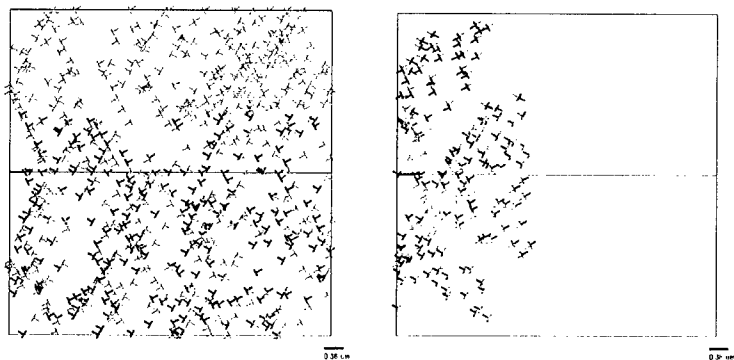


Figure 3. The effect of nucleation strength on the resulting dislocation structure around a crack. Left: the strengths are dispersed with a Gaussian distribution function with a spread of 20 MPa around an average of 140 MPa. Right: uniform nucleation strength of 150 MPa.

REFERENCES

- ¹ H.F. Bueckner, J. appl. Mech. 80, 1225 (1958).
- ² E. Van der Giessen, A. Needleman, Modelling Simul. Mater. Sci. Eng. 3, 689(1995).
- ³ M.H. Aliabadi and D.P. Rooke, Numerical Fracture Mechanics, Kluwer, Dordrecht, 1991.
- ⁴ J. D. Eshelby, F.C. Frank, F.R.N. Nabarro, Phil. Mag. 42, 351(1951).
- ⁵ G. Leibfried, Z. Phys. 130, 214 (1951).
- ⁶ J. Weertman, Dislocation based fracture mechanics, World Scientific, Singapore, 1996.
- ⁷ G. Leibfried, Z. Phys. 127, 344(1950)
- ⁸ J.D. Eshelby, Solid State Phys. 3, 134 (1956)
- ⁹ E. Nadgorny, Progress in Materials Science 31, Pergamon (1988) and references therein.
- ¹⁰ A.D. Brailsford, Phys. Rev. 186, 959 (1969)
- ¹¹ M. Comninou, J. Appl. Mech. 44, 631 (1977)
- ¹² J.W. Hutchinson, M.E. Mear, J.R. Rice, J. Appl. Mech. 54,829 (1987)
- ¹³ J.R. Rice, J. Appl. Mech., 55, 98 (1988)
- ¹⁴ A.K. Gaudes, J. Dundurs, J. Appl. Mech. 55, 580 (1988)
- ¹⁵ A. Roos, J.Th.M. De Hosson, E. van der Giessen, Comp. Mat.Sci., 20,1-19,2001 and 20,20-26 (2001)

Mechanics Of Crack Bridging Under Dynamic Loads

N.Sridhar^{1*}, B.N.Cox¹, C.L.Dunn² and I.J.Beyerlein³

¹Rockwell Science Center, 1049 Camino Dos Rios, Thousand Oaks, CA, U.S.A

²Massachusetts Institute of Technology, Cambridge, MA, U.S.A

³Los Alamos National Laboratory, Los Alamos, NM, U.S.A

ABSTRACT

A bridging law for fiber reinforced composites under dynamic crack propagation conditions has been derived. Inertial effects in the mechanism of fibre pullout during dynamic propagation of a bridged crack are critically examined for the first time. By reposing simple shear lag models of pullout as problems of dynamic wave propagation, the effect of the frictional coupling between the fibres and the matrix is accounted for in a fairly straightforward way. The solutions yield the time-dependent relationship between the crack opening displacement and the bridging traction. Engineering criteria and the role of material and geometrical parameters for significant inertial effects are identified.

INTRODUCTION

The mechanics of pullout and the resulting traction law have been much studied and are well understood for static loading. Simple analytical forms are available for $p(u)$ when the frictional coupling of the reinforcement to the matrix is uniform and slip extends over distances that are large compared to the reinforcement diameter [1-3]. In this limit, which is a common case in ceramic composites and textile polymeric composites, the shear lag model of load transfer between the reinforcement and the matrix is accurate.

In this paper, we extend existing models of the mechanics of pullout to high loading rates. An approach to evaluating a traction law that takes account of the inertia of the reinforcement and the matrix is formulated as a direct extension of the elementary static loading model. Attention will be focused on identifying a characteristic time for the frictional pullout problem that will allow rapid assessment of when inertial effects will be important.

THEORY

The crack propagation and pullout problem can idealized as follows. A matrix crack propagates on the plane $z = 0$ and is bridged by intact fibres in its wake. The crack propagation problem is represented by replacing the process zone by elastic composite material down to the fracture plane and representing the phenomena within the process zone by bridging tractions applied continuously on the fracture surfaces. The bridging tractions, p , are related to the axial stress in the fibres. The total crack opening displacement, $2u$, is defined as the difference in the actual displacement evaluated across the process zone and the displacement that would be

expected if the material in the process zone was elastic. The traction law, $p(u)$, is derived by considering the micromechanics of frictional sliding. The traction boundary conditions are as follows. At $z = 0$, the matrix is traction-free, while the fibres sustain the axial traction p . At $z = l_s$, the strain in the fibres and the matrix must equal the average strain in the composite adjacent to the process zone ($z > l_s$). Shear tractions may arise along the vertical boundaries of the representative volume (parallel to z), but these are neglected.

Micromechanics of Dynamic Pullout

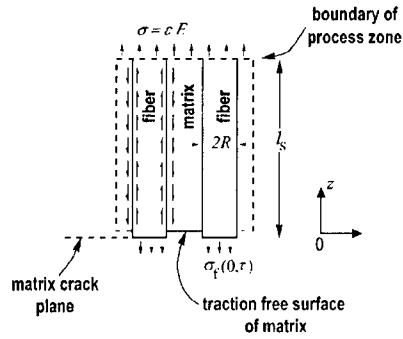


Figure 1: Schematic of the dynamic pullout problem in a composite near the fracture plane.

When friction is the only active force of resistance, the dynamic pullout problem is one of wave propagation along a fibre in the presence of frictional retardation. A representative volume (Fig. 1) consists of cylindrical fibres of radius R and volume fraction f embedded in a matrix ($z \geq 0$). The fibre and the matrix have axial Young's moduli E_f and E_m and densities ρ_f and ρ_m respectively. The axial displacement, strain, and stress of the fibre and the matrix are denoted u_f and u_m , ϵ_f and ϵ_m , and σ_f and σ_m , respectively. The axial displacements will be assumed to be the only nonzero displacement components induced by loading and to be uniform across any section of the fibre or the matrix. Thus the displacement, strain, and stress in the fibre and the matrix are functions of z and t only. The fibres are coupled to the matrix by friction tractions, τ_f , which are assigned the following properties. If relative motion exists between the fibres and the matrix, then, $\tau_f = \tau$ if $\dot{u}_f < \dot{u}_m$ and $\tau_f = -\tau$ if $\dot{u}_f > \dot{u}_m$. The dot indicates time differentiation, τ is a positive constant and $\tau_f > 0$ indicates friction tractions acting on the fibres in the positive z direction. The friction law is simplified to be rate independent since the focus in this analysis is get analytical results and engineering estimates for inertial effects on bridging. With such a friction law, the dynamic wave equations for the fibre and the matrix are:

$$\frac{\partial^2 u_f}{\partial z^2} = -\frac{2\theta\tau}{RE_f} + \frac{1}{c_f^2} \frac{\partial^2 u_f}{\partial t^2} \quad (1a)$$

$$\frac{\partial^2 u_m}{\partial z^2} = \frac{2f}{1-f} \frac{\theta\tau}{RE_m} + \frac{1}{c_m^2} \frac{\partial^2 u_m}{\partial t^2} \quad (1b)$$

where $c_i = \sqrt{E_i / \rho_i}$, $\theta = 1$ if $\dot{u}_m > \dot{u}_f$ and $\theta = -1$ otherwise. The boundary conditions are as follows: On the fracture plane $u_f(0, t) = 0$ and $\sigma_m(0, t) = 0$; On the boundary of the process zone ($z = l_s$), $u_f = u_m = u_c$, where u_c is the displacement of the adjacent intact composite. Conditions also exist on stress or strain and particle velocities at the process zone boundary. These conditions depend on the nature of the loading history, which can be expressed as the function $\varepsilon(t)$, where ε is the strain in the z direction in the intact composite adjacent to the process zone boundary.

Composite Stress Rising Linearly in Time

In the depiction of Fig. 1, the process zone boundary will propagate away from the fracture plane as $\varepsilon(t)$ rises. If the load history, $\varepsilon(t)$, possesses discontinuities, e.g., a step load, then discontinuities in stress and velocity will also propagate at the boundary of the process zone [4]. A case of representative interest for dynamic bridged crack problems and for which analytical results can be found is that of a load or bridging traction that increases linearly in time. A linearly increasing load might give insight, for example, into bridging effects in a specimen in which substantial bending arises, such as a standard double cantilever beam delamination specimen. In such specimens, the crack profile is often approximately linear and the rate of increase of the bridging tractions at any point might also be approximately linear if the crack propagates at approximately constant speed. Therefore, $\varepsilon(t) = kt$, where k is constant and all displacements and boundary tractions are zero for $t < 0$. The location of the zone boundary at time t may then be written as $l_s = \eta(t)c_m t$, where the function $\eta(t)$ depends on material and geometrical parameters and the form of $\varepsilon(t)$ and it will be shown to be bounded by $0 < \eta(t) \leq 1$. For the loading conditions considered, the additional boundary conditions at $z = l_s$ are: $\dot{u}_f = \dot{u}_m = \dot{u}_c$ and $\varepsilon_f = \varepsilon_m = \varepsilon(t)$. In this case, $\theta = 1$ and the wave equations have the solutions

$$u_f = -\frac{k}{c_m} \alpha z^2 + [1 + 2\eta\alpha] \varepsilon z \quad (2a)$$

$$u_m = \frac{k}{c_m} \frac{1}{2\eta} z^2 + \frac{1}{2} [1 + 2\eta\alpha] \varepsilon l_s \quad (2b)$$

where η is independent of time and satisfies

$$\alpha\eta^3 + \frac{1}{2}\eta^2 + \beta\alpha\eta - \frac{1}{2} = 0 \quad (2c)$$

with the dimensionless parameters α and β given by

$$\alpha = \frac{\tau c_m}{E_f R k} \quad \& \quad \beta = \frac{f}{1-f} \frac{E_f}{E_m} \quad (3)$$

Analysis shows that Eqn. (3) has only one real root, which always lies in (0,1). The displacement, u , is given by the common fibre/matrix displacement at the boundary of the process zone minus the displacement expected if the process zone material were elastic:

$$u = \frac{c_m \alpha \eta^2}{k E^2} p^2 \quad (4)$$

Equation 4 constitutes the traction law for the case of linearly rising loads. The limit of very fast loading corresponds to $k \rightarrow \infty$, whereupon $\alpha \rightarrow 0$ and $\eta \rightarrow 1$, since the first and third terms in Eqn. (2c) become negligible. The disturbance then propagates at the bar wave speed in the matrix. Static loading is represented by the limit $\alpha \rightarrow \infty$, for which the first two terms of Eqn.

(2c) become small and one has the asymptotic solution $\eta \rightarrow 1/(2\alpha\beta)$ which coincides with the results obtained by McCartney [2]. We can also show that for loads that increase linearly with time [5], the form of the traction law is identical in the static and dynamic cases and

$$\frac{u}{u_{(st)}} = 2\alpha\beta\eta \quad (5)$$

Since $2\alpha\beta\eta < 1$ always, inertial effects increase the stiffness, dp/du , of the traction law for loads that increase linearly in time.

Fibre Pullout from a Rigid Matrix

In this section, the pullout of a single fibre from a rigid matrix to which it is coupled by friction is examined. The problem considered for a rigid matrix is the case of the fibre being loaded on the fracture plane by tractions, $p = (\sigma_f(0, t))$. The response of the system that is of interest is wholly represented by the load point displacement, i.e., the displacement, $u_0(t)$, of the fibre at $z = 0$, since the matrix is rigid (motionless). Specifying a boundary condition on the fracture plane, rather than at the end of the slip zone, as for the composite problem, is preferred because it allows for a simpler statement on the imposed loading. This is then exactly identical to the problem of an end loaded rod damped by friction [6]. Analytical solutions can be found for step loads as well as for linearly increasing loads.

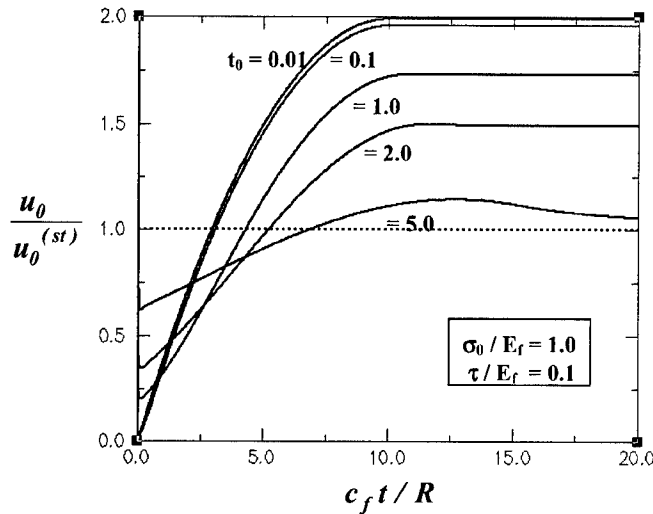


Figure 2: The variation of the load point displacement (normalized by the corresponding quasi-static value) as a function of the normalized time for various values of t_0 .

The most interesting features are the following. While the load point displacement is reduced by inertial effects for linearly increasing loads, for a step load it is increased. For a linearly increasing load, $e_0 = kt$,

$$\frac{u_0}{u_0^{(st)}} = 2 \left[\frac{\sqrt{1 + (kt_r)^2} - 1}{(kt_r)^2} \right] \quad (6)$$

where the characteristic time of the system, t_r , is given by $t_r = E_f R / (\tau c_f)$, with the subscript “r” referring to the matrix being rigid. The expression in (6) is always less than unity. In contrast, for a step function load $\varepsilon_0(t) = \varepsilon_0$, a constant for $t > 0$, all motion ceases when $t = \varepsilon_0 t_r$, at which point $u_0 = 2u_0^{(st)}$: inertial effects double the displacement expected from loading statically to the same applied load. Correspondingly, the strain gradient left in the fibre following dynamic (step) loading is exactly half that found after static loading.

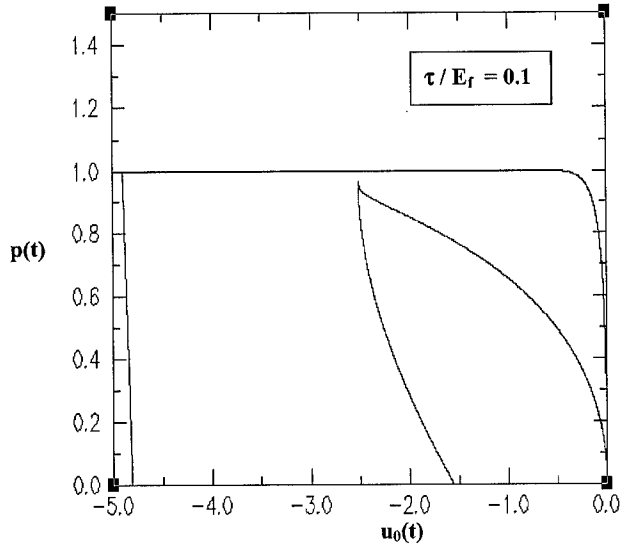


Figure 3: The traction law for load-unload case. The traction is normalized by the fibre modulus and the load point displacement is normalized by the fibre radius. The inner loop corresponds to the quasistatic load-unload case and the outer loop to the step load-unload case.

For more general loading configurations, a finite difference numerical scheme is used to solve the non-linear wave equation [7]. The finite difference method is based on a second-order upwind scheme written for the linearized scalar form of the Euler equations. Further, by directional discretization of the derivatives, the local Euler equation is solved for discontinuous neighboring states [8]. This approach results in artificial viscosity being introduced into the governing equation but solutions thus generated allow resolution of the discontinuities without oscillations. This last aspect is important since discontinuities in stresses and particle velocities at the wavefront are essential phenomena for loading histories having discontinuous time derivatives.

With the numerical method, the load-point displacement when the boundary traction is $p(t) = \sigma_0(1 - e^{-t/t_0})$ is computed. In the limit $t_0 \rightarrow 0$, this approximates the step loading case. For fast loading (small t_0), the bridging traction law is initially stiff and then softens (see Fig.2). The crack opening displacement when all particle motion stops is greater than the corresponding value for the static loading to that stress level. Significant deviation from the static value even for moderate loading rates (especially from small time) is observed. Finally, the numerical scheme was also used to examine the influence of inertial effects on the traction law during a load-unload cycle. Next, consider loading the fiber instantaneously with a unit step load, wait for particle motion to cease and then remove the load instantaneously. The hysteresis behavior (Fig. 3) and the energy dissipated are significant when inertial effects are present.

CONCLUSIONS

Analytical results have been presented for the problem of bridging by the mechanism of fibre pullout when the inertia of the fibre and the matrix are taken into account. Simple criteria for significant inertial effects in the bridging mechanism in representative mode I crack propagation problems are calculated. For pullout or bridging stresses that rise linearly in time, the instantaneous crack displacement is less in the presence of inertial effects than it would be under static loading to the same bridging stress. However, solutions for pullout from a rigid matrix suggest that, if the bridging stress rises rapidly and is then held at a constant value, the crack displacement when all particle motion finally stops will be greater than it would have been under static loading to that stress level. Thus regimes of both hardening and softening of the bridging traction law due to inertial effects can be expected in bridged crack problems. To conclude, inertial effects can significantly modify bridging behavior, even at moderate loading rates.

ACKNOWLEDGMENTS: NS and BNC are grateful for support from the U.S. Army Research Office through contract number DAAD19-99-C-0042, administered by Dr. David Stepp, and IJB thanks the U.S. Dept. Of Energy for support through contract W-7405-ENG-36.

REFERENCES:

1. D. B. Marshall, B. N. Cox and A. G. Evans, *Acta Metall.* **33**, 2013-2021 (1985).
2. L. N. McCartney, *Proc. Roy. Lond.* **A409**, 329-350 (1987).
3. J. W. Hutchinson and H. M. Jensen, *Mechanics of Materials*, **9**, 139-163 (1990).
4. J. D. Achenbach, *Wave Propagation in Elastic Solids*, North-Holland, 1973, pp.138
5. B.N.Cox, N.Sridhar, and I.J.Beyerlein, submitted to *J. Mech. and Phys. Solids*, June 2000
6. L.V.Nikitin and A. N.Tyurekhodgaev, *Wave Motion*, **12**, 513-526 (1990)
7. N.Sridhar, B.N.Cox and C.L.Dunn, in preparation for submission.
8. C.Hirsch, *Num. Computation of Internal and External Flows*, John Wiley,1988,p 408

Multiscale Simulations of Brittle Fracture and the Quantum-Mechanical Nature of Bonding in Silicon

N. Bernstein and D. Hess

Center for Computational Materials Science, Naval Research Laboratory,
Washington, DC 20375, USA.

ABSTRACT

We simulate the microscopic details of brittle fracture in silicon by dynamically coupling empirical-potential molecular dynamics of a strained sample to a quantum-mechanical description of interatomic bonding at the crack tip. Our simulations show brittle fracture at loads comparable to experiment, in contrast with empirical potential simulations that show only ductile crack propagation at much higher loading. While the ductility of the empirical potentials can be attributed to their short range, it is unclear whether the increased range of the tight-binding description is sufficient to explain its brittle behavior. Using the multiscale method we show that at a temperature of 1100 K, but not at 900 K, a dislocation is sometimes nucleated when the crack tip impinges on a vacancy. While this result is too limited in length and time scales to directly correspond to experimental observations, it is suggestive of the experimentally observed brittle to ductile transition.

INTRODUCTION

Many materials, ranging from silicon to ferritic steels, exhibit a transition between brittle and ductile fracture as a function of temperature [1]. The qualitative differences between these two modes of failure lead to great differences in material toughness. While long-range elastic strain fields, well described by continuum elasticity theory, provide the energy that drives fracture and failure, the nature of fracture itself is ultimately determined on the scale of atoms and the electrons that bind them. Therefore, a microscopic description is required for reliable prediction of the nature of fracture in a given material.

Silicon has become a model system for the brittle to ductile transition (BDT) since it shows a particularly sharp transition between the two types of behavior [1]. Below the BDT temperature (about 850 K) failure occurs at the Griffith criterion [2], when elastic energy relief due to crack elongation balances the energetic cost of the new surface. Atomistic simulations of fracture in silicon using empirical potentials (EP) show a disordered zone around an atomically blunt crack, shown in Fig. 1, which propagates only at much higher loadings than the Griffith criterion [3, 4, 5]. Ab-initio simulations of quasistatic fracture of small samples show brittle behavior with some lattice trapping but no disorder [6, 7].

To explore the nature of fracture in silicon at the atomic scale, we have developed an atomistic simulation technique based on molecular dynamics (MD). The method incorporates a simple quantum-mechanical description of atomic interactions near the crack tip, dynamically coupled to EP MD far from the crack tip. In contrast to simulations

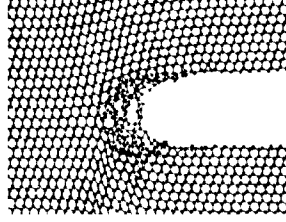


Figure 1: A snapshot from a simulation of fracture using the EDIP empirical potential. The crack tip is blunt, and a disordered region has formed ahead of the crack.

utilizing EP models alone, our results show good agreement with experiment. This suggests that an accurate quantum-mechanical treatment of bonds near the crack tip provides a qualitative improvement in description of fracture over the EP models used previously.

METHOD

Recognizing that fracture involves physical processes on a wide range of length scales, Abraham *et al.* constructed a multiscale tool for simulating fracture. They dynamically coupled time-dependent finite elements for the far field, EP MD for atoms on the mesoscopic length scales, and tight-binding (TB) MD in a nm sized region that includes the crack tip [8]. Other groups have also presented similar approaches that couple various subsets of these methods [9, 10, 11, 12, 13]. Here, we simulate the process of dynamic fracture in silicon with a coupling of length scales approach using two regions [5]. Far from the crack we use EP MD with the environment dependent interatomic potential (EDIP) [14, 15]. In the immediate vicinity of the crack tip we include explicitly the electrons that mediate interatomic bonds through a quantum-mechanical model based on a semi-empirical TB total-energy method [16]. The tight-binding forces are computed using a Green's function based method that scales linearly with the number of atoms [5, 17].

The MD time evolution is computed using the velocity Verlet algorithm [18] at constant energy with a 1.0 fs time step. The system consists of a $3 \times 25 \times 60$ supercell of a 12 atom $(\frac{1}{2}\bar{1}0) \times (11\bar{1}) \times (\frac{1}{2}\bar{1}\bar{1})$ (from here on denoted as x , y , and z) unit cell. Periodic boundary conditions are used along x and z . The thin, periodic geometry of the system along x leads to a nearly two-dimensional plane-strain configuration in the y - z plane.

A seed crack with $(11\bar{1})$ faces and a $\langle 1\bar{1}0 \rangle$ crack front is introduced by removing a bilayer in the the x - z plane. The crack extends through the entire system along x , and is 198.6 Å long (half the system size) along z . The crack is centered with respect to the sample in the z direction, so that it has two tips, one at each end. The entire system includes over 53000 atoms. We use a TB region that is about 17 Å (five bilayers) thick along y , and about 45 Å long (17 lattice periodicities) along z , surrounded by a 6.5 Å coupling layer. This volume, including the coupling layer, includes about 1000 atoms. The TB region is placed around one of the tips of the seed crack, and is not moved during the simulation. Fig. 2 shows the configuration of atoms and the TB region near the crack tip.

The initial configuration is set by moving each atom according to the elastic displacement

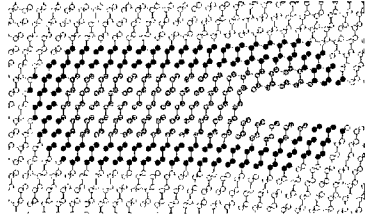


Figure 2: Atomic configuration in the vicinity of one of tips of the seed crack. EP region atoms are drawn in white, TB region atoms in grey, and coupling layer atoms in black.

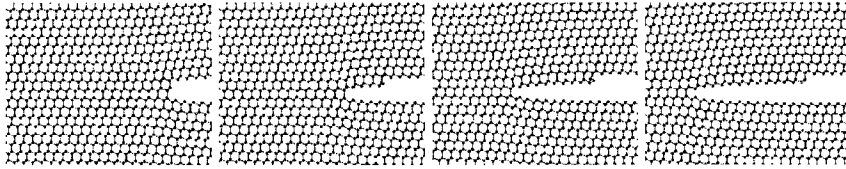


Figure 3: Snapshots from a multiscale simulation at $T = 200$ K and 1.7% applied strain at 0.4 ps, 1.0 ps, 1.6 ps and 2.1 ps (from left to right).

field in a strained infinite plate with an infinitely thin crack [19], and fixing the $+y$ and $-y$ surfaces. We rescale the EDIP length scale (parameter c of ref. [15]) to reduce the EDIP equilibrium lattice constant to the TB model equilibrium value of 5.406 Å.

RESULTS

Four snapshots from a simulation of a system under 1.7% strain at $T = 200$ K are shown in Fig. 3. The crack retains an atomically sharp tip, propagating in a straight line without branching or meandering, and leaves behind a smooth, unreconstructed surface. The velocity of the crack tip as a function of loading is plotted in Fig. 4. Onset of crack propagation is just above the Griffith criterion, in good agreement with experiment. The limiting speed of the crack, about 2.7 m/s, is 0.6 times the Rayleigh wave speed of EDIP. The saturation of the crack speed at about 0.6 to 0.9 of the Rayleigh wave speed appears to be universal, having been observed in our simulations using EDIP and Stillinger-Weber (SW), as well as a modified form of SW that gives brittle fracture [3], and experiment [2, 20, 21]. It is interesting to note that this speed is close to the critical speed for instability to branching seen in ball and spring models [21], although we have not observed such an instability.

In experiment, ductile behavior above the BDT temperature is accompanied by a large number of dislocations. To see if our model can shed some light on the microscopics of the BDT, we simulated the fracture of a sample at 1100 K. While we observed no dislocations in simulations of fracture in a perfect crystal, a vacancy directly ahead of the crack tip altered this behavior. Snapshots from one such simulation are shown in Fig. 5. Upon reaching the vacancy a 90° shuffle set partial dislocation is nucleated immediately above

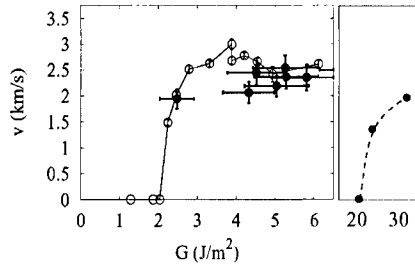


Figure 4: The speed of the crack tip as a function of energy release rate, which is proportional to the applied strain squared. Solid line with open circles is the results of the present work, solid circles with error bars are experimental data from ref. [2], and dashed line is an approximate sketch of EDIP simulation. The vertical line indicates the Griffith criterion for the multiscale simulation.

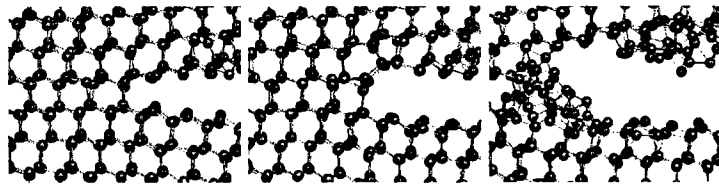


Figure 5: Snapshots from a multiscale simulation at $T = 1100$ K and 1.7% applied strain of a sample with a vacancy ahead of the crack. The left panel shows the crack tip immediately before reaching the vacancy. The middle panel shows the nucleated dislocation core, visible as a seven-fold ring adjacent to a five-fold ring. The right panel shows the system at the end of the simulation, with the arrested crack tip.

the crack tip, and the crack arrests. Repeating the same simulation 11 times, changing only the initial velocities, has shown this behavior twice. At a temperature of 900 K, no dislocations nucleated in 10 repetitions of the simulation.

DISCUSSION

The material properties that lead to the difference between the EP and multiscale simulation are not obvious despite the striking contrast in their morphologies. One model, proposed by Rice, provides a quantitative measure of the tendency of a material to be brittle or ductile in terms of the ratio of the energies for surface and dislocation formation γ_s/γ_{us} [22]. Values of Rice's criterion for silicon computed using different methods are shown in Table 1. While none of the models agree perfectly with the LDA calculation, which is expected to be quite accurate, no trend is apparent. For both glide and shuffle set dislocations, Rice's criterion for the TB model is quite similar to at least one of the EP models. Therefore application of Rice's criterion would predict that the multiscale simulation should be quite similar to an EP simulation. Since this is not the case, clearly something other than this energetic criterion is controlling the behavior. One alternative is a criterion based on stresses rather than energies [4]. To describe covalent

Table 1: Rice criterion for glide and shuffle set dislocations computed using LDA, TB, EDIP, and SW.

	LDA	BK-TB	EDIP	SW
γ_s/γ_{us} (glide)	0.90	0.40	0.59	0.45
γ_s/γ_{us} (shuffle)	1.02	0.90	0.85	1.71

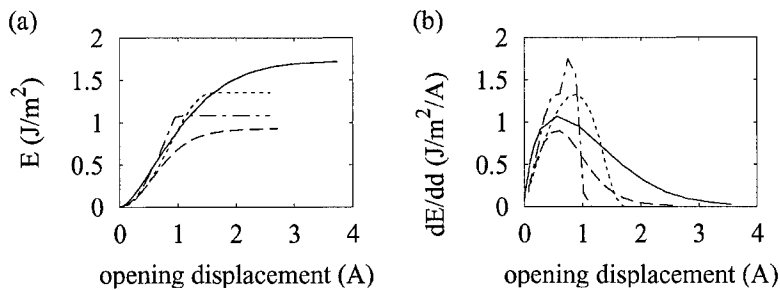


Figure 6: Energy as a function of displacement for two blocks of silicon pulled apart rigidly, exposing a (111) surface (panel a), and the stress, defined as the derivative of the energy (panel b). Solid line is LDA, dashed line is TB, dotted line is SW and dash-dotted line is EDIP.

bonding in a simple functional form, EP models such as SW and EDIP include only nearest neighbor interactions. In TB and LDA, and presumably in experiment, two surfaces interact even when the atoms are substantially farther apart. Since the surface energies of all the models are similar, the stresses needed to pull apart two blocks of silicon to form a new surface are much higher for the short range potentials, as shown in Fig. 6. Therefore, even when it is energetically favorable for the crack to propagate, the stress at the crack tip may not be high enough to break a bond. The stress needed to form a dislocation, on the other hand, is not systematically overestimated by the short range EP models. As a result, for the EP models the shear stress directly above the crack tip exceeds the value needed to nucleate a dislocation before the tensile stress is high enough to break a crack tip bond. While the range of the potential appears to explain why the empirical potentials are ductile, it is not necessarily sufficient to explain why TB is brittle. Another possibility is suggested by the explicitly quantum-mechanical description of the electrons that form the interatomic bonds. This inherently non-local description is only approximated by the three body and coordination dependent terms in the EP models. However, some more subtle non-local effect, for example a weakening of the crack-tip bond by the local strain, could also reduce the effect of the peak stress for the TB model and therefore the multiscale simulation.

CONCLUSION

We have developed a multiscale simulation tool that allows us to study fracture and other multiscale phenomena with accuracy and efficiency. The dynamical coupling of TB and EP atomistic simulations has produced a simulation of dynamic brittle fracture in silicon that

is in good agreement with experiment. In contrast, EP simulations so far have shown only ductile fracture at unphysically high loads. The quantum-mechanical description of bonding at the crack tip gives the multiscale method the necessary accuracy, while the rest of the system is more efficiently (and sufficiently accurately) described by an EP. The qualitative difference in the morphology of fracture between empirical potentials and the multiscale approach cannot be attributed to Rice's energetic criterion. It seems likely that for the empirical potentials the short range of the interactions magnifies the peak stress that the system can sustain to unphysical levels. However, it is not clear that the intermediate range of the TB model is sufficient to explain its brittleness, and the fundamental reason for the qualitative differences is still an open question. Our observation of dislocation nucleation at 1100 K, but not at 900 K, suggests that a BDT may occur at a temperature close to the experimental value.

ACKNOWLEDGEMENTS

This work is supported in part by a grant of computer time through the DOD HPC Grand Challenge program at the ASC MSRC and MHPCC DSRC. The authors thank the Office of Naval Research for its support.

REFERENCES

- [1] P. B. Hirsch and S. G. Roberts, *Phil. Mag. A* **64**, 55 (1991).
- [2] J. A. Hauch *et al.*, *Phys. Rev. Lett.* **82**, 3823 (1999).
- [3] D. Holland and M. Marder, *Phys. Rev. Lett.* **80**, 746 (1998).
- [4] D. Holland and M. Marder, *Adv. Mat.* **11**, 793 (1999).
- [5] F. F. Abraham *et al.*, *Mat. Res. Soc. Bull.* **25**, 27 (2000).
- [6] J. C. H. Spence, Y. M. Huang, and O. Sankey, *Acta Metall. Mater.* **41**, 2815 (1993).
- [7] R. Percz and P. Gumbsch, *Phys. Rev. Lett.* **84**, 5347 (2000).
- [8] F. F. Abraham *et al.*, *Europhys. Lett.* **44**, 783 (1998).
- [9] S. Kohlhoff, P. Gumbsch, and H. F. Fischmeister, *Phil. Mag. A* **64**, 851 (1991).
- [10] W. G. Hoover, A. J. D. Groot, and C. G. Hoover, *Comp. Phys.* **6**, 155 (1992).
- [11] J. A. Nieminen and S. Paavilainen, *Phys. Rev. B* **60**, 2921 (1999).
- [12] W. Cai *et al.*, *Phys. Rev. Lett.* **85**, 3213 (2000).
- [13] G.-H. Wen *et al.*, *Int. J. Quant. Chem.* **78**, 459 (2000).
- [14] M. Z. Bazant, E. Kaxiras, and J. F. Justo, *Phys. Rev. B* **56**, 8542 (1997).
- [15] J. F. Justo *et al.*, *Phys. Rev. B* **58**, 2539 (1998).
- [16] N. Bernstein and E. Kaxiras, *Phys. Rev. B* **56**, 10488 (1997).
- [17] N. Bernstein, In preparation.
- [18] M. Tuckerman, B. J. Berne, and G. J. Martyna, *J. Chem. Phys.* **97**, 1990 (1992).
- [19] K. B. Broberg, in *Cracks and Fracture* (Academic Press, San Diego, 1999), p. 132.
- [20] T. Cramer, A. Wanner, and P. Gumbsch, *Phys. Rev. Lett.* **85**, 788 (2000).
- [21] M. Marder and X. Liu, *Phys. Rev. Lett.* **71**, 2417 (1993).
- [22] J. R. Rice, *J. Mech. Phys. Solids* **40**, 239 (1992).

**Crack Behaviour at Bi-Crystal Interfaces:
A Mixed Atomistic and Continuum Approach**

Arun R. Pillai and Ronald E. Miller

Department of Mechanical Engineering, University of Saskatchewan, Saskatoon, SK, Canada
S7N5A9

ABSTRACT

Interfacial defects like grain boundaries and phase boundaries play an important role in the mechanical behaviour of engineering alloys. In this work the problem of a crack on a bi-crystal interface is studied at the atomic scale, with the goal of elucidating the effects of varying interatomic interaction on crack behaviour and to assess the suitability of existing fracture criteria to the anisotropic bi-crystal case. Calculations are performed using the Quasicontinuum (QC) method [1]. Using suitable approximations, some of the existing fracture criteria were used to predict ductile or brittle fracture and compared to the QC results.

INTRODUCTION

One goal of theoretical studies of fracture has been the ability to predict whether a given crack system is inherently brittle or ductile. Two widely used models with this predictive capability are the model of Rice and Thomson (RT) [2] and that of Rice [3]. Rice and Thomson computed the critical energy release rate G for dislocation emission in single materials [2]. The RT model was later modified by Rice *et al.* to make it suitable for isotropic bimaterials [4]. Later, dislocation emission from a stressed crack tip was analysed based on the Peierls concept by Rice [3] for isotropic single materials. The aim of the present work is to provide, via atomistic simulation, a library of different bi-crystal crack results against which to test the suitability of these models. We find that even though the Rice model has been formulated for an isotropic single crystal, it does a reasonably good job of predicting the behaviour of bi-crystal interfacial fracture. The RT model is not as successful at matching the simulations.

Crack studies have been done extensively using atomistic modelling or a mixed atomistic and continuum approach. Numerous authors (see for example [5], [6], [7] and [8]) have studied fracture in single crystals using atomistic techniques. Thomson and Zhou [9] studied a bi-crystal interface crack in an interface in a model 2D-hexagonal lattice and compared their results to continuum models. Atomistic modelling has been used to study the behaviour of cracks in grain boundaries by Cleri *et al.* [10] whose work helped interpret the direction dependence of fracture experiments on copper bi-crystals.

The main disadvantage of atomistic modelling tools is that they are computationally very slow. To circumvent this problem, various approaches have been developed whereby a mixed atomistic/continuum formulation is employed to reduce the computational demand. These include the FEAt (finite element-atomistic) method of Gumbsch [11], the MAAD method of Abraham *et al.* [12] and the Quasicontinuum (QC) method of Tadmor *et al.* [1]. In this work the QC technique is used to simulate cracks on interfaces between a variety of crystals described by EAM [13] interatomic potentials. By systematically varying the interface strength, we have produced a library of results, for which the critical energy release

rate for failure (either brittle or ductile) has been computed. The continuum models to predict these material responses were then tested against these simulation results.

FRACTURE SIMULATIONS

In this work we have considered a very simple crack geometry using FCC (face centered cubic) crystals. The crack is in the $\langle 110 \rangle$ direction and this geometry is selected so that the slip planes intersect the crack line, which is one of the requisites for applying the existing fracture criteria. The four slip planes are at angles 54.7, 125.3, 234.7 and 305.3 degrees from the crack direction, as shown schematically in figure 1(A) (Note that the actual dimensions of the models are 70x70 Å).

The loading of this crack is quasi-static, applied by incrementing the displacement in small steps. The increment in displacement for every load step is found using the functional form of an isotropic, linear elastic material:

$$\Delta u_i^{(I)} = \frac{\Delta t_i}{2} \left(\frac{r}{2\pi} \right)^{\frac{1}{2}} f_i^{(I)}(\theta), \quad (1)$$

where $\Delta u_i^{(I)}$ is the increment in displacement and Δt_i is the incrementing factor. After each increment, the boundary nodes in the QC model are held fixed while the internal nodes are allowed to relax to their minimum potential energy configuration. Note that the form of (1) is taken only as a good initial guess to the incremental displacement field of the anisotropic bi-crystal. By taking small load steps Δt_i between relaxations, this has been found to lead to quick convergence and good solutions. Note also that only the boundary nodes on the specimen are fixed, keeping the nodes on the crack surfaces stress free.

The critical energy release rate for crack propagation or dislocation emission is calculated using a J integral calculation just before the critical load step. For the anisotropic bi-crystal, J can be calculated numerically. In this work we have followed the domain integral method given by Shih *et al.* [14]. As well, the stress intensity factors K_I and K_{II} are calculated based on the work by Cho *et al.* [15].

In order to avoid the complexity of misfit dislocations at the interface, we have modified the EAM potentials of Cu, Ag, Ni, Pt, Pd, originally due to by Foiles, Daw and Baskes [16]. We have done this by making the lattice constants the same for all these elements, using a scaling factor $f = \tilde{a}_0/a_0$, the ratio of the scaled lattice constant to the original lattice constant. Thus the scaled EAM potentials (indicated by the $\tilde{}$) are derived from the original potentials as:

$$\tilde{\phi}_{ij}(\tilde{r}) = f^3 \phi_{ij}(f\tilde{r}), \quad \tilde{F}(\rho) = f^3 F(\rho), \quad \tilde{\rho}(\tilde{r}) = \rho(f\tilde{r}), \quad (2)$$

where ϕ_{ij} is the pair potential between atoms i and j , F is the embedding energy and ρ is the electron density.

Using this scaling will change the lattice constants but leave the elastic moduli unchanged, and thus the elastic properties remain as they were in the original reference [16]. We have arbitrarily chosen to scale all lattice parameters to $\tilde{a}_0 = 3.84\text{Å}$.

The consequence of the scaling is that we are not using real materials, but from this work we hope to get insight into generic fracture behaviour. Scaling does not mean that we are simply using the same materials with different elastic constants, since other parameters like

the unstable stacking fault energy, stacking fault energy and cohesive energy are different between these materials. Hence these can be considered to be different materials with only the lattice constants the same. We vary the interface strength by introducing a constant, φ in the pair potential between the unlike atoms. Thus for atom types A and B

$$\phi_{AB}(r) = \varphi \sqrt{\phi_{AA}(r)\phi_{BB}(r)}. \quad (3)$$

To systematically name each system we have studied, we will use the notation (lower grain)-(upper grain)- φ . Thus for example the system with Ni in the lower grain and Pt in the upper grain, with $\varphi = 1.0$ would be indicated as Ni-Pt-1.0.

CONTINUUM MODELS FOR FRACTURE PREDICTION

The critical energy release rate for crack propagation was calculated for each system using the Griffith model. The energy release rate for crack propagation is given as

$$G_{crack} = \gamma_s^1 + \gamma_s^2 - \gamma_{int}, \quad (4)$$

where γ_s^1 and γ_s^2 are the free surface energies of material 1 and material 2, respectively, and γ_{int} is the energy of the interface between the two materials.

In this work we have used both the Rice model [3] and the RT model [2] to calculate the energy release rates for dislocation emission. The RT model was originally developed for the isotropic bimaterial case [17], so we have used Voigt averages of our anisotropic constants [18]. The Rice model was originally developed for isotropic single materials and so an average of the elastic constants of the two materials was used here.

The end result of both models is an expression for the critical energy release rate for the emission of a dislocation, G_{dist} , which is compared to G_{crack} to decide brittle or ductile response. The RT model requires a dislocation core radius, which we take to be equal to b , the Burgers vector. It also requires the elastic constants of the two materials and the atomic scale phase angle, $\hat{\psi}$, which is the arctan of the ratio of the stress intensity factors. The Rice model requires the elastic constants, the unstable stacking fault energy and the stress intensity factors at the crack tip. In our work, we find the stress intensity factors numerically and use the minimum of the unstable stacking fault energy between the two materials.

In this work we make use of the Rice model for a bi-crystal case by recognizing two facts: (1) ϵ for our materials is small and therefore the two materials are elastically very similar, and (2) we can compute local values of K_I and K_{II} at our crack tip from the numerical simulations. In addition, for both the Rice and the RT models we are assuming that the anisotropy of our crystals can be neglected. Whether or not these approximations are valid will be borne out by the comparisons described next.

SIMULATION RESULTS AND COMPARISON TO CONTINUUM MODELS

The different kinds of results obtained from the simulations are shown in parts B to F in figure 1. Figure 1(B) shows Ni-Pt-1.0 just before dislocation emission. This is shown just as a typical example of the specimen just before the critical event (i.e. either cleavage or dislocation emission). Figure 1(C) shows dislocation emission. The case shown is the dislocation emission into platinum for a combination of Ni-Pt-1.0. As seen in the figure, the

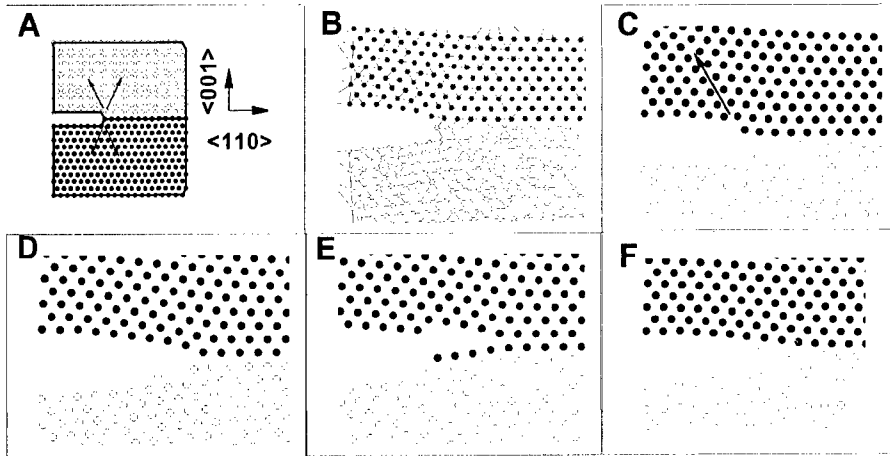


Figure 1: (A) Geometry of the crack at a bimaterial interface; (B-F) typical results, as described in the text.

crack tip has become blunt as a result of dislocation emission. The dislocation is caused due to the slip of a block of atoms along the slip plane shown.

Figure 1(D) shows crack propagation along the interface (in Ni-Pt-1.15), the second type of result observed. Part E shows crack propagation one layer above the interface into Cu (in Ni-Cu-1.0). As a result of the crack propagation, the free surfaces formed are a free surface of Cu and a surface of Ni with one layer of Cu atoms attached. For the case of Ag-Pt-1.0, the result observed was crack propagation into Ag. Part F of figure 1 shows the crack propagating one layer below the interface into Ag.

The seven columns on the left of Table 2 give the details of all the simulations and will be discussed next. The remaining columns present the predictions of the continuum models and will be discussed later in this section.

The variation in behaviour can be explained using the example of Ni-Pt. For $\varphi = 1.0$ the result observed was dislocation emission. As the value of φ was increased the crack behaviour changed from dislocation emission to crack propagation along the interface. The transition from dislocation emission to crack propagation took place at the value of 1.15. The values of G_{crit} for dislocation emissions remains the same. For the case of crack propagation, the value of G_{crit} is gradually decreasing because as the constant φ is increased the interface becomes weaker.

In the case of Ni-Ag-1.0, the crack propagation took place one layer above the interface, parallel to the interface plane. The transition of behaviour from crack propagation into one of the materials, to crack propagation along the interface took place at $\varphi = 1.4$. The critical energy release rate decreases as the interface is made weaker with the exception of Ni-Ag-1.4. The higher value in this case can be attributed to bigger load steps (Δt) = $0.1, 5 * \Delta t$ taken for this combination, and thus greater uncertainty in this result. The different values of the

System	Load	K_{II}/K_I	γ_{int} eV/Å ²	G_{crit} eV/Å ²	Description	QC	G_{crack} eV/Å ²	G_{disl} (R) eV/Å ²	P(R)	G_{disl} (RT) eV/Å ²	P(RT)
Ni-Pt-1.12	0.485 ± 0.005	0.0481	0.00274	0.23	Disl in Pt	D	0.205	0.0999	D	0.19005	D
Ni-Pt-1.13	0.4815 ± 0.0005	-0.0481	0.00587	0.231	Disl in Pt	D	0.202	0.0999	D	0.19005	D
Ni-Pt-1.14	0.4815 ± 0.0005	-0.0481	0.00893	0.23	Disl in Pt	D	0.199	0.0999	D	0.19005	D
Ni-Pt-1.15	0.4765 ± 0.0005	-0.0481	0.0119	0.225	Crack -0	B	0.196	0.0999	D	0.19005	D
Ni-Pt-1.2	0.455 ± 0.005	-0.048	0.0261	0.199	Crack -0	B	0.182	0.0999	D	0.19005	B
Ni-Pt-1.4	0.3855 ± 0.0005	-0.0481	0.145	0.135	Crack -0	B	0.136	0.0999	D	0.19005	B
Ag-Pt-1.0	0.345 ± 0.005	-0.0807	0.000401	0.0741	Crack -1	B	0.0817	0.0807	D	0.0604	D
Ag-Pt-1.2	0.355 ± 0.005	-0.0809	0.0471	0.0729	Crack -1	B	0.0832	0.0807	D	0.0604	D
Ag-Pt-1.3	0.465 ± 0.005	-0.0808	0.0633	0.123	Crack -0	B	0.0788	0.08073	B	0.0604	D
Ag-Pt-1.4	0.325 ± 0.005	-0.0807	0.0762	0.0987	Crack -0	B	0.0658	0.08073	B	0.0604	D
Ni-Cu-1.0	0.55 ± 0.05	0.0317	0.00229	0.199	Crack +1	B	0.165	0.111	D	0.182	B
Ni-Cu-1.2	0.435 ± 0.005	0.0318	0.0528	0.146	Crack -0	B	0.139	0.111	D	0.182	B
Ni-Cu-1.4	0.25 ± 0.05	0.0318	0.0864	0.0286	Crack -0	B	0.106	0.111	B	0.182	B
Ni-Ag-1.0	0.4545 ± 0.0005	0.0666	0.00859	0.138	Crack +1	B	0.0779	0.0769	D	0.20603	B
Ni-Ag-1.2	0.3855 ± 0.0005	0.0665	0.0484	0.0937	Crack +1	B	0.0789	0.0769	D	0.20603	B
Ni-Ag-1.4	0.55 ± 0.05	0.0664	0.0737	0.142	Crack -0	B	0.0743	0.0786	B	0.20603	B
Ni-Ag-1.6	0.335 ± 0.005	0.0666	0.0909	0.0622	Crack -0	B	0.0571	0.0769	B	0.20603	B
Ag-Ni-1.0	0.335 ± 0.005	0.00059	0.00658	0.0729	Crack -1	B	0.0779	0.0859	B	0.0439	D
Ag-Cu-1.0	0.365 ± 0.005	-0.035	0.000571	0.0812	Crack -1	B	0.0811	0.0829	B	0.05803	D
Cu-Pt-1.0	0.445 ± 0.005	-0.0653	-0.0373	0.16	Crack -1	B	0.178	0.0996	D	0.0825	D
Cu-Pt-1.13	0.475 ± 0.005	-0.0651	0.00197	0.178	Crack -1	B	0.179	0.0996	D	0.0825	D
Pt-Cu-1.13	0.4815 ± 0.0005	0.0604	0.00197	0.192	Disl in Pt	D	0.184	0.1004	D	0.0631	D
Ni-Pd-1.0	0.45 ± 0.05	-0.0111	-0.0321	0.147	Crack +1	B	0.132	0.101	D	0.195	B
Pd-Cu-1.0	0.45 ± 0.05	0.0305	-0.0324	0.125	Crack -1	B	0.146	0.0997	D	0.0649	D
Pd-Pt-1.0	0.395 ± 0.005	-0.0297	0.0007	0.139	Crack -1	B	0.158	0.105	D	0.0691	D
Pt-Pd-1.0	0.4325 ± 0.0005	0.0202	0.0007	0.171	Disl PtPd	D	0.184	0.107	D	0.0697	D
Pd-Ag-1.0	0.375 ± 0.005	0.0583	-0.00448	0.0883	Crack +1	B	0.0842	0.0822	D	0.0713	D

Figure 2: Results obtained from the simulations. "Load" is the total load ($\sum \Delta t_i$) just before the critical event, K_{II}/K_I gives the ratio of stress intensity factors, " γ_{int} " is the interface energy, " G_{crit} " is the critical energy release rate calculated using the J-integral, "Description" gives details of the observed behaviour, which is further indicated in the column "QC" as either brittle (B) or ductile (D). Columns right of the double line pertain to the predictions of the continuum models. " G_{crack} " is the Griffith energy release rate for crack propagation from equation 4, " G_{disl} " is the energy release rate for dislocation emission. R indicates the Rice model, RT the Rice-Thomson model, and P denotes the prediction, either brittle(B) or ductile(D), for the two models.

critical energy release rates G_{crit} , on switching the materials (Cu-Pt vs Pt-Cu) is due to the unsymmetric crack tip. The crack tip in this work is not a perfectly sharp crack, but one atom layer thick, with the crack tip on a layer of atoms which belongs to the lower material as seen from the figures in 1(A) and 1(B).

In the case of Ni and Cu it is seen that as φ is changed the crack behaviour changes from crack propagation one layer above the interface to crack propagation along the interface. As the interface is made weaker the critical energy release rate obtained (G_{crit}) decreases.

The last five columns of table 2 gives details of the comparison of simulation results with the Rice and RT model predictions. In this table all the predictions shown in bold indicate that the predictions are the same as the simulation results. In the case of ductile predictions it is noted that the Rice model systematically underpredicts G_{dist} , as can be very clearly seen for the case of Ni-Pt in table 2. The RT model predictions are more sporadic, for the case of ductile predictions in Ni-Pt G_{dist} values are in good agreement with the G_{crit} , but for the case of Pt-Cu and Pt-Pd the G_{dist} values are not in good agreement with the G_{crit} values. G_{crack} tends to be in good agreement with G_{crit} for the brittle cases, so long as care was taken to use the correct surface energies in equation (4). Specifically, the fact that the materials often chose to cleave one layer above or below the interface must be incorporated by computing the energy of a surface of material A covered by a single layer of B atoms. Further details of the comparison of predictions are given in the thesis by Pillai [19].

From the above observations it was concluded that G_{crack} obtained from the Griffith model is reliable as long as the correct surface energy is used for the calculations. The RT model predictions are very sporadic hence not very reliable. The Rice model, even though it underpredicts the value of G_{dist} , is very systematic and the underprediction can partly be attributed to the slightly blunted crack used in this study.

ACKNOWLEDGEMENTS

Financial support from Natural Sciences and Engineering Research Council (NSERC) is thankfully acknowledged.

REFERENCES

- [1] V. B. Shenoy, R. Miller, E. B. Tadmor, D. Rodney, R. Phillips, and M. Ortiz. *J. Mech. Phys. Sol.*, 47:611–642, 1999.
- [2] J. R. Rice and R. Thomson. *Phil. Mag.*, 29(1):73–97, 1974.
- [3] J. R. Rice. *J. Mech. Phys. Sol.*, 40:239–271, 1992.
- [4] J. R. Rice, Z. Suo, and J. S. Wang. *Metal Ceramic Interfaces*, pages 269–294. Pergamon Press, New York, 1990.
- [5] F. F. Abraham, D. Schneider, B. Land, D. Lifka, J. Skovira, J. Gerner, and M. Rosenkrantz. *J. Mech. Phys. Sol.*, 45(9):1461–1471, 1998.
- [6] Diana Farkas. *Scripta Materialia*, 39(4):533–536, 1998.
- [7] Julia Panova and Diana Farkas. *Metallurgical and Materials Transactions A*, 29:951–955, 1998.
- [8] S. J. Zhou, D. M. Beazley, and P. S. Lomdahl. *Phys. Rev. Lett.*, 78(3):479–482, 1997.
- [9] R. Thomson and S. J. Zhou. *Phys. Rev. B*, 44(1):44–55, 1991.
- [10] F. Cleri, S. R. Phillpot, D. Wolf, and S. Yip. *J. Amer. Ceramic Soc.*, 81(3):501–516, 1998.

- [11] Peter Gumbsch. *J. Mater. Res.*, 10(11):2897–2907, 1995.
- [12] F. F. Abraham, J. Q. Broughton, N. Bernstein, and E. Kaxiras. *Comput. Phys.*, 12:538, 1998.
- [13] M. S. Daw and M. I. Baskes. *Phys. Rev. B*, 29:6443–6453, 1984.
- [14] F. Z. Li, C. F. Shih, and A. Needleman. *Engng. Fracture Mech.*, 21(2):405–421, 1985.
- [15] S.B. Cho, K.R. Lee, Y.S. Choy, and R. Yuuki. *Engng. Fracture Mech.*, 43(4):603–614, 1992.
- [16] S. M. Foiles, M. I. Baskes, and M. S. Daw. *Phys. Rev. B*, 33:7983–7991, 1986.
- [17] G. E. Beltz and J. R. Rice. *Acta Met. et Mat.*, 40:S321–S331, 1992.
- [18] J. P. Hirth and J. Lothe. *Theory of Dislocations*. Krieger, Malabar, Florida, 1992.
- [19] A. R. Pillai. *Crack Behaviour at Bimaterial Interface: A Mixed Atomistic and Continuum Approach*. University of Saskatchewan, Thesis, Saskatoon, Canada, 2000.

Cosserat Modeling of Size Effects in Crystalline Solids

Samuel Forest

Centre des Matériaux / UMR 7633

Ecole des Mines de Paris / CNRS

BP 87, 91003 Evry France. 91003 Evry France

ABSTRACT

The mechanics of generalized continua provides an efficient way of introducing intrinsic length scales into continuum models of materials. A Cosserat framework is presented here to describe the mechanical behavior of crystalline solids. The first application deals with the problem of the stress strain field at a crack tip in Cosserat single crystals. It is shown that the strain localization patterns developing at the crack tip differ from the classical picture : the Cosserat continuum acts as a bifurcation mode selector, whereby kink bands arising in the classical framework disappear in generalized single crystal plasticity. The problem of a Cosserat elastic inclusion embedded in an infinite matrix is then considered to show that the stress state inside the inclusion depends on its absolute size l_c . Two saturation regimes are observed : when the size R of the inclusion is much larger than a characteristic size of the medium, the classical Eshelby solution is recovered. When R is much smaller than the inclusion, a much higher stress is reached (for an inclusion stiffer than the matrix) that does not depend on the size any more. There is a transition regime for which the stress state is not homogeneous inside the inclusion. Similar regimes are obtained in the study of grain size effects in polycrystalline aggregates of Cosserat grains.

INTRODUCTION

The incompatibility of plastic deformation in heterogeneously deforming single crystals can be the origin of size effects in their mechanical behavior. It is related to the so-called dislocation density tensor α arising in the continuum theory of dislocations [1]. In contrast, classical crystal plasticity [2] relies on hardening variables related to the scalar densities of dislocation well-known in physical metallurgy. The question then is how to introduce α into a general constitutive framework. Two main ways have been traced. According to the first one, the dislocation density tensor is regarded as an additional non local internal variable [3]. The second one acknowledges the fact α is related, on the one hand, to the gradient of plastic deformation and therefore indirectly to the second gradient of the displacement. On the other hand, the dislocation density tensors is directly related to lattice curvature, namely the gradient of the lattice rotation vector. That is why the second class of models resorts to the mechanics of generalized continua [4]. Generalized continua can be classified into three main groups. Higher grade media involve higher order gradients of the displacement field or of some internal variables. In higher order media, independent degrees of freedom are introduced in addition to the usual displacements. Fully non local media are characterized by an integral formulation of the constitutive equations [5]. In this work, attention is drawn to the Cosserat continuum for which independent displacement \underline{u} and microrotation $\underline{\Phi}$ degrees of freedom are attributed to each material point. The vector $\underline{\Phi}$ describes the rotation of

an underlying triad of rigid directors, here the crystal lattice directions in an intermediate stress released configuration. Deformation and curvature tensors can be defined [8], so that there exist two associated stress tensors : the force-stress tensor $\underline{\sigma}$ and the couple-stress tensor $\underline{\mu}$. They are not necessarily symmetric. Two balance equations must be fulfilled, namely the balance of momentum and the balance of moment of momentum :

$$\sigma_{ij,j} = 0; \quad \mu_{ij,j} - \epsilon_{ijk}\sigma_{jk} = 0 \quad (1)$$

where volume forces and couples have been excluded for simplicity.

There have been at least two main attempts to deal with the single crystal as a generalized continuum : a Mindlin-type strain gradient theory [6,7] and a Cosserat model [8]. Both theories account for additional hardening due to lattice curvature. The slight differences concern the treatment of elastic curvature and the ability of the Cosserat continuum to account for non-symmetric stresses. This last possibility is not exploited in this work and only effects associated with lattice curvature are presented.

The whole constitutive framework of Cosserat single crystal plasticity is detailed in [8,10,11] and is not recalled here. It is based on a generalized Schmid law and the most important part of the model lies in the hardening rule :

$$\tau^s = \tau_0 + \sum_{i=1}^n H_{sr}(1 - e^{-b\gamma^r}) + H'\theta^s \quad (2)$$

where τ^s is the resolved shear stress on slip system s , τ_0 the initial critical resolved shear stress. Non-linear hardening is introduced as a function of cumulative slip γ^r on slip system r , H_{sr} being the interaction matrix accounting for latent and self-hardening. Additional hardening associated with lattice curvature θ^s/l_c is added, l_c being an intrinsic length scale. The consequences of the introduction of this non-classical term are investigated in three cases in the sequel. The first example deals with Cosserat plasticity in a single crystal. In the second one, only Cosserat elasticity is regarded. And the last one concerns aggregates of Cosserat single crystals.

STRAIN LOCALIZATION PHENOMENA AT A CRACK TIP

The asymptotic stress-strain field at a stationary crack tip in elastic-ideally plastic f.c.c. and b.c.c. single crystals, as determined by Rice *et al.* [9], turns out to be locally constant within angular sectors. It involves shear displacement discontinuities at sector boundaries, that can be interpreted as strain localization bands. The numerical analysis of the same problem using finite strain crystal elastoplasticity in [2] reveals that the condition of constant stress state in each sector must be relieved because of possible local unloading, but also that the strain localization patterns pertain. Two types of deformation bands exist in single crystals undergoing single slip : slip bands lying in the slip plane of the locally activated slip system, or kink bands lying in a plane normal to the slip direction of the slip system [10]. The formation of a kink band is associated with the development of strong lattice rotation gradients at its boundary and may therefore be precluded if the model incorporates additional hardening due to lattice curvature [10]. An example is given in this section but a more thorough analysis of application of generalized crystal plasticity at the crack tip can be found in [12].

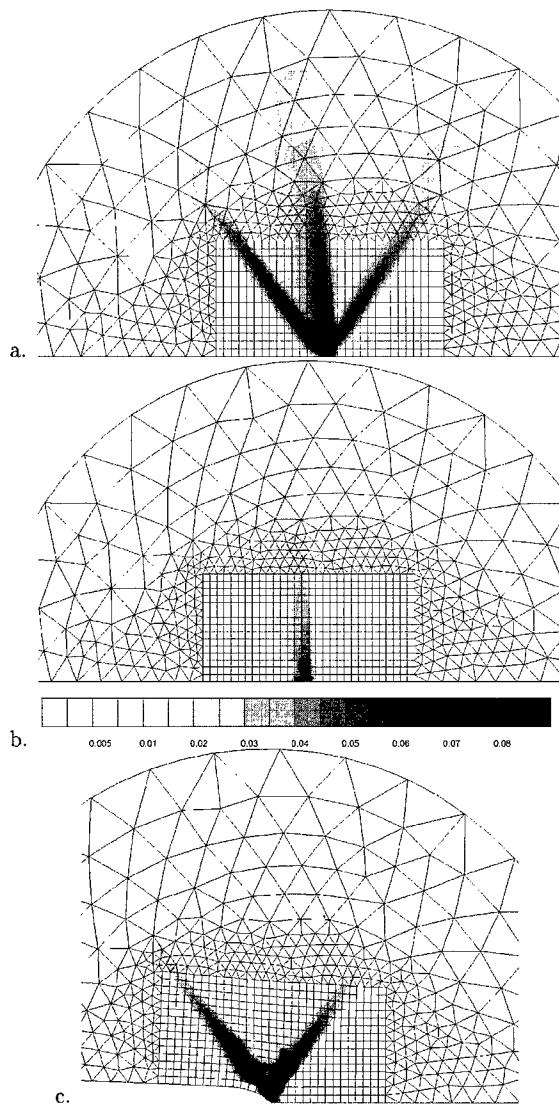


Figure 1. Strain localization phenomena at the crack tip of a f.c.c. single crystalline CT specimen with vertical orientation [001] and horizontal one [110] : equivalent plastic strain (a), lattice rotation (b) in the classical case. The picture (c) gives the equivalent plastic strain distribution when the Cosserat continuum is used : the vertical kink band has disappeared.

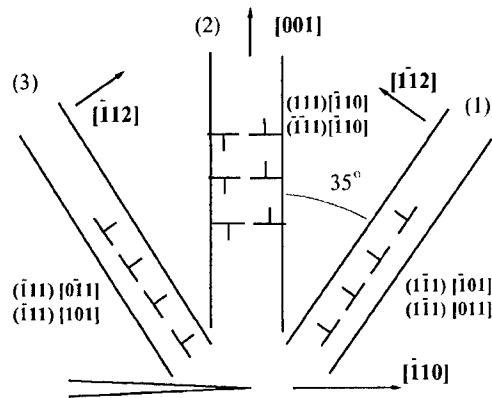


Figure 2. Interpretation of the strain localization pattern at the crack tip of a single crystal CT specimen : (1) and (3) are effective slip bands, (2) is an effective kink band.

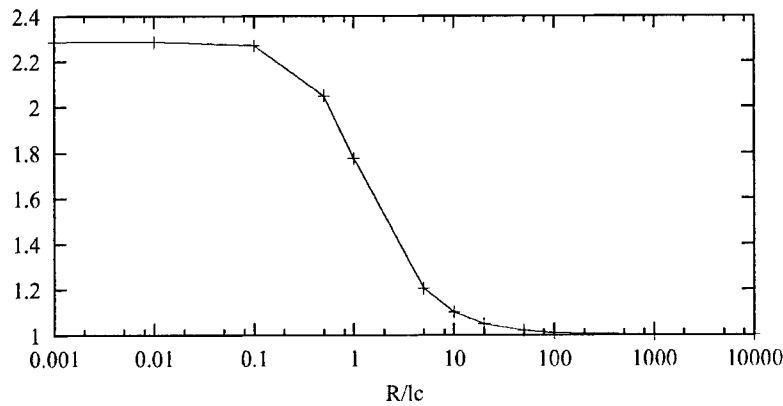


Figure 3. Ratio of the mean stress in a heterogeneous inclusion over the classical Eshelby result as a function of R/l_c .

Discrete models based on dislocation dynamics also lead to strongly localized dislocation distributions near the crack tip and to the progressive formation of the predicted sectors, but kink bands do not seem to form [13]. A single crystal CT specimen is considered here and its deformation is computed with the finite element method using firstly classical multiplicative single crystal plasticity. A ideal plastic f.c.c. crystal with 12 octahedral slip is computed under plane strain conditions. Three localization bands are observed at the crack tip (figure 1) : two intense slip bands and one kink band are obtained, as explained on figures 1 and 2. The application of Cosserat extra hardening leads to the disappearance of the kink band as

shown figure 1c. The physical relevance of this result cannot be definitively assessed, because there are only scarce detailed experimental analysis of the crack tip field in a single crystal.

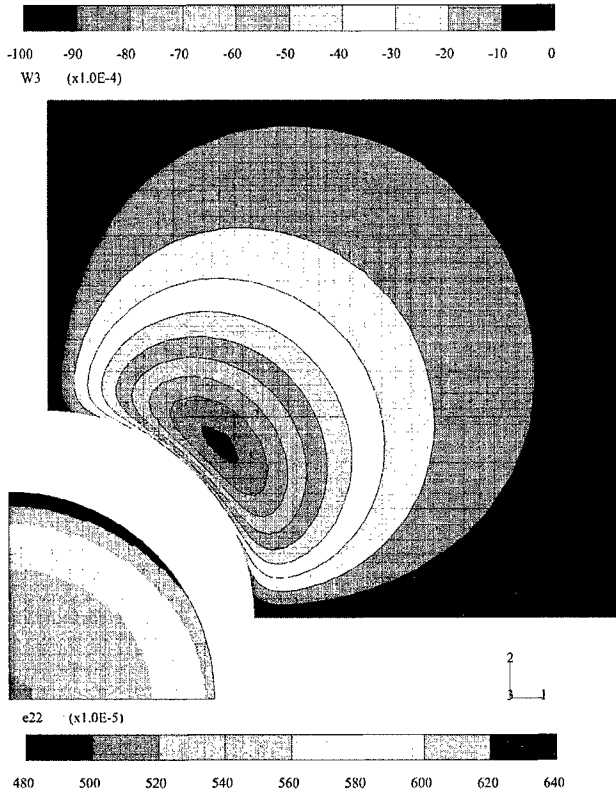


Figure 4. Deformation field in a heterogeneous elastic inclusion and microrotation field in the matrix submitted to tension; the deformation field is non-homogeneous inside the inclusion contrary to the classical case.

HETEROGENEOUS COSSERAT INCLUSION IN AN INFINITE MATRIX

The extension of the classical Eshelbian inclusion problem to the Cosserat framework may well be of the major importance to design homogenization techniques being able to account for absolute size effects in heterogeneous materials. Some aspects of the Eshelby inclusion problem have been reported in [14]. Let us consider a Cosserat elastic inclusion having elastic properties $(E^I, \nu^I, \mu_c^I, l_c^I)$ embedded in an infinite matrix endowed with different moduli (E, ν, μ_c, l_c) . Furthermore the matrix is loaded at infinity and a tensile test is considered (axisymmetric case).

For a given set of Cosserat elastic parameters for the inclusion and the matrix, the influence of the inclusion size R on the mean stress within the inclusion has been investigated and the results are presented on figure 3. For a large ratio R/l_c , the solution tends towards the classical one. For lower ratios, in the case of an inclusion more rigid than the matrix, higher values of the mean stress are reached. Again, the stress tends to an asymptotic value for ever decreasing inclusion sizes. Note that in our example, the stress in the tiny inclusion is more than twice as large as in the big one. In the transition domain, generalized stresses and deformations are non-homogeneous within the inclusion, as seen on figure 4, and contrary to the classical case. The typical curve with two saturation plateaus of figure 3 shows that the characteristic length of the Cosserat medium acts as a resolution parameter (as in microscopy). When the geometry interacts with this length scale, size effects will be observed.

GRAIN SIZE EFFECTS IN POLYCRYSTALS

Efficient homogenization techniques are available to derive the overall mechanical properties of polycrystals, starting from the knowledge of single crystal constitutive equations and the texture (orientation distribution function). They also provide an estimation of the mean stress and strain of the grains having a same given orientation. However, two major shortcomings of these now classical approaches must be recalled. Firstly, they do not provide the stress concentration inside the grains that are relevant for damage prediction, and therefore strongly underestimate the intergranular and intragranular stress-strain heterogeneity [11,15]. Secondly, the effective properties deduced from classical homogenization theories do not depend on the absolute size of heterogeneities but only on their volume fraction and, at best, on the morphology of the constituents. In contrast, it is well-known in experimental metallurgy, that microstructures can be optimized for the desired overall nonlinear properties by varying the size of inclusions or grains.

That is why polycrystalline aggregates have been considered containing a detailed description of grain morphology and intragranular fields. A volume element with up to 1000 grains has been computed in [15] to show the tremendous dispersion of stress and strain. The grains of a polycrystal are regarded as three-dimensional Voronoi polyhedra, and the finite element mesh is fine enough to get a converged solution of the field inside each grain. This requires parallel computing as explained in [15]. This approach has been used in classical crystal plasticity but also using Cosserat crystal plasticity so as to introduce an actual scale in the computation. Small periodic aggregates have been computed in [11] to derive a grain size effect for f.c.c. crystals.

A larger but not periodic volume element is considered here containing 50 Cosserat grains, the mesh remaining small enough to allow a sequential computation. A crystal orientation is attributed to each grain in a random way. The displacement in direction z is prescribed at the bottom and top faces of the aggregates to simulate a tensile test. Six computations are reported here with the same set of material parameters, the same number and morphology of grains and the same mesh. The only difference is the absolute size of the cube edge length d which will vary from $10\mu\text{m}$ to 10mm . Due to the Cosserat hardening effect (2), a different overall curve $\Sigma_{zz} = \langle \sigma_{zz} \rangle$ vs. $E_{zz} = \langle \epsilon_{zz} \rangle$ is obtained in each case as show on figure 7. The considered material is an alloyed zinc polycrystal for which material

parameters are available from [16]. The only essential additional parameter is H' which has been arbitrarily fixed to evidence the induced size effects. Two slip sytem families must be taken into account : the 3 basal slip systems with a low initial critical resolved shear stress, and the 6 pyramidal Π_2 slip systems with a ten times higher initial threshold.

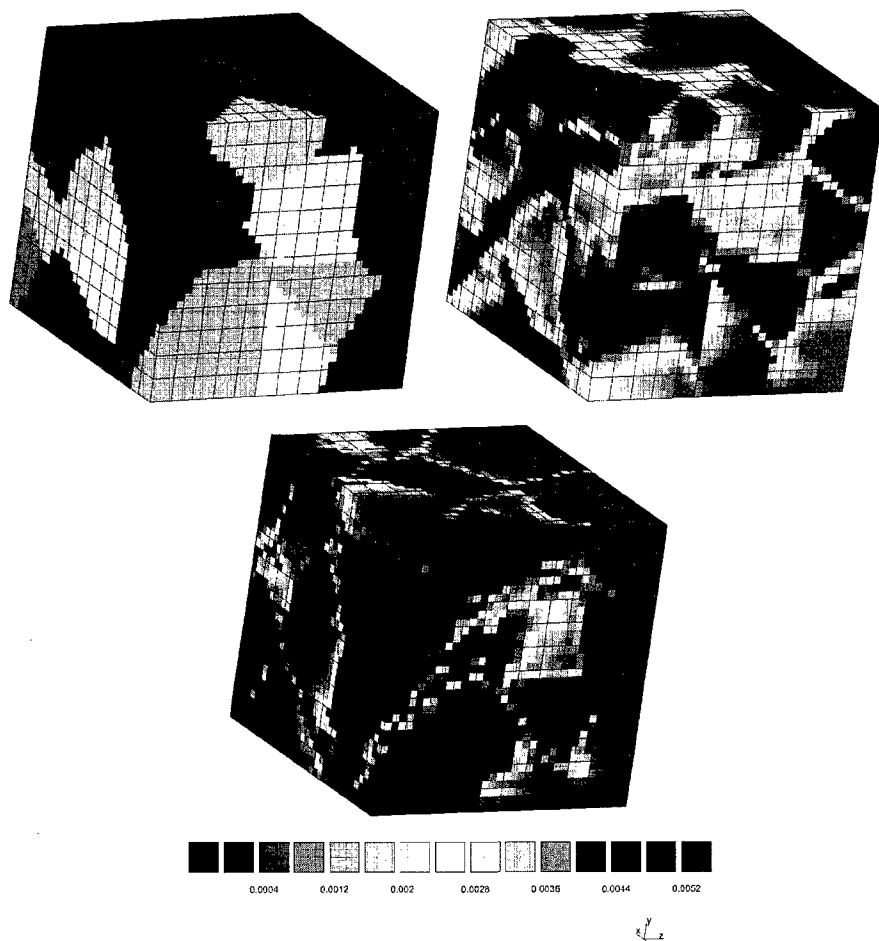


Figure 5. *Tension of a 50-grain zinc aggregate : morphology and map of cumulated basal slip (top) and cumulated pyramidal Π_2 slip (bottom).*

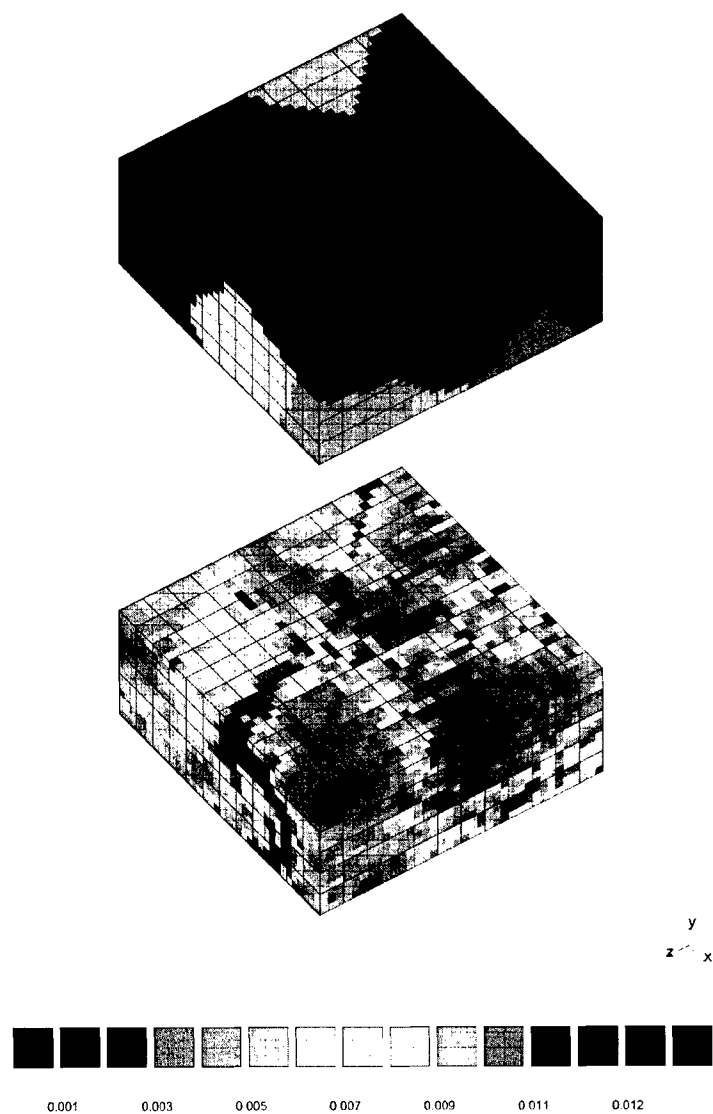


Figure 6. *Slice of a zinc aggregate (top) and corresponding equivalent lattice curvature field.*

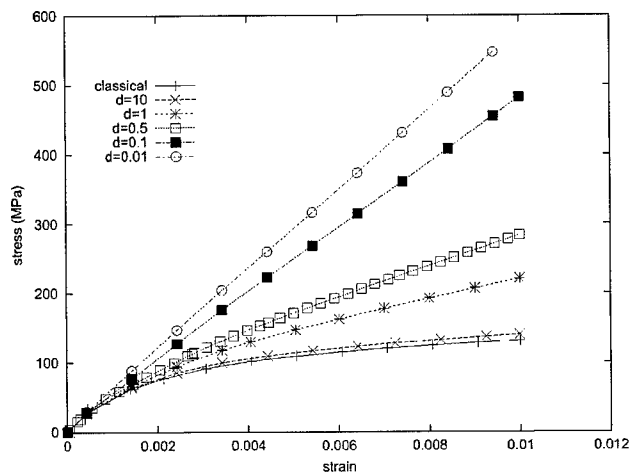


Figure 7. Mean stress-strain curves for the same 50-grain zinc aggregates but different absolute sizes d of the cube.

Figure 5 shows the grain distribution in the aggregate and that basal slip is predominantly activated in the grains. In contrast, pyramidal slip exclusively develops at the grain boundaries where basal slip alone cannot accommodate plastic incompatibilities between neighbouring grains. A map of a norm of the lattice curvature tensor in a slice of the sample is given in figure 6, showing that plastic curvature preferentially develops near the grain boundaries. This confirms the fact mentioned in [11] that lattice rotation tends to be relatively homogeneous in the core of the grains and is disturbed near the boundary. The curves of figure 7 shows that when the grains are very large, there is no difference between the computation using classical crystal plasticity and the Cosserat case. In contrast, when the grain size decreases, the response becomes more and more elastic. Figure 8 gives the same overall stress-strain curves but after removing the overall elastic deformation from the total one. This enables us to plot the difference between the mean axial stress Σ reached by the aggregate for each grain size at a given mean strain $E = 0.1\%$, minus the corresponding strain for the classical size-insensitive case, as a function of the grain size (figure 9). Three regimes appear in a similar way as for the inclusion problem (figure 3) : for very small and very large grains, a slope of approximately $-1/2$ is observed, whereas the transition regime is characterized by a slope of approximately -1 .

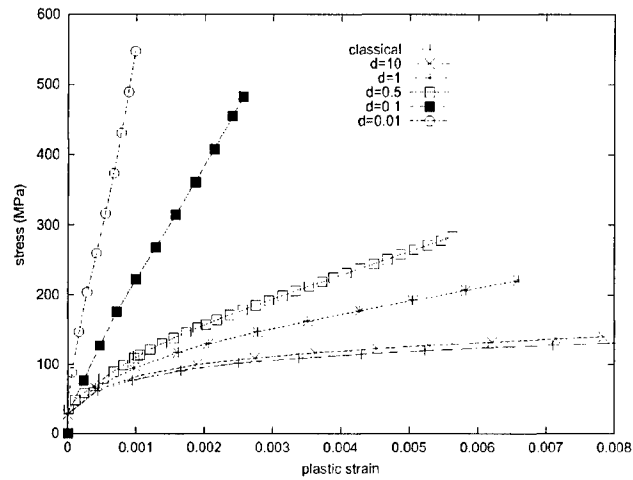


Figure 8. Mean stress-plastic strain curves corresponding to the overall curves of figure 7.

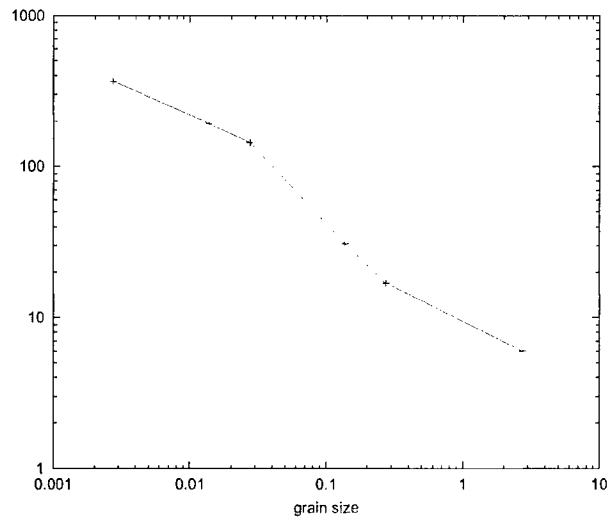


Figure 9. $\Sigma - \Sigma_0$ for a plastic strain of 0.1% as a function of grain size, Σ_0 being the stress reached by the classical solution.

CONCLUSION AND PROSPECTS

The proposed Cosserat framework to model size-dependent crystal plasticity is based on the introduction of additional hardening proportional to lattice curvature. Physically more relevant constitutive equations should be proposed. In particular, the reference [17] indicates that the effect of so-called geometrically necessary dislocations associated with lattice curvature is more important at the beginning of plastic flow, so that a nonlinear additional hardening term with possible saturation would be better. In particular, this would affect the initial yield stress of polycrystalline aggregates and not subsequent hardening, contrary to the result of figure 7.

Generalized crystal plasticity has been shown to strongly affect the stress-strain field at a crack tip in an ideally plastic single crystal. In particular, strain localization bands of kink type are significantly weakened or even precluded. Experimental investigations are necessary to assess the physical relevance of the result but some experimental results and discrete dislocations models seem to confirm this feature of crystal plasticity.

The prediction of the overall properties of polycrystals including grain size effects are possible using Cosserat crystal plasticity and corresponding homogenization techniques [18]. The promising results on small polycrystal volume element presented here for hexagonal crystal structures must be confirmed by more intensive computations involving more grains and much finer meshes. Parallel computing will play a major rôle in the future investigations.

REFERENCES

1. E. Kröner, *Kontinuumstheorie der Versetzungen und Eigenspannungen*, Ergebnisse der angewandten Mathematik, Vol. 5, Springer-Verlag, (1958).
2. A.M. Cuitino and M. Ortiz, *Modelling Simul. in Mater. Sci. Eng.*, **1**, 225 (1993).
3. H. Dai and D.M. Parks, Geometrically-necessary dislocation density and scale-dependent crystal plasticity. In *Proceedings of Plasticity '97*, ed. A.S. Khan, pp. 17-18. Neat Press, Fulton, Maryland, (1997).
4. E. Kröner, *Mechanics of generalized continua*, Proc. of the IUTAM-Symposium on the generalized Cosserat continuum and the continuum theory of dislocations with applications, Freudenstadt, Stuttgart, Springer-Verlag, (1967).
5. A.C. Eringen, *Polar and non local field theories*, in Continuum Physics, edited by Eringen A.C., Volume IV, Academic Press, (1976).
6. N.A. Fleck and J.W. Hutchinson, Strain gradient plasticity. *Advances in Applied Mechanics* **33**, 295 (1997).
7. J.Y. Shu and N.A. Fleck, *J. Mech. Phys. Solids*, **47** 297 (1999).
8. S. Forest, G. Caillaud and R. Sievert, *Arch. Mech.*, **49**, 705 (1997).
9. J.R. Rice, *Mechanics of Materials*, **6**, 317 (1987).
10. S. Forest, *Acta Mater.*, **46**, 3265 (1998). **1**, 225 (1993).
11. S. Forest, F. Barbe and G. Caillaud, *Int. J. Solids Structures*, **37**, 7105 (2000).
12. S. Forest, P. Bonbidi, R. Sievert, Strain Localization Patterns at a Crack Tip in Generalized Single Crystal Plasticity, to appear in *Scripta Materialia*, (2001).
13. E. van der Giessen, H.H.M. Cleveringa and A. Needleman, *Discrete Dislocation Plasticity and Crack Tip Fields in Single Crystals*, submitted (2000).

14. S. Forest S., R. Dendievel, G.R. Canova, Estimating the overall properties of heterogeneous Cosserat materials, *Modelling Simul. Mater. Sci. Eng.*, **7**, 829 (1999).
15. F. Barbe, G. Cailletaud, S. Forest, L. Decker and D. Jeulin, Intergranular and intragranular behavior of polycrystalline aggregates, Parts I and II, to appear in *Int. J. Plasticity* (2001).
16. R. Parisot, S. Forest, A.-F. Gourgues, A. Pineau, A., *Computational Materials Science*, **19**, 189 (2001).
17. M.F. Ashby, *The deformation of plastically non-homogeneous alloys*, in Strengthening Methods in Crystals, edited by Kelly A. and Nicholson R.B., Applied Science Publishers, London, 137 (1971).
18. S. Forest and K. Sab, Ninth International Symposium on Continuum Models and Discrete Systems, CMDS9, ed. by E. Inan and Z. Markov, World Scientific Publishing Company, 445 (1998).

Intrinsic and Extrinsic Size Effects in Plasticity by Dislocation Glide

J. Gil Sevillano

CEIT (Centro de Estudios e Investigaciones Técnicas de Guipúzcoa) and Faculty of Engineering, University of Navarra. P.O. Box 1555, 20080 San Sebastián, Spain.

ABSTRACT

A classification of size effects (SE) in plasticity is attempted.

"Intrinsic" SE are perceived when any internal length scale directly influencing some process or property interferes with the size of the material region where the process is going on or when two internal length scales directly affecting the same process or property interfere.

"Extrinsic" SE arise from the external imposition of spatial gradients in the plastic process or by the building up of internal gradients by the (externally induced) process itself. In dislocation-mediated plasticity plastic strain gradients are resolved by the storage of geometrically necessary dislocations (GND) leading to prominent size effects.

Of course, mixed effects with intrinsic and extrinsic contributions can be found as well as superposed effects involving more than two characteristic lengths (i.e., size effects on size effects). The inclusion of both types of SE in continuum or crystallographic theories is commented.

INTRODUCTION.

The strong impetus experienced by a broad spectrum of micro-technologies has recently awakened the interest on the mechanical behaviour of small volumes. As it has occurred with other physical phenomena, small-scale plasticity has afforded many surprises.

Some effects of size on the plastic behaviour, namely the indentation size effect, ISE, on the hardness value of a material, the torsional size effect of small wires or the ductile-brittle size transition observed on crystalline *whiskers* were known since a long time [1-3]. However, with the exception of the "normal size"/whisker transition, the question of their origin was far from settled and a quantitative explanation for them was not yet conceived. When the technological importance of size effects (SE) on plasticity was highlighted by the publication of a remarkable paper by Ashby and co-workers [4], interest in the exploration and understanding of plastic size effects boomed.

That size matters was nothing new for materials scientists and engineers. Structural SE like the Hall-Petch effect on the strength of polycrystals or the strength dependence on the inter-particle distance and particle size in precipitation or dispersion strengthened materials, crucial for structural materials design, are very well studied. The abundant structural size/plasticity relationship knowledge could guide the understanding of non-structural size effects of micro-technological interest. In fact, the aforementioned paper [4] already offered a successful link between many non-structural SE and the concept of "geometrically necessary dislocations" (GND) proposed by Nye [5] and applied by Ashby to the extra strengthening of non-homogeneous materials [6,7].

Atomistic and discrete dislocation approaches to plasticity automatically incorporate internal lengths in their analysis and plastic SE naturally come out in their results. However, at present they are limited to the simulation of very small volume elements even at the price of large computing power and time. In order to reasonably reproduce the mechanical behaviour of complex microstructures or the development of plastic zones in patterned regions of microelectronic devices it is still necessary to make use of numerical solutions of continuum

or crystallographic theories of plasticity. By contrast, results of conventional (local, first order) continuum or crystallographic theories are scale independent. Consequently, a strong activity is being currently devoted to the building up and validating of non-local or second order continuum or crystallographic plasticity theories capable of dealing with SE without any ad-hoc hypothesis (like introducing an explicit structural size dependence, i.e., the Hall-Petch relationship, in the flow stress equation). Among others, higher order theories making a connection with the underlying dislocation accumulation/annihilation processes have been proposed by Aifantis, Nix and Gao, Fleck and Hutchinson, Acharya and Bassani, Forest [4, 8-13]. The state of the question, from a Continuum-Mechanics point of view, has been reviewed by Hutchinson and by Needleman [14-16].

In this paper, a classification of SE in Plasticity is attempted. Intrinsic and extrinsic SE are distinguished. Of course, there are mixed SE where intrinsic and extrinsic effects superpose, as well as SE on SE. The distinction between intrinsic and extrinsic SE is not artificial. For instance, some non-negligible intrinsic effects are not incorporated to the currently available gradient-dependent plasticity theories. Also this paper stresses the need for a further combined theoretical and experimental effort for attaining a reliable quantitative prediction of SE with continuum or crystallographic theories of general application to structured materials or patterned devices up to the sub-micron scale.

A CLASSIFICATION OF SIZE EFFECTS IN PLASTICITY.

Intrinsic size effects.

"Intrinsic" SE occur,

- when the size of the material region where the plastic process is taking place interferes with the order of magnitude of any internal length scale influencing the plastic properties involved in the process,
- when two internal lengths independently influencing the plastic process interfere.

By the term "intrinsic" we want to emphasise that such effects are due to the limited size of the plastic domain and their existence does not require the presence of any mesoscopic strain gradient. The size, L , we are speaking of can be either

- the physical size limited by free surfaces if we are deforming a single crystal,
- the size of a plastic island embedded in elastic material or
- the size of a plastic domain limited by grain or phase boundaries not penetrable to dislocation-mediated slip, when deforming polycrystals or polyphasic materials.

Many effects of structural size on mechanical properties are intrinsic size effects: e.g., the strengthening effect of inter-particle distance, the blocking of slip in low stacking-fault energy materials leading to pile-up formation, the confinement of slip in narrow corridors in layered materials, or in thin coatings, etc. Given the scale of integrated circuits and microsystems, any plastic activity in them will be affected by intrinsic size effects. Artz [17] has recently made a review of such effects with a perspective on micro-technology.

The number of possible internal lengths is high even for a single-phase region. Going from the modulus of the Burgers vector, b , to the grain size, D , the mean distance between foreign solute atoms on the slip plane, $c^{-1/2}$, the average inter-dislocation distance, $\rho^{-1/2}$, the cell or subgrain average size, d , the mean-free-path of mobile dislocations, λ , etc., are to be considered, among others. There will always be, at least, b , as internal length, with respect to the continuum, of course.

Most usually there is a hierarchy of the internal length variables, e.g.,

$$b \ll c^{-1/2} \ll \rho^{-1/2} \ll d \ll \lambda \ll D \ll L \quad (1)$$

and each one varies in a range respecting the above hierarchy. The "normal" structural dependence of some plastic property (strength, work hardening rate, etc.) is manifested as the partial derivative of the property relative to an internal length, e.g., the Taylor relationship $[\partial\sigma/\partial(\rho^{-1/2})]_{\epsilon, D, L}$, provided the variable remains in its "normal" range. We thus have many intrinsic SE of structural type and we are so accustomed to them that we often forget to call them SE.

Sometimes either one internal length or the external size take a value out of its usual range. An interference between two lengths occurs and the subsequent "anomalous" behaviour is clearly perceived as a genuine SE. Possible SE of this crossed type are very numerous. In fact, they are SE on SE. Examples of crossed SE can be, for L or D decreasing their size,

- when $L \approx D$, a deviation from the Hall-Petch effect sets-in
- when $L \approx \lambda$ or $D \approx \lambda$, the work hardening ability of the material starts to weaken [18]
- when $L \approx \rho^{-1/2}$ a transition towards a whisker type behaviour will be perceived
- when $b \approx \rho^{-1/2}$ is reached, mechanical amorphisation would be around.

Extrinsic size effects.

"Extrinsic" SE arise from the external imposition of spatial strain gradients in the plastic process or by the building up of internal gradients during the development of the (externally induced) process itself.

It is well known that, in dislocation-mediated plasticity, plastic strain gradients are resolved by the storage of geometrically necessary dislocations (GND) leading to prominent size effects, fig. 1.

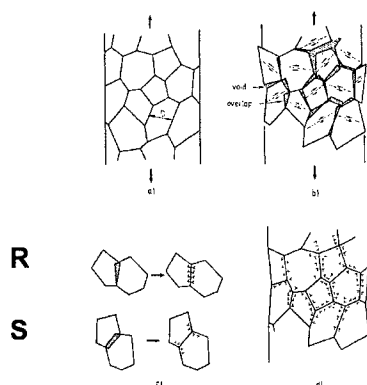


Fig. 1. The original sketch (Ashby, 1970 [6, 7]) of storage of geometrically necessary dislocations during plastic deformation of a polycrystal. Notice the distinction of strain (S) or rotation (R) gradients.

As it has been mentioned in the introduction to this paper, the indentation size effect on hardness, ISE, and the strengthening effect induced by decreasing the diameter of torsional samples are paradigmatic examples of SE produced by externally imposed strain gradients. The strengthening effect derived from the curling of the grains in transverse sections of axisymmetrically drawn wires of BCC or HCP polycrystals developing $\langle 110 \rangle$ fibre textures is a good example of the effect of internal gradients [19-20].

In the ISE case, the plastic zone under the indenter is embedded in elastic material. At the elastic-plastic border, plastic strain is zero and it raises up to a high value close to the sharp indenter tip. Ignoring second order effects (i.e., assuming similarity of the plastic field for

different plastic zone sizes), the plastic gradient at equivalent locations in plastic zones will be inversely proportional to the size of the indentations. The later can be measured by the indentation depth or by the size of the imprint projection on the material surface).

In the case of torsion of cylindrical samples, a constant simple shear gradient develops anywhere in the sample, proportional to the twisted angle and to the inverse of the sample diameter.

In largely strained BCC or HCP wires, the elongating individual grains deform by plane strain elongation and compatibility of the grain ensemble requires their continuous inter-bending around the axial direction, creating increasing rotational gradients.

The plastic relaxation of second order displacement gradients, $u_{ij,k}$, is performed by the storage of an array of geometrically necessary dislocations, GND. In a volume element the density of GND to be stored, ρ_g , is proportional to the current value of the displacement gradient. For instance, a purely rotational gradient can be absorbed by the Nye's tensor of GND dislocation density,

$$\rho_{ji} = \chi_{ij}/b - \delta_{ij}\chi_{kk}/b \quad (2)$$

where χ_{ij} represents the curvature tensor [5].

Nye's tensor distinguishes different virtual dislocation families (i and j represent the virtual Burgers vector direction and the direction of the virtual dislocation line) but notice that such dislocations are not lattice dislocations. The Burgers vectors of those "equivalent" or virtual dislocations are given in terms of the external reference system of coordinates [5].

In a real crystal, the GND dislocation density corresponding to the Nye's tensor represents a lower bound of the actual ρ_g , the later being composed of available real lattice dislocations forming a geometrically equivalent array in terms of Burgers circuits around the element. Between the Nye's GND dislocation density and the actual one in the real crystal, the link must be a redundancy numerical factor, $M_g > 1$, orientation dependent.

$$\rho_g = M_g \sum \rho_{ji} \quad (3)$$

Nye's tensor accounts only for rotational gradients. Stretching gradients can also make a contribution to the GND density (fig. 1). Some of the proposed high-order theories include them and have made experimental tests for calibrating their relative importance versus the contribution of rotational gradients [11, 14, 15, 21]. The transition from a coherent to a semi-coherent interface beyond some critical thickness of a growing thin film on a flat substrate is the simplest example of relaxation of a pure stretching gradient by a GND array.

Consequently, in principle, the contribution of the gradient $u_{ij,k}$ of the whole relative (plastic) displacement tensor, u_{ij} should be considered.

$$\begin{aligned} u_{ij} &= \varepsilon_{ij} + \omega_{ij} \\ u_{ij,k} &= \varepsilon_{ij,k} + \omega_{ij,k} \end{aligned} \quad (4)$$

where ε_{ij} and ω_{ij} , the symmetric and anti-symmetric part of u_{ij} , are respectively the plastic strain (pure distortion) and the rotation tensors. By analogy with eq. (3), it appears reasonable to write

$$\rho_g = M_g / (u_{ij,k})/b \quad (5)$$

where $f(u_{ij,k})$ is some convenient function of the invariants of $u_{ij,k}$. For instance, one possibility would be

$$\rho_g = M_g(u_{ij,k}u_{ij,k})^{1/2}/b = M_g(\epsilon_{ij,k}\epsilon_{ij,k} + \omega_{ij,k}\omega_{ij,k})^{1/2}/b \quad (6)$$

(on account of $\epsilon_{ij,k}\omega_{ij,k} = 0$). Hutchinson and Fleck [11] have considered an independent contribution of stretching and rotational gradients that we can thus translate in our notation

$$\rho_g = M_{gS}(\epsilon_{ij,k}\epsilon_{ij,k})^{1/2}/b + M_{gR}(\omega_{ij,k}\omega_{ij,k})^{1/2}/b \quad (7)$$

Available experimental evidence suggests that $M_{gS} \cong 0.1M_{gR}$ [11, 14, 15, 21], but much more work is needed for assessing eq.(7) and the numerical value of its two orientation/redundancy factors.

Mixed effects.

In many practical situations confined plasticity occurs in the presence of important external or internal plastic gradients. Experimentally observed SE will thus often be mixed effects.

The Hall-Petch effect is probably the most prominent mixed SE. Classic interpretations of the Hall-Petch effect are classified as "pile-up theories" and "non pile-up theories" [22], both of them leading to the same functional form between the plastic strength and the grain size. Pile-up theories correspond to intrinsic SE. They predict a direct effect on the elastic limit, σ_y

$$\sigma_y = \sigma_0 + K_y D^{1/2} \quad (8)$$

Non pile-up theories are, in general, work hardening theories and are based on the storage of GND in order to accommodate plastic heterogeneities arising from the orientation dependent plastic response of the grains. They predict a work hardening enhancement as grain size diminishes, i.e., a Hall-Petch effect on the flow stress,

$$\sigma(\epsilon) = \sigma_0(\epsilon) + K(\epsilon) D^{1/2} \quad (9)$$

$$K(\epsilon \rightarrow 0) = 0$$

but no effect on the elastic limit, σ_y .

The elastic limit (lower yield point) of ferritic steel and in general, of BCC and FCC alloys age-hardened by dislocation-locking solute elements, shows a strong Hall-Petch effect, indicative of an important intrinsic SE. After the yield plateau their flow stress approximately obeys eq. (9).

The most frequent behaviour of FCC alloys and interstitial-free BCC alloys [23, 24] is well fitted by eq. (9) too but the intrinsic grain SE is negligible all along the stress-strain curve. In both cases the value of the constant $K(\epsilon)$ is of the right order of magnitude predicted from GND calculations [25, 26], figs. 2 and 3.

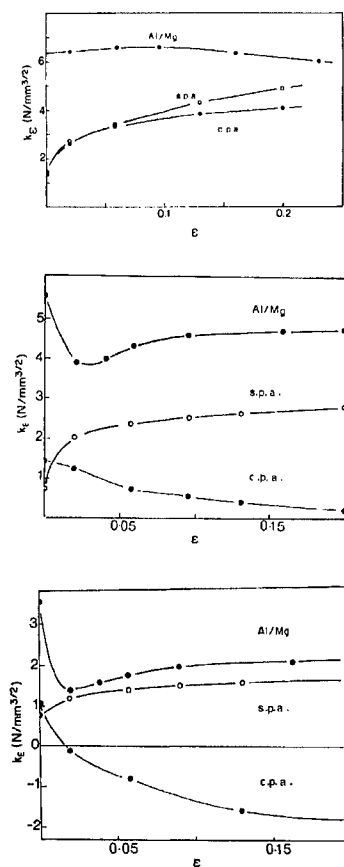


Fig. 2a

Figure 2. a) Hall-Petch slope of commercial purity Al (cpa), super-purity Al (spa) and Al-Mg alloy as a function of tensile strain at three temperatures. From El-Haidary, Petch and de los Ríos [23].

b) Normalised (adimensional) Hall-Petch slope of super-purity Al as a function of strain. Data from the previous figure.

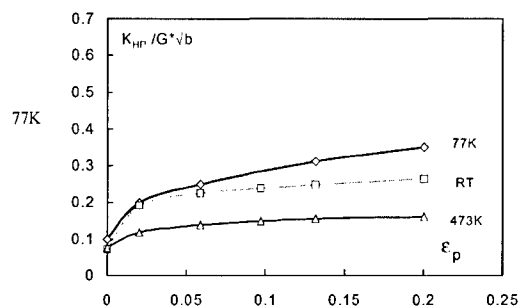


Fig. 2b

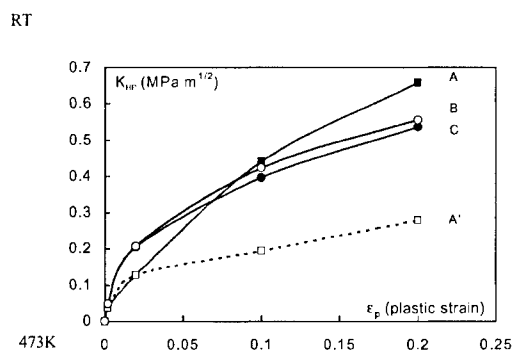


Fig. 3

Figure 3. Predicted Hall-Petch slope of polycrystalline ferrite as a function of strain (Badiola [26]). Results of a calculation based on a continuum approximation using a rotational strain gradient plasticity theory (elastoplastic data valid for an IF steel). The "toy model" polycrystal was approximated by an aggregate of 12 "grains" of randomly chosen strength from a continuous distribution between limits ranging from simple to double. Curves A, A', Hollomon hardening law (resp., fine and coarse grain size range). Curves B and C: id., Voce hardening law.

The numerical value of K_{HP} of ferrite coincides with its adimensional ratio $K_{HP}/G b^{1/2}$.

INCLUSION OF THE EFFECTS OF PLASTIC GRADIENTS IN HIGH-ORDER PLASTICITY THEORIES: THE "GRADIENT HARDENING LOCUS".

There remain some points of controversy among continuum mechanics specialists about the correct structure of a gradient dependent plastic theory, for instance, the necessity or not of including higher order stresses in the plastic work calculations [14, 27]. However, the key point to be solved in order to make reliable applications of the theories is the relationship between the plastic gradient and the density of GND, eq. (3) or its equivalents. And for achieving that there is urgent need a profusion of experimental support under theoretical guiding.

The current situation bears a strong analogy with the development of the conventional theory of plasticity during the first half of the XXth century. Supported on a huge amount of empirical knowledge, phenomenological yield criteria and flow rules were first formulated. Based on a microscopic yield criterion supported by experimental observations and physical interpretations - the "Schmid law" - Taylor [28, 29] put the foundations for the complete explanation by Bishop and Hill [30-32] of the validity (and limitations) of the Tresca or Von Mises empirical yield criteria and the Levy-Mises flow equations. This represented, by 1950, the completion of the "mathematical theory of plasticity" and the building up of the crystallographic theory of plasticity. Today, what we need to know for fully exploiting semi-phenomenological versions of strain gradient plasticity is, at least, a "*gradient hardening locus*" (GHL): a surface of equal density of geometrically necessary dislocations in the space of the components of the plastic displacement gradient tensor. This is, of course, the simplest one-parameter version of a gradient dependent theory. The GHL defines a set of "equivalent plastic gradients" characterised by some value of the GND density, ρ_g .

We do already have some experimental data for validating possible GHL equations: mainly ISE, torsional and bending results, together with a huge amount of microstructural SE data. Furthermore, there is the possibility of macro, meso and microscopic modelling of the experiments and there is the possibility of quantitatively assessing actual dislocation arrays by TEM (in fact, some attempts of an integral approach to the ISE problem have been made [33]).

The above statement constitutes a whole program for future research. The difficulties ahead are however bigger than those faced by the past generation of researchers on plasticity, because the GHL is presumably much more complicated than the yield locus. Its dimensionality is higher (24 vs. 5 independent dimensions), i.e., grasping its physical sense, covering its surface with experimental data points or simply visualising it will be still more complicated. Moreover, the physically guided linking of the plastic gradients with the corresponding GND is not well mastered. Firstly, GND arrays are not univocally determined; the same plastic gradient can be solved in a single crystalline volume element by different dislocation arrays. This is a kinematical problem quite similar to the solution of a prescribed strain by polyslip [29,30]. In the case of the strain of a crystal, on the basis of an equilibrium argument, the Schmid law justifies the "maximum plastic work principle" that enables to select the actual set of active slip systems, as shown by Bishop and Hill [30, 31]. However, up to now there is no internal energy minimisation argument valid for the selection of the actual GND array for a given strain gradient. A criterion of selection of the GND array on the basis of stored energy minimisation has been used [34] but in plasticity the stored energy is most often only a fraction of the spent plastic work necessary for creating and positioning the dislocation array.

The complexity of the GND selection is very well illustrated by the experimental evidence of multiplicity of GND arrays resolving a pure "simple shear" gradient built up by single slip of

a crystal element containing a spherical non-deforming inclusion, a problem thoroughly studied and reviewed by Humphreys [35]. It is difficult to imagine a simpler situation involving plastic gradients but it turns out that the observed GND arrays depend on the particle size (an intrinsic size effect superposed to an extrinsic one!) and on the gradient level. The results collected by Humphreys can be displayed in a two-dimensional map, fig. 4. Small plastic gradients are resolved by GND arrays of Orowan loops in a first stage of pure primary glide. A transition to GND arrays of primary prismatic loops follows. Finally, there is a transition to a stage of GND arrays containing secondary dislocations. The later stage corresponds to increasing rotations of the crystalline material containing the GND array whereas the first two stages do not imply lattice rotations. The borders of the regions of the map correspond to critical stress criteria at the particle matrix interface.

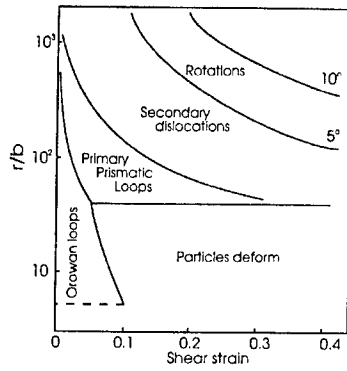


Figure 4. Map of GND arrays developed by single slip in aluminium single crystals containing spherical non-deforming particles, as a function of strain and normalised particle radius. Reproduced from Humphreys [35].

The results of Humphreys suggest that the ratio of the factors M_{eS} and M_{eR} changes as a function of strain. At small gradient values stretching arrays predominate, $M_{eS} \gg M_{eR}$, but rotational ones prevail in presence of larger gradients, $M_{eS} \ll M_{eR}$. This is easily seen if eq. (7) is particularised for the gradient of simple shear situation:

$$\rho_g = 2^{1/2} (M_{eS} \epsilon_{12,1} + M_{eR} \omega_{12,1}) / b \quad (10)$$

The transition from stretching to rotational arrays occurs the sooner the larger the absolute size of the region (the critical stress is proportional to the absolute number of piled-up dislocations in the stretch type GND array). According to fig. 4, complex rotational arrays will be observed for sizes above 0.1 μm almost right from the beginning of the straining. The result $M_{eS} \cong M_{eR}/10$ was obtained in bending experiments of beams not thinner than 0.1 μm [21].

If the above considerations were correct, one can have a glimpse of the aspect of a particular 3d section of the GHL. For plane plastic strain and gradients developing only in one direction, eq. (7) reduces to

$$\rho_g = 2^{1/2} [M_{eS} (\epsilon_{11,1}^2 + \epsilon_{12,1}^2)^{1/2} + M_{eR} \omega_{12,1}] / b \quad (11)$$

For small density of GND, the GHL will be cigar shaped along the $\omega_{12,1}$ direction of the space of the gradient components. Increasing ρ_g will change the shape of the dilating GHL towards an oblate spheroid parallel to the $(\epsilon_{11,1}, \epsilon_{12,1})$ plane, fig. 5.

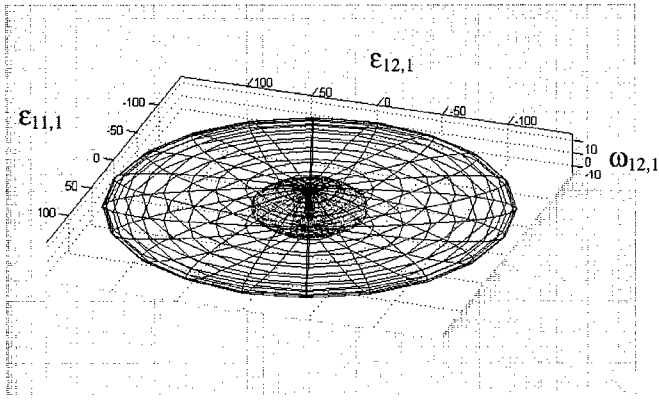


Figure 5. Hypothetical shape evolution of a particular section of the GHL (gradient hardening locus), according to eq. (11). Plane plastic strain. Arbitrary units.

When performing detailed micromechanical calculations, most frequently the plastic zones under consideration will be single-crystalline. Crystallographic gradient plasticity will be then a much better approximation to reality than continuum gradient plasticity. Use of crystallographic gradient plasticity offers a straightforward possibility for achieving a much more detailed calculation of the GND density. If we consider a single crystalline volume element with k possible slip systems, the GND density of gliding dislocations corresponding to each slip system is simply given by the slip gradient normalised by b

$$\rho_g = (M_g/b) \sum_k \Sigma_i (\partial \Gamma_k / \partial x_i) \quad (12)$$

where i represents the three directions of the external reference system and Γ_k the total amount of slip in the k system in the element (fig. 6). A redundancy factor has also been included on account of possible reactions inside the "primary" GND array. If the slip gradients are calculated relative to the reference system associated to each slip system, the density of screw and edge GND dislocations can be distinguished allowing for much more detailed work hardening calculations, as proposed by Shu and Fleck [36].

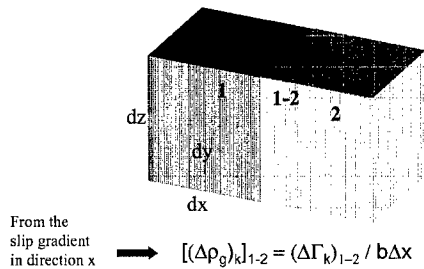


Figure 6. The geometrically necessary dislocation density calculated from crystallographic slip gradients.

To close this section a final word must be said concerning the separate treatment of the statistically stored and geometrically necessary dislocation densities that should be given in the plastic constitutive equation. For simplicity we do not distinguish here the different dislocation families. The macroscopic deviatoric stress and strain increment components (or the equivalent stress and strain increment) are respectively related to the resolved shear stress and total slip increment in a volume element by an appropriated orientation factor M

$$\begin{aligned}\sigma &= M\tau \\ d\epsilon &= d\Gamma/M\end{aligned}\tag{13}$$

The crystallographic yield criterion

$$\begin{aligned}\tau &< \tau_c && \rightarrow \text{no dislocation glide increment} \\ \tau &= \tau_c = (\tau_c)_0 + \alpha Gb(\rho)^{1/2} && \rightarrow \text{slip increment } d\Gamma \text{ (dislocation glide)}\end{aligned}\tag{14}$$

where ρ is the total dislocation density

$$\rho = \rho_s + \rho_g\tag{15}$$

The moving dislocations will not distinguish between statistically stored and GND dislocations, at least as a first approximation. However, their different behaviour should not be ignored in the evolution equations of the dislocation density. The value of the GND density is determined by the current value of the plastic gradient. The multiplication term of the statistically stored dislocations is a function of the total density of obstacles, i.e., of the total dislocation density, but the annihilation term should concern only the density of statistically stored dislocations. The reason is that GND arrays are locally constituted by sets of dislocations of the same family and the same sign, unaffected by dynamic recovery at low or moderate temperatures. Consequently,

$$\begin{aligned}d\rho_s/d\Gamma &= k_1(\rho)^{1/2} - k_2\rho_s && \rho_s < (\rho_s)_{\text{sat}} \\ \rho_g &= \rho_g(u_{ij,k}) && \rho_g < (\rho_g)_{\text{sat}}\end{aligned}\tag{16}$$

In eqs. (16) provision has been made of saturation limits for both types of dislocation densities. Because of the redundancy of the statistically stored dislocations and the same sign of the GND of the same set,

$$(\rho_s)_{\text{sat}} \ll (\rho_g)_{\text{sat}}\tag{17}$$

A very important consequence derives from inequality (17): at large strains, attainment of the saturation limit of the density of statistically stored dislocations marks the end of Stage III of deformation. Persistence of deformation does not mean the end of work hardening: as far as plastic gradients monotonically increase, the GND density can still increase. This is Stage IV! Of course, other contributions to the existence of Stage IV are possible [25] but it could turn out that this one was the most important, at least for polycrystalline materials.

INCLUSION OF INTRINSIC SIZE EFFECTS IN HIGH-ORDER PLASTICITY THEORIES.

The inclusion of intrinsic SE in high-order plastic theories without making *ad hoc* hypothesis could be done, even in continuum theories, by defining independent plastic domains having recourse to higher order plastic gradients through some edge-enhancing numerical technique. This is still an unexplored territory but the simplest approach could be to employ the spatial gradient of ρ or ρ_g for defining plastic domains. Grain or phase boundaries could be distinguished in polycrystals or in two-phase materials because of the orientation dependence of strength. Moreover, inside each grain, a strain-induced subdivision in blocks would appear from the influence of the neighbouring grains, as observed by detailed TEM studies of sub-structural development [37]. Using crystallographic plasticity, the sub-division in independent plastic domains can simply make use of a criterion of a critical misorientation complemented by a consideration of the gradient of ρ on account of the possible non penetrability of a domain by gliding dislocations beyond some critical value of the total dislocation gradient.

CONCLUSIONS

- Two types of size effects in plasticity, intrinsic SE and extrinsic SE, can be distinguished.
- Intrinsic SE can directly influence the critical resolved shear stress or the work hardening ability since the elastic limit of an undeformed material.
- Extrinsic SE derive from the imposition or the development of plastic gradients. They enhance the work hardening rate because they imply the storage of a surplus of geometrically necessary dislocations, GND, besides the statistical storage of dislocations that would occur in the absence of gradients.
- For a reliable inclusion of the effect of plastic gradients in plasticity calculations, the configuration of the "gradient hardening locus", GHL, the surface of equal GND density in the space of the components of the plastic gradient tensor, is to be explored. Critical experiments are to be selected and performed, complemented by TEM observations and by simulations using continuum, crystallographic and discrete-dislocations plasticity calculations.
- Proper inclusion of intrinsic SE in plasticity theories other than discrete-dislocations ones needs to make use of higher-order gradients than those needed for include the effect of extrinsic SE..
- The effect of the plastic gradients offers an explanation for the quasi-universal existence of Stage IV of deformation.

Acknowledgements

Many ideas of this paper have been repeatedly discussed with my colleague J. M. Martínez-Esnaola. Financial support from the Basque Government (Industry Department, Research Project no. 121998) is gratefully acknowledged.

REFERENCES

1. Meyer, E., Verein D. Ing., **52**, 645 (1908).
2. Morrison, J. M., Proc. Inst. Mech. Eng., **142**, 193 (1939).
3. Griffith, A. A., Phil. Trans. R. Soc., **A221**, 163 (1920).

4. Fleck, N. A., Muller, G. M., Ashby, M. F. and Hutchinson, J. W., *Acta Mater.*, **42**, 475 (1994)
5. Nye, J. F., *Acta Metall.*, **1**, 153 (1953).
6. Ashby, M. F., *Philos. Mag.*, **21**, 399 (1970).
7. Ashby, M. F., *Strengthening Methods in Crystals*, chap. 3. A. Kelly and R. B. Nicholson, eds., Elsevier, Amsterdam, (1970).
8. Aifantis, E. C., *J. Eng. Mater. Technol.*, **106**, 326 (1984).
9. Aifantis, E. C., *Material Instabilities in Solids*, R. de Borst and E. van der Giessen, eds., p. 533. Wiley, New York (1998).
10. Nix, W. D. and Gao, H. J., *J. Mech. Phys. Solids*, **46**, 411 (1998).
11. Fleck, N. A. and Hutchinson, J. W., *Adv. Appl. Mech.*, **33**, 295 (1997).
12. Acharya, A. and Bassani, J. L., *Micromechanics of Plasticity and Damage of Multiphase Materials* (IUTAM Symposium, Paris, 1995), p. 3. A. Pineau, A. Zaoui, eds., Kluwer Academic publishers, Amsterdam (1996).
13. Forest, S., this volume.
14. Hutchinson, J., *Int. J. Mech. Sci.*, **37**, 225 (2000).
15. Hutchinson, J. and Evans, A. G., *Acta Mater.*, **37**, 125 (2000).
16. Needleman, A., *Acta Mater.*, **37**, 105 (2000).
17. Artz, E., *Acta Mater.*, **46**, 5611 (1998).
18. Gil Sevillano, J., Ocaña, I. and Kubin, L. P., *Mater. Sci. Eng.*, in press..
19. Gil Sevillano, J., Matey Muñoz, L. and Flaquer Fuster, J., *J. Phys. IV France*, **8**, Pr 4-155 (1998).
20. Gil Sevillano, J., *Phil. Trans. R. Soc. Lond. A*, **357**, 1603 (1999).
21. Stölken, J. S. and Evans, A. G., *Acta Mater.*, **46**, 5109 (1998).
22. Li, J. C. M. and Chou, Y. T., *Metall. Trans.*, **1**, 1145 (1970).
23. Al-Haidary, J. T., Petch, N. J. and de los Rios, E. R., *Philos. Mag. A.*, **47**, 869 (1983).
24. Al-Haidary, J. T., Petch, N. J. and de los Rios, E. R., *Philos. Mag. A.*, **47**, 891 (1983).
25. Gil Sevillano, J., *Plastic Deformation and Fracture of Materials*, chap. 2, p. 19. H. Mughrabi, ed. (vol. 6, *Materials Science and Engineering. A Comprehensive Treatment*, R. W. Cahn, P. Haasen and E. J. Kramer, eds.). VCH, Weinheim, Germany (1993).
26. Badiola, V., Licence Thesis, Faculty of Engineering, University of Navarra, San Sebastian (Spain), 2000.
27. Acharya, A. and Shawki, T. G., *J. Mech. Phys. Solids*, **43**, 1751 (1995)
28. Taylor, G. I., *Timoshenko 60th Anniversary Volume*, p. 218, Mac Millan, New York (1938).
29. Taylor, G. I., *J. Inst. Met.*, **62**, 307 (1938).
30. Bishop, J. F. W. and Hill, R., *Philos. Mag.*, **42**, 414 (1951).
31. Bishop, J. F. W. and Hill, R., *Philos. Mag.*, **42**, 1298 (1951).
32. Bishop, J. F. W., *Philos. Mag.*, **44**, 51 (1953).
33. Fivel, M. C., Robertson, C. F., Canova, G. R. and Boulanger, L., *Acta Mater.*, **46**, 6183 (1998).
34. Arsenlis, A. and Parks, D. M., *Acta Mater.*, **47**, 1597 (1999).
35. Humphreys, F. J., *Dislocations and Properties of Real Materials*, p. 175. The Institute of Metals, London (1985).
36. Shu, J. Y. and Fleck, N. A., *J. Mech. Phys. Solids*, **47**, 297 (1999).
37. Godfrey, A. and Hughes, D., *Acta Mater.*, **48**, 1897 (2000).

Experimental Assessment of Strain Gradient Plasticity

Monica M. Barney, Geoffrey H. Campbell, James S. Stölken, Adam J. Schwartz,
Jürgen M. Plitzko, Wayne E. King, and John W. Morris, Jr.¹

Chemistry and Materials Science Directorate, University of California, Lawrence Livermore
National Laboratory P.O. Box 808, Livermore, CA 94550, U.S.A.

¹Materials Sciences Division, Ernest Orlando Lawrence Berkeley National Laboratory, One
Cyclotron Road, MS 66-200, Berkeley, CA 94720, U.S.A.

ABSTRACT

Classical plasticity theories generally assume that the stress at a point is a function of strain at that point only. However, when gradients in strain become significant, this localization assumption is no longer valid. These conventional models fail to display a 'size effect'. This effect is seen experimentally when the scale of the phenomenon of interest is on the order of several microns. Under these conditions, strain gradients are of a significant magnitude as compared to the overall strain and must be considered for models to accurately capture observed phenomena.

The mechanics community has been actively involved in the development of strain gradient theories for many years. Recently, interest in this area has been rekindled and several new approaches have appeared in the literature. Two different approaches are currently being evaluated. One approach considers strain gradients as internal variables that do not introduce work conjugate higher order stresses. Another approach considers the strain gradients as internal degrees of freedom that requires work conjugate higher order stresses. Experiments are being performed to determine which approach models material behavior accurately with the least amount of complexity. A key difference between the two models considered here is the nature of the assumed boundary conditions at material interfaces. Therefore, we are investigating the deformation behavior of aluminum/sapphire interfaces loaded under simple shear. Samples are fabricated using ultra-high vacuum diffusion bonding. To determine the lattice rotations near the boundary, we are examining the samples with both electron backscatter diffraction methods (EBSD) in the scanning electron microscope and with a variety of diffraction techniques in the transmission electron microscope. The experimentally found boundary conditions shall be subsequently used to determine whether the simpler internal variable model is adequately descriptive or if the greater complexity associated with the internal degree of freedom approach is warranted.

INTRODUCTION

Although not predicted by classical models, an increase in flow stress is seen during deformation when the observed phenomena is on the order of a micron and inhomogeneities are present. For example, Fleck et.al [1] showed that when loaded in torsion, a wire displays greater strength for smaller radii. Others authors have observed this type of effect in other systems, including bending [2], indentation hardness [3], and particle hardened alloys [4]. The increase in hardness under these conditions is due to additional dislocations needed for compatibility. These dislocations are commonly referred to as geometrically necessary dislocations [5]. The presence

of these dislocations can be ignored and continuum theories applied at large size scales since gradients in strain are small. However, at smaller size scales, more dislocations are formed in a smaller area, resulting in large strain gradients and higher flow stresses. This effect is not captured in continuum models because these models assume that the stress at a point is a function of strain at the same point only. When strain gradients become significant, this localization assumption is no longer valid [6]. This must be accounted for in a non-local theory to accurately reflect material response. Two distinct classes of models that extend classical theories to include strain gradient effects are currently being evaluated. Fleck and Hutchinson [7] have developed one approach in which strain gradients are included in the hyperelastic work function. This type of formulation considers strain gradients as internal degrees of freedom and requires work conjugate higher order stresses, which need additional boundary conditions. Acharya and Bassani [8] have developed an alternative approach in which a strain gradient term is included in the hardening function. In this method, the strain gradients are considered to be internal variables, which do not introduce work conjugate higher order stresses or additional boundary conditions. This approach has the advantages that it is simpler overall, preserves the structure of the classical boundary value problem, and can easily be implemented into existing finite element codes. However, the additional boundary conditions in the higher order theory allow for the presence of a boundary layer. Specifically, Fleck and Hutchinson [7] determined theoretically that a boundary layer of lattice rotation should be present at an interface between dissimilar materials loaded under remote simple shear. Since boundary layers are not allowed in Acharya and Bassani's approach, detecting the presence of these layers at interfaces will supply critical information in the continued development of strain gradient plasticity theories. Boundary layers seem likely in real materials, since dislocation motion is governed by stress fields that are strongly affected by boundaries [9]. The presence of a boundary layer, however, has not yet been definitively determined. Although previous experimental work on bicrystals by Sun et.al [10] suggests the presence of a boundary layer, the data is difficult to interpret due to the movement of the grain boundary. Therefore, experiments performed at a metal-ceramic interface are proposed to determine deformation behavior without the complication of grain boundary movement.

EXPERIMENTAL DETAILS

Samples have been designed to study the deformation behavior at a metal-ceramic interface. The samples consist of a metal foil sandwiched between two polished ceramic cylinders. C-axis oriented sapphire polished to $\lambda/10$ flatness as obtained from General Ruby & Sapphire is used for the ceramic. Aluminum is used for the metal because of its relatively simple deformation behavior as compared with other available choices. 99.999% pure aluminum foils are obtained from Metron Company. An ultra-high vacuum diffusion-bonding machine [11] is used to bond the sapphire cylinders to the aluminum foil. The aluminum foils are 25 or 50 microns thick and the sapphire rods measure 16 mm in diameter and 20 mm long. Prior to bonding, the surfaces are cleaned by sputtering and characterized by Auger spectroscopy. The samples are held at 600°C for 38 hours with an applied pressure of 10 MPa. These samples were tested in a prior study [12] to determine the strength of the aluminum-sapphire bond. A notch was cut in the aluminum and symmetric four-point bend tests were performed. The fracture surfaces had the dimpled morphology characteristic of ductile fracture, indicating that failure occurred in the aluminum

and not at the interface. This shows that the aluminum is strongly bonded to the sapphire and is assumed to deform before debonding in this study.

DISCUSSION

In order to shed light on existing strain gradient models, a simple stress state is needed for testing. This is because all models predict length scale effects to occur during inhomogeneous deformation modes. A shear stress state can be accomplished by testing the samples under *asymmetric* four-point bending [13]. A schematic illustration of the test geometry is shown in Figure 1.

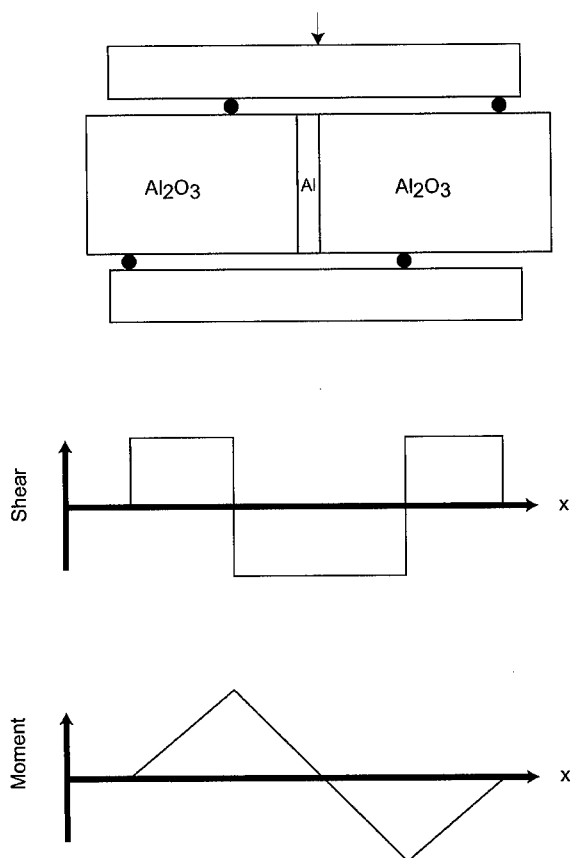


Figure 1. Schematic of the sample, loading, and the shear and moment along the length of the sample

A constant amount of shear is present between the inner contact pins, but it is only directly underneath the load-point that there is no bending moment. Therefore, proper alignment of the interface underneath the load-point is essential to avoid mixed-mode loading of the interface. To prepare for testing, the cylindrical sandwiched samples are cut into rectangular rods that are approximately 40 mm long, 2.5 mm high, and 3 mm wide. The top and bottom are ground flat for ease of mechanical testing and polished to $1\mu\text{m}$ to remove surface flaws that would lead to premature fracture of the sapphire. A bending test apparatus has been made for use in an Instron mechanical test frame. The test apparatus is designed to be self-aligning, so that the load from the mechanical test frame is transmitted directly onto the center of the bending apparatus. A 5kN-load cell is used to measure the force. Displacement is measured by an LVDT as well as by a feeler gauge placed underneath one side of the interface. The stress-strain curve from a mechanical test is shown in Figure 2.

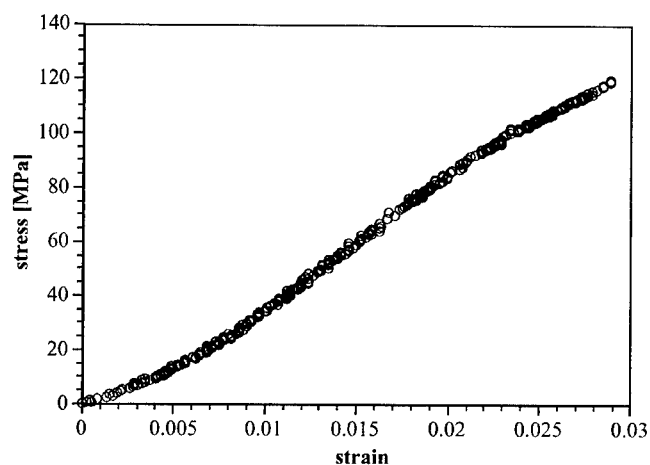


Figure 2. Stress-strain curve from an asymmetric four-point bend test

The surfaces of the samples are observed using a scanning electron microscope (SEM) and displacement between the sapphire rods is observed. The displacement within the aluminum appears to be non-uniform. An average value of $48 \pm 3\mu\text{m}$ of displacement has been determined by confocal optical microscopy. Undeformed samples are also scanned to ensure the accuracy of this method. These scans show that displacements between the sapphire were not present before testing.

In order to detect the presence of a boundary layer in the aluminum near the sapphire, the lattice rotations need to be measured from the center of the aluminum layer to the interface. To measure the rotation, electron backscatter diffraction patterns (EBSD) were generated in a SEM on these samples (see [14] for a description of EBSD). However, the signal was too weak to obtain accurate data under current sample preparation methods. Instead, the mechanically tested

samples were cut into slices for observation in a transmission electron microscope (TEM). Lattice rotation can be measured using selected area electron diffraction patterns that display both Kikuchi lines as well as diffraction spots. The type of rotation in the diffraction pattern depends on which way the rotation occurs in the lattice. Depending on the axis of rotation within the aluminum, either the lines will move with respect to the spots or the whole pattern will rotate with respect to the optic axis. Either type of rotation can be measured with a precision of at least one degree. Unfortunately, standard TEM sample preparation methods cause the aluminum to recrystallize. Alternate sample preparation methods has been employed, and an unrecrystallized sample has been made out of an undeformed bar. From initial inspection of the diffraction patterns from these samples, no trend in rotation is detected. Undeformed samples will be fully characterized and used to establish a baseline trend in lattice rotation. Deformed samples are currently being prepared in this newly established method to avoid recrystallization complications.

Once deformed samples have been successfully prepared, lattice rotations will be measured using selected area diffraction in the TEM. Diffraction patterns will be used to determine the trend in lattice rotation as the interface is approached. The trends in rotation will be confirmed using electron backscatter diffraction methods (EBSD) in the scanning electron microscope once improved sample preparation techniques are found that will allow for a stronger signal. Also, samples using single crystal metal layers will be fabricated. Copper will be used since it is easier to polish for diffusion bonding as well as TEM sample preparation. It should also produce a stronger signal for the EBSD, since copper generates more backscattered electrons than aluminum. Single crystal aluminum may be used later if necessary.

CONCLUSIONS

We are currently evaluating two models of strain gradient plasticity. They differ from one another in their levels of complexity and concomitant computational demands. The comparison with experimentally observed deformation boundary layers at interfaces should allow for an evaluation of the level of complexity that is necessary to capture relevant materials behavior in simulations. Samples have been fabricated with interfaces strong enough for the metal layer to deform without the interface debonding. A successful preparation method for TEM samples has been found and an initial investigation performed on undeformed samples. From these first observations, no trend in rotation has been detected. The initial microstructure will be fully characterized by quantitative measurement of the diffraction patterns. The successful sample preparation method will be used on deformed samples to detect lattice rotation trends.

ACKNOWLEDGMENTS

The authors would like to thank Dr. J. M. McNaney for discussions and assistance with the mechanical tests, and Dr. J. W. Chan for assistance with the confocal microscope. One of the authors (MMB) was supported through the Materials Research Institute at Lawrence Livermore National Laboratory. This work was performed under the auspices of the U.S. Department of Energy by the University of California, Lawrence Livermore National Laboratory under contract number W-7405-Eng-48.

REFERENCES

1. N. A. Fleck, G. M. Muller, M. F. Ashby, and J. W. Hutchinson, *Acta Metall. Mater.* **42**, 475 (1993)
2. J. S. Stölken and A. G. Evans, *Acta. Mater.* **46**, 5109 (1998)
3. N. A. Stelmashenko, M. G. Walls, L. M. Brown, and Y. V. Milman, in *Mechanical Properties and Deformation Behavior of Materials Having Ultra-Fine Microstructures*, edited by M. Nastasi, D. M. Parkin, and H. Gleiter. (NATO ASI Series E 233, 1993) pp. 605-610
4. D. J. Lloyd, *Int. Mater. Rev.* **39**, 1 (1994)
5. M. F. Ashby, *Philos. Mag.* **21**, 399 (1970)
6. E. C. Eringen, *Microcontinuum field theories* (Springer, New York, 1999)
7. N. A. Fleck and J. W. Hutchinson, *J. Mech. Phys. Solids* **41**, 1825 (1993)
8. A. Acharya and J. Bassani, in *Micromechanics of Plasticity and Damage of Multiphase Materials*, IUTAM Symposium, Paris. Aug. 29 - Sept 1, 1995
9. A. Wikström, Report **261**, Department of Solid Mechanics, Royal Institute of Technology, Stockholm, Sweden, 2000
10. S. Sun, B.L. Adams, C. Shet, S. Saigal, and W. King, *Scripta Met.* **39**, 501 (1994)
11. W. E. King, G.H. Campbell, A.W. Coombs, G.W. Johnson, B.E. Kelly, T.C. Reitz, S.L. Stoner, W.L. Wien, and D.M. Wilson, in *Joining and Adhesion of Advanced Inorganic Materials*, edited by A. H. Carim, D. S. Schwartz and R. S. Silbergliitt (Mat. Res. Soc. Symp. Proc. **314**, Pittsburgh, PA, 1993) p. 61
12. W. E. King, G. H. Campbell, D. L. Haupt, J. H. Kinney, R. A. Riddle and W. L. Wien, *Scripta Metall. Mater.* **33**, 1941 (1995).
13. G. Hognestad, and D. A. Hills, *Journal of Strain Analysis for Engineering Design* **29**, 79 (1994)
14. B. L. Adams, S. I. Wright, and K. Kunze, *Met. Trans. A* **24A**, 819 (1993)

Micromechanical Modeling of Two-Phase Steels

Mikael Nygåards, Dilip Chandrasekaran¹ and Peter Gudmundson

Department of Solid Mechanics

¹Department of Materials Science and Engineering

Royal Institute of Technology

100 04 Stockholm, SWEDEN

ABSTRACT

A two-dimensional micromechanical model based on the finite element method is presented to model two-phase ferritic/pearlitic steels, by aid of generalised plane strain elements. A periodic representative cell containing 100 ferrite grains, and the desired fraction pearlite is used. By applying periodic boundary conditions, loading by an average stress or strain state is possible.

Uniaxial tensile tests were performed on specimens containing the ferrite and pearlite microstructures, and on two-phase materials containing 25% and 58% pearlite respectively. The stress-strain data of the pearlite material is used to fit a laminar dependent Taylor relation to represent the pearlite workhardening. Thereafter, laminar spacings in the two-phase materials are measured, and the total stress-strain response of the materials is modelled. Comparisons between generated data and experiments show good agreement up to a strain of 2%.

INTRODUCTION

Modeling of two-phase materials can be approached with self-consistent methods [1], Mori-Tanaka methods [2] or can easily be amenable with the finite element method (FEM). The advantage with FEM is that all kinds of materials may be modelled, as long as it is possible to define a realistic geometry into the FEM problem formulation, as done by e.g. Böhm *et al.* [3] and Johansson *et al.* [4]. Since this work focuses on modeling of two-phase materials from a microstructural viewpoint, the geometric model generated must be representative of the material at the microstructural scale. A good approach in modeling microstructures is to model only a representative cell that is characteristic of the material. In this case a small fraction of the whole material is considered, typically a certain number of grains. If the cell also is periodic, one may use periodic boundary conditions, which is favourable. A periodic boundary condition formulation that allows one to introduce dummy nodes to control the average strains and average stresses over a periodic cell has been proposed by Adolfsson and Gudmundson [5].

MATERIAL CHARACTERISATION

Four different ferrite/pearlite steels are used in this study. The materials were supplied by SSAB Swedish Steel AB, and have varying amount of pearlite: 0%, 25%, 58% and 100%. Micrographs of Material 2 and Material 3 are shown in Figure 1. From microstructure micrographs (SEM) it is apparent that the pearlite laminar spacing differs between the different materials. By measuring the finest laminar spacing in each material the pearlite in the material could be characterised, as presented in Table 1. The trend is that the pearlite laminar spacing decreases with pearlite content.

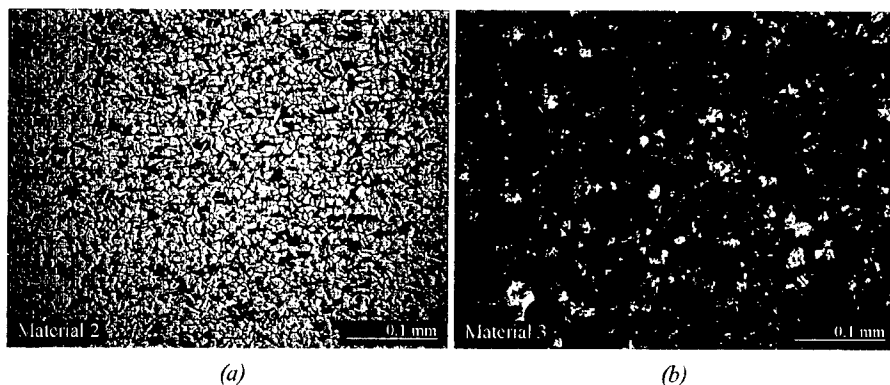


Figure 1. Microstructures of (a) Material 2 (25% pearlite) and (b) Material 3 (58% pearlite).

Table 1. Pearlite laminar spacing, l , in the materials.

	Material 1	Material 2	Material 3	Material 4
$l / \mu\text{m}$	-	0.3	0.25	0.15

The materials have been tested in uniaxial loading, which is presented in Figure 2. Pearlite is a laminar structure, built up of ferrite and cementite, and is harder than pure ferrite. Therefore, a higher pearlite content gives a harder material.

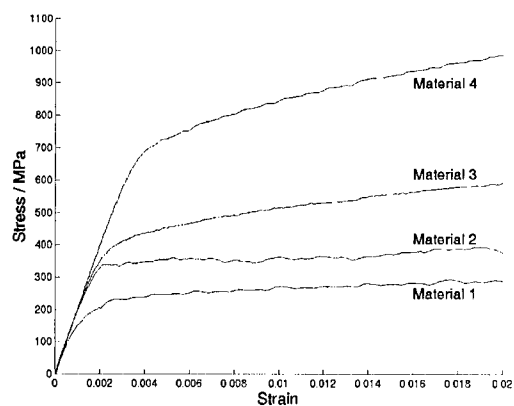


Figure 2. Measured stress-strain curves. Materials 1, 2, 3, 4 contain respectively 0%, 25%, 58% and 100% pearlite.

NUMERICAL MODEL

The idea behind the numerical modeling is to use a unit cell model. In this case a representative part of the microstructure is modelled. The advantage with such a unit cell is that a fairly small part of the material can be considered (in this study the cell contains 100 grains), which considerably saves computational time. Still the average behaviour of the materials is captured, as long as the unit cell is representative.

For modeling of microstructures, the Voronoi algorithm has been found to be applicable. In the general two-dimensional case, the algorithm partitions space into polygons. This structure shows resemblance with real microstructures, which is advantageous. The original unit cell used in this study contains 100 Voronoi cells. It is worth noting (in Figure 3) that the unit cell is periodic, it has three pairs of equivalent sides, and this enables us to use periodic boundary conditions.

It has been shown earlier that the model predicts the experimental data quite well [6], but it can be improved by considering microstructural data. The purpose of this study is to incorporate the pearlite lamellar spacing in the material description, for modeling of the two-phase materials.

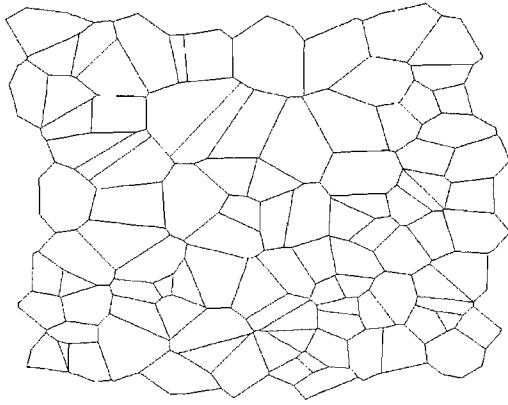


Figure 3. The periodic Voronoi cell containing 100 grains. Note the periodicity, there are three pairs of equivalent edges: left-right, top-bottom and upper left-lower right.

According to Ashby [7] the stress-strain relationship for the pearlitic structure can be assumed to depend on the interlaminar spacing, l , as,

$$\sigma = \sigma_0 + C_p \sqrt{\frac{\epsilon^{pl}}{l}},$$

where σ_0 is the yield strength and ϵ^{pl} is plastic strain. The equation above is fitted to the stress-strain curves for Material 4, and thereby the constant C_p is determined ($C_p = 1.18 \text{ MPam}^{1/2}$). For

the ferrite, the plastic properties are fitted to the stress-strain curve for Material 1, and are also assumed to behave in the same manner for all materials.

The finite element method is used to solve the micromechanical problem. To enable the use of FEM, the cell is meshed. Meshing of irregular structures is a fairly difficult task, but there are several commercial and public domain softwares available. In this case a Matlab [8] routine with an adaptive mesh generator is used. Thereby, finer elements are created around short boundaries. This fact is utilised to create our two-phase materials, by adding the pearlite structure in a physically motivated manner. The mesh generator creates smaller elements close to grain boundaries and short boundaries, which also is the pearlite location in the materials. Therefore, as the cell is meshed the desired fraction of the smallest elements is sorted out to represent the pearlite. In this way, the pearlite “grows” out of the boundaries as the amount increases. It also creates a pearlite structure, with smaller and larger pearlite colonies, that is irregular within the cell. In Figure 4, the periodic cell representing Material 2 and Material 3 is shown. Note that the same finite element mesh is used for the two volume fractions pearlite. The only feature that differs between the cells is the amount of elements that represent the pearlite. In Material 2, 25 % of the cell is pearlite, while in Material 3, it is 58 %.

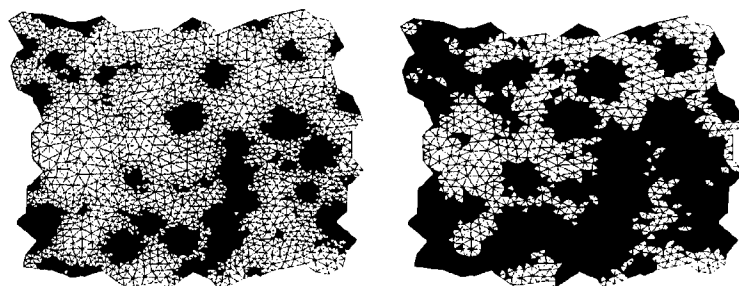


Figure 4. Meshed periodic cells, Material 2 (25% pearlite) and Material 3 (58% pearlite). Dark grey elements represent the pearlite and light grey elements represent ferrite.

The finite element problem is solved with the commercially available program ABAQUS [9]. In the model, 5-noded generalized plane strain elements are used. The ferrite and pearlite is modelled as elastic-plastic materials ($E = 202$ GPa and $\nu=0.3$), with von Mises plasticity and isotropic hardening.

RESULTS AND DISCUSSION

We are primarily interested in studying the materials on a continuum basis, particularly the average stresses and strains over the periodic cells. By aid of the periodic boundary condition formulation we introduce dummy nodes, one node for each component in the average strain tensor. In the formulation, the displacement of the nodes are interpreted as average strains, and by use of the principle of virtual work, the reaction forces of the same nodes can be identified as the average stresses times the volume of the cell. This formulation makes it possible to compare average stress-strain curves of the models, with experimental uniaxial tension tests. In Figure 4,

the results for Material 2 and Material 3 are plotted. First, we have the solid lines that represent the experiments. Secondly, the dotted lines that are generated by the Voronoi model, without compensation for the differences in pearlite lamellar spacing. Thirdly, the results for the Voronoi model with the pearlite model included are plotted as dashed lines. It is obvious that the Voronoi model overestimates the stresses, but when the pearlite lamellar spacing dependency is incorporated in the model, the stresses at high strains come much closer to the experimental curves. A major advantage with the random generation of the Voronoi model is that it is possible to generate several different periodic cells, which gives a statistical basis for the pearlite locations because of the different meshes. As ten different cells were generated, the standard deviation of the stress at 2% strain was 5.0 MPa for Material 2 and 6.6 MPa for Material 3, i.e. about 1% deviation.

However, around the yield point, none of the models predicts the results very well. This is basically due to the fact that more complicated deformation mechanisms are operating around the yield point, e.g. Lüders band formation, and other dislocation based mechanisms that are difficult to catch with continuum models. Even though the pearlite structure has a complicated lamellar structure, it is fairly well predicted with continuum mechanics after some loading. This fact makes us optimistic in modeling two-phase microstructures by the finite element method, and especially with the Voronoi model, which has been compared to other models elsewhere [6]. In that study it was concluded that the Voronoi model best captured the behaviour of this two-phase steel.

If one chooses a material system that consists of two phases that are better described by a continuum, one would probably predict the average properties even better. Especially, as the finite element method offers the opportunity to model very realistic microstructures, and periodic boundary conditions make it possible to model a representative part of the materials, instead of modeling the structure in whole.

A way to further improve the model, but still keeping the continuum approach, would be to model the microstructure in three dimensions. Then, even more realistic microstructures could be modelled. As for now, the microstructure is only elongated in the third direction. However, finite element modeling of arbitrary structure in three dimensions is a difficult task. It is especially the meshing procedure complicates the model generation, since it is difficult to keep the number of elements low enough, and at the same time maintain good aspect ratios of the elements.

CONCLUSIONS

Modeling of two-phase ferrite/pearlite steels has been performed with the finite element method. It was found that better agreement could be reached between experimental uniaxial tension tests and simulations, if the pearlite lamellar spacing was incorporated as a work hardening parameter in the two-phase materials.

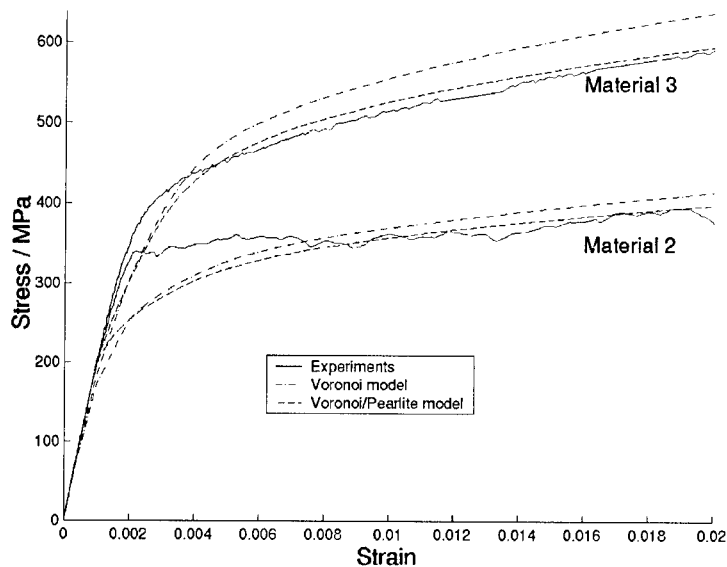


Figure 5. Comparisons between experiments and Voronoi model, with and without pearlite model.

REFERENCES

1. R. Hill, *J.Mech.Phys.Solids*, **15**, 89, 1965.
2. T. Mori and K. Tanaka, *Acta Metall.*, **21**, 571, 1973.
3. H.J. Böhm, F.G. Rammerstorfer, F.D. Fischer and T. Siegmund, *J. Eng. Mater. Technol.*, **116**, 268, 1994.
4. J. Johansson, M. Odén and X.H. Zeng, *Acta Mater.*, **47**, 2669, 1999.
5. E. Adolfsson and P. Gudmundson, *Int. J. Solid Struct.*, **34**, 2035, 1997.
6. M. Nygård and P. Gudmundson, Report 280, Department of Solid Mechanics, Royal Institute of Technology, Stockholm, Sweden, 2000.
7. M.F. Ashby, in *Strengthening methods in crystals*, edited by A. Kelly and R.B. Nicholson, Elsevier Science Publisher, 1971.
8. The MathWorks Inc, Matlab 5.1, 1997 edition, Natick, Massachusetts 01760, USA.
9. Hibbitt, Karlsson & Sorensen Inc, ABAQUS 5.8, 1998 edition, Pawtucket, RI, USA.

Transition regime fracture toughness-temperature properties of two advanced ferritic-martensitic steels

Philippe Spätig, Eric Donahue¹, George R. Odette¹, Glenn E. Lucas¹ and Max Victoria

Fusion Technology, Centre de Recherches en Physique des Plasmas, Ecole Polytechnique
Fédérale de Lausanne, CH-5232 Villigen PSI, SWITZERLAND

¹Department of Mechanical and Environmental Engineering, University of California, Santa
Barbara, CA 93106-5080, U.S.A.

ABSTRACT

Advanced martensitic steels are leading candidate materials for fusion reactor structural components due to their resistance to void swelling, and good balance of physical and mechanical properties. However, irradiations at temperatures below about 400°C result in increases in the cleavage-to-microvoid coalescence transition temperature, as well as reductions in the upper-shelf tearing toughness. This paper reports on the transition regime fracture toughness properties of two unirradiated 7-9Cr martensitic alloys, F82H and T91. Effective fracture toughness-temperature curves, $K_{IC}(T)$, were measured in the transition regime using relatively small pre-cracked specimens. Three sets of data obtained on different specimen sizes and geometries for the two steels are analyzed. All the data can be placed on a single so-called master-curve, when shifts due to size/geometry and material are taken into account. The results from mechanical tests, finite element method (FEM) simulations of crack tip fields and confocal microscopy-fracture reconstruction observations are presented. The link between the different mechanisms taking place at various length scales, resulting in the complex process of cleavage fracture, is discussed.

INTRODUCTION

While tempered martensitic steels are among the most promising candidate materials for structural components of fusion reactors [1], they experience a so-called ductile to brittle fracture mode transition from high-temperature microvoid coalescence to low-temperature cleavage [2]. As a consequence of neutron irradiation, the transition between the ductile and brittle regime is shifted to higher temperature, possibly limiting the use of these steels in some applications to fusion first wall and blanket structures. It is therefore of primary importance to characterize both the fracture properties of the unirradiated material and to develop a methodology, based upon an understanding of the fundamental mechanisms, to assess the changes in fracture toughness under irradiation in order to safely manage reactor structures.

The macroscopic failure in real structures results from the interplay and succession of a series of atomic-, microscopic-, mesoscopic- and macroscopic-scale mechanisms which eventually lead to fracture. Studies and efforts to link the information obtained at an atomic level to macroscopic continuum mechanics scales have been undertaken, e.g. [3, 4, 5]. The goal of this paper is to link our results and investigations performed at different length scales. First, macroscopic measurements of effective fracture toughness data are obtained on two different steels of the 7-9Cr class with relatively small specimens. Second, finite element simulations are shown to be a powerful tool to model the fracture toughness curve based on a local fracture criterion. Finally, support for FEM simulations and insight into the fracture processes are given by means of a fracture reconstruction technique using confocal microscopy, which allows observation of the sequence of events leading to failure from analysis of the three dimensional topographies of the two conjugate fracture surfaces of a broken specimen.

EXPERIMENTAL PROCEDURES

Two plates of advanced reduced activation F82H tempered martensitic steel were investigated as part of an International Energy Agency (IEA) coordinated program on ferritic/martensitic steels. The F82H steel contains 7.65 wt% Cr, 2 wt% W, 0.1 wt% C and a total of less than 1 wt% Mn, Mo, V, Ta, Ti, Si, with the balance Fe. The steel was produced by NKK Corporation under the sponsorship of Japan Atomic Energy Research Institute and was heat-treated by normalizing at 1313 K for 0.5 h and tempering at 1013 K for 2 h [6]. The results of F82H presented here were obtained on specimens cut out from two different plates. In addition, a modified vanadium-niobium-stabilized martensitic steel was studied. The alloy is close to the ASTM designation T91 (Fe-8.26Cr-0.1C-0.95Mo-0.2V-0.075Nb). It was normalized for 2.5h at 1343K and tempered for 4.75h at 1038K. It was produced by CEA-CEREM-DEM-GRENOBLE and provided by ECN Nuclear Energy at Petten.

As a part of an extensive study of the effect of specimen geometry and size on fracture toughness, tests were carried out on fatigue pre-cracked, 20% side-grooved, small compact tension specimens, with crack length a to specimen width W ratios of about $a/W \approx 0.5$ and a specimen thickness (B) to width ratio of $B/W = 0.5$. For F82H, $B = 4.6$ mm (0.18T CT) and for T91, $B = 5.0$ mm (0.2T CT). Static tests, at a ram displacement rate of about $4 \mu\text{m/s}$, were carried out under displacement control on a servohydraulic load frame at temperatures ranging from 77 to 188 K. Temperature control was provided by either a liquid-nitrogen-cooled alcohol bath or a regulated N_2 gas environment. Test and analysis procedures to determine K_{Jc} or K_Q , representing valid small scale yielding elastic-plastic toughness and large scale yielding toughness, respectively, were based on ASTM Standard Practice E813 and E1921-97, where the specimen geometry can also be found.

EXPERIMENTAL RESULTS AND DISCUSSION

Mechanical testing

It is now well established that the fracture toughness temperature curves of reactor pressure vessel steels (RPV steels) have a relatively constant shape [7]. In 1998, the ASTM Standard Practice E 1921-97 was approved, which allows establishing a transition toughness curve with a relatively small number of specimens based upon several key assumptions including that the toughness temperature curve has a constant master curve (MC) shape. The MC can be indexed on an absolute temperature at a reference temperature T_0 corresponding to a given reference toughness value ($100 \text{ MPa m}^{1/2}$) for a specific loading conditions. The MC equation for RPV steels is given by:

$$K_I(T) = 30 + 70 \exp\{0.019(T - T_0)\} \quad (1)$$

Empirical evidence on RPV steels suggests that irradiation elevates T_0 by ΔT_0 without affecting the shape of the toughness-temperature curve [7]. Therefore, the temperature shifts ΔT_0 induced by irradiation can be used to place the fracture toughness curve on an absolute scale, by replacing T_0 measured on the unirradiated material by $T_0 + \Delta T_0$. More generally, other factors such as specimen size and geometry as well as loading rate also induce ΔT_0 shifts. Using the MC concept and the MC- ΔT shift approach, data obtained in this study with small compact tension specimens (CT) on the T91 and F82H steel are presented and compared with previous data obtained on F82H with larger pre-cracked Charpy (PCC) 3-point bend specimens [8]. Note that the analysis that follows is not based on the procedure in ASTM1921-97. Rather, we follow the

MC- ΔT approach and simply compare the experimental toughness data associated with severe constraint loss as well as more valid elastic plastic data to the MC shape.

The 0.2T CT fracture test results obtained on the T91 steel are shown in Figure 1. Note that all the specimens failed by a quasi-cleavage fracture mode. The data plotted on the figure are K_{Ic} , the static effective fracture toughness, which intrinsically depends on the metallurgical state, loading rate and specimen size and geometry factors.

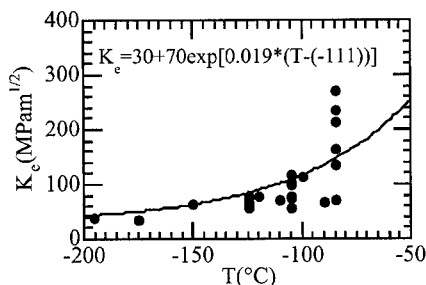


Figure 1. Effective fracture toughness curve versus temperature T91 steel, 0.2T CT specimens

Only for restricted conditions (plane strain, mode I loading, and much smaller plastic zone than the characteristic specimen dimensions), can K_{Ic} be considered as a material property. For the 0.2T CT geometry used here, the K_{Ic} data are reasonably valid up to about 100 MPa m^{1/2} [9] where in-plane constraint is maintained. The few data points lying above 200 MPa m^{1/2} clearly underwent extensive loss of constraint. Using the equation of the MC for the RPV steels, the temperature T_0 for the data of the Figure 1 was about -111°C. K_{Ic} data for F82H have already been presented in [9] and, for the sake of clarity, have not been included in the Figure 1. A fit of the MC on the F82H 0.18T CT data yielded a temperature T_0 of -132°C. It was previously shown that the MC for RPV steels well represented the $K_{Ic}(T)$ trends for another plate of F82H data. In this case the tests were on PCC specimens with $a/W = 0.5$ and $W=B=10$ mm. In this case T_0 was found to be about -75°C. In order to plot all the data along a single MC, chosen as the curve for the F82H PCC specimens, the data of the CT specimens of T91 and F82H steels have been shifted by ΔT s of 36 and 57°C, respectively. The data are plotted in Figure 2. Table I summarizes the different conditions and respective shifts of the MC with respect to the reference curve of the PCC specimens of F82H. It appears that the RPV MC satisfactorily models the experimental K_{Ic} data. However, toughness data are associated with large constraint loss and are far from valid at higher temperatures; thus, the agreement is not entirely consistent with the MC-type behavior assumed in E1921-97.

As might be expected, the smaller 0.18TCT specimens of F82H exhibit a lower indexed temperature T_0 than that of the PCC specimens. In addition to plate-to-plate variations, one difference is the crack front length B , since the ligament length $b = W-a$ is only slightly smaller. Effects of the crack front length B on fracture toughness are usually associated with statistical effects [10], but loss of lateral or out-of-plane constraint also occurs for specimens with smaller crack front length. Both effects of decreasing B (statistical and out-of-plane constraint loss) lead to a higher effective toughness, which is equivalent to a lower index temperature T_0 . It is still not well established how these two effects can be separated and quantified and studies are ongoing to address this issue [11]. Of course, as noted above, material differences can also partly explain the differences in T_0 in the three cases. However, the major conclusion is that different sets of

fracture toughness data for tempered martensitic steels can be described by an MC curve-type shape.

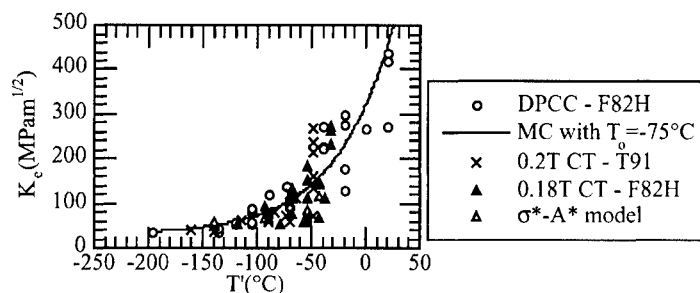


Figure 2. Effective fracture toughness curve versus adjusted temperature T' , 0.2TCT T91 steel, 0.18TCT F82H and DPCC F82H

Table I. Summary of the MC T_0 indexes for the different size/geometry and materials used in this study

Steel	Specimen geometry	W (mm)	B (mm)	a/w	T_0 (°C)	ΔT (°C)
F82H (UCSB plate)	Charpy	10	10	0.5	-75	0
F82H (PSI plate)	0.18T CT	9	4.5	0.5	-132	57
T91	0.2 T CT	10	5	0.5	-111	36

FEM simulations

The microscopic fracture behavior was modeled using FEM simulations of the stress/strain fields at the blunting crack tip. Two dimensional plane strain simulations were performed with the ABAQUSTM 5.8 code for both the PCC specimens and 0.18T CT specimens using an empirical constitutive model for F82H. ABAQUS models the effect of the multiaxial stress state using the Mises stress potential and associated J_2 flow law. The micromechanical model was based on the criteria originally proposed by Ritchie, Knott and Rice [12] stating that the cleavage occurs when a critical stress σ^* exceeds a certain value over a critical distance λ^* , modified by replacing λ^* by a critical area A^* or a critical volume V^* . The local quasi-cleavage fracture condition used here assumes that quasi-cleavage occurs when σ^* encompasses A^* in front of the crack tip. As described in [2], quasi-cleavage involves multiple microcrack nucleation, followed by propagation and arrest at lath packet and prior austenite grain boundaries. Ductile tear ridges separate the planar cleavage facets, which coalesce into a microcrack/tear ridge process zone which stably grows up to a point of instability. The instability condition corresponds to a critical stress σ^* over a critical distance x^* ahead of the crack tip and requires a critical displacement y^* perpendicular to the fracture plane to accommodate the opening of the process zone. The combination of x^* and y^* results in A^* . The σ^* and A^* are assumed to be independent of temperature. In the references [8, 9], the results of these simulations have been previously presented for the F82H 0.18T CT and PCC specimens. Values of σ^*-A^* were estimated by fitting the $K_{IC}(T)$ to experimental data, and were found to be about $2400\text{MPa}\cdot 10^{-8}\text{m}^2$ and $2200\text{MPa}\cdot 8\cdot 10^{-9}\text{m}^2$ for the 0.18CT and PCC specimens, respectively. The σ^*-A^* calculated values are also plotted on Figure 2.

Confocal microscopy-Fracture reconstruction

The local approach to fracture assessment based upon the σ^*/A^* criterion can be further developed and validated by novel techniques such as confocal microscopy (CM)-fracture reconstruction (FR). This technique was developed several years ago [13] using the specificity of a confocal microscope. Confocal microscopy is used to characterize three-dimensional images of the conjugate fracture surfaces with a resolution of about $0.5\mu\text{m}$ in each direction. The detailed description of this technique can be found in [8, 13]. The objective of this technique is to use the CM information to reproduce the sequence of microscopic events leading to macroscopic failure of the specimens. The location of critical features such as micro-crack initiation, void nucleation, crack growth and propagation of unstable crack can in principle be identified. This is achieved by overlapping the two deformed fracture surfaces to reproduce the crack configuration at the beginning of the test. During FR, the surfaces are then computationally separated by a distance corresponding to the crack tip opening displacement δ . The corresponding locations that separate at various δ are revealed. Thus, the overall evolution of the damage leading to macroscopic fracture can be followed up to a critical value of δ . Example results from the analysis are given in Figure 3, corresponding to the tougher 0.2T CT specimen of T91 tested at -85°C .

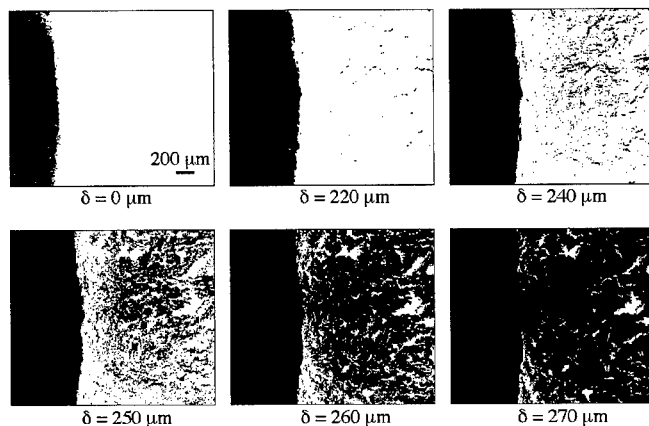


Figure 3. Example of fracture reconstruction, 0.2T CT specimen of T91 at $T = -85^\circ\text{C}$ exhibiting a large amount of plastic deformation before failure by quasi-cleavage.

The separated areas appear in black, while the white areas represent intact material. This specimen failed by quasi-cleavage after a large amount of plastic deformation. It can be seen that the damage initiates at a δ of about $220\mu\text{m}$. As the crack blunts, the damage evolves into a bridged process zone crack [2] and ultimately the micro-cracks coalesce into a macroscopic unstable cleavage crack. The unstable crack propagates at about $\delta_c = 260\mu\text{m}$. This δ_c can be used to calculate the fracture toughness K_{δ} as $K_{\delta} = (2E'\delta_c\sigma_y)^{1/2}$ [8]. In this case the K_{δ} was found equal to $264\text{ MPa m}^{1/2}$ while the K_e measured from the load displacement curve was equal to $270\text{ MPa m}^{1/2}$. Thus, CM-FR provides important insights into the fundamental process of fracture as well as direct measures of fracture toughness. Moreover, correlation between the position of the damage initiation as found by fracture reconstruction and that of the peak stress ahead of the crack tip and ultimately with the σ^*-A^* criterion can be made [2].

CONCLUSIONS

A comparison between fracture toughness data of two advanced tempered martensitic steels was presented. It was shown that the effective fracture toughness curves obtained from the various small specimens of the two different steels tend to follow a constant master curve shape. The master curve was placed on an absolute temperature scale by a reference temperature T_0 . The effects on T_0 of specimen size and geometry, material and material variability were accounted for using the ΔT -MC method. Thus, three sets of different fracture data could be placed on a single master curve after estimation of the ΔT shift with respect to a selected reference curve. FEM simulations of crack tip stress fields were combined with critical stress-critical area local fracture criterion model $K_{IC}(T)$ curves. Finally, it was shown that the CM-FR technique can be used to follow the initiation and development of damage ahead of the crack tip as a function of the crack tip opening and to compare the critical distance from cleavage models to measured distance on the corresponding tomographic images of the damage development

ACKNOWLEDGMENTS

The financial support of the Swiss National Science Foundation and of the DOE Office of Fusion Energy are gratefully acknowledged.

REFERENCES

- [1] A. Hishinuma, A. Kohyama, R. L. Klueh, D. S. Gelles, W. Dietz, K. Ehrlich, J. Nucl. Mat. **258-263** 193 (1998).
- [2] G. R. Odette, J. Nucl. Mat., **212-215** 45 (1994).
- [3] F. Cleri, S. R. Phillpot, D. Wolf, S. Yip, J. of the American Ceramics Society, **81** Nr. 3 501 (1998).
- [4] G.R. Odette, D. Preninger, to appear in J. Nucl. Mat., 283-287 (2001).
- [5] G. R. Odette, M. Y. He, to appear in J. Nucl. Mat., 283-287 (2001).
- [6] M. Tamura, H. Hayakawa, M. Tanimura, A. Hishinuma, T. Kondo, J. Nucl. Mat., **141-143** 1067 (1986).
- [7] K. Wallin, Int. J. Pres. Ves. & Piping, **55** 61 (1993).
- [8] G. R. Odette, K. Edsinger, G. E. Lucas, E. Donahue, ASTM-STP-1328, American Society for Testing and Material, Philadelphia, PA 298 (1998).
- [9] P. Spätig, G. R. Odette, E. Donahue, G. E. Lucas, J. Nucl. Mat., **283-287** 721 (2001).
- [10] K. Wallin, Eng. Fracture Mech. **19** Nr. 6 1085 (1984).
- [11] H. J. Rathbun, G. R. Odette, M. Y. He, G. E. Lucas, J. W. Sheckherd, Pressure Vessels and Piping, **393**, Fracture, Fatigue and Weld Residual Stress, p. 17 ASME (1999).
- [12] R. O. Ritchie, J. F. Knott, J. R. Rice, J. Mechanics and Physics of Solids, **21** 394 (1973).
- [13] K. Edsinger, *PhD Thesis*, University California Santa Barbara (1995).

A Theory for Multi Damage Evaluation of TiN Thin Film

Kazunori Misawa¹, Tomonaga Okabe², Masaaki Yanaka³,
Masao Shimizu¹, Nobuo Takeda²

¹Department of Mechanical Engineering, Keio University, 3-14-1 Hiyoshi,
Kohoku-ku, Yokohama 230, Japan

²Department of Advanced Energy, Graduate School of Frontier Sciences,
The University of Tokyo, c/o Komaba Open Laboratory (KOL), Takeda Lab.,
4-6-1 Komaba, Meguro-ku, Tokyo 153-8904, Japan

³Toppan Technical Research Institute, Sugito-machi, Kitakatsushika-gun, Saitama 345,
Japan

ABSTRACT

The present paper experimentally studies the cracking phenomena of a TiN thin film on a titanium alloy, and presents a new approach to predict the number of cracks under tensile load. An elastoplastic shear-lag model is developed to obtain the stress distribution caused by the film cracks, which is found to agree well with that calculated with FEM. The number of thin film cracks is predicted using a Monte Carlo simulation using the present approach, and favourably compared with the experimental results.

INTRODUCTION

Engineering titanium alloys have attractive mechanical properties and have been used in the aerospace field. However, its poor wear characteristics prevent titanium alloys from being widely used as an engineering material. Then, the surface treatment has been required to overcome this problem. One of such techniques is the thin film coating. However, many studies[1, 2] have already reported that the multiple film cracks are generated by the residual thermal stress and/or the applied load, and can be the cause of the decrease in wear resistance. The main aim of the present study is to experimentally investigate the crack phenomena of a TiN thin film on the titanium alloy substrate and to propose an appropriate crack evolution model. In the present paper, we propose an elastoplastic shear-lag model for a bi-material (Ti-alloy/TiN) plate. This model can easily and accurately calculate the stress distribution in the film on the elastoplastic substrate. Utilizing the present model, a Monte Carlo simulation is conducted for predicting the number of film cracks based on the strength distribution of the observed initial cracks.

EXPERIMENTAL PROCEDURE

A TiN film was deposited on Ti-alloy flat plates (SP-700 (NKK Corporation)) with dimensions of 100 mm x 10.0 mm x 2.0 mm by the arc ion plating method. The

thickness of TiN film was 1.7 μm . A uniaxial tensile test was performed at a constant crosshead speed of 0.4 mm/min.

EXPERIMENTAL RESULTS

Figure 1 shows crack density versus the applied strain ε_c for film thickness 1.7 μm . The crack density was defined as the number of cracks per unit length (1mm). An initial crack was observed at about $\varepsilon_c = 0.2\%$. The crack density kept increasing as the applied strain increased, and was saturated at about 1.1 % strain. From the view point of the engineering application, it should be noted that the film crack can be generated at such a low applied strain. Figure 2 shows the photograph of multiple film cracks after the saturation. Figure 3 shows that the film crack penetrating into the substrate. The substrate crack length was found approximately 4 times as long as the film thickness.

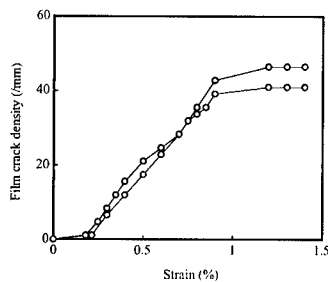


Figure 1. Experimental results of film crack density

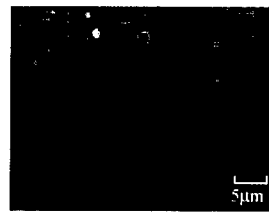
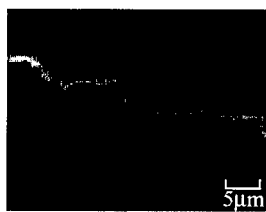


Figure 2. Photograph of multiple film cracks after the saturation



(a)



(b)

Figure 3. Photograph of a crack penetrating into the substrate

When the film is relatively thick, the cracks are generated only due to thermal residual stresses. So, we fabricated several specimens with different film thicknesses to evaluate the thermal residual stress. Figure 4 shows the crack driven only by the thermal residual stress (film thickness: 10 μm). When the thickness was less than 10 μm , the film cracks were not generated. The thermal residual stress σ_{th} calculated by the Beuth model [2] was 358 MPa. Figure 5 shows the Weibull distribution for the stress of the initial crack in the film obtained from experiments with different films. Then, we can

assume that the initial film crack strength within the observed region is $E_f \epsilon' + \sigma_{th}$. When the final crack interval is longer than the critical interval for the influence of crack interactions (8 times of the film thickness), the strength distribution is controlled only by the distributed flaw size in the film. Therefore, it is found that they reasonably follow the Weibull distribution as shown in Fig. 5.



Figure 4. Photograph of a channeling crack

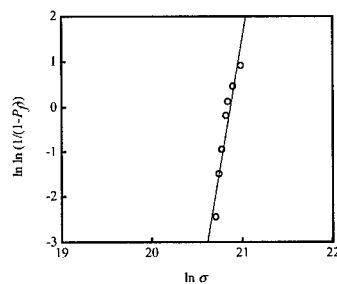


Figure 5. Determination of Weibull parameters using linear regression

ELASTOPLASTIC SHEAR-LAG MODEL

The present paper proposes a new approximate approach which considers the strain hardening effect of the substrate. The present model is shown in Fig. 6. The model includes a substrate, an interfacial shear region and a thin film. The substrate and interfacial shear region are assumed to follow the bilinear elastoplastic stress-strain curve as shown in Fig. 7. In addition, we assume that an interfacial shear region does not carry any axial load and follows the pure shear stress-strain curve of the substrate. The model is divided into $k = 100$ elements and each node is called, in turn, $i = 0, 1, \dots, k$ as shown in Fig. 6. The superscript s and f denote substrate and film, respectively. E^s and E^p are Young's and plastic tangent moduli of the substrate and interfacial shear region, respectively as shown in Fig. 7, and G is the shear modulus of the substrate and interfacial shear region. The thicknesses of the film and interfacial shear region are h and d , respectively.

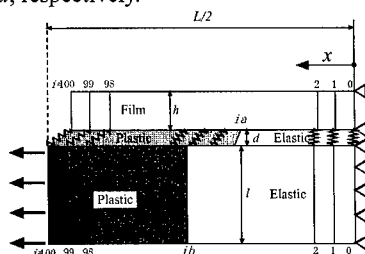


Figure 6. Schematic of the present model

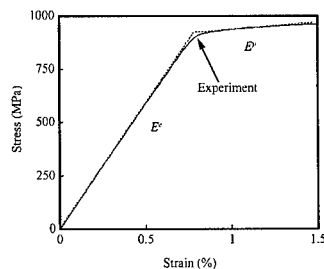


Figure 7. Experimental stress-strain curve of titanium alloy

The shear-lag equations for film elements are divided into two regions as shown in

Fig. 6. One is the case where the film stress is transferred by the elastic interfacial shear region. The other is the case where the film stress is transferred by the plastic interfacial shear region. The shear-lag equations for both regions are given by

$$\frac{d\sigma^f}{dx} = -\frac{\tau}{h} \quad (1)$$

and $\tau = G\gamma$ (Elastic interfacial shear region) (2)

or
$$\tau = \left\{ \frac{3(E^e - E^p)}{E^e E^p} + \frac{1}{G} \right\}^{-1} \left\{ \gamma + \frac{\sqrt{3}(E^e - E^p)}{E^e E^p} \sigma_y \right\} \quad (3)$$

$$= A(\gamma + B) \quad (\text{Plastic interfacial shear region})$$

where γ is the shear strain and σ_y is the yield stress given by the Von-Mises relation. The equation (3) is expressed with the Hencky relation.

The above equations can be approximately rewritten by the nodal displacements and given by

(Elastic interfacial shear region)

$$\left(\frac{G}{hd} + \frac{2E^f}{\Delta x^2} \right) u_i^f = \frac{G}{hd} u_i^s + \frac{E^f}{\Delta x^2} (u_{i-1}^f + u_{i+1}^f) \quad (4)$$

(Plastic interfacial shear region)

$$\left(\frac{A}{hd} + \frac{2E^f}{\Delta x^2} \right) u_i^f = \frac{E^f}{\Delta x^2} (u_{i-1}^f + u_{i+1}^f) + \frac{A}{h} \left(\frac{u_i^s}{d} + B \right) \quad (5)$$

The shear-lag equations for substrate elements are divided into four regions. It is because the substrate itself will be yielded at the higher strain. Thus it should be considered whether the interfacial shear region is elastic or plastic and the substrate is elastic or plastic.

The shear-lag equation for substrate elements are given by

$$\frac{d\sigma^s}{dx} = \frac{\tau}{l} \quad (6)$$

$$\tau = G\gamma \quad (\text{Elastic interfacial shear region}) \quad (7)$$

$$\tau = A(\gamma + B) \quad (\text{Plastic interfacial shear region}) \quad (8)$$

where l is the thickness of the substrate. Though the substrate follows the elastoplastic stress-strain curve shown in Fig. 7, we assume that the interfacial shear stress does not contribute to the increase of the Von-Mises equivalent stress. The above equations can be rewritten by the nodal displacements and given by

(Substrate: Elastic, Interface: Elastic)

$$\left(\frac{G}{ld} + \frac{2E^e}{\Delta x^2}\right)u_i^s = \frac{G}{ld}u_i^f + \frac{E^e}{\Delta x^2}(u_{i-1}^s + u_{i+1}^s) \quad (9)$$

(Substrate: Elastic, Interface: Plastic)

$$\left(\frac{A}{ld} + \frac{2E^e}{\Delta x^2}\right)u_i^s = \frac{A}{l}\left(\frac{u_i^f}{d} - B\right) + \frac{E^e}{\Delta x^2}(u_{i-1}^s + u_{i+1}^s) \quad (10)$$

(Substrate: Plastic, Interface: Elastic)

$$\left(\frac{G}{ld} + \frac{2E^p}{\Delta x^2}\right)u_i^s = \frac{G}{ld}u_i^f + \frac{E^p}{\Delta x^2}(u_{i-1}^s + u_{i+1}^s) \quad (11)$$

(Substrate: Plastic, Interface: Plastic)

$$\left(\frac{A}{ld} + \frac{2E^p}{\Delta x^2}\right)u_i^s = \frac{A}{l}\left(\frac{u_i^f}{d} - B\right) + \frac{E^p}{\Delta x^2}(u_{i-1}^s + u_{i+1}^s) \quad (12)$$

The stress distribution in the TiN film is given by solving Eqs. (1) to (12) numerically[3].

In order to assert the validity of the present model, we conducted the elastoplastic FEM calculation (ABAQUS code). Comparison between the elastoplastic shear-lag model and the FEM analysis for different fragment intervals ($L/2 = 100$ and $50 \mu\text{m}$) is shown in Fig. 8. In this calculation, we used $d=27h$ for arbitrary strain and interval cracks. Although the present model is very simple, the results have good agreements with various kinds of FEM results using one fitting parameter d .

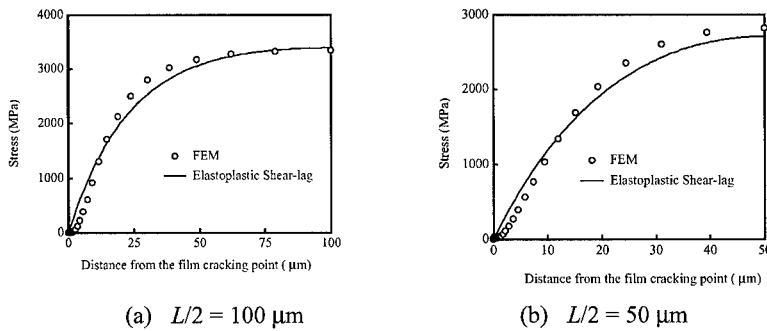


Figure 8. Analytical results for different fragment intervals

MONTE CARLO SIMULATION

To study the film cracking process, a Monte Carlo simulation[4] is conducted. In the simulation program, a film/substrate system of length L_0 , which is the same as the observed field length within the microscope, is subjected to the tensile strain increasing with a discrete step, $\Delta\epsilon$ and the whole length of the film is divided into a number of smaller elements. Assuming the strength of every element follows a Weibull distribution as shown in Fig. 5, the element strength σ_i^{ss} is computationally given by

$$\sigma_i^{ss} = \left[\ln \left(\frac{1}{1 - \eta_i} \right) \frac{L_0}{\delta} \right]^{\frac{1}{m}} \sigma_0 - \sigma_{th} \quad (13)$$

where δ is a length of an unit element, η_i is a random number generated between 0 and 1 in the computer and σ_{th} is the residual thermal stress in the film. As the applied strain increases, it is judged whether the elements are broken or not by comparing each strength with the axial stress obtained from the present shear-lag analysis.

Figure 9 shows the simulated results compared with experiments. The obtained results are reasonably in good agreement with the experimental results. Therefore, it is found that the spatial strength distribution follows the Weibull-Poisson statistics and the cracking phenomena is controlled by the nonlinear stress transfer and the penetration length, which affects the free parameter d .

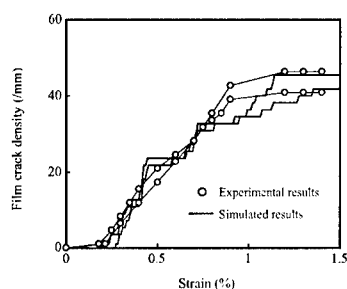


Figure 9. Comparison between present simulation and experimental results

CONCLUSION

The present paper proposed a new theoretical approach to predict the damage process of the TiN thin film on the titanium alloy substrate under the tensile load. A new elastoplastic shear-lag model provided the stress distribution which agreed well with that calculated with the FEM analysis. The number of cracks was successfully simulated by the Monte Carlo Simulation with the present shear-lag approach. This result can be very useful for the damage characterization of TiN thin film coatings.

REFERENCES

1. M. S. Hu and A. G. Evans. The cracking and decohesion of thin films on ductile substrates. *Acta Metall.*, **37**(1989), pp. 917-925
2. J. L. Beuth, JR. Cracking of thin bonded films in residual tension. *Int. J. Solids Structures*, **29**(1992), pp. 1657-1675
3. W. H. Press, B. P. Flannery, S. A. Teukolsky and W. T. Vetterling. *Numerical recipes in C*, Cambridge University Press (1993)
4. W. A. Curtin, A. N. Netravali and J. W. Park. Strength distribution of Carborundum polycrystalline SiC fibers as derived from the single fiber composite. *J. Mater. Sci.*, **29**(1994), pp.4718-4728

Modeling of the Heterogeneous Deformation of an Aggregate of Grains

Philippe P. Eriau, Thierry P. Hoc and Colette C. Rey

Laboratoire MSS-Mat, UMR CNRS 8579, Ecole Centrale Paris,
Grande Voie des Vignes, 92295 Châtenay-Malabry, France

ABSTRACT

Multiple layers of an Interstitial Free (IF) steel microstructure are polished and analyzed using EBSD and Orientation Imaging Microscopy (OIM) technique. This enables to build a 3D finite element mesh which represents the actual grains arrangement. Then a 30 % reduction plane strain compression is applied on this mesh in order to capture the heterogeneous deformation of the aggregate. After deformation, many grains show large orientation spreads, and thus do not follow a Taylor type assumption. This computation also shows that the stored energy distribution depends on the chosen definition.

INTRODUCTION

In polycrystals, nucleation preferential locations prior to recrystallization are located near strain heterogeneities [1], e.g. grain boundaries and triple junction areas, or interfaces between different slip domains. These areas are frequently related to high local stored energy distributions and also to orientation gradients. An accurate understanding of the mechanisms governing recrystallization requires the description of the dislocations arrangements development and the evolution of the mechanical fields arising from their presence. The study of polycrystals deformation has been realized for a long time with homogenization models, especially the Taylor model and its modified versions for computing texture evolution at large strain [2]. In spite of its simplicity and its ability to produce results in qualitative agreement with experiments, the Taylor model does not describe the intra-granular heterogeneity. Moreover, as it is based on the assumption of homogeneous plastic deformation, it can not be used for computing the stored energy. On the contrary, finite element method enables to simulate the inhomogeneous deformation of crystalline aggregates, and brings a new approach to get mesoscopic information. Coupling it with a recrystallization model brings a new way to study the development of recrystallization textures [3]. The interest in such computations is to analyze the bulk interaction effects between grains. Nevertheless, most of the studies dealing with such problems have not considered the grains arrangement in the aggregate according to experimental considerations. In the next part of this paper, a methodology to build a 3D mesh will be detailed which will take into account an actual microstructure discretization. Then a constitutive law based on a hardening matrix depending on dislocation densities on all slip systems will be presented. Dislocation density and plastic work distributions, textures evolution and strain maps will then be deduced from the computation results.

METHODOLOGY

The material used in this simulation is a hot rolled IF steel, presenting an equiaxe grain shape, an isotropic texture, and a grain size about 100 μm . Its composition is given in table I. The crystallographic orientations determination is carried out using a SEM operating at 25 kV and OIM software.

Table I. IF steel chemical composition (10⁻³ % weight)

C	Mn	P	S	N	Al	Ti	Mo	Si	Cu	Cr	Ni	Fe
4.2	129	7	5	3.5	44	108	3	13	17	21	20	Bal.

In order to prepare the EBSD acquisition, a sample is cut from a plate, and a RD-ND section is polished. An area of 504*504 μm^2 is identified and analyzed. The incident electron beam is displaced every 8 μm , in order to obtain a grid of 63*63 elements, which orientations are known by the Bunge angles. The Kikuchi patterns indexations are automatically performed with TSL-OIM analysis software, according to the maximum confidence index computed with all indexations for a given pattern. Once the analysis of the first layer is complete, the sample is polished one more time in order to remove a 25 μm thickness from the surface. Another EBSD analysis of the area which was previously identified is realized and the procedure described above is repeated in order to obtain 6 layers (figure 1). A 150 μm thickness is analyzed using this technique. In order to integrate the results produced by the EBSD acquisition, a 3D mesh was created, which dimensions in the RD-ND plane correspond to the ones of the 6 analyzed layers. This mesh is composed of 12 layers, in order to obtain well-balanced elements. On every layer, every 8-nodes element with selective integration is assigned the exact position and orientation provided by the experimental analysis, in order to obtain the mesh shown on figure 2. Boundary conditions are applied such that the sample deforms by compression along ND and by extension along RD. The moving face which normal is parallel to ND is supposed to remain plane, and the ones normal to TD are enforced not to displace. The imposed thickness reduction is 30 %, which corresponds to a von Mises plastic strain $\epsilon^p=0.41$. The simulation is carried out using AbaqusTM finite element software.

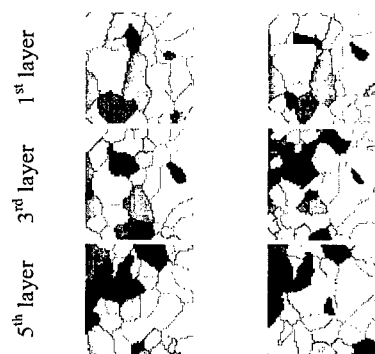


Figure 1. Layers analyzed using EBSD technique

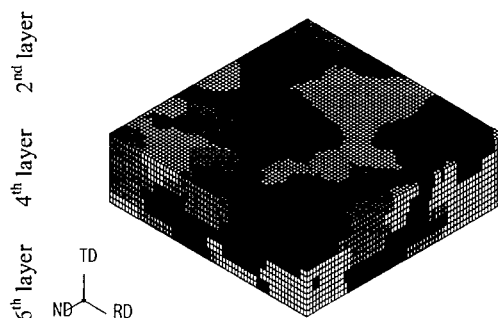


Figure 2. 3D finite element mesh

CRYSTAL PLASTICITY MODEL

The crystalline plasticity constitutive law uses a large deformation framework based on the multiplicative decomposition of the deformation gradient into elastic and plastic parts. At room temperature, slip occurs on the 24 slip systems $\{110\}\langle 111 \rangle$ and $\{112\}\langle 111 \rangle$. The resolved shear stress τ^s , the critical shear stress τ_c^s and the slip rate $\dot{\gamma}^s$ are related by a viscoplastic power law

$$\frac{\dot{\gamma}^s}{\dot{\gamma}_0} = \left(\frac{\tau^s}{\tau_c^s} \right)^n \text{sgn}(\tau^s) \text{ if } |\tau^s| \geq \tau_c^s \text{ and } \dot{\gamma}^s = 0 \text{ otherwise} \quad (1)$$

with $\dot{\gamma}_0$ as a reference slip rate.

As long as slip occurs, hardening is caused by the interactions of different slip systems. This is usually modeled by a phenomenological relationship between a critical shear stress increment and all slip strain increments weighted with an hardening matrix h^{su} .

$$\tau_c^s = \sum_u h^{su} |\dot{\gamma}^u| \quad (2)$$

The hardening terms contained in h^{su} do not remain constant during deformation, but depend on internal variables (dislocation densities on all slip systems) in order to take into account the physical aspects of plasticity [4]. On a particular slip system (s), the evolution of the dislocation density ρ^s is governed by a production term based on Orowan's relationship and is balanced by an annihilation term which takes into account the dynamic recovery during deformation. Thus, it may be shown [5] that

$$h^{su} = \frac{\mu}{2} \frac{1}{\sqrt{\sum_t a^{st} \rho^t}} \left(\frac{1}{L^u} - g_c \rho^u \right) \quad (3)$$

with L^u representing the mean free path of the mobile dislocations gliding on the system u .

$$L^u = \frac{K}{\sum_{t \neq u} \rho^t} \quad (4)$$

μ and b are the respective shear modulus and burger vector magnitude; g_c is proportional to the annihilation distance of dislocation dipoles; K is a material parameter. a^{su} is an hardening matrix which coefficients depend on interactions between dislocation families s and u (table II). The physical meaning of the whole parameters set is detailed in [6]. The parameters used for this simulation were identified [7] using a polycrystalline model and an inverse method from experimental results. They are recapitulated in table III.

Table II. a^{311} matrix interaction coefficients

Plane	$\{110\} \cap \{110\}$	$\{110\} \cap \{112\}$	$\{112\} \cap \{112\}$
Identical	0.125		0.162
Collinear	0.125	0.131	0.162
Not collinear	0.143	0.138	0.186

Table III. Behavior law parameters

Anisotropic elasticity			Viscoplasticity					
C_{11} (MPa)	C_{12} (MPa)	C_{44} (MPa)	K	τ_0 (MPa)	g_s (nm)	n	$\dot{\gamma}_0$ (s^{-1})	ρ_0 (m^{-2})
230	135	116	30	30	10	200	10^{-10}	$66 \cdot 10^9$

τ_0 and ρ_0 are the respective initial shear rate and dislocation density on every slip system s . C_{ij} are the elastic moduli

RESULTS

Texture evolution

The texture evolution is presented on figure 3. The area of the black circle is proportional to the volume fraction of the considered orientation in the aggregate. The initial texture can be assimilated as a random one. According to the finite element modeling, the grains split in many orientations after 30 % reduction. As a comparison, the texture predicted by a Taylor model in which is introduced the same hardening law as presented above, shows that grain rotation has occurred, but of course without any development of orientation spreading.

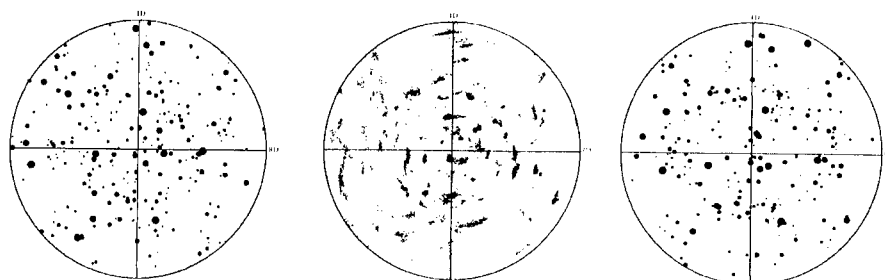


Figure 3. $\{200\}$ pole figure: initial texture(left), FE computation (center), Taylor model computation (right)

Deformation distribution

In this subsection, the effect of the surrounding grains on a particular layer located in the bulk of the aggregate is analyzed (figure 4). This layer presents heterogeneities with highly deformed areas. Although a macroscopic 30% reduction is applied, the deformation in the compressive direction extends from 0.02 to 1. Some highly deformed bands seem to be tilted 30 degrees from the extension direction. They form a quite regular pattern. Some of them cross several grains and do not seem to be affected by the grain boundary presence (figures 4 and 5).

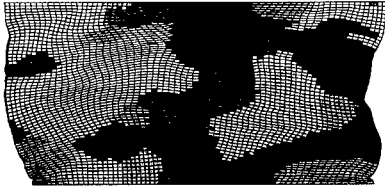


Figure 4. Deformed grains shapes

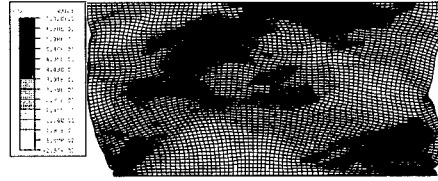


Figure 5. Deformation isovalues in the compression direction

Stored energy

Finally, two ways of estimating the stored energy are performed. After cold work, the stored energy is caused by the elastic energy of the dislocations arrangements. Thus, in first approach, we assume that the stored energy per unit volume is proportional to the total dislocation density ρ and can be computed with the formula

$$E_{st}^p = \frac{1}{2} \mu b^2 \rho \quad (5)$$

According to many papers, the stored energy can be considered as a constant fraction of the plastic work used for straining, and the ratio between the last quantities ranges between 0.5 and 15 % [8]. In the present simulation, the plastic work per unit volume is calculated according to

$$W^p = \frac{1}{V} \int_V \int_0^{\epsilon^p} \sigma d\epsilon^p dV \quad (6)$$

where V is the volume of the considered element. The both simulations results can be seen on figures 6 and 7. In both cases, these quantities are higher near grain boundaries (figure 4). However, the dislocation density gradient between the center of a grain and the grain boundary is higher than the plastic work one. Moreover, the dislocation density is inhomogeneous on both sides of a grain boundary. It is not worthy to correlate the plastic work distribution with the deformation one.

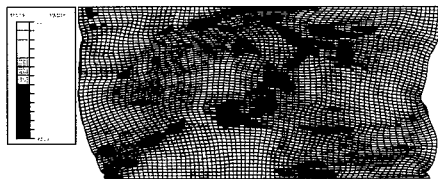


Figure 6. Dislocation density map (arbitrary units)

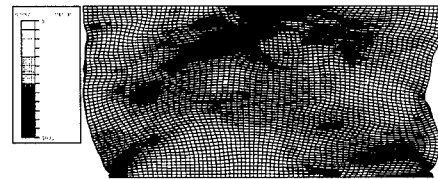


Figure 7. Plastic work distribution (arbitrary units)

It may be seen that high strained areas received a great amount of plastic work (figures 5 and 7). This means in this computation that the plastic work is mainly representative of a glide activity. It is now necessary to analyze the discrepancies between these both computations. In the present model, the dislocation density and the slip evolutions on a particular system are not coupled, as it

is written in equation (3). Thus, the model enables to get a slip increment on the system (s) and at the same time, a steady-state regime for the dislocation density.

Now, the question of the pertinence of these stored energy estimations has to be discussed. First, the total plastic work is not a state variable. Equation (6) depends on the deformation path. Thus, it is not of great evidence that this quantity represents the stored energy.

In the same way, it has been recently shown [9] that the stored energy does not follow a linear law with the dislocation density for high strains. Then, it seems to be necessary to analyze in a more specific way the means of computing the stored energy of cold work before trying to modeling recrystallization.

CONCLUSION

A 3D finite element mesh has been built, according to an actual microstructure. Then a plane strain compression was computed. It enabled to obtain cartographies which have shown the heterogeneous deformation of the grains. Moreover, the texture evolution was analyzed and does not follow a Taylor type assumption. Then, two usual ways of estimating the stored energy of cold work were performed. Some discrepancies were observed between the both results. They proceed from the non-proportionality between the strain and dislocation densities rates in the model.

REFERENCES

- 1 F.J. Humphreys, and M. Hatherly, in *Recrystallization and related annealing phenomena*, 2nd ed. (Pergamon Press, 1996)
- 2 E. Aernoudt, P. van Houtte, and T. Leffers, in *Material Science and Technology, a comprehensive treatment*, edited by R.W. Cahn, P. Haasen, and E.J. Kramer, **6**, pp 89-136 (1993)
- 3 B. Radhakrishnan, G. Sarma, and T. Zacharia, in *Proceeding of the Twelfth International Conference on Textures of Materials*, edited by J.A. Szpumar, (Montreal, 1999), pp 352-357
- 4 P. Franciosi, *Acta metall.* **33**, 1601, (1985)
- 5 C. Teodosiu, J.L. Raphanel, and L. Tabourot, in *Large Plastic Deformation. Proceeding of the seminar MECAMAT'91*, edited by C. Teodosiu, J.L. Raphanel, and F. Sidoroff, (Fontainebleau, 1991), pp 153-168
- 6 T. Hoc, C. Rey, and J. Raphanel, accepted in *Acta Mater.*
- 7 T. Hoc, and S. Forest, *Inter. J. Plast.*, **1**, 65, (2001)
- 8 M.B Bever, D.L. Holt, and A.L. Titchener, *The stored energy of cold work* (Pergamon Press, Oxford, 1973)
- 9 M. Verdier, I. Groma, L. Flandin, J. Lendvai, Y. Bréchet, and P. Guyot, *Scripta mater.*, **37**, 449, (1997)

AUTHOR INDEX

- Adams, James B., Z10.1
Andia, Pedro C., Z10.3
Antonelli, Alex, Z10.9
- Bachlechner, Martina E., Z9.3
Bacon, D. J., Z3.4
Barney, Monica M., Z8.6
Bassman, Lori C., Z9.6
Bernstein, N., Z2.7
Beyerlein, I. J., Z2.5
Bulatov, Vasily V., Z1.3
- Cai, Wei, Z1.3
Campbell, Geoffrey H., Z8.6
Chandrasekaran, Dilip, Z8.8
Charbonnier, Corinne, Z1.7, Z5.7
Costanzo, Francesco, Z10.3
Couteau, Olivier, Z1.7
Cox, B. N., Z2.5
- Darden, Thomas, Z7.22
De Hosson, J. Th. M., Z2.4
de Koning, Maurice, Z10.9
Devincre, Benoit, Z1.8
Domain, C., Z3.8
Donahue, Eric, Z7.8
Dunn, C. L., Z2.5
- Erieau, Philippe P., Z7.11
- Farkas, D., Z6.4
Forest, Samuel, Z8.2
Francis, Lorraine F., Z10.5
- Garikipati, Krishna, Z9.6
Gerberich, William W., Z10.5
Gray, Gary L., Z10.3
Gu, X. M., Z4.7
Gudmundson, Peter, Z8.8, Z10.4
Guerrero, C., Z7.7
- Hess, D., Z2.7
Hinojosa, M., Z7.7
Hoc, Thierry P., Z7.11
- Ito, Takehiko, Z10.8
- Kalia, Rajiv K., Z6.5, Z9.3
King, Wayne E., Z8.6
Kliem, H., Z10.10
Kohyama, Masanori, Z7.17
Kruml, Tomas, Z1.7, Z5.7
Kubin, Ladislav P., Z1.8
- Legris, A., Z3.8
Lei, Herong, Z10.5
Li, Xianghong, Z4.9
Lidorikis, Elefterios, Z9.3
Lu, Guang-Hong, Z7.17
Lucas, Glenn E., Z7.8
Luo, Wei-Dong, Z5.4
- Madec, Ronan, Z1.8
Martin, Jean-Luc, Z1.7, Z5.7
Mehl, M. J., Z6.4
Metselaar, E. D., Z2.4
Miller, Ronald E., Z2.9
Misawa, Kazunori, Z7.10
Moriarty, John A., Z1.2
Morris, John W., Z8.6
Mrovec, Matous, Z6.3
- Nakano, Aiichiro, Z6.5, Z9.3
Nguyen-Manh, Duc, Z6.3
Nygårds, Mikael, Z8.8
- Odette, George R., Z7.8
Ogata, Shuji, Z6.5
Okabe, Tomonaga, Z7.10
Onzawa, Tadao, Z10.8
Ortiz, U., Z7.7
Osetsky, Yuri N., Z3.4, Z9.8
- Papaconstantopoulos, D. A., Z6.4
Pelfort, Marta, Z9.8
Pettifor, David G., Z6.3
Pillai, Arun R., Z2.9
Plitzko, Jürgen M., Z8.6
- Rey, Colette C., Z7.11
Reyes, E., Z7.7
Rhee, Moon, Z1.3

Sagui, Celeste, Z7.22
Saito, Shigeki, Z10.8
Schwartz, Adam J., Z8.6
Scriven, L. E., Z10.5
Selinger, Robin L. B., Z5.4
Serra, Anna, Z3.4, Z9.8
Sevillano, J. Gil, Z8.5
Shimizu, Masao, Z7.10
Shimojo, Fuyuki, Z6.5
Singh, B. N., Z3.4
Smith, Brian B., Z5.4
Spätig, Philippe, Z7.8
Sridhar, N., Z2.5
Stölken, James S., Z8.6
Sun, Y. Q., Z4.7

Takahashi, Kunio, Z10.8
Takeda, Nobuo, Z7.10
Tang, Meijie, Z1.2
Tong, Wei, Z4.9
Totsuji, Chieko, Z6.7

Totsuji, Hiroo, Z6.7
Tsuruta, Kenji, Z6.7

Van der Giessen, E., Z2.4
Vashishta, Priya, Z6.5, Z9.3
Victoria, Max, Z7.8
Vitek, Vaclav, Z6.3
Voyiadjis, George Z., Z9.3

Wagner, A., Z10.10
Wikström, A., Z10.4

Yamamoto, Ryoichi, Z7.17
Yanaka, Masaaki, Z7.10
Yang, L. H., Z1.2
Yang, Seung-Yong, Z4.9
Yip, Sidney, Z10.9
Yurick, Thomas J., Z10.3

Zhang, Jie, Z10.1

SUBJECT INDEX

- ab initio
 - calculation, Z7.17
 - simulations, Z3.8
- advanced martensitic steels, Z7.8
- AFM, Z7.7
- Al grain boundary embrittlement, Z7.17
- aluminum/sapphire, Z8.6
- atomistic
 - potential development, Z6.4
 - simulation, Z1.2
- bi-material interfacial fracture, Z2.9
- biomolecular simulations, Z7.22
- bond-order potentials, Z6.3
- boundary conditions, Z1.3
- coating, Z10.5
- composition, Z9.6
- computer simulation, Z5.4
- continuum mechanics, Z10.3
- crack propagation, Z2.4
- crystal plasticity, Z4.9
- curvature measurements, Z10.4
- density functional theory, Z6.5
- dipolar interactions, Z7.22
- discrete dislocation plasticity, Z2.4
- dislocation, Z1.8
 - dynamics, Z1.3
 - exhaustion, Z1.7
 - kink-pair mechanism, Z1.2
 - loop, Z9.8
 - multiplication, Z5.7
 - patterning, Z5.4
- ductile substrate, Z7.10
- dynamic
 - pullout, inertia, crack bridging, Z2.5
 - strain aging, Z4.7, Z4.9
- electron backscatter diffraction, Z8.6
- FACET, Z10.1
- FEM, Z8.8
- film crack, Z7.10
- finite element, Z9.3
 - computation, Z7.11
- fracture, Z2.7
 - surface, Z7.7
 - toughness, Z7.8
- geometrically necessary dislocations, Z8.5
- germanium, Z5.7
- grain boundary, Z6.7
- high frequency, Z10.8
- hybrid simulation, Z6.5
- hydrogen embrittlement, Z3.8
- IF-steel, Z7.11
- image stress, Z1.3
- interface diffusion, Z10.8
- ion dynamics, Z10.10
- iron, Z6.4, Z9.8
- junctions, Z1.8
- kinetic Monte Carlo, Z4.7
- Lennard-Jones, Z10.9
- magnetism, Z6.4
- master-curve, Z7.8
- mechanics, Z9.6
- mesoscopic simulation, Z1.8
- molecular dynamics, Z6.5, Z9.3, Z10.9
- molybdenum, Z6.3
- multiscale
 - modeling, Z2.9
 - simulations, Z2.7, Z9.3
- Na impurity, Z7.17
- nanophase silicon carbide, Z6.7
- non-flat substrates, Z10.4
- particle-mesh Ewald, Z7.22
- phase coexistence, Z10.9
- phonon drag, Z2.4
- plasticity, Z8.5, Z8.8

polycrystal, Z8.2
poly(ethylene oxide), Z10.10
Portevin-Le Chatelier, Z4.7
 effect, Z4.9

quasicontinuum method, Z2.9

residual stresses, Z10.3

self-affinity, Z7.7
self-interstitial cluster, Z9.8
shrinkage, Z10.5
silicon, Z2.7
simulation, Z10.1
size effects, Z8.2, Z8.5
solid state bonding, Z10.8
space charge relaxation, Z10.10
stored energy, Z7.11
strain gradient cosserat, Z8.2

stress(-), Z10.5
 relaxation, Z1.7, Z5.7

thermodynamic formulation, Z9.6
thin films, Z7.10, Z10.3, Z10.4
 growth, Z10.1
three-dimensional dislocation
 dynamics, Z1.2
tight-binding, Z6.3
 molecular dynamics, Z6.7
transmission electron microscopy,
 Z8.6
two-phase, Z8.8

work-hardening, Z1.7

XY rotor model, Z5.4

zirconium alloys, Z3.8